VOLUME 36 JANUARY 1958 NUMBER 1

Canadian Journal of Physics

Editor: H. E. DUCKWORTH

Associate Editors:

L. G. ELLIOTT, *Atomic Energy of Canada, Ltd., Chalk River*
J. S. FOSTER, *McGill University*
G. HERZBERG, *National Research Council of Canada*
L. LEPRINCE-RINGUET, *Ecole Polytechnique, Paris*
B. W. SARGENT, *Queen's University*
G. M. VOLKOFF, *University of British Columbia*
W. H. WATSON, *University of Toronto*
G. A. WOONTON, *McGill University*

Published by THE NATIONAL RESEARCH COUNCIL

OTTAWA CANADA

CANADIAN JOURNAL OF PHYSICS

(*Formerly Section A, Canadian Journal of Research*)

Under the authority of the Chairman of the Committee of the Privy Council on Scientific and Industrial Research, the National Research Council issues THE CANADIAN JOURNAL OF PHYSICS and five other journals devoted to the publication, in English or French, of the results of original scientific research. Matters of general policy concerning these journals are the responsibility of a joint Editorial Board consisting of: members representing the National Research Council of Canada; the Editors of the Journals; and members representing the Royal Society of Canada and four other scientific societies.

EDITORIAL BOARD

Representatives of the National Research Council

R. B. Miller, *University of Alberta*
H. G. Thode, *McMaster University*
D. L. Thomson, *McGill University*
W. H. Watson (Chairman), *University of Toronto*

Editors of the Journals

D. L. Bailey, *University of Toronto*
T. W. M. Cameron, *Macdonald College*
H. E. Duckworth, *McMaster University*
K. A. C. Elliott, *Montreal Neurological Institute*
Léo Marion, *National Research Council*
R. G. E. Murray, *University of Western Ontario*

Representatives of Societies

D. L. Bailey, *University of Toronto*
Royal Society of Canada
T. W. M. Cameron, *Macdonald College*
Royal Society of Canada
H. E. Duckworth, *McMaster University*
Royal Society of Canada
Canadian Association of Physicists
K. A. C. Elliott, *Montreal Neurological Institute*
Canadian Physiological Society
R. G. E. Murray, *University of Western Ontario*
Canadian Society of Microbiologists
H. G. Thode, *McMaster University*
Chemical Institute of Canada
T. Thorvaldson, *University of Saskatchewan*
Royal Society of Canada

Ex officio

Léo Marion (Editor-in-Chief), *National Research Council*
J. B. Marshall (Administration and Awards), *National Research Council*

Manuscripts for publication should be submitted to Dr. H. E. Duckworth, Editor, Canadian Journal of Physics, Hamilton College, McMaster University, Hamilton, Ontario.

(For instructions on preparation of copy, see **Notes to Contributors** (inside back cover).)

Proof, correspondence concerning proof, and orders for reprints should be sent to the Manager, Editorial Office (Research Journals), Division of Administration and Awards, National Research Council, Ottawa 2, Canada.

Subscriptions, renewals, requests for single or back numbers, and all remittances should be sent to Division of Administration and Awards, National Research Council, Ottawa 2, Canada. Remittances should be made payable to the Receiver General of Canada, credit National Research Council.

The journals published, frequency of publication, and prices are:

Canadian Journal of Biochemistry and Physiology	Monthly	$3.00 a year
Canadian Journal of Botany	Bimonthly	$4.00 a year
Canadian Journal of Chemistry	Monthly	$5.00 a year
Canadian Journal of Microbiology	Bimonthly	$3.00 a year
Canadian Journal of Physics	Monthly	$4.00 a year
Canadian Journal of Zoology	Bimonthly	$3.00 a year

The price of regular single numbers of all journals is 75 cents.

VOLUME 36 1958

Canadian Journal of Physics

Editor: H. E. DUCKWORTH

Associate Editors:

L. G. ELLIOTT, *Atomic Energy of Canada, Ltd., Chalk River*
J. S. FOSTER, *McGill University*
G. HERZBERG, *National Research Council of Canada*
L. LEPRINCE-RINGUET, *Ecole Polytechnique, Paris*
B. W. SARGENT, *Queen's University*
G. M. VOLKOFF, *University of British Columbia*
W. H. WATSON, *University of Toronto*
G. A. WOONTON, *McGill University*

Published by THE NATIONAL RESEARCH COUNCIL

OTTAWA CANADA

Canadian Journal of Physics

Issued by THE NATIONAL RESEARCH COUNCIL OF CANADA

VOLUME 36 JANUARY 1958 NUMBER 1

A CONTINUOUSLY RECORDING AUTOMATIC AURORAL RADAR[1]

A. G. MCNAMARA

ABSTRACT

A simple, low-power 50 Mc./s. radar is described which has been designed for automatic recording of radio reflections from auroral ionization. The system features high sensitivity with good reliability. Photographic records are taken in the form of a continuous film strip displaying range and time. A complementary recording system employs circuitry which cancels interference and noise signals but produces an output signal proportional to the integrated echo intensity. The display in this latter case is in the form of a chart record from which data are immediately available.

1. INTRODUCTION

To obtain consistent and continuous data on the occurrence of radar echoes from aurora, a sensitive, reliable, and unattended radar is essential. The radar described here was specifically designed for back-scatter detection of auroral echoes at Ottawa (lat. 45.4° N., long. 75.9° W., geomagnetic lat. 56.8° N.) and the basic principles have been incorporated in the auroral radars used in the Canadian I.G.Y. program. Modifications for use in the I.G.Y. network will be described in later papers concerned with I.G.Y. results. Radars previously used for auroral research (Currie, Forsyth, and Vawter 1953; McNamara and Currie 1954) have usually been modified, high-power, costly, military equipment requiring constant attendance by an operator and much maintenance. The system described here can operate unattended except for film changes at 4-day intervals and periodic checks on transmitter performance and recording sensitivity. Since the radar is also an efficient detector of meteoric ionization, the records yield a continuous count of meteoric activity within the coverage area. Continuous recording with this radar was commenced in April of 1955 and is continuing. During the period April, 1955, to January, 1957, lost recording time from all causes has been less than 4% of the period.

2. THE RADAR EQUIPMENT

The transmitter and receiver block diagram is shown in Fig. 1. The crystal oscillator runs continuously but all other stages are pulsed to eliminate feed-through. To obtain a simple and reliable modulator, the high-power

[1]Manuscript received August 14, 1957.
Contribution from the Division of Radio and Electrical Engineering, National Research Council, Ottawa, Canada.
Issued as N.R.C. No. 4546.

pulsed stages are operated with steady voltages on the plates, and modulation is introduced at the screens. The modulator pulse power requirement is only

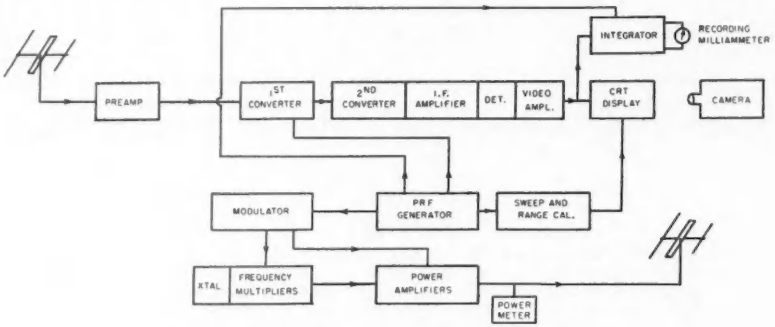

FIG. 1. Block diagram of 50 Mc./s. auroral radar.

20 watts peak. The exciter multiplies the 6 Mc./s. crystal frequency to 48 Mc./s. in three stages using plate and screen pulsing. Peak r-f. pulse output of the exciter is 2 watts. The power amplifier chassis contains an intermediate power-amplifier push-pull stage and final power-amplifier push-pull stage. With up to 4 kv. direct voltage on the plates and fixed negative bias on the grids, the power stages are easily modulated with pulses of about 300 volts amplitude on the screens. Peak r-f. powers of 1 kw. are obtained, the average power being 20 watts. Reliability is thus obtained by simple circuitry and as low peak power as is consistent with the desired sensitivity and range resolution.

Usable range to be displayed is determined by the geometry of the curved earth and the height of reflection of auroral echoes (100 km.) (McNamara and Currie 1954). The geometry of the radar situation is shown in Fig. 2.

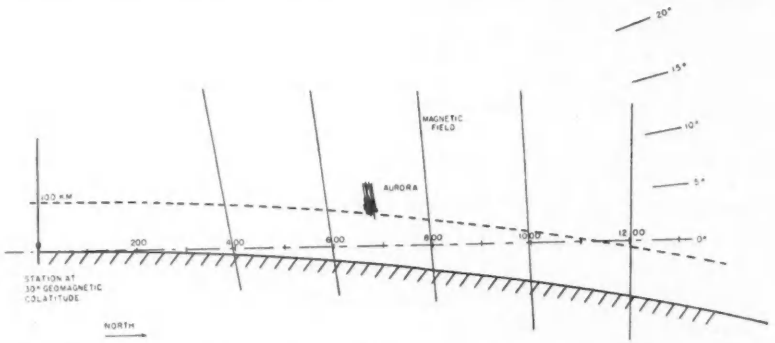

FIG. 2. The geometry of auroral reflections for a typical radar installation directed northward from 60° magnetic latitude.

A value of 1500 km. was adopted for the display. On this range base and with the known characteristics of auroral echoes, the range resolution was set at about 45 km., corresponding to a transmitter pulse length of 300 μseconds.

The receiver is a double-conversion superheterodyne type. A cascode r-f. preamplifier with a noise figure of 3.5 db. is located near the receiving antenna. Crystal-controlled conversion is employed, first to 12 Mc./s. and then to 456 kc./s. where the bandwidth is 10 kc./s.

Long pulse operation permits the use of a modified commercial communications receiver as the final i-f. amplifier. The serious pulse blocking which is characteristic of most communications receivers is circumvented by introducing a blanking pulse in the first converter during the period of the transmitter pulse.

3. ANTENNA SYSTEM

Operation with a fixed antenna orientation (directed horizontally toward magnetic north) contributes to the simplicity and reliability of operation, and also makes operation with separate antennas for transmitting and receiving preferrable. Since auroral echoes are believed to be aspect sensitive owing to anisotropic electron configurations which are elongated along the earth's magnetic field, maximum echo response is obtained from regions in which the radar line-of-sight approaches most closely to orthogonality with

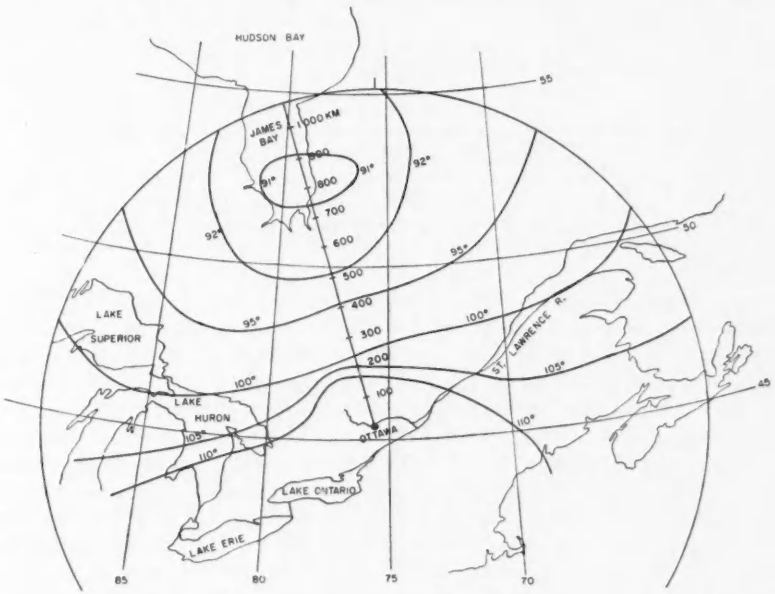

FIG. 3. Contours of the angle of intersection made by the radar line of sight from Ottawa with the earth's magnetic field at a constant height of 100 km. Ranges are measured along the earth's surface.

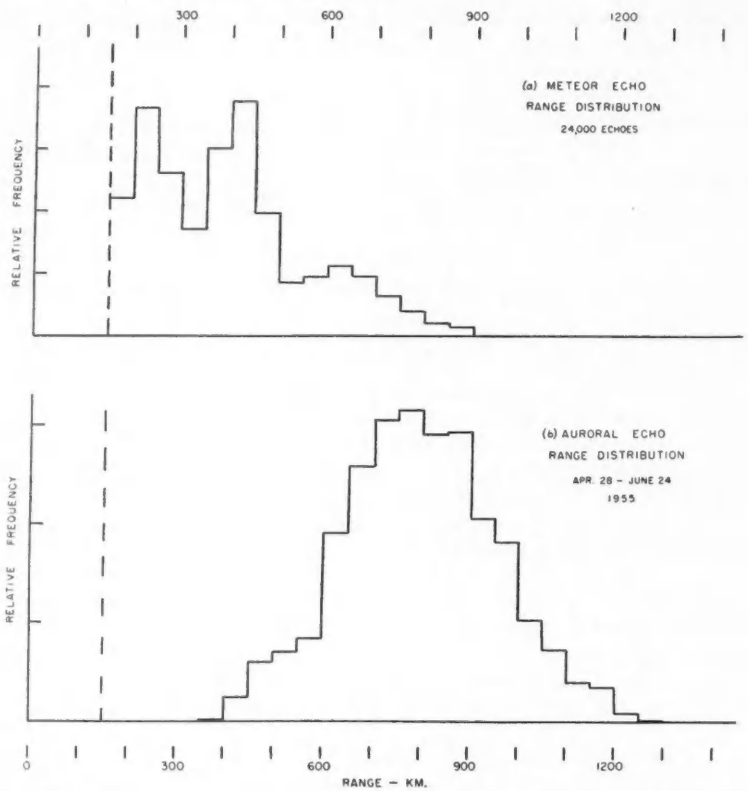

FIG. 4. Range distribution of meteor echoes (*a*) and auroral echoes (*b*). Ranges are slant ranges as measured by the radar.

the earth's field (Moore 1952; Dyce 1955; Booker 1956). Near 50 Mc./s., echoes have been obtained at incident angles of up to 20° from normality. Although the geomagnetic pole controls the geographical distribution of the auroral occurrence, radio and optical data suggest that the final orientation of ionic irregularities at auroral heights is controlled more closely by the magnetic dip-pole. In Fig. 3 contours of the intersection angle are plotted, utilizing smoothed data of the earth's surface field (Vestine *et al.* 1947). The antenna employed is designed to cover the region as effectively as possible. The antennas are horizontally polarized three-element Yagis with free-space *E*- and *H*-plane half-power beamwidths of 80° and 55° respectively. The antenna gain relative to a half-wave dipole is 7 db. The transmitting antenna is elevated about one wavelength above ground and the receiving antenna about three wavelengths with somewhat irregular terrain in front. The vertical-plane propagation pattern is usually calculated by assuming level

terrain. However, a useful check on the propagation pattern, particularly for lobe structure and irregularities in the pattern due to uneven terrain, is afforded by an analysis of the range distribution of the meteor echoes received on the radar. To locate only the null values in the pattern an assumption is made of a certain restricted height of the meteoric ionization, but for more detailed estimation of the relative field strength variation, assumptions must also be made about the radiant distribution, size distribution, and reflection mechanism of the meteors. Examples of the range distributions of aurora and meteor echoes are given in Fig. 4.

4. RECORDING SYSTEMS

Records of the echo signal are made in two complementary ways. The first is a conventional range–time recording of an intensity-modulated cathode ray tube on 35 mm. film with the film moving continuously at 1 foot per hour. A range of 1500 km. is displayed with range markers at 100 km. intervals. The second recording method is somewhat novel in radar applications, employing an Esterline-Angus recording milliammeter to present continuously the integrated (with respect to range and time) echo strength. By using a balanced gating system (Fig. 5) the effects of interference and changing noise level are cancelled from the record. Time integration (normally set at about

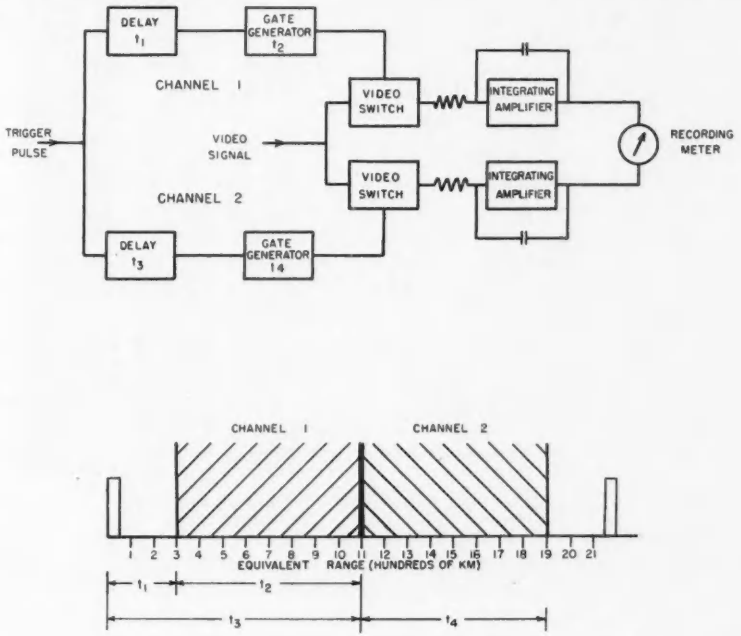

FIG. 5. Block diagram of signal integrator showing the time relationships of the gated channels.

10 seconds time constant) provides signal enhancement and protection against slowly drifting interference pulses.

The video gate of each channel of the integrator is switched on at a predetermined interval after the transmitter pulse. The first gate, or 'signal gate', is switched on during the interval from 300 to 1100 km. and the noise, or 'reference gate', is switched on for an equal period from 1100 to 1900 km. The video gates are designed to produce no pedestal, so that only the signal is integrated. Outputs of the gates are fed to identical integrating amplifiers and the resulting difference signal is applied across a recording milliammeter. A paper speed of 3 feet per day is employed. During the early part of the program the gates were positioned 250–850 km. and 850–1450 km., giving a bidirectional signal on the recorder with short and long range discrimination. This was later changed to the gating system of Fig. 5 for measurements of total integrated signal strength. Occurrence of echoes beyond 1100 km. is sufficiently infrequent that signal cancellation is not a problem. Hence the function of the second gate is now largely that of balance or reference. The two-gate system is simple, very stable, and the excess 'bandwidth' of the gate length results in no more than a 6 db. signal-to-noise loss (the greatest loss is for the case of a discrete echo). At the expense of additional circuitry and a more complex recording instrument, the number of gates can be increased (e.g. to 16 signal and 1 reference gate), to yield echo range analysis and greater sensitivity. The two-gate chart recording system is admirably suited to early-warning monitoring, and to make immediately available measures of daily occurrence and intensity as an activity index. As such, it is anticipated to be of value in the Canadian I.G.Y. auroral program.

5. CALIBRATION AND MONITORING

Routine checks of transmitter and receiver calibration have been developed for the radar. The over-all receiving system is calibrated by disconnecting the antenna and introducing a signal from a noise diode. The output is recorded by deactivating one channel of the integrator and observing the deflection due to noise and signal-plus-noise in the active channel. Transmitter performance is monitored regularly under operating conditions by r-f. voltage and s.w.r. measurements with a peak-reading diode probe on a multitapped section of transmission line in series with the antenna line. Since the probe is practically peak-reading on pulses, no measurement of pulse length, pulse shape, or PRF is required. Peak transmitted power is computed directly from the voltage readings on the s.w.r. section.

6. PERFORMANCE AND RELIABILITY

The radar has been in continuous operation on a 24-hour basis for over 2 years. During that period, lost operating time from all causes has amounted to less than 4%. In the 2-year period, echoes were obtained on 85% of the days, and the mean echo occurrence has been approximately 13% of the total period. Although these figures may appear high when viewed with respect to existing knowledge of visual aurora, it should be remembered that visual

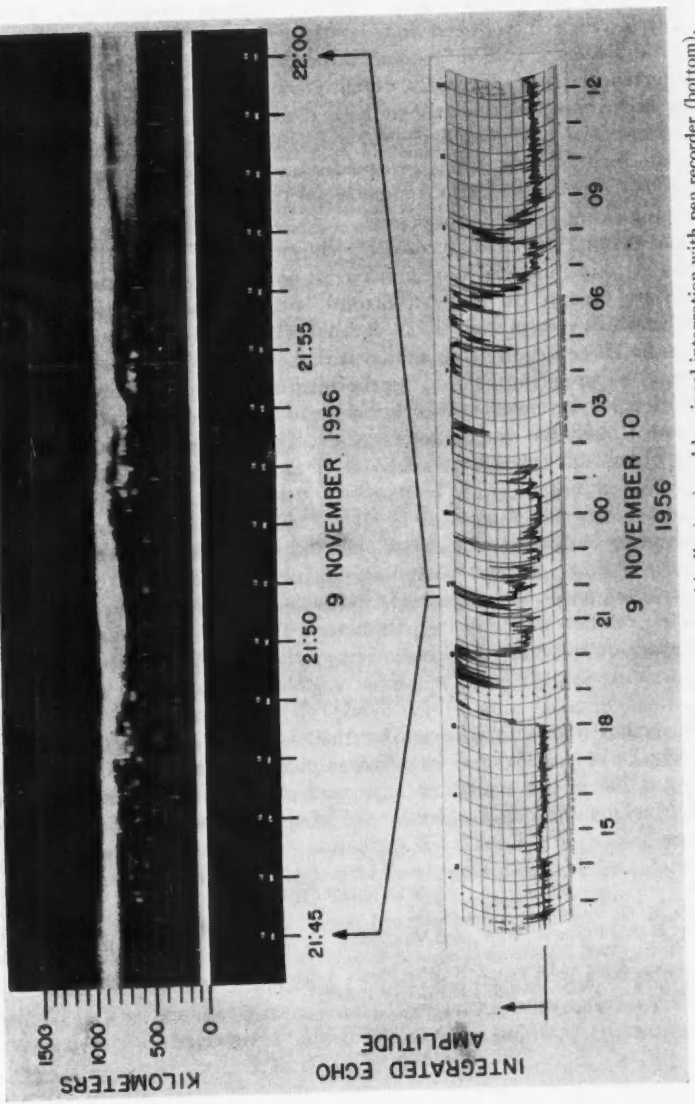

FIG. 6. Example of auroral echoes recorded photographically (top) and by signal integration with pen recorder (bottom).

observations are very restricted by daylight and atmospheric conditions but the radar is not. Actually, Fritz and Vestine's auroral charts suggest that, in the auroral zone, some aurora may occur nearly every night. A limited amount of research has been done on the simultaneous occurrence of visual aurora and echoes, and, in general, the correlation is good—at least in time of occurrence if not always in detailed configuration. Exact knowledge of visual occurrence, particularly at higher geomagnetic latitudes, is not well known but it is anticipated that this will be forthcoming from the I.G.Y. program. Furthermore, it may be noted from Fig. 3 that the region of greatest echo sensitivity for the Ottawa radar is not far (about 5° of latitude) from the nominal location of the auroral zone.

Some examples of radar records are shown in Fig. 6. Fig. 6 (top) is a 15-minute strip of range-vs.-time film record on which both auroral and meteor echoes are present. In Fig. 6 (bottom) is shown the deflection of the pen recorder which results from the integrated echo signal produced by the circuit of Fig. 5. The entire 24-hour period is depicted, and includes the 15-minute interval of Fig. 6 (top). Owing to the integration period in the chart record, most of the meteor echoes visible on the film do not register on the chart. However, those that endure for more than a few seconds produce the sharp spikes observable on the record.

7. CONCLUSIONS

This paper has described a simple and reliable automatic radar system which has proved most effective in monitoring echo activity and characteristics. A companion paper will discuss an analysis of the auroral echo characteristics and their relation to the radar parameters. These are interpreted in terms of their effect on variously defined activity indices of echo occurrence.

ACKNOWLEDGMENTS

The author wishes to acknowledge the assistance of many in the laboratory who have participated in different phases of the design, construction, and operation of this equipment. In particular, B. E. Bourne, L. A. Petch, F. D. MacDonald, J. B. L. Heney, and M. J. Neale have made many contributions.

REFERENCES

Booker, H. G. 1956. J. Atmospheric and Terrest. Phys. **8**, 204.
Currie, B. W., Forsyth, P. A., and Vawter, F. E. 1953. J. Geophys. Research, **58**, 179.
Dyce, R. B. 1955. J. Geophys. Research, **60**, 317.
McNamara, A. G. and Currie, B. W. 1954. J. Geophys. Research, **59**, 279.
Moore, R. K. 1952. Trans. I.R.E., PGAP-3, 217.
Vestine, E. H. *et al.* 1947. Carnegie Inst. of Wash. Publ. No. 578.

ON THE THEORY OF PROPAGATION OF ELECTROMAGNETIC WAVES ALONG A CURVED SURFACE[1]

JAMES R. WAIT

ABSTRACT

The problem of propagation of vertically polarized waves along a surface whose curvature and electrical properties have a discontinuity is considered. The mutual impedance Z between two short vertical antennas on either side of the boundary of separation is considered to be the fundamental quantity which is sought. By utilizing the principle of stationary phase and the concept of surface impedance, an approximate expression is derived for Z. It is shown that to a first order of magnitude, the effects of the conductivity contrast and curvature change are additive corrections to the mutual impedance between dipoles over a single homogeneous spherical surface.

INTRODUCTION

Considerable interest has been shown recently in the problem of vertically polarized electromagnetic waves propagating along an inhomogeneous surface. For the purpose of estimating coverage of broadcast transmitters, it is usually sufficient to assign an equivalent conductivity to the path. Empirical techniques which are simple to apply have been proposed by Suda (1954), Kirke (1949), and Millington (1949). The method of Millington, in particular, has been very successful. Clemmow (1953) in an elegant dissertation obtains a rigorous solution for a line source on a flat earth parallel to a boundary separating two media. In a further theoretical treatment, Bremmer (1954) formulates the problem in terms of an integral equation which he solves by operational methods.

The author (Wait 1956) has recently extended Bremmer's analysis to include the case of propagation along a surface with an oblique traverse at a boundary separating two media. Extensive curves were given in parametric form to permit rapid calculation of the field intensity for mixed path propagation. It was indicated there that the results could be generalized to a spherical earth.[2] It is the purpose of the present note to discuss this problem further and to show that approximate solutions can be obtained for propagation along a curved surface with a sharp boundary. Furthermore, both the electrical constants and the curvature of the media on either side of the boundary can be different.

FORMULATION

The mutual impedance Z between two electric dipoles located at A and B depicted in Fig. 1*a* will be considered. The surface between A and B has a convex curvature. Between A and a point O, the radius of curvature is a;

[1]Manuscript received August 29, 1957.
Contribution from the Central Radio Propagation Laboratory of the National Bureau of Standards, Boulder, Colorado.

[2]In a recent report which has only just become available, Furutsu (1956) considers propagation along mixed paths over a spherical surface. His method is based on solving the dual integral equations for the problem by an iterative procedure.

and between O and B, the radius of curvature is a_1. At the point O, the cylindrical surfaces have a common tangent. It can be anticipated that the mutual or transfer impedance Z is only dependent on the electrical properties and

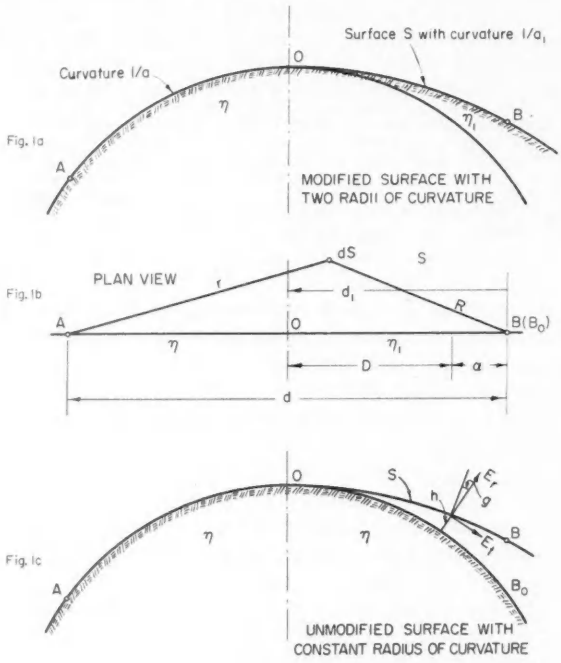

FIG. 1.

the curvature of a narrow strip of the surface between A and B. Therefore, only the curvature of the surface in the principal plane AOB, which normally intersects the cylinder axes, will be significant (Hufford 1952). For this reason it is permissible to consider the contours AO and OB to lie on spherical surfaces of radius a and a_1, respectively. For the purposes of the initial formulation, however, it is really better to retain the idea that the surfaces are cylindrical.

The mutual impedance Z is now expressed in the following form (Ballantine 1929; Monteath 1951):

$$Z - Z_0 = \frac{1}{I^2} \int\int_S [E_A \times H_B' - E_B' \times H_A] \, dS, \tag{1}$$

where Z_0 is the mutual impedance between the dipoles A and B in the instance that the surface is of constant radius of curvature, a, as depicted in Fig. 1*c*. E_A, E_B', H_A, and H_B' are the electric and magnetic fields tangential to the surface S, which is the surface of the cylinder of radius a_1 to the right of O

in Fig. 1. The unprimed quantities refer to the case where the dipoles A and B are in the presence of the single cylinder of radius a (Fig. 1c). The primed quantities refer to the case where A and B are on the modified surface (Fig. 1a). The subscripts A and B on E_A, and E_B', etc., specify that the source of the respective field is a dipole carrying a current I at A or B.[3]

Over the surface S on the modified surface, i.e., the surface of the cylinder of radius a_1, it is assumed that the tangential fields are related by (Monteath 1951)

$$E_B' = -\eta_1 H_B', \tag{2}$$

where η_1 is the surface impedance. The surface of the smaller cylinder containing AOB_0 is considered to have a surface impedance η.

Denoting an arc length along OB by D and invoking the restriction that a and a_1 are large compared to D, it follows that the angle g between the normals on OB and OB_0 is given by

$$g \simeq D\left(\frac{1}{a} - \frac{1}{a_1}\right). \tag{3}$$

The field tangential to S on OB due to a dipole source at A is then

$$E_A = E_r \sin g + E_t \cos g, \tag{4}$$

where E_r and E_t are the electric field components at B radial and tangential to AOB_0. Therefore

$$E_A \simeq E_r(g+w), \tag{5}$$

where

$$w = E_t/E_r \tag{6}$$

and furthermore, since $E_r \simeq \eta_0 H_A$ with $\eta_0 = 120\pi$, it follows that

$$E_A \simeq -\eta_0(g+w)H_A \tag{7}$$

over the surface S. The surface integral now has the form

$$Z - Z_0 \simeq \iint_S [\eta_1 - \eta_0(g+w)]H_A \cdot H_B'\, dS. \tag{8}$$

In the above equation it should be remembered that g and w are functions of position on S; however, it can be expected that only the value of $g+w$ along the arc AOB is significant.

The tangential magnetic fields are now expressed in the following form:

$$H_A = \frac{ik\, I\, ds}{2\pi r}\, e^{-ikr}\, W(r, \eta, a)G(r), \tag{9}$$

$$H_B' = \frac{ik\, I\, ds}{2\pi R}\, e^{-ikR}\, W'(R, \eta, \eta_1, a, a_1), \tag{10}$$

[3] E_A and E_B are essentially contained in the plane AOB whereas H_A and H_B are perpendicular to E_A and E_B, respectively, and to AOB.

where r and R are distances measured from the dipoles of length ds at A and B along the surface containing AOB to dS, and $k = 2\pi/\text{wavelength}$. The quantity W is slowly varying compared to e^{-ikr} and is a function of the surface impedance η of the surface whose principal radius of curvature is a. $W(r, \eta, a)$ is an attenuation function which is characteristic of propagation from A *along the surface* of the sphere of radius a, and it becomes unity in the case of $a = \infty$ and $\eta = 0$. $G(r)$ is a height gain function which accounts for the fact that H_A is to be integrated over the surface S which is above the smaller sphere. $W'(r, \eta, \eta_1, a, a_1)$ is an attenuation factor which is characteristic of propagation from B to a distance R over the modified surface S (i.e., the larger sphere). It is a function of η_1, η, a, and a_1. It is assumed that $a \leqslant a_1$.

Now, in the unmodified system, the mutual impedance between A and B is given by

$$Z_0 = \frac{(ds)^2\, ik\, \eta_0}{2\pi d}\, e^{-ikd}\, W(d, \eta, a)G(d_1) \tag{11}$$

and for the modified system

$$Z = \frac{(ds)^2\, ik\, \eta_0}{2\pi d}\, e^{-ikd}\, W'(d, \eta, \eta_1, a, a_1), \tag{12}$$

where d is the distance between A and B.

THE SOLUTION

The argument leading to the reduction of the surface integration over S in equation (8) to a line integration along OB is exactly the same as in the case of mixed path propagation over a flat surface (Wait 1956). This application of the principle of stationary phase leads to

$$W'(d, \eta, \eta_1, a, a_1) - G(d_1)W(d, \eta, a) = -\frac{1}{\eta_0}\left(\frac{ikd}{2\pi}\right)^{\frac{1}{2}} \int_0^{d_1} [\eta_1 - \eta_0(g+w)]\, \frac{W(d-\alpha, \eta, a)W'(\alpha, \eta, \eta_1, a, a_1)G(d-\alpha)d\alpha}{[\alpha(d-\alpha)]^{\frac{1}{2}}}, \tag{13}$$

where d_1 is always measured to the right of the boundary O. This is an integral equation for W'. It can be immediately noted that if A and B are both to the left of O, the integral vanishes and $W' = W$ since $G(d_1) = 1$. In other words, subject to the stationary phase approximation, the attenuation function W' between two points, when they are located on one side of the boundary, is characteristic only of the electrical properties and the curvature of the homogeneous surface between them.[4] For exactly the same reason, the function $W'(\alpha, \eta, \eta_1, a, a_1)$, where it occurs in the integrand of equation (13), can be replaced by the function $W(\alpha, \eta_1, a_1)$ which is characteristic of propagation from B to a distance α over a homogeneous sphere of surface impedance η_1 and radius a_1.

[4]In other words, the wave reflected from the boundary is neglected. This effect is very small (Wait 1957; Monteath 1951).

The functions W are now expressed in a series expansion in powers of the distance. For example (Bremmer 1953)

$$W(d-\alpha, \eta, a) = \sum_{m=0}^{\infty} A_m'(d-\alpha)^{m/2}\, T^{-m/2}, \tag{14}$$

where $1/T = -(ik/2)(\eta/\eta_0)^2$. The coefficients A_m' up to order nine are given by

$$A_0' = 1, \qquad A_1' = -i\sqrt{\pi}, \qquad A_2' = -2, \qquad A_3' = i\sqrt{\pi}.(1-\delta^3/2),$$

$$A_4' = \frac{4}{3}(1-\delta^3), \qquad A_5' = \frac{-i\sqrt{\pi}}{2}\left(1-\frac{3}{2}\delta^3\right),$$

$$A_6' = -\frac{8}{15}\left(1-2\delta^3+\frac{7}{8}\delta^6\right), \qquad A_7' = \frac{i\sqrt{\pi}}{6}\left(1-\frac{5}{2}\delta^3+2\delta^6\right),$$

$$A_8' = \frac{16}{105}\left(1-3\delta^3+\frac{27}{8}\delta^6\right), \qquad A_9' = \frac{-i\sqrt{\pi}}{24}\left(1-\frac{7}{2}\delta^3+5\delta^6-\frac{21}{8}\delta^9\right),$$

where $\delta = -i(ka)^{-1/3}(\eta_0/\eta)$. The expansion for $W(\alpha, \eta_1, a_1)$ is of exactly the same form with α replacing $d-\alpha$, T_1 replacing T, and δ_1 replacing δ. In this case

$$1/T_1 = -(ik/2)(\eta_1/\eta_0)^2 \tag{15}$$

and

$$\delta_1 = -i(ka)^{-1/3}(\eta_0/\eta_1). \tag{16}$$

Therefore

$$W(\alpha, \eta_1, a_1) = \sum_{m=0}^{\infty} A_m''(\alpha)^{m/2}\, T_1^{-m/2}, \tag{17}$$

where A_m'' are functions of δ_1.

The height gain function G is by definition the ratio of the radial field at a point h above a sphere to its value on the surface. For vertically polarized waves over a homogeneous sphere of surface impedance η, it is given by (Bremmer 1949)

$$G \simeq 1+ik(\eta/\eta_0)h \tag{18}$$

subject to $|(\eta/\eta_0)\delta| < 1/2kh$. But

$$h \simeq \frac{(d_1-\alpha)^2}{2}\left(\frac{1}{a}-\frac{1}{a_1}\right) \tag{19}$$

and therefore

$$G(d_1-\alpha) \simeq 1+\frac{ik\eta}{2\eta_0}(d_1-\alpha)^2\left(\frac{1}{a}-\frac{1}{a_1}\right) \tag{20}$$

and

$$G(d_1) \simeq 1+\frac{ik\eta}{2\eta_0}d_1^2\left(\frac{1}{a}-\frac{1}{a_1}\right).$$

To the same approximation, the wavetilt w at a height h over the homogeneous sphere is given by

$$w \simeq \frac{\eta}{\eta_0}\frac{1}{1+i(\eta/\eta_0)kh}. \tag{21}$$

Therefore

$$G(g+w) \simeq \frac{\eta}{\eta_0}+\left(\frac{1}{a}-\frac{1}{a_1}\right)(d_1-\alpha)\left[1+\frac{i\eta k}{2\eta_0}(d_1-\alpha)^2\left(\frac{1}{a}-\frac{1}{a_1}\right)\right].$$

The second term within the square brackets can be neglected since it is of second order in magnitude. To the same approximation[5]

$$[\eta'-\eta_0(g+w)]G \simeq (\eta_1-\eta)-\eta_0\left(\frac{1}{a}-\frac{1}{a_1}\right)(d_1-\alpha). \tag{22}$$

The equation for the transmission between A and B over the mixed path now becomes

$$\begin{aligned} W'(d)-G(d_1)W(d) &= -\left(\frac{ikd}{2\pi}\right)^{\frac{1}{2}}\left\{\frac{\eta_1-\eta}{\eta_0}\int_0^{d_1}\frac{W(d-\alpha,\eta,\delta)W(\alpha,\eta_1,\delta_1)}{[\alpha(d-\alpha)]^{\frac{1}{2}}}\,d\alpha\right. \\ &\quad \left.-\left(\frac{1}{a}-\frac{1}{a_1}\right)\int_0^{d_1}\frac{W(d-\alpha,\eta,\delta)W(\alpha,\eta_1,\delta_1)(d_1-\alpha)}{[\alpha(d-\alpha)]^{\frac{1}{2}}}\,d\alpha\right\}. \end{aligned} \tag{23}$$

The two integral expressions on the right-hand side of this equation have a clear physical meaning. The first one is a result of the contrast in the surface impedance on the two portions of the path AOB. The second one is a result of the change of curvature on OAB. The reduction of equation (23) to a form useful for computation is a matter of integration. Since the W functions are specified by propagation along a simple homogeneous spherical surface, numerical values of these functions can be readily obtained by standard methods (Norton 1941). The integration with respect to α over the range 0 to d_1 can be effected by a numerical technique. Such a process was carried out in the case of a flat earth for a wide range of the parameters (Wait 1956). The alternative is to insert the appropriate analytical form for the W's in equation (21) and to carry out the integration explicitly. For example, using the series expansions given by equations (14) and (17), it is seen that

$$\begin{aligned} W'(d)-G(d_1)W(d) &= -\left(\frac{ikd}{2\pi}\right)^{\frac{1}{2}}\int_0^{d_1}\sum_{n=0}^{\infty}A_n'\frac{(d-\alpha)^{\frac{1}{4}(n-1)}}{T^{\frac{1}{4}(n-1)}}\sum_{m=0}^{\infty}A_m''\frac{\alpha^{\frac{1}{4}(m-1)}}{T_1^{\frac{1}{4}(m-1)}}\left[\frac{\eta_1-\eta}{\eta_0}\right. \\ &\quad \left.-(d_1-\alpha)\left(\frac{1}{a}-\frac{1}{a_1}\right)\right]d\alpha \\ &= -\left(\frac{ikd}{2\pi}\right)^{\frac{1}{2}}\sum_{n=0}^{\infty}\sum_{m=0}^{\infty}A_n'A_m''\left\{\left[\frac{\eta_1-\eta}{\eta_0}-d_1\left(\frac{1}{a}-\frac{1}{a_1}\right)\right]I_{m,n}\right. \\ &\quad \left.+\left(\frac{1}{a}-\frac{1}{a_1}\right)I_{m+2,n}\right\}, \end{aligned} \tag{24}$$

[5]Equation (22) can be derived directly from the general formula of Feinberg (1946) which is applicable to undulating surfaces.

where

$$I_{m,n} = \int_0^{d_1} \alpha^{\frac{1}{2}(m-1)} (d-\alpha)^{\frac{1}{2}(n-1)}\, d\alpha. \tag{25}$$

The integral $I_{m,n}$ can be reduced by the formulas

$$I_{m,n} = \frac{2}{m+n}(d_1)^{\frac{1}{2}(m+1)}(d-d_1)^{\frac{1}{2}(n-1)} + \frac{(n-1)d}{m+n} I_{m,n-2}, \tag{26a}$$

$$I_{m,n} = \frac{1}{m+n}[(m-1)d I_{m-2,n} - 2(d-d_1)^{\frac{1}{2}(n+1)}\, d_1{}^{\frac{1}{2}(m-1)}], \tag{26b}$$

$$I_{m,1} = \left(\frac{2}{m+1}\right) d_1{}^{\frac{1}{2}(m+1)}, \tag{26c}$$

$$I_{1,n} = \left(\frac{2}{n+1}\right)[d^{\frac{1}{2}(n-1)} - (d-d_1)^{\frac{1}{2}(n-1)}], \tag{26d}$$

$$I_{0,0} = 2 \arctan \left(\frac{d_1}{d-d_1}\right)^{\frac{1}{2}}. \tag{26e}$$

Despite the presence of the double summation in equation (24), the convergence is rapid at lower frequencies and shorter distances (i.e., $d_1 < T$ and T_1). At higher frequencies and greater distances, it is better to employ the representation of the W functions in terms of the residue series (Bremmer 1949). These are given by

$$\frac{W(d-\alpha, \eta, \delta)}{(d-\alpha)^{\frac{1}{4}}} = \left(-\frac{2\pi i}{a}\right)^{\frac{1}{2}} (ka)^{1/6} \sum_{s=0}^{\infty} \frac{\exp[-i\tau_s (ka)^{1/3}(d-\alpha)/a]}{(2\tau_s - 1/\delta^2)} \tag{27}$$

and

$$\frac{W(\alpha, \eta_1, \delta_1)}{\alpha^{\frac{1}{4}}} = \left(-\frac{2\pi i}{a_1}\right)^{\frac{1}{2}} (ka_1)^{1/6} \sum_{q=0}^{\infty} \frac{\exp[-i\tau_q (ka_1)^{1/3}\alpha/a_1]}{(2\tau_q' - 1/\delta_1{}^2)} \tag{28}$$

with

$$\tau_s = v_s - \frac{1}{2v_s\delta} - \frac{1}{8v_s{}^3\delta^2} - \frac{1+3/4v_s{}^3}{12v_s{}^2\delta^3} - \frac{1}{32v_s{}^4}\left(\frac{7}{3} + \frac{5}{4v_s{}^3}\right)\frac{1}{\delta^4} \cdots$$

and

$$\begin{aligned} v_0 &= 0.808\, e^{-i\pi/3}, \\ v_1 &= 2.577\, e^{-i\pi/3}, \\ v_2 &= 3.824\, e^{-i\pi/3}, \\ v_3 &= 4.892\, e^{-i\pi/3}, \\ v_s &\simeq \tfrac{1}{2}[3\pi(s+1/4)]^{2/3}\, e^{-i\pi/3} \text{ for } s > 3. \end{aligned}$$

An expansion for τ_s in a power series in δ is also available (Bremmer 1949). The corresponding series for τ_q' is identical to the above with δ replaced by δ_1. Carrying out the integration indicated in equation (23) leads to

$$(29)\quad W'(d)-G(d_1)W(d)$$

$$= \frac{(2\pi ikd)^{1/2}k^{1/3}}{(aa_1)^{1/3}}\left\{\left[\frac{\eta_1-\eta}{\eta_0}-\left(\frac{1}{a}-\frac{1}{a_1}\right)d_1\right]\right.$$

$$\times\sum_{s=0}^{\infty}\sum_{q=0}^{\infty}\frac{\exp[-i\tau_s(ka)^{1/3}d/a]\,[\exp(iQ_{s,q}d_1)-1]}{(2\tau_s-1/\delta^2)(2\tau_q'-1/\delta_1^{\,2})Q_{s,q}}$$

$$+i\left(\frac{1}{a}-\frac{1}{a_1}\right)\sum_{s=0}^{\infty}\sum_{q=0}^{\infty}\frac{\exp[-i\tau_s(ka)^{1/3}d/a]}{(2\tau_s-1/\delta^2)(2\tau_q'-1/\delta_1^{\,2})}$$

$$\left.\times\left[\frac{\exp[iQ_{s,q}d_1](1-id_1Q_{s,q})-1}{(Q_{s,q})^2}\right]\right\},$$

where

$$Q_{s,q}=\frac{\tau_s(ka)^{1/3}}{a}-\frac{\tau_q'(ka_1)^{1/3}}{a_1}.$$

When the curvature over the path AOB is constant, such that $a_1 = a$, the above equation reduces to

$$(30)\quad W'(d)-W(d)$$

$$= (2\pi ikd)^{1/2}\frac{\eta_1-\eta}{\eta_0}\sum_{s=0}^{\infty}\sum_{q=0}^{\infty}\frac{\exp[-i\tau_s(ka)^{1/3}d/a][\exp[i(ka)^{1/3}(\tau_s-\tau_q')d_1/a]-1]}{(2\tau_s-1/\delta^2)(2\tau_q'-1/\delta_1^{\,2})(\tau_s-\tau_q')}.$$

This special case was given in equivalent form by Furutsu (1956), who obtained it by a different method.

CONCLUDING REMARKS

The preceding discussion has been limited to a two-part medium. Actually the same method can be employed to obtain an approximate formula for the attenuation factor for a path traversing any number of homogeneous segments, each with a different curvature. To illustrate such an extension, a three-part medium is considered which has constant curvature for all three of the segments. The situation is illustrated in Fig. 2. The three media are assumed to have surface impedances η, η_2, and η_1. The separation between

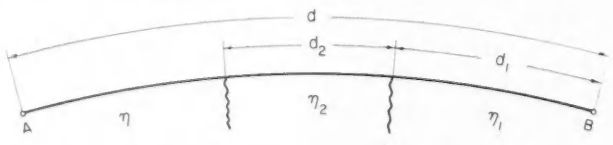

FIG. 2. The three-part path on a smooth surface with constant radius of curvature.

the dipoles A and B is again denoted by d and is measured along the arc of the great circle of radius a. The distances d_1 and d_2 are the lengths of the two segments of surface impedance η_1 and η_2 respectively.

Using the above method, it readily follows that the expression for the attenuation function for this case is

$$W'(d, \eta, \eta_2, \eta_1) = W(d, \eta) - \left(\frac{ikd}{2\pi}\right)^{\frac{1}{2}}\left(\frac{\eta_1-\eta}{\eta_0}\right)\int_0^{d_1} \frac{W(d-\alpha, \eta)W(\alpha, \eta_1)}{[\alpha(d-\alpha)]^{\frac{1}{2}}}\, d\alpha$$

$$-\left(\frac{ikd}{2\pi}\right)^{\frac{1}{2}}\left(\frac{\eta_2-\eta}{\eta_0}\right)\int_{d_1}^{d_1+d_2} \frac{W(d-\alpha, \eta)W'(\alpha, \eta_1, \eta_2)}{[\alpha(d-\alpha)]^{\frac{1}{2}}}\, d\alpha,$$

where $W(d, \eta)$ is the attenuation factor characteristic of propagation from A to B over a homogeneous surface of surface impedance η. $W(d-\alpha, \eta)$ and $W(\alpha, \eta_1)$ are also attenuation functions for propagation over homogeneous surfaces whose surface impedances are η and η_1 respectively. $W'(\alpha, \eta_1, \eta_2)$, on the other hand, is the appropriate two-media attenuation function for propagation from B to the point α on the middle segment.[6]

It follows from equation (23) that

$$W'(\alpha, \eta_1, \eta_2) = W(\alpha, \eta_1) - \left(\frac{ik\alpha}{2\pi}\right)^{\frac{1}{2}}\left(\frac{\eta_2-\eta_1}{\eta_0}\right)\int_0^{\alpha-d_1} \frac{W(\alpha-\alpha', \eta_1)W(\alpha', \eta_2)}{[(\alpha-\alpha')\,\alpha']^{\frac{1}{2}}}\, d\alpha'.$$

The integrals in the above expressions are of precisely the same form as discussed for the two-part medium, and, consequently, series formulas for the three-part path are readily obtained.

For practical field calculations (Wait and Householder 1957) at moderate radio-frequencies over a spherical earth with several homogeneous segments, it turns out to be more convenient to employ numerical integration techniques rather than attempting to sum the doubly infinite series expansions. There may be other instances, however, where the series formulas may be very useful and, in any case, they serve as a valuable check on the numerical integration.

ACKNOWLEDGMENTS

I would like to thank Mr. Z. Godzinski, who carefully read the manuscript, and Mr. K. A. Norton for his helpful comments.

REFERENCES

BALLANTINE, S. 1929. Proc. I.R.E. **17**, 929.
BREMMER, H. 1949. Terrestrial radio waves (Elsevier Publishing Co., Amsterdam).
——— 1953. C.C.I.R. Document 162-E (March).
——— 1954. Physica, **20**, 441.
CLEMMOW, P. C. 1953. Phil. Trans. Roy. Soc. London, **246**, 1.
FEINBERG, E. 1946. J. Phys. (U.S.S.R.), **10**, 410.
FURUTSU, K. 1956. J. Radio Research Lab. (Japan), **3**, 391.
HUFFORD, G. A. 1952. Quart. Appl. Math. **9**, 391.
KIRKE, H. L. 1949. Proc. I.R.E. **37**, 489.
MILLINGTON, G. 1949. Proc. I.E.E. **96**, 53.
MONTEATH, G. D. 1951. Monograph No. 31. Proc. I.E.E. **98**, 1.
NORTON, K. A. 1941. Proc. I.R.E. **29**, 623.
SUDA, K. 1954. Wireless Engineer, **31**, 243.
WAIT, J. R. 1956. J. Research N.B.S. **56**, 237; **57**, 1.
——— 1957. J. Research N.B.S. **58**, 237.
WAIT, J. R. and HOUSEHOLDER, J. 1957. J. Research N.B.S. **59**, 19.

[6]The W functions are understood to be functions of the radius of curvature a.

EVIDENCE FOR THE FORMATION OF LONG-LIVED Bi^{208} BY THE $(n, 2n)$ REACTION ON BISMUTH[1]

J. C. Roy, T. A. Eastwood, and R. C. Hawkings

ABSTRACT

Long-lived Bi^{208} has been observed through its decay by electron capture to the first excited state of Pb^{208} at 2.61 Mev. It has been produced by the $(n, 2n)$ reaction on Bi^{209} in the NRX reactor. The half-life of Bi^{208} has been estimated to be 3×10^4 years, with an uncertainty of a factor of about 2.

INTRODUCTION

Although 17 or 18 isotopes of bismuth are known, the radioactive decay of Bi^{208}, just one mass unit removed from Bi^{209} (the only naturally occurring bismuth isotope), has not been detected (Templeton *et al.* 1947; Kelly and Segrè 1949; and Karraker and Templeton 1951). Neumann and Perlman (1950 and 1951) showed that the half-life is less than 30 seconds or greater than 50 years. Recent experiments of De Benedetti and co-workers (1957) eliminate the former possibility and they conclude that the half-life is long. From studies of β-stability diagrams Kohman (1953) predicted that the half-life is greater than 100 years. However, it is not so long that Bi^{208} occurs in nature; the upper limit to its natural abundance is 0.002% (Nier 1938).

A long half-life for Bi^{208} is also suggested by other evidence. The spin of the ground state of Bi^{208} is likely to be high and Pryce (1952) has argued that it is 5 units while Wahlborn (1957) has suggested that it is 4. The energy difference between the ground state of Bi^{208} and the ground state of Pb^{208} has been estimated by Feather (1953) and Huizenga (1955) to be 2.93 ± 0.07 Mev. Fig. 1 shows the situation of Bi^{208} relative to the isobars of mass 208 (Dzelepov and Peker 1957). A spin of 4 or 5 would exclude a mass for Bi^{208} intermediate between the first excited state of Pb^{208} at 2.615 Mev. and the ground state, since Bi^{208} would be able to decay only by a fourth-forbidden transition to the ground state of Pb^{208} and the lifetime would be so long that primordial Bi^{208} should still be present in natural bismuth. Thus the disintegration energy of Bi^{208} may be higher than 2.61 Mev. and close to the calculated value of 2.93 Mev. If the spin of the ground state of Bi^{208} is $4+$ or $5+$ the transition to the $3-$ first excited state of Pb^{208} would be first-forbidden, and an energy of 0.3 Mev. available for decay by electron capture is consistent with a fairly long half-life.

Charged particle reactions capable of producing Bi^{208}, such as proton, deuteron, or alpha particle bombardments of lead or thallium, or more generally spallation reactions of heavy elements, suffer from the disadvantage that it is often difficult to obtain long irradiations. However, the $Bi^{209}(n, 2n)Bi^{208}$ reaction using reactor neutrons is feasible. From Huizenga's (1955) table of

[1]Manuscript received October 21, 1957.
Contribution from Chemistry and Metallurgy Division, Atomic Energy of Canada Limited, Chalk River, Ontario.
Issued as A.E.C.L. No. 521.

atomic masses the threshold of the reaction is 7.3 Mev. and neutrons of this energy are readily available in a nuclear reactor where long irradiations are

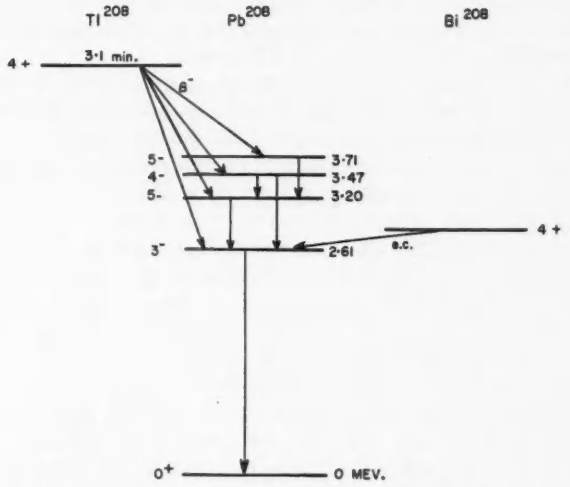

FIG. 1. Mass relationships and energy levels at mass 208. Feather and Huizenga have calculated that the mass difference $Bi^{208}-Pb^{208}$ is 2.93 ± 0.07 Mev.

also possible. This is the reaction we have used to prepare Bi^{208}, and preliminary results are presented here.

The $(n, 2n)$ reaction on bismuth has been studied by other workers (Iampol'ski *et al.* 1955) using pulsed 14 Mev. neutrons and they have found a 2.3–2.4 millisecond γ-activity. This has been attributed to the decay of an excited state of Bi^{208} and not the ground state decay. Vegors and Axel (1956) and De Benedetti *et al.* (1957) have observed this short-lived activity from the (γ, n) reaction on bismuth and the latter group confirms the assignment to Bi^{208}. They also agree that it is the decay of an isomeric state that is observed.

EXPERIMENTAL

A sample of 0.16 g. of bismuth metal was irradiated to an integrated neutron flux of about 2×10^{21} neutrons/cm.^{2} in an empty fuel rod position in the NRX reactor at Chalk River. Chemical treatment began 9 months after the end of the irradiation.

Chemical Purification

In order to show that the activity isolated in this experiment is due to a bismuth isotope the chemical purification procedure will be described in detail.

The irradiated bismuth was dissolved in 6 *N* HNO_3, converted to the chloride, and dissolved in 3 *N* HCl. Tellerium chloride was added to the solution and tellerium metal, which carried Po, was precipitated by the addition of $SnCl_2$

(Meinke 1949). The precipitate was discarded and the Po removal step was repeated twice more. The solution was made 0.1 *N* in HCl and the bismuth was absorbed on an anion exchange resin column (Dowex A-1). After being washed thoroughly with 1 *N*, 8 *N*, and 13 *N* HCl to remove Tl, Pb, Ra, and many lighter elements (Kraus and Nelson 1955) the bismuth was eluted from the column with conc. HNO_3.

The nitric acid was removed by evaporation and the bismuth solution was made 2 *N* in HCl after which bismuth sulphide was precipitated in the presence of the following holdback carriers: Ca, Mn, Fe, Zn, In, and Cd. This step and those outlined below have been described in greater detail by Hutchin (1954). The sulphide precipitate was dissolved in HNO_3 and converted to the chloride form in 0.1 *N* HCl. Bismuth was again absorbed on Dowex A–1, washed, eluted, and Bi_2S_3 reprecipitated as just described. Gamma activity, probably due to Zn^{65}, was detected in the supernatant solution of the first sulphide precipitations and so the Bi_2S_3 cycle was repeated four times until this contamination was removed. Lanthanum carrier was then added to the solution and the fluoride precipitated; no activity was detected in this precipitate.

The bismuth solution was made basic and Bi_2S_3 was precipitated in the presence of Sb, As, Sn, Ba, and Sr holdback carriers. The sulphide precipitate was dissolved in HNO_3 and $Bi(OH)_3$ was precipitated with NH_4OH in the presence of Ni, Co, Cu, and Ag holdback carriers. The Bi_2S_3 precipitation from basic solution and the $Bi(OH)_3$ precipitation were repeated twice more although no activity was detected in the supernatant solutions.

The $Bi(OH)_3$ precipitate was reduced to bismuth metal using sodium stannite and then dissolved in HNO_3. Specific separations of Bi from Pb, Tl, Hg, Sn, Sb, and Ag were done using standard methods. These metals were considered to be most likely impurities but no γ-activity followed the carriers. Finally, $Bi(OH)_3$ was precipitated and reduced to metallic bismuth, which was used for the examination of the radioactivity.

Counting Techniques

Two scintillation spectrometers were used. One had a $1\frac{1}{2}$ in. by 1 in. NaI(Tl) crystal coupled to a 5819 RCA photomultiplier tube. The other had a 3 in. by 3 in. NaI(Tl) crystal coupled to a 6363 DuMont photomultiplier tube. The energy scale of the small crystal spectrometer was calibrated with the 2.76 Mev. gamma ray of Na^{24} and the sum peak of the two Co^{60} gamma rays at 2.50 Mev. The large crystal was calibrated with Na^{24} and the 1.85 and 2.76 Mev. gamma rays of Y^{88}. The efficiency of both crystals at 2.76 Mev. was measured using a Na^{24} source whose disintegration rate had been determined by 4π β-counting. The efficiency at 2.61 Mev. was obtained by making a small correction for the variation of efficiency with energy using Lazar's graphs (Lazar, Davis, and Bell 1956).

The β-activity of the irradiated bismuth was studied using an end window, methane flow, proportional counter. Its window thickness was 2.9 mg./cm.^{2}

RESULTS AND DISCUSSION

The β-particle absorption curve in aluminum showed the presence of only

one β-group of 1.5 Mev. maximum energy. This is probably 4.2 minute Tl^{206} which rapidly comes into equilibrium with its parent, the 2.6×10^6 year isomer of Bi^{210} which, in turn, is formed by the $Bi^{209}(n, \gamma)Bi^{210}$ reaction during the irradiation. The amount observed is in agreement with the calculated yield using the published cross section of 14 millibarns (Hughes and Palevsky 1953).

Following the argument presented in the Introduction Bi^{208} should decay through the 2.61 Mev. excited state of Pb^{208}. The gamma spectrum of the irradiated bismuth was therefore studied in this energy region. Typical results are shown in Fig. 2. Using the $1\frac{1}{2}$ in. by 1 in. crystal a photopeak is evident at 2.61 Mev. and using the larger crystal it is seen at 2.60 Mev. These energies are the same, and agree with 2.61 Mev. for Pb^{208}, within experimental error. As is to be

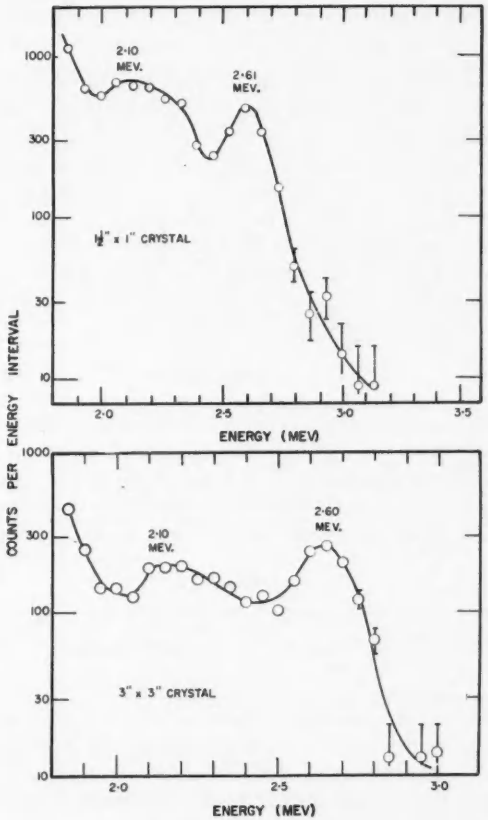

FIG. 2. Gamma spectra of purified, irradiated bismuth after background has been subtracted. The peak at 2.60 Mev. is the photopeak assigned to Bi^{208}; the less clearly resolved peak at 2.1 Mev. is due to pair production with the escape of one annihilation photon. At energies greater than 2.6 Mev. the counting rate of the bismuth sample approaches the background rate of the counter so that the counting errors (indicated by the vertical lines) are large.

expected (Bell 1955) a small peak is present at 2.1 Mev. due to pair production with the escape of one annihilation photon.

No other γ-rays arising from the decay of excited states of Pb^{208} were observed, indicating that Tl^{208} and its parents, if present in the irradiated bismuth, have been removed by the chemical purification. Support to this conclusion is given by preliminary coincidence counting experiments in which no 510 kev. or 590 kev. gamma rays were observed in coincidence with the 2.61 Mev. gamma ray.

The agreement of the energy of the observed gamma ray with the first excited state of Pb^{208} and the fact that the chemical purification of the irradiated bismuth excludes the other radionuclides which can give the same radiation leads to the conclusion that Bi^{208} has been produced by the $Bi^{209}(n, 2n)Bi^{208}$ reaction.

Bi^{208} Half-Life

The half-life of Bi^{208} can be calculated from the disintegration rate and an estimate of the number of atoms present. Assuming that Bi^{208} decays completely through the 2.61 Mev. state of Pb^{208} the disintegration rate is about 1000/sec./g. of irradiated bismuth based on the observed counting rate of the 2.61 Mev. photopeak and the efficiency of the scintillation spectrometer.

The number of atoms of Bi^{208} is more difficult to estimate since it depends on the effective cross section for the $Bi^{209}(n, 2n)Bi^{208}$ reaction in the particular neutron spectrum used for the irradiation. At the moment the only effective cross sections measured in a neutron spectrum similar to that used for the bismuth irradiation are those summarized in Table I.

TABLE I

CROSS SECTIONS FOR $(n, 2n)$ REACTIONS

Target	$(n, 2n)$ reaction threshold (Mev.)	Calculated cross section for fission spectrum neutrons (millibarns)	Observed effective cross sections (millibarns)	Ratio calculated to observed	Reference
Fe^{54}	14	0.0045	0.0001	45	Betts (1957)
I^{127}	9.4	1.7	0.09	19	Roy (1957)
Th^{232}	6.3	22	<1.0	>22	Tunnicliffe (1957)
U^{238}	6.1	29	0.5	57	Hanna (1957)
Bi^{209}	7.3	9.3	[Expected 0.26]	[35]	

The thresholds in the table have been taken from the atomic mass tables of Wapstra (1955) and Huizenga (1955). The cross section for the reaction in a fission neutron spectrum has been calculated by Hughes' method (1953). The effective cross section given in column 4 of the table is that obtained when the integrated neutron flux as measured with a cobalt monitor is used.

All irradiations were done in a fuel rod position in the NRX reactor; however the iron and iodine reactions were observed under conditions more like

those used in the bismuth irradiation. The U^{238} reaction was done in natural uranium, and fission neutrons from the sample itself, as well as neutrons from adjacent fuel rods, were present. The effect of the two types of neutrons had to be resolved, some uncertainty thus being introduced in the result. Similarly, the thorium irradiation conditions were complex because, as the irradiation progressed, fission neutrons arising from fission of the U^{233} which gradually accumulates became more prominent. Neutrons from this source are not detected efficiently by the cobalt flux monitor and for this reason the value of 1.0×10^{-27} cm.^{2} given in Table I is an upper limit and is perhaps twice too large. From the point of view of threshold and mass, on the other hand, the bismuth reaction is more like the U and Th reactions than those of Fe and I. For these reasons all the results have been given about equal weight and from the data in Table I it is observed that the ratio of the calculated cross section to the effective cross section is 35, with an uncertainty of a factor of about 2. This value has been coupled with the calculated cross section of 9.3×10^{-27} cm.^{2} for the $Bi^{209}(n, 2n)$ Bi^{208} reaction to give the expected effective cross section of 0.26×10^{-27} cm.^{2} shown in brackets in Table I. From this value of the cross section it follows that the half-life of Bi^{208} is 3×10^4 years. This result is very approximate, and may be in error by a factor of 2 for the reasons given above. Experiments which should reduce this uncertainty are in progress.

If the decay from Bi^{208} to the first excited state in Pb^{208} is first-forbidden as the predicted spin of Bi^{208} would indicate and the half-life is 3×10^4 years, then the energy available for decay by electron capture would be expected to be considerably less than the estimated 310 kev. Measurements of lead X-rays in coincidence with the 2.61 Mev. gamma rays are being made in an attempt to determine this energy difference.

ACKNOWLEDGMENTS

The coincidence counting experiments referred to were done with the kind co-operation of Dr. C. H. Millar and R. L. Graham. Dr. D. R. MacKenzie prepared the standard Na^{24} sources and W. J. Edwards assisted with the measurement of the gamma spectra; their help is gratefully acknowledged.

REFERENCES

BELL, P. R. 1955. *In* Beta and gamma-ray spectroscopy, *edited by* K. Siegbahn (North-Holland Publishing Co., Amsterdam), chap. V.

BETTS, R. H. and DAHLINGER, O. 1957. Chalk River Laboratories. Private communication.

DEBENEDETTI, S., FARINELLI, U., FERRERO, F., MALVANO, R., PELLI, G., and TRIBUNO, C. 1957. Nuovo cimento, **6**, 682.

DZELEPOV, V. S. and PEKER, L. K. 1957. Decay Schemes of Radioactive Isotopes, Publication of the Academy of Sciences, U.S.S.R., Moscow. Translated and issued at Chalk River as A.E.C.L. Rept. No. 457.

FEATHER, N. 1953. Phil. Mag. Suppl. **2**, 141.

HANNA, G. C. 1957. Chalk River Laboratories. Private communication.

HUGHES, D. J. 1953. Pile neutron research (Addison-Wesley Publishing Co., Inc., Cambridge, Mass.).

HUGHES, D. J. and PALEVSKY, H. 1953. Phys. Rev. **92**, 1206.

HUIZENGA, J. R. 1955. Physica, **21**, 410.

HUTCHIN, W. H. 1954. Radiochemical Procedures in Use at the University of California Radiation Laboratory, *compiled by* M. Lindner, U.S. Atomic Energy Commission Document UCRL-4377.

IAMPOL'SKI, P. A., LEIPUNSKI, O. I., GEN, M. I., and TIKHOMIROV, A. M. 1955. Bull. Acad. Sci. U.S.S.R., Phys. Ser. **19**, 338 (Columbia Technical Trans. p. 312).
KARRAKER, D. G. and TEMPLETON, D. H. 1951. Phys. Rev. **81**, 510.
KELLY, E. L. and SEGRÈ, E. 1949. Phys. Rev. **75**, 999.
KOHMAN, T. P. 1953. U.S. Atomic Energy Commission Document NYO-3621.
KRAUS, K. A. and NELSON, F. 1955. Proceedings of the International Conference on the Peaceful Uses of Atomic Energy, Geneva, Vol. 7, paper P/837, p. 113.
LAZAR, N. H., DAVIS, R. C., and BELL, P. R. 1956. Nucleonics, **14**, No. 4, 52.
MEINKE, W. W. 1949. Chemical Procedures Used in Bombardment Work at Berkeley, U.S. Atomic Energy Commission Document AECD-2738.
NEUMANN, H. M. and PERLMAN, I. 1950. Phys. Rev. **78**, 191.
——— 1951. Phys. Rev. **81**, 958.
NIER, A. O. 1938. Phys. Rev. **54**, 275.
PRYCE, M. H. L. 1952. Proc. Phys. Soc. A, **65**, 773.
ROY, J. C. and MUNRO, D. 1957. To be published.
TEMPLETON, D. H., HOWLAND, J. J., and PERLMAN, I. 1947. Phys. Rev. **72**, 766.
TUNNICLIFFE, P. R. 1957. Chalk River Laboratories. Private communication.
VEGORS, S. H. and AXEL, P. 1956. Phys. Rev. **101**, 1067.
WAHLBORN, S. 1957. Nuclear Phys. **3**, 644.
WAPSTRA, A. H. 1955. Physica, **21**, 378.

THE VISCOSITY OF LIQUID HELIUM AT FREQUENCIES OF 11.8 AND 35.5 KC./SEC.[1]

K. M. Eisele and A. C. Hollis Hallett

ABSTRACT

A solid cylinder set into torsional oscillation at its natural frequency has been used to measure the viscosity of liquid helium in the range 4.2° K. to 1.2° K. Values of the viscosity calculated from the logarithmic decrement of the decay of the oscillations at the natural frequency of 11.8 kc./sec. of the cylinder are in good agreement within the errors, which are of the order of 30%, with the most recent oscillating disk values. Values obtained at a frequency of 35.5 kc./sec. (a harmonic of the cylinder) might be of the order of 10% lower. The depth of penetration of the viscous waves in these experiments was less than 5×10^{-5} cm.

INTRODUCTION

Experimental determinations of the viscosity of liquid helium have been made using essentially two methods: the rotating cylinder viscometer (Heikkila and Hollis Hallett 1955) and the oscillating disk (Hollis Hallett 1952; Dash and Taylor 1957; Taylor and Dash 1957). The rotating cylinder method is a steady state experiment in which measurements are made of the couple exerted on a cylinder by the steady coaxial rotation of the liquid around it. The oscillating disk experiment, on the other hand, is not a steady state experiment, but one in which measurements are made of the damping of torsional oscillations of a disk. It would appear that there is some discrepancy between the results of the two experiments (Taylor and Dash 1957) in that the values of the viscosity deduced from the damping of the oscillations of the disk are somewhat larger than the values from the rotating cylinder viscometer, particularly at temperatures less than about 1.5° K. Accordingly, it seemed worth while to investigate the effect of increasing the frequency of oscillation of an oscillating disk in order to see if the effective viscosity changed with frequency. It was decided to study the decay of oscillations of a cylinder oscillating at its natural frequency, since this method would enable studies to be made at frequencies of the order of 10 kc./sec., considerably greater than the maximum frequency of 0.26 cycles/sec. (period 3.78 sec.) (Hollis Hallett 1952) which had been used before.

In the experiment described a solid cylinder was excited electrically into torsional oscillation of frequency equal to the natural frequency of the cylinder, and then the source of power was shut off and measurements were made of the characteristic time of the exponential decay of the amplitude of oscillation. This procedure was carried out twice, once with the cylinder immersed in liquid helium and once with the cylinder in a high vacuum. The difference between the logarithmic decrements calculated from the measured decay times in helium and in vacuum gave a measure of the frictional damping exerted by the liquid helium on the cylinder, and, from these, values of the effective viscosity were calculated.

[1]Manuscript received July 18, 1957.
Contribution from the Department of Physics, University of Toronto, Toronto, Ontario.

Although the accuracy of the experimental results is only of the order of 30%, it seems clear that there is no major difference between the results at a frequency of 11.8 kc./sec. and those of the oscillating disk. It is possible that the values of the viscosity deduced from measurements made at 35.5 kc./sec. (a harmonic of the cylinder) are slightly lower (about 10%), but it is not possible to decide this definitely.

In the present experiment, only the liquid in a layer of the order of 5×10^{-5} cm. thick surrounding the cylinder is affected by the oscillations of the cylinder. It is interesting to note that in liquid helium II the damping is entirely due to the motion of the normal component only in this small distance, which is only about ten times larger than the thickness of the helium film.

THE APPARATUS

The cylinder and its mounting are shown schematically in Fig. 1. The cylinder A was turned from a solid rod of Duralumin alloy (Alcan 24ST)

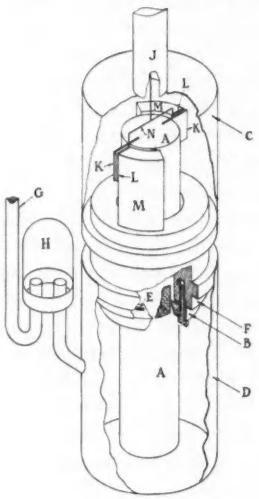

FIG. 1. Schematic drawing of the apparatus.

together with the mounting flange B which supported the cylinder at its mid-length. Although the flange B was of substantial thickness (3/16 in.), it was cut away at the surface of the cylinder so that its thickness there was only 0.001 in. This ensured that the damping effect of the supporting flange would be extremely small since the cylinder was so excited that there was a node of vibration at the flange. The upper and lower halves of the cylinder were separately enclosed by the chambers C and D separated by the flange B; a vacuum-tight seal was effected by squeezing the indium O-ring E between the flange B and the brass chamber support F. The lower chamber D could either be evacuated by pumps connected to the tube G, or filled with liquid helium by admit-

ting and condensing helium gas, previously purified by passage over charcoal immersed in liquid air, through the same tube G. The gauge-glass H served to indicate when the chamber D was full of liquid. The upper chamber C was continuously pumped through the tube J, which also served to support the apparatus at the bottom of a Dewar flask of liquid helium. The pressure in C was maintained at a value less than 10^{-5} mm. of mercury in order to ensure that the upper half of the cylinder would contribute no unaccountable damping.

The principle of the driving mechanism relied on the electrostatic force between two pairs of plates K and L when an alternating voltage was applied between them. The plates K were of thin but rigid titanium sheet pressed into slots cut into the upper end of the cylinder, and, for some cylinders, also secured by very small screws. The static plates L were of brass sheet and were mounted on the supports M of bakelized fabric, which also served to insulate them from the electrical ground of the cylinder. Provision was also made for adjustment of the supports M so that the static plates L could be placed 0.1 mm. from the opposing plates K, and parallel to them. The static plates were connected by a copper strip N to which was soldered a wire which passed up through the supporting tube J to an insulated lead-in seal above.

The cylinder used had a total length of 13.9 cm. and a radius of 1.35 cm.

The driving of the cylinder and the detection of the oscillations and their decay were accomplished electronically. The voltage required between the plates K and L to drive the cylinder was obtained from an a-f. oscillator whose output was amplified to give the 300 volts necessary to obtain an initial amplitude of oscillation sufficiently above noise level to enable the decay to be measured accurately. The frequency of the a-f. oscillator could be adjusted so that it was exactly equal to one-half the resonant frequency of the cylinder, and a microswitch connected it to the driving plates so that the driving voltage could be applied or removed at will. Provision was also made for measurement of the frequency of the driving voltage.

The detection system utilized a principle of F.M. radio detection and recognized that during the oscillation of the cylinder, the capacity between the plates K and L (Fig. 1) would vary with the frequency of oscillation and have an amplitude which was reasonably proportional to the amplitude of oscillation. By connecting a small inductance between the lead-in wire and ground, the plates K and L were made the capacity of an L–C circuit which was slightly detuned from resonance with the induced fields of a 10 Mc./sec. crystal-controlled oscillator. Thus, as the cylinder oscillated, the voltage across the L–C circuit was a 10 Mc./sec. voltage modulated by the frequency of oscillation of the cylinder.

A small calibrated variable condenser connected in parallel with the plates K and L of the cylinder enabled adjustment of the amount of detuning of the L–C circuit from resonance to be made. By means of such adjustment, the amplitude of modulation could be made proportional to the variation of capacity between the cylinder plates, and this was checked experimentally using the small calibrated condenser. This system also enabled measurements to be made of the amplitude of oscillation of the cylinder, and since this was at all times

less than 10^{-6} radian, the amplitude of modulation was proportional to the amplitude of oscillation to a high degree of precision.

The remainder of the detection circuit comprised suitable amplifiers and a system whereby the time τ taken for the amplitude of the a-c. voltage across the L–C circuit to decay from one calibrated amplitude ϕ_1 to another ϕ_2 could be accurately measured using an electronic interval timer. Thus, knowing the ratio ϕ_1/ϕ_2 and the time of decay τ, the logarithmic decrement Δ could be calculated from the relation

$$\Delta = (1/\omega\tau)\log_e(\phi_1/\phi_2), \tag{1}$$

where $\omega = 2\pi f$ if f is the frequency of oscillation of the cylinder. This equation follows from the assumption that the amplitude ϕ of oscillation of the cylinder at time t is given by

$$\phi = \phi_0 \exp(-\omega\Delta t)\cos\omega t, \tag{2}$$

where ϕ_0 is the amplitude at $t = 0$.

EXPERIMENTAL PROCEDURE AND RESULTS

The experimental procedure was to evacuate both the upper and lower chambers to a pressure less than 10^{-5} mm. of mercury and to surround both chambers with a liquid helium bath. The temperature of the bath was then lowered to various successive values and a number of determinations (10 or more) were made of the time for decay of the oscillations between two calibrated levels. This process was continued until the lowest attainable temperature (1.1° K.) was reached. Then the Dewar was refilled with liquid helium and the temperature raised to the normal boiling point. Helium gas, purified by contact with charcoal immersed in liquid air, was then admitted and condensed in the lower chamber, the condensing process being continued until a level was seen in the gauge-glass H of Fig. 1. Determinations were then made of the time of decay between the two calibrated levels at various temperatures between 4.2° K. and 1.1° K.

Two curves representative of the results, one at a frequency of 11.8 kc./sec. and one at 35.5 kc./sec., are shown in Fig. 2. Here the logarithmic decrements derived at various temperatures from the measured decay times using equation (1) are plotted against temperature. The lower curve at each frequency was obtained when the cylinder oscillated in vacuum and represents the variation with temperature of the energy dissipative mechanisms within the cylinder itself. The upper curves were obtained when liquid surrounded the lower half of the cylinder. The difference between the upper and lower curves therefore represents the damping produced by the viscous forces of the liquid helium surrounding the lower half of the cylinder.

It was important to ensure that the frequencies studied corresponded definitely to torsional modes of vibration since the calculation of the viscosity from the observed decrement assumed specifically that the viscous forces were the only source of energy dissipation. Consequently identification of the operating frequencies with those of torsional modes was essential to ensure that no

other energy dissipative mechanisms, such as sound radiation from longitudinal and flexural modes, occurred. Accordingly, a preliminary experiment was carried out to determine the frequency spectrum of the cylinder used, and the torsional modes were readily identified since of all the modes they are the most truly harmonic ones, and their damping is the smallest.

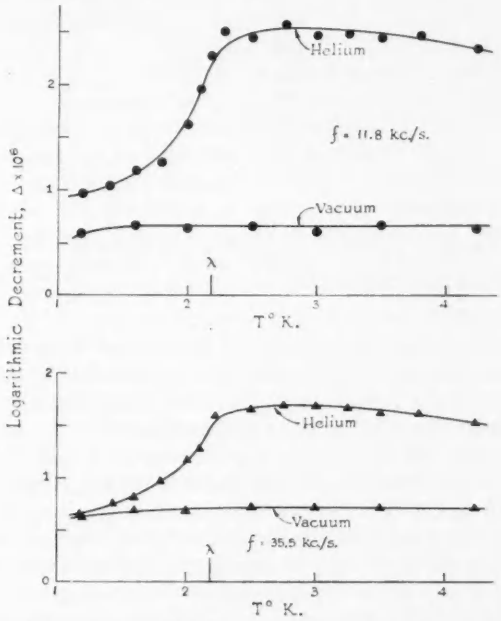

FIG. 2. The variation of the logarithmic decrement with temperature.

Using values for the decrement Δ due to the viscous damping of the helium as determined from the difference between curves such as those of Fig. 2, it was possible to calculate values for the viscosity of the liquid using the equation

$$\eta = 4\pi \frac{\Delta^2}{\rho} \left(\frac{2l.R}{2l+R} \right)^2 \rho_0^2 f, \tag{3}$$

where η and ρ are respectively the viscosity and density of the liquid, R, $2l$, and ρ_0 are respectively the radius, the total over-all length, and density of the cylinder, and f is the frequency of oscillation. This equation may be obtained by calculating the work done by the viscous forces in one cycle of oscillation and equating this to the energy lost by the cylinder in one cycle. A brief indication of the derivation of equation (3) is given in the Appendix.

Values of the viscosity so calculated from the measurements at the natural frequency of 11.8 kc./sec. of the cylinder and at the next harmonic 35.5 kc./sec. which gives a node at the mid-length of the cylinder, are plotted

against temperature in Fig. 3. The full curve shown in this figure was drawn from the oscillating disk results of Dash and Taylor (1957) and Taylor and

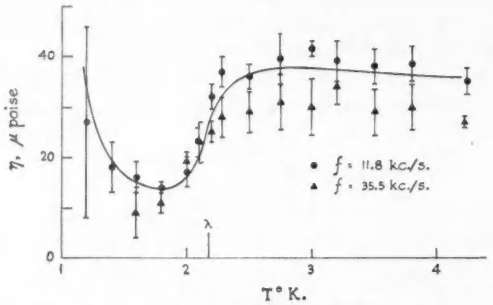

FIG. 3. The variation of the viscosity of liquid helium with temperature at frequencies of 11.8 kc./sec. and 35.5 kc./sec. The full curve is drawn from the oscillating disk results of Dash and Taylor (1957) in the helium II region, and of Taylor and Dash (1957) in the helium I region.

Dash (1957). At temperatures below the lambda-point the relevant density used in the above equation is the density of the normal component obtained from calculations using the velocity of second sound and the entropy and specific heat data of Kramers, Wasscher, and Gorter (1952).

Each of the points on the 11.8 kc./sec. curve is the average of the results of three separate experiments carried out on different days; similarly each point on the 35.5 kc./sec. curve is the average of the results of four separate experiments. The same cylinder was used for all the experiments described. The estimated experimental error of the decrement determined in any one experiment is of the order of 5%, and the resulting error in the viscosity is thus of the order of 10% since the decrement enters as the square into the calculation. The vertical bars drawn in Fig. 3 extend up and down from the experimental points by an amount equal to the average deviation of the results of the different experiments from the plotted mean. At temperatures lower than about 2° K., however, the errors in the viscosity are greater than the 10% figure quoted above, simply because the difference between the decrement curves for helium and for vacuum (Fig. 2) became increasingly smaller as the temperature was lowered.

It can be seen from Fig. 3 that the values of the viscosity at a frequency of 11.8 kc./sec. are in good agreement with the results of Taylor and Dash (full curve) which were obtained using an oscillating disk of period of oscillation of the order of 6 seconds. The values obtained at a frequency of 35.5 kc./sec. might appear to be consistently lower by about 10 to 15% but, as will be discussed below, it is not possible to state categorically that this difference is completely real.

DISCUSSION

The only experimental results reported in the literature which appear to

have been obtained from a similar type of experiment to that described above are those of Welber (1957). Welber measured the decay of torsional oscillations of a piezoelectric crystal immersed in liquid helium, and obtained a high degree of reproducibility. Unfortunately little more detail is given, and no viscosity or frequency values are published to permit comparison with the present results.

The question of whether or not there is a real difference between the 11.8 kc./sec. and the 35.5 kc./sec. results is intimately connected with the question of reproducibility of the experimental results as obtained from experiments on different days. In this connection it is relevant to record the results of the earliest experiments for which the apparatus differed from that described above in one important respect, namely, that the chamber surrounding the lower half of the cylinder was removed completely for determinations of the decrement in the liquid helium. The decrement in vacuum was obtained on another day with the lower chamber soldered in place and connected by a tube to the upper chamber so that the two chambers were evacuated together. In these experiments, the decrements in helium and in vacuum were considerably larger than those shown in Fig. 2 and varied considerably from day to day. Only when the apparatus was rebuilt so that the lower chamber could be evacuated continuously to a pressure less than 10^{-5} mm. of mercury before an experiment did the decrements fall to a reasonable value. It is believed that the higher decrements found in the earlier experiments resulted from an effective roughening of the surface of the cylinder by the deposition of small amounts of solid air and impurities. Since the depth of penetration into the liquid helium of the viscous waves propagated from the surface of the cylinder is of the order of 3×10^{-5} cm., small amounts of solid air and impurities adhering to the surface of the cylinder could readily give additional kinetic energy to the liquid and thus give rise to a larger decrement. It is interesting to note that a comparable amount of impurity condensed on a surface apparently gives rise to 'ridges', which effectively increase the rate of transport over the surface of the helium film, whose thickness ($\backsim 2\times10^{-6}$ cm.) is only one order of magnitude smaller than the penetration depth in the present experiment.

It was also found that if the cylinder was allowed to warm up to room temperature between experiments at liquid helium temperatures, the low temperature decrement changed by a few per cent in a rather random manner. This effect was believed to be due to small changes in the internal structure of the cylinder which modified the internal frictional forces within the cylinder, and affected the helium and vacuum decrements alike. The influence of this effect on the experimental results was avoided by performing both the vacuum experiment and the liquid helium experiment on the same day, and ensuring that the temperature of the cylinder did not rise above 4° K. until all measurements were made. Only under these conditions did the experimental values, obtained on different days, of the difference between the vacuum and liquid helium decrements become reproducible to any degree.

The reproducibility of the decrements obtained with the apparatus described above was $\leqslant 5\%$ for several determinations at one temperature in any one

experiment. The day-to-day reproducibility was not quite so good, and the vertical bars of Fig. 3 indicate some measure of the day-to-day reproducibility. Presumably, this comparatively poor day-to-day reproducibility is connected with the effectiveness of the evacuation of the lower chamber and with the initial cleanliness of the surface. The difference between the 11.8 kc./sec. and the 35.5 kc./sec. values of the viscosity might possibly, therefore, be due to different surface conditions in the different experiments. However, it should be pointed out that at 35.5 kc./sec. the penetration depth, which varies inversely as the square root of the frequency, is about 70% smaller than at 11.8 kc./sec. Consequently, one would expect a greater loss of energy due to surface irregularities at 35.5 kc./sec., with a resulting larger effective viscosity at this frequency. Experimentally, the 35.5 kc./sec. results, if different from the 11.8 kc./sec., are lower by about 10%, not higher. Consequently one might, on experimental grounds, consider the difference real. If the 35.5 kc./sec. results are genuinely lower, this is suggestive of a relaxation time in the liquid, probably of the order of 10^{-5} or 10^{-6} sec., and a 10% difference is all that would be expected, since the two frequencies studied are not very different. However, the only relaxation times suggested for helium are those involving phonon and roton 'collisions' suggested by Landau and Khalatnikov (1949), but these are of the order of 10^{-10} sec. and are too small to be relevant in these experiments.

Perhaps the most significant result of these experiments is that the results in helium II agree, within the admittedly large error, with the oscillating disk results. Certainly it can be seen from Fig. 2 that the decrement falls rapidly with temperature below the lambda-point in much the same manner as that found with an oscillating disk (compare with Fig. 1 of Hollis Hallett (1955)). Thus even in the small penetration depth, which is less than 5×10^{-5} cm., the normal component alone appears to damp the cylinder, and thus the two-fluid model is still apparently valid for these small distances.

Finally it should be mentioned that the maximum amplitude of oscillation of the cylinder was estimated to be 7×10^{-7} radian at 11.8 kc./sec. and 7×10^{-8} radian at 35.5 kc./sec.; there was no evidence of any increase in the decrement up to these amplitudes.

ACKNOWLEDGMENTS

The authors wish to acknowledge the financial assistance of the National Research Council of Canada and the Ontario Research Foundation, whose grants in aid of research enabled this work to be carried out. One of us, K.M.E., is indebted to the trustees of the Garnet W. McKee – Lachlan Gilchrist Scholarship Fund for the award of a Scholarship. The authors are indebted to Dr. W. H. Watson and Dr. J. M. Anderson for many helpful discussions and to Mr. H. Hellenkamp for his patience and skill in machining the cylinders and constructing the apparatus.

APPENDIX

The theoretical problem is to relate the logarithmic decrement of the oscillations of the cylinder shown in Fig. 4 to the damping forces exerted by the fluid

on both the lower end (at $z = 0$) and the cylindrical surface from $z = 0$ to $z = l$. The upper half of the cylinder from $z = l$ to $z = 2l$ is supposed to be in a perfect vacuum at all times. The simplest approach is that used by Voelz (1951) and is to calculate the work done in one cycle by the viscous forces on the cylinder and to equate this to the energy lost by the cylinder in one cycle of its oscillation.

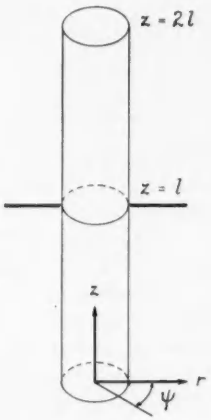

FIG. 4.

If the amplitude of oscillation of the cylinder is $\psi(r, z, t)$ and decays from its initial value $\psi(r, z, 0)$ according to the equation

$$\psi(r, z, t) = \psi(r, z, 0)\cos \omega t\, e^{-\omega \Delta t},$$

where $\omega = 2\pi f$ is the circular frequency of the oscillation and Δ is the logarithmic decrement, it can be shown that

$$\Delta E/E = 4\pi\Delta(1-\pi\Delta+\dots) = 4\pi\Delta \quad \text{if } \Delta \ll 1, \tag{1}$$

where ΔE = the energy lost in one cycle and E is the total energy of the cylinder.

Calculation of the work done in one cycle by the fluid on the circular end of the cylinder at $z = 0$ leads to the expression

$$(\Delta E)_{\text{end}} = \int_0^{2\pi/\omega} \left\{ \int_0^R 2\pi r dr.\eta r\, (\partial\psi/\partial z)_0\, r\psi(r, 0, t) \right\} dt.$$

From Hollis Hallett (1952), $(\partial\psi/\partial z)_0 = q\psi(r, 0, t)$, where $q \approx \sqrt{(\omega\rho/2\eta)}.(1+i)$ since $\Delta \ll 1$, and it follows that the real part of

$$(\Delta E)_{\text{end}} = \tfrac{1}{2}\pi^2 R^4 \eta \sqrt{(\omega\rho/2\eta)}.\omega\psi^2(R, 0, 0). \tag{2}$$

In a similar way the work done in one cycle by the fluid on the walls of the cylinder can be calculated. In this case, however, it is necessary to take into account the particular variation of ψ with z which results from the fact that the cylinder oscillates with a node of oscillation at $z = l$ and a maximum at $z = 0$.

Accordingly (Love 1920), $\psi(R, z, 0) = \psi(R, 0, 0)\cos(\pi z/2l)$, and the expression for $(\Delta E)_{cyl}$ becomes

$$(\Delta E)_{cyl} = \int_0^{2\pi/\omega} \left\{ \int_0^{l} 2\pi R dz . R \left(\frac{\partial \psi(r, 0, t)}{\partial r} \right)_R \cos \frac{\pi z}{2l} . R\psi(R, 0, t) \cos \frac{\pi z}{2l} \right\} dt.$$

Again by Hollis Hallett (1952), $(\partial\psi/\partial r)_R \approx p\psi(R, 0, t)$, where $p \approx \sqrt{(\omega\rho/2\eta)}.(1+i)$, and the real part of

$$(\Delta E)_{cyl} = \pi^2 R^3 \eta \sqrt{(\omega\rho/2\eta)}.\omega\psi^2(R, 0, 0)l. \tag{3}$$

Consequently, the total (ΔE) is equal to the sum of equations (2) and (3):

$$(\Delta E) = \tfrac{1}{2}\pi^2 R^3 \eta \sqrt{(\omega\rho/2\eta)}.\omega\psi^2(R, 0, 0)[2l+R]. \tag{4}$$

The total energy of the cylinder $= \frac{1}{2}I\{\psi(R, z, 0)\}^2$ can likewise be evaluated by calculating the energy of an elementary disk of thickness dz and integrating over z from 0 to $2l$ since the whole cylinder oscillates. Thus,

$$E = \tfrac{1}{4}\pi R^4 l \rho_0 \omega^2 \psi^2(R, 0, 0), \tag{5}$$

where ρ_0 = the density of the material of the cylinder.

The final result follows from substituting equations (3), (4), and (5) into equation (1):

$$\eta = 4\pi \frac{\rho_0^2}{\rho} \Delta^2 f \left[\frac{2l.R}{2l+R} \right]^2. \tag{6}$$

This is the equation (3) in the text of the paper. It can also be shown that equation (6), which was developed for the fundamental frequency of vibration, is not changed if the frequency of oscillation is three times as great, i.e. at the second harmonic.

It should be pointed out that the use of the above method of relating the decrement to the viscosity of the fluid is severely restricted. It can be applied with accuracy only if the ratio of the penetration depth λ $(= \sqrt{(2\eta/\omega\rho)})$ to the smallest dimension of the cylinder is very small. More precise investigation shows that the right-hand side of equation (6) should be multiplied by a quantity $(1+f(\lambda/R))^{-2}$, where $f(\lambda/R)$ may be expanded as a power series the first term of which is of the order of λ/R. Since λ in these experiments is at most $\backsim 5\times10^{-5}$ cm., and $R \backsim 1$ cm., the method is adequately valid for the experiments described.

REFERENCES

DASH, J. G. and TAYLOR, R. D. 1957. Phys. Rev. **105**, 7.

HEIKKILA, W. J. and HOLLIS HALLETT, A. C. 1955. Can. J. Phys. **33**, 420.

HOLLIS HALLETT, A. C. 1952. Proc. Roy. Soc. (London), A, **210**, 404.

——— 1955. *In* Progress in low temperature physics, Vol. I, *edited by* C. J. Gorter (North-Holland Publishing Co., Amsterdam), chap. IV.

KRAMERS, H. C., WASSCHER, J. D., and GORTER, C. J. 1952. Physica, **18**, 329.

LANDAU, L. D. and KHALATNIKOV, I. M. 1949. J. Exptl. Theoret. Phys. U.S.S.R. **19**, 637, 709.

LOVE, A. E. H. 1920. A treatise on the mathematical theory of elasticity (Cambridge University Press), p. 292.

TAYLOR, R. D. and DASH, J. G. 1957. Phys. Rev. **106**, 398.

VOELZ, K. 1951. Z. angew. Phys. **3**, 185.

WELBER, B. 1957. Bull. Am. Phys. Soc. **2**, 183-F3.

ABSORPTION SPECTRA OF THE HALOGEN MONOXIDES[1]

R. A. DURIE[2] AND D. A. RAMSAY

ABSTRACT

Absorption spectra of ClO, BrO, and IO have been observed during the flash photolysis of Cl_2–O_2, Br_2–O_2, and I_2–O_2 mixtures. Rotational and vibrational analyses of the ClO and BrO spectra have been carried out and appropriate molecular constants derived. The transitions are of the type $^2\Pi_i$(case *a*)—$^2\Pi_i$ (case *a*). Extensive predissociation has been observed in all three spectra. Theoretical and experimental evidence is presented to show that the excited states dissociate to $X(^3P_{3/2}) + O(^1D)$. From the observed or extrapolated convergence limits of the absorption spectra the dissociation energies of the ground states are shown to be $D_0''(ClO) = 63.31 \pm 0.03$ kcal./mole, $D_0''(BrO) = 55.2 \pm 0.6$ kcal./mole, $D_0''(IO) = 42 \pm 5$ kcal./mole. Mechanisms for the production of the halogen monoxides are discussed and evidence is presented for the participation of excited $^2P_{\frac{1}{2}}$ halogen atoms.

INTRODUCTION

Spectra of chlorine, bromine, and iodine monoxides have been observed in emission from flames of the methyl halides burning with oxygen (Vaidya 1937, 1938) and in oxyhydrogen flames to which the halogens have been added (Coleman and Gaydon 1947; Pannetier and Gaydon 1948; Coleman, Gaydon, and Vaidya 1948). Vibrational analyses of these spectra have been carried out but no rotational analysis has been given. No spectrum of fluorine monoxide has yet been reported.

The spectrum of chlorine monoxide was observed in absorption during the flash photolysis of mixtures of chlorine and oxygen by Porter (1950). A dissociation limit was determined and a vibrational analysis given. The spectrum was also investigated under high resolution by Herzberg and Ramsay (1950) and the presence of predissociation in the excited state was deduced from the diffuseness of the rotational lines of some of the bands. A revised dissociation limit was also given. None of the other halogen monoxides has previously been reported in absorption.

Recently we have carried out a series of experiments on the flash photolysis of mixtures of the halogens with oxygen and have observed absorption spectra of bromine and iodine monoxides with Br_2–O_2 and I_2–O_2 mixtures. We have also rephotographed the chlorine monoxide bands. With F_2–O_2 mixtures we did not observe any bands which could be attributed to fluorine monoxide but we did observe numerous bands which could be attributed to absorption by vibrationally excited oxygen. These bands will be discussed in a separate publication. The present paper is concerned with the vibrational and rotational analyses of the ClO, BrO, and IO bands and a discussion of the dissociation energies of these molecules.

[1]Manuscript received August 29, 1957.
Contribution from the Division of Pure Physics, National Research Council, Ottawa, Canada.
Issued at N.R.C. No. 4561.
[2]N.R.C. Postdoctorate Fellow 1955. Present address: C.S.I.R.O. Coal Research Section, Sydney, Australia.

EXPERIMENTAL

The experiments were carried out with the "microsecond" flash photolysis apparatus described recently (Callomon and Ramsay 1957). The reaction cell was a quartz tube 25 cm. long and contained a mixture of a halogen with oxygen. The photolysis flash was produced by discharging a 40 μf. condenser charged to 8000 v. through a quartz flash tube 25 cm. long. Absorption spectra of the photolysis products were photographed using a quartz capillary flash tube as a source of continuum. A 2 μf. condenser charged to 10,000 v. discharged through the "source" tube in $\backsim$10 μsec. The duration of the photolysis flash was $\backsim$20 μsec. The time interval between the photolysis and "source" flashes was controlled by means of a delay circuit. Spectra were photographed with a 21 ft. concave grating spectrograph and with a Hilger El spectrograph.

(*i*) *ClO*

A mixture of 20 mm. Cl_2 and 600 mm. O_2 was subjected to flash photolysis and the ClO bands in the region 2600 to 3100 Å were photographed using the fourth order of the 21 ft. grating spectrograph. The spectrum consists of a long progression of red-degraded bands and is reproduced in Fig. 1. At the short wavelength end of the spectrum a convergence limit is observed near 2630 Å beyond which there is only a continuous absorption. Before the limit the rotational lines are sharp but the structure is complex owing to the overlapping of successive vibrational bands. At the long wavelength end of the spectrum the rotational structure is much simpler but in most of the bands the rotational lines are diffuse owing to predissociation in the excited state. In the (7,0) band the rotational structure is completely diffuse and no individual rotational lines are seen. The band in which the rotational structure is most clearly resolved is the (12,0) band with its head at 2771.7 Å. A reproduction of this band is given in Fig. 2. The wavelengths of the band heads of the various vibrational bands have been given by Porter (1950). The vacuum wavenumbers and assignments of the rotational lines for all the bands shown in Fig. 1, except the (7,0) and (8,0) bands, are given in Table I. The relative accuracy of the measurements of the sharp lines is $\backsim$0.05 cm^{-1}, but for some of the diffuse lines the error of measurement may be a few tenths of a cm^{-1}. The origins and assignments of the various bands are given in Table II.

(*ii*) *BrO*

A progression of 20 new bands was observed in the region 2890 to 3550 Å during the flash photolysis of mixtures of bromine and oxygen. The bands decayed to half their maximum intensity in $\backsim$50 μsec. and have been assigned to BrO. The intensity of the bands was favored by a large excess of oxygen and a comparatively low pressure of bromine. Final plates were taken using a mixture of 3 mm. Br_2 and 600 mm. O_2. A reproduction of the spectrum taken with the Hilger El spectrograph is shown in Fig. 3. The wavelengths of the band heads and the vibrational assignments are given in Table III.

Investigation of the spectrum with the 21 ft. grating spectrograph revealed that 16 of the bands were completely diffuse. The other four bands showed evidence of rotational fine structure but even in these bands the individual

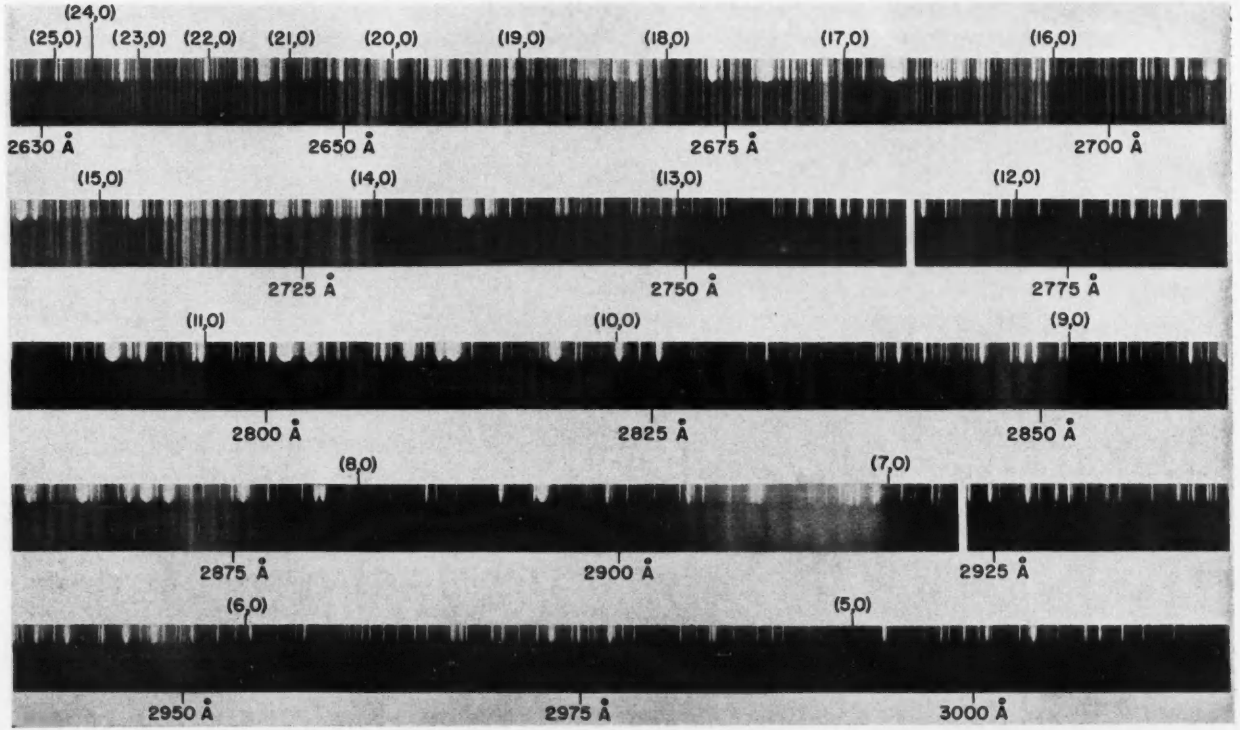

FIG. 1. Absorption spectrum of ClO observed during the flash photolysis of a mixture of chlorine and oxygen and photographed using the fourth order of a 21 ft. concave grating spectrograph.

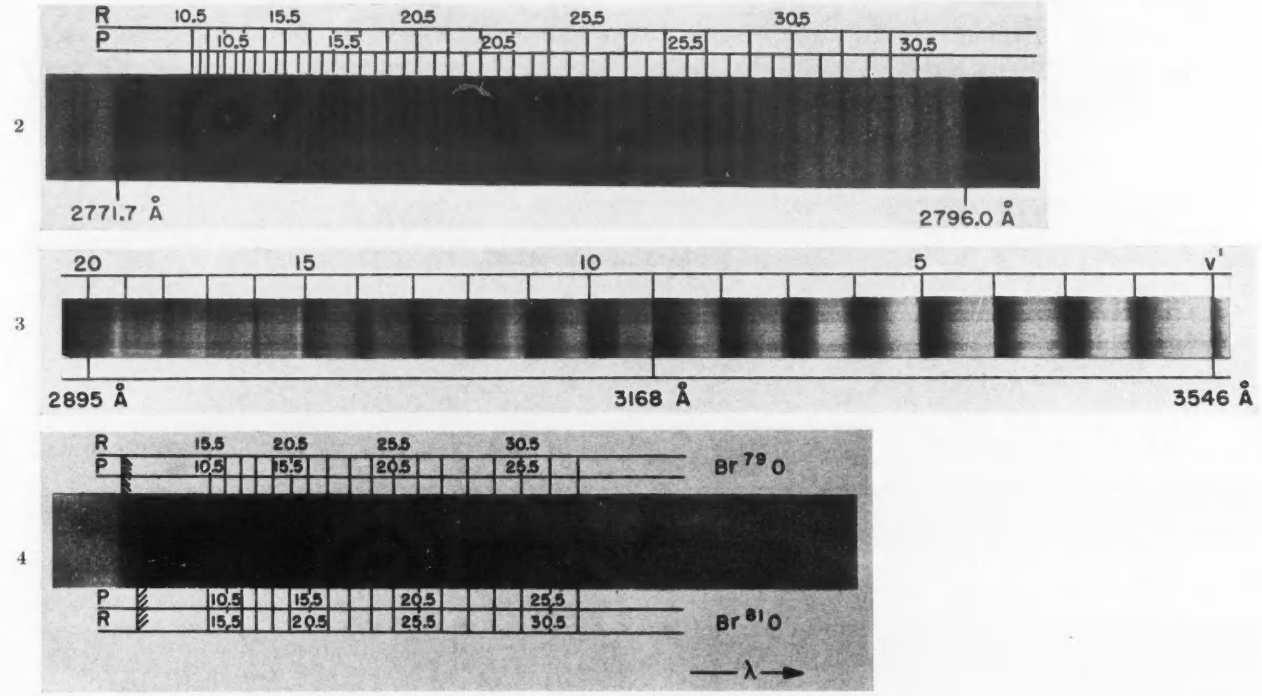

FIG. 2. Enlargement of the (12,0) band of ClO showing the assignments of the rotational lines.
FIG. 3. Absorption spectrum of BrO observed during the flash photolysis of a mixture of bromine and oxygen and photographed using a Hilger E1 spectrograph.
FIG. 4. Rotational fine structure of the (4,0) band of BrO photographed with a 21 ft. concave grating spectrograph.

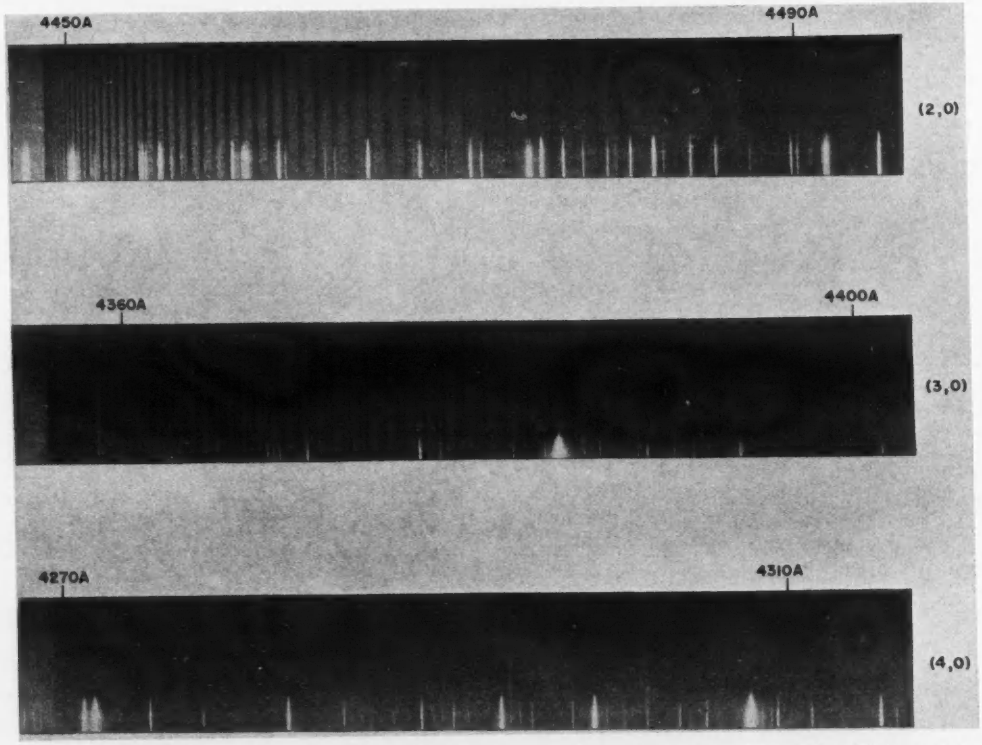

FIG. 5. Photographs of the (2,0), (3,0), and (4,0) bands of IO in absorption, taken with a 21 ft. concave grating spectrograph.

TABLE I

VACUUM WAVENUMBERS AND ROTATIONAL ASSIGNMENTS FOR ClO

A. $^2\Pi_{3/2}$—$^2\Pi_{3/2}$ SUBBANDS

	(5,0)		(6,0)		(9,0)		(10,0)	
J	$P(J)$	$R(J)$	$P(J)$	$R(J)$	$P(J)$	$R(J)$	$P(J)$	$R(J)$
2.5								
3.5								
4.5								
5.5								
6.5								
7.5								
8.5						35040.7$_s$		
9.5	33378.0				35022.2	037.0	35383.3	35397.6
10.5	373.0$_s$	33391.6	33809.6		016.6	032.7	377.5	393.8
11.5	367.1	386.8$_s$	804.0		010.2	027.9	370.6	389.4
12.5	361.3	382.2	798.6		003.9	022.2	363.5	383.3
13.5	354.8	378.0	791.8		34996.1$_s$	016.6	356.2	377.5
14.5	348.0	373.0$_s$	784.4	33809.6	988.3	010.2	348.0	370.6
15.5	340.7	367.1	776.0	804.0	980.6	003.9	339.6	363.5
16.5	333.6	361.3	769.1	798.6	972.0	34996.1$_s$	330.8	356.2
17.5	325.3	354.8	760.5	791.8	962.7	988.3	321.2	348.0
18.5	316.5	348.0	752.8	784.4	952.6	980.6	311.0	339.6
19.5	308.0	340.7	743.8	776.0	942.7	972.0	300.0	330.8
20.5	297.8$_s$	333.6	734.0	769.1	931.8	962.7	288.9$_s$	321.2
21.5	288.4	325.3	723.9	760.5	921.1$_s$	952.6	277.3$_s$	311.0
22.5	278.3	316.5	713.0	752.8	909.5	942.7	266.0	300.0
23.5	268.1	308.0	702.0	743.8	897.7	931.8	253.0	288.9$_s$
24.5	257.2	297.8$_s$	691.3	734.0	884.5	921.1$_s$	239.7	277.3$_s$
25.5	245.6	288.4		723.9	871.2	909.5	225.7	266.0
26.5	233.7	278.3		713.0	857.9	897.7	211.7	253.0
27.5	221.9	268.$_1$		702.0	842.8	884.5	197.4	239.7
28.5		257.2		691.3	829.2$_s$	871.2	183.2	225.7
29.5		245.6			814.6	857.9	167.0	211.7
30.5		233.7			799.1	842.8	150.6	197.4
31.5		221.9				829.2$_s$	134.3	183.2
32.5		208.9				814.6	116.3	167.0
33.5						799.1	098.4$_s$	150.6
34.5						782.3$_s$	080.7	134.3
35.5						764.8		116.3
36.5								098.4$_s$
37.5								080.7

	(11,0)		(12,0)		(13,0)		(14,0)	
J	$P(J)$	$R(J)$	$P(J)$	$R(J)$	$P(J)$	$R(J)$	$P(J)$	$R(J)$
2.5								
3.5								
4.5								
5.5								
6.5						36346.4		36610.6
7.5						342.3		606.4
8.5	35726.0		36037.63		36326.0	337.6	36589.0	601.7
9.5	719.5		031.65		319.0	333.2	581.8	595.4
10.5	713.9		024.79		313.4	326.0	575.2	589.0
11.5	706.0	35726.0	017.66	36034.89	303.1	319.0	566.6	581.8
12.5	699.0	719.5	009.81	028.30	299.7	313.4	557.9	575.2
13.5	691.0$_s$	713.9	001.44	021.38	285.7	305.9	548.6	566.6
14.5	682.5$_s$	706.0	35992.48	014.10	275.6$_s$	299.7	538.6	557.9
15.5	674.5	699.0	982.85	005.74	265.7	288.2	527.4	548.6
16.5	665.6	691.0$_s$	972.74	35996.93	254.7	278.5	516.4	538.6
17.5	655.7	682.5$_s$	962.37	987.99	244.0	269.1	504.4	527.4
18.5	644.0	674.5	950.76	977.90	231.7	258.4	492.7	516.4
19.5	634.8	665.6	939.27	967.72	219.0	246.1	479.7	504.4
20.5	622.0	652.4	927.00	957.23	206.4	225.3	466.2	492.7
21.5		642.2	914.01	945.08	192.2	223.0	452.3	479.7
22.5		631.5	900.76	933.40	178.0	209.8	436.3	466.2
23.5			886.19	921.18	—	196.4	421.6	452.3
24.5			871.74	907.61	147.3	182.5	405.0$_s$	436.3
25.5			857.18	893.96	131.6	—	388.2	421.6
26.5			841.05	879.41	115.9	151.8		405.0$_s$
27.5			825.32	865.32	098.9	137.1		388.2
28.5			808.39	850.05	079.8	120.2		371.5
29.5			790.76	834.14		103.4		
30.5			772.54	818.00		085.3		
31.5			754.79	800.17				
32.5			734.99	782.68				
33.5				764.50				
34.5				745.37				

TABLE I (*continued*)

VACUUM WAVENUMBERS AND ROTATIONAL ASSIGNMENTS FOR ClO (*continued*)

A. $^2\Pi_{3/2}$—$^2\Pi_{3/2}$ SUBBANDS (*continued*)

	(15,0)		(16,0)		(17,0)		(18,0)	
J	$P(J)$	$R(J)$	$P(J)$	$R(J)$	$P(J)$	$R(J)$	$P(J)$	$R(J)$
2.5								
3.5								
4.5								
5.5								
6.5	36844.9$_5$	36854.2$_5$			37243.25			
7.5	839.2$_5$	849.8	37044.98		237.28	37246.04	37395.35	
8.5	833.1	844.9$_5$	039.77		230.62	240.54	388.01	37396.75
9.5	826.6	839.2$_5$	032.99	37043.35	223.14	234.12	379.85	390.61
10.5	819.9	833.1	024.37	037.82	214.91	226.53	370.67	382.90
11.5	811.8	826.6	014.66	030.22	205.66	218.75	361.32	373.84
12.5	803.1	819.9	005.57	021.82	196.21	210.41	350.38	364.03
13.5	794.1	811.8	36995.41	012.33	186.04	200.84	338.92	352.76
14.5	784.2$_5$	803.1	984.83	002.64	175.00	191.10	326.80	342.28
15.5	773.8	794.1	972.96	36992.14	162.90	180.32	313.93	329.91
16.5	762.3$_5$	784.2$_5$	960.83	981.41	150.25	168.61	300.02	316.55
17.5	751.1	773.8	947.87	969.44	137.14	156.49	285.07	302.51
18.5	738.7	762.3$_5$	933.96	956.19	123.23	143.78	269.36	287.93
19.5	726.4	751.1	919.97	943.68	108.51	130.25		
20.5	712.1	738.7	905.09	930.08	092.73	115.90		
21.5	697.9$_5$	726.4	888.98	915.22	076.17	100.63		
22.5	683.8	712.1	872.75	899.87		085.28		
23.5	668.8	697.9$_5$		884.08		068.06		
24.5	649.7	683.8				051.50		
25.5		668.8						
26.5		649.7						
27.5								
28.5								

	(19,0)		(20,0)		(21,0)		(22,0)	
J	$P(J)$	$R(J)$	$P(J)$	$R(J)$	$P(J)$	$R(J)$	$P(J)$	$R(J)$
2.5								
3.5								
4.5								
5.5								
6.5				37661.39				
7.5				655.15	37741.67			
8.5	37523.72	37533.10	37639.90	648.21	733.17	37741.67		
9.5	—	525.54	630.92	639.90	723.54	733.17		37804.82
10.5	507.35	518.45	621.10	630.92	713.16	721.86	37788.62	796.84
11.5	496.10	509.29	610.73	621.10	703.44	713.16	776.99	785.87
12.5	486.22	498.59	599.05	610.73	691.32	701.72	764.38	774.45
13.5	474.83	488.20	586.99	599.05	678.63	689.03	751.29	761.85
14.5	462.04	477.64	573.71	586.99	665.12	676.53	737.07	747.84
15.5	448.98	464.62	559.86	573.71	650.08	662.81	721.86	733.17
16.5	434.38	451.21	544.80	559.86	634.58	648.21	705.86	717.79
17.5	419.87	437.31	529.62	544.80	618.45	632.08	689.03	
18.5	404.70	422.54	513.08	529.62	601.28	616.19	672.28	
19.5		406.95	496.10	513.08	583.19	599.05		
20.5			477.64	496.10		580.61		
21.5			458.70	477.64				
22.5			438.81	458.70				
23.5			418.09	438.81				
24.5			396.75	418.09				
25.5			373.84	396.75				
26.5			350.38	373.84				
27.5			326.80	350.38				

TABLE I (*concluded*)

VACUUM WAVENUMBERS AND ROTATIONAL ASSIGNMENTS FOR ClO (*concluded*)

A. $^2\Pi_{3/2}$—$^2\Pi_{3/2}$ SUBBANDS (*concluded*)

	(23,0)		(24,0)		(25,0)	
J	*P*(*J*)	*R*(*J*)	*P*(*J*)	*R*(*J*)	*P*(*J*)	*R*(*J*)
2.5						37993.78
3.5				37954.32		990.50
4.5				950.22		986.27
5.5			37941.43	944.47	37977.66	980.57
6.5	37892.16		934.08	938.43	971.11	974.26
7.5	884.69		926.45	930.14	963.11	966.84
8.5	876.75	37882.55	917.42	921.62	954.32	958.21
9.5	867.80	873.91	907.43	912.16	944.47	948.96
10.5	857.42	864.24	896.62	902.10	934.08	938.43
11.5	846.80	853.92	884.69	889.95	921.62	
12.5	834.39	842.52	871.06	877.63	907.43	
13.5	821.64	830.11	857.42	864.24		
14.5	807.07	816.59	842.52	849.81		
15.5	792.79	802.25	826.05	834.39		
16.5	776.99	786.97	808.73	817.76		
17.5	760.27	771.08	788.62	799.92		
18.5	741.67	753.20	771.08	781.54		
19.5	723.54	735.11				
20.5	703.44	715.84				
21.5	683.89	695.64				
22.5		674.15				

B. $^2\Pi_{1/2}$—$^2\Pi_{1/2}$ SUBBANDS

	(5,0)		(10,0)	
J	*P*(*J*)	*R*(*J*)	*P*(*J*)	*R*(*J*)
6.5				
7.5	33583.9			
8.5	579.7			
9.5	575.2		35573.3$_8$	35590.0
10.5	570.1		567.2	585.6
11.5	564.5	33583.9	560.5	580.9
12.5	557.8$_8$	579.7	553.4	575.5$_8$
13.5	551.7	575.2	545.6	569.5
14.5	545.0	570.1	537.1	562.8
15.5	538.2	564.5	528.4	555.7
16.5	530.3	557.8$_8$	—	548.3$_8$
17.5	522.3	551.7	511.0	540.2
18.5	513.6	545.0	500.8	532.1
19.5	503.6	538.2	490.3	522.6
20.5	495.2	530.3	478.9	513.0
21.5		522.3		503.0
22.5		513.6		492.6$_8$
23.5		503.6		481.2
24.5		495.2		470.2
25.5				457.2
26.5				445.4

TABLE II

BAND ORIGINS AND B' VALUES FOR THE $^2\Pi_{3/2}$—$^2\Pi_{3/2}$ SUBBANDS OF ClO

Band	ν_0 (cm^{-1})	B' (cm^{-1})
(5,0)	33406.6	0.435 ±0.003
(6,0)	33844.4	0.430 ±0.002
(7,0)*		
(8,0)†		
(9,0)	35053.6	0.400 ±0.005
(10,0)	35415.8	0.390 ±0.002
(11,0)	35754.5	0.377 ±0.004
(12,0)	36066.5_7	0.358_8±0.0010
(13,0)	36355.8	0.335 ±0.004
(14,0)	36619.5	0.324 ±0.003
(15,0)	36864.3	0.327 ±0.002
(16,0)	37072.8	0.289 ±0.003
(17,0)	37264.8	0.277 ±0.002
(18,0)	37425.1	0.238 ±0.005
(19,0)	37561.9	0.231 ±0.003
(20,0)	37678.7	0.206 ±0.003
(21,0)	37772.9	0.187 ±0.002
(22,0)	37849.5	0.166 ±0.004
(23,0)	37917.8	0.171 ±0.004
(24,0)	37960.7	0.131 ±0.003
(25,0)	37997.4	0.132 ±0.004

For all these bands D' was assumed to be 1.4×10^{-6} cm^{-1}.

*The rotational structure of the (7,0) band was completely diffuse.

†The rotational lines of the (8,0) band were so diffuse that no satisfactory rotational analysis was possible.

TABLE III

BAND HEAD MEASUREMENTS AND VIBRATIONAL ASSIGNMENTS OF THE BrO BANDS

Band	λ_{air} (Å)	ν_{vac} (cm^{-1})
(1,0)	3545.9	28193
(2,0)	3487.0	28670
(3,0)	3433.8	29114
(4,0)*†	3383.40	29547.6 $Br^{79}O$
	3383.84	29543.8 $Br^{81}O$
(5,0)†	3333.2	29993
(6,0)	3288.6	30399
(7,0)	3247.7	30782
(8,0)	3207.9	31164
(9,0)*	3168.5	31551
(10,0)	3132.6	31913
(11,0)	3100.4	32245
(12,0)	3069.6	32568
(13,0)	3041.5	32869
(14,0)	3014.7	33161
(15,0)	2989.5	33440
(16,0)	2967.0	33694
(17,0)*	2945.3	33942
(18,0)*	2926.0	34166
(19,0)	2910.3	34351
(20,0)	2895.3	34529

*Denotes band which shows rotational fine structure under high resolution.

†Denotes band also recorded by Coleman and Gaydon in emission.

rotational lines were still distinctly diffuse. In only one band, the (4,0) band, was the rotational structure sufficiently well resolved to permit a rotational analysis. A reproduction of this band is given in Fig. 4; the vacuum wavenumbers and rotational assignments are given in Table IV.

TABLE IV

VACUUM WAVENUMBERS AND ASSIGNMENTS OF THE ROTATIONAL LINES OF THE 3383 Å BAND OF BrO

Assignment		
$Br^{79}O$	$Br^{81}O$	ν_{vac} (cm^{-1})
$P(10\frac{1}{2})R(15\frac{1}{2})$	$P(9\frac{1}{2})\ R(14\frac{1}{2})$	29525.1
$P(11\frac{1}{2})R(16\frac{1}{2})$	$P(10\frac{1}{2})R(15\frac{1}{2})$	29521.5
$P(12\frac{1}{2})R(17\frac{1}{2})$	$P(11\frac{1}{2})R(16\frac{1}{2})$	29517.1
$P(13\frac{1}{2})R(18\frac{1}{2})$	$P(12\frac{1}{2})R(17\frac{1}{2})$	29513.0
$P(14\frac{1}{2})R(19\frac{1}{2})$	$P(13\frac{1}{2})R(18\frac{1}{2})$	29508.7
$P(15\frac{1}{2})R(20\frac{1}{2})$	$P(14\frac{1}{2})R(19\frac{1}{2})$	29504.0
$P(16\frac{1}{2})R(21\frac{1}{2})$	$P(15\frac{1}{2})R(20\frac{1}{2})$	29499.4
$P(17\frac{1}{2})R(22\frac{1}{2})$	$P(16\frac{1}{2})R(21\frac{1}{2})$	29494.1
$P(18\frac{1}{2})R(23\frac{1}{2})$	$P(17\frac{1}{2})R(22\frac{1}{2})$	29488.9
$P(19\frac{1}{2})R(24\frac{1}{2})$	$P(18\frac{1}{2})R(23\frac{1}{2})$	29482.7
$P(20\frac{1}{2})R(25\frac{1}{2})$	$P(19\frac{1}{2})R(24\frac{1}{2})$	29477.2
$P(21\frac{1}{2})R(26\frac{1}{2})$	$P(20\frac{1}{2})R(25\frac{1}{2})$	29471.3
$P(22\frac{1}{2})R(27\frac{1}{2})$	$P(21\frac{1}{2})R(26\frac{1}{2})$	29465.6
$P(23\frac{1}{2})R(28\frac{1}{2})$	$P(22\frac{1}{2})R(27\frac{1}{2})$	29457.6
$P(24\frac{1}{2})R(29\frac{1}{2})$	$P(23\frac{1}{2})R(28\frac{1}{2})$	29451.4
$P(25\frac{1}{2})R(30\frac{1}{2})$	$P(24\frac{1}{2})R(29\frac{1}{2})$	29443.9
$P(26\frac{1}{2})R(31\frac{1}{2})$	$P(25\frac{1}{2})R(30\frac{1}{2})$	29436.8
$P(27\frac{1}{2})R(32\frac{1}{2})$	$P(26\frac{1}{2})R(31\frac{1}{2})$	29429.5

(*iii*) *IO*

Six bands of IO were observed in absorption during the flash photolysis of mixtures of iodine vapor and oxygen at room temperature. The bands are degraded to the red and have heads at 4269.8 Å, 4355.6 Å, 4448.8 Å, 4549.2 Å, 4586.2 Å, and 4655.2 Å. The first five of these bands have been observed in emission by Coleman, Gaydon, and Vaidya and assigned by them to the (4,0), (3,0), (2,0), (1,0), and (2,1) bands. The sixth band has not previously been recorded and is presumably the (0,0) band. The rotational lines of the (0,0), (2,0), and (2,1) bands are sharp while the rotational lines of the (3,0) band are distinctly diffuse. The rotational structures of the (1,0) and (4,0) bands are completely diffuse. Reproductions of the (2,0), (3,0), and (4,0) bands taken with the 21 ft. grating spectrograph are given in Fig. 5.

No measurements on the rotational lines of the absorption spectrum have been carried out, since the same bands, extending to much higher J values, have been photographed with the 21 ft. grating spectrograph in emission from an oxyhydrogen flame to which methyl iodide was added. Approximately 40 bands have been photographed in this way, the bands corresponding very closely to those observed earlier by Coleman, Gaydon, and Vaidya. The analysis of these bands will be reported in a later publication.

In all the experiments reported above, the band systems recorded were the only band systems in the region 2200 to 9000 Å due to the halogen monoxides. It is interesting to note that while the lifetime of the ClO radicals

was of the order of a few milliseconds, the lifetimes of the BrO and IO radicals were of the order of 50 to 100 microseconds. The short lifetimes of the BrO and IO radicals may account for the fact that the spectra of these radicals have not previously been reported in absorption.

ROTATIONAL ANALYSIS

On the basis of electron configuration arguments (see below) the electronic transitions responsible for the observed halogen monoxide spectra are expected to be of the type $^2\Pi_i$—$^2\Pi_i$. These predictions are consistent with the observed spectra if it is assumed that the doublet splittings in the $^2\Pi$ states are large, i.e. that the states belong to Hund's case (*a*). This is not unreasonable in view of the large doublet splittings in the ground states of the halogen atoms. With case (*a*) coupling each band splits up into two well-defined subbands, viz. $^2\Pi_{3/2}$—$^2\Pi_{3/2}$ and $^2\Pi_{1/2}$—$^2\Pi_{1/2}$, and each subband consists predominantly of a single P and R branch and a very weak Q branch. In the case of the ClO bands both subbands have been observed, although the $^2\Pi_{1/2}$—$^2\Pi_{1/2}$ subbands are considerably weaker than the $^2\Pi_{3/2}$—$^2\Pi_{3/2}$ subbands. In the case of the BrO and IO bands only one of the subbands has been observed, presumably on account of much larger doublet separations in the respective ground states.

For a $^2\Pi$(case *a*)—$^2\Pi$(case *a*) transition the wavenumbers of the P and R lines may be expressed by the equation (Herzberg 1950)

$$(1)\quad \nu = \nu_0+(B'+B'')m+(B'-B''-D'+D'')m^2-2(D'+D'')m^3-(D'-D'')m^4,$$

where $m = J+1$ for the R branch and $m = -J$ for the P branch.

Ground state rotational constants are obtained from the relation

$$(2)\qquad R(J-1)-P(J+1) = 4B''(J+\tfrac{1}{2})-8D''(J+\tfrac{1}{2})^3,$$

while values of ν_0 and $(B'-B'')$ are derived from the equation

$$(3)\qquad R(J-1)+P(J) = 2\nu_0+2(B'-B'')J^2-2(D'-D'')J^2(J^2+1)$$

using the usual graphical procedures.

The detailed analyses of the ClO and BrO bands were carried out as follows:

(*i*) *ClO*

The most satisfactory band for the determination of the ground state rotational constants is the (12,0) band with its head at 2771.7 Å. This band is fairly free from overlapping by neighboring bands, the P and R branches are well resolved, and the rotational lines are fairly sharp. A reproduction of this band together with the rotational assignments is given in Fig. 2. The J numbering was determined by comparing the ground state combination differences with the values obtained from the other bands. The ground state rotational constants were determined by the method described above and are

$$B_0'' = 0.642_6\ \text{cm}^{-1}, \qquad D_0'' = 2.2\times10^{-6}\ \text{cm}^{-1}.$$

These constants apply to the $^2\Pi_{3/2}$ component of the ground state of the $Cl^{35}O$ species.

For most of the other bands satisfactory assignments could be made (see Table I), but in one or two cases where the lines are very broad or badly overlapped by neighboring bands it was not possible to make unambiguous assignments. Band origins were determined by the method of combination sums and are given in Table II.

Upper state rotational constants were determined in the following manner. The equation for the P branch of any subband is given by

$$(4) \qquad P(J) = \nu_0 + B'J(J-1) - D'J^2(J-1)^2 - B''J(J+1) + D''J^2(J+1)^2,$$

which may be rewritten as

$$(5) \quad [P(J) - \nu_0 + B''J(J+1) - D''J^2(J+1)^2]/[J(J-1)] = B' - D'J(J-1).$$

Since the ground state rotational constants and the band origins are known, the left-hand side of equation (5) was evaluated for each P line and plotted against $J(J-1)$. A similar procedure was carried out for each R line except that $J(J-1)$ was replaced by $(J+1)(J+2)$. The constants B' and D' were then obtained from the intercept and slope of the best straight line. For most of the bands the measurements were not sufficiently accurate to determine a satisfactory value for D'. A value of $D' = 1.4 \pm 0.4 \times 10^{-6}$ cm^{-1} was therefore determined from the 2771.7 Å band and the same value was adopted for all the bands. There was no evidence from the measurements of any appreciable systematic variation of D' with vibrational quantum number even at the highest vibrational quantum numbers. The values of B' for the various vibrational levels are given in Table II. Using the vibrational numbering given in the following section the B' values were fitted by the method of least squares to the quadratic equation

$$(6) \qquad B' = 0.478 - 0.0053v' - 0.00040v'^2.$$

The variation of B' with v' is shown graphically in Fig. 6. It is seen that the B' values for a few of the bands, e.g. the (15,0) band, deviate from the smooth curve by considerably more than the experimental error. Similar irregularities are found in the vibrational intervals and are probably due to perturbations by the various electronic excited states which cross the upper potential curve (see later).

In two or three of the bands rotational lines of the $^2\Pi_{1/2}$—$^2\Pi_{1/2}$ subbands were observed but in no case were the lines sufficiently sharp or free from overlapping by the $^2\Pi_{3/2}$—$^2\Pi_{3/2}$ subbands to permit satisfactory rotational analyses. In particular the measurements were not sufficiently accurate to provide an experimental proof that both $^2\Pi$ states are inverted as predicted from the electron configurations.

One important deduction which can be made from a consideration of the $^2\Pi_{1/2}$—$^2\Pi_{1/2}$ subbands involves the nature of the coupling case in the excited state. In the present analysis it has been assumed that case (a) coupling applies to the excited state but as the dissociation limit is approached it is clear that the doublet separation between the $^2\Pi_{3/2}$ and $^2\Pi_{1/2}$ components must change depending on the multiplet states of the atoms into which the two components dissociate. According to theoretical arguments given in a later section, the

$^2\Pi_{3/2}$ and the $^2\Pi_{1/2}$ components of the upper state should both dissociate into $Cl(^2P_{3/2}) + O(^1D)$ so that the doublet separation in the excited state should decrease to zero at the dissociation limit and a transition to case (*c*) coupling

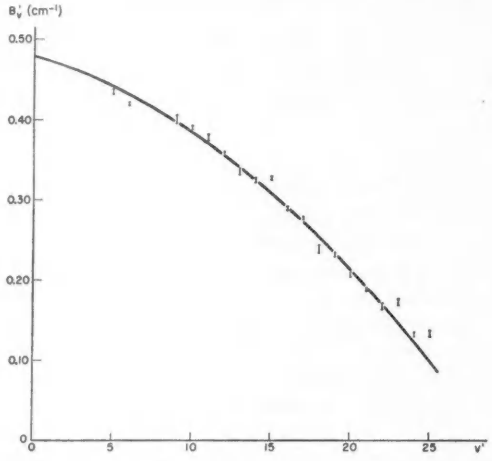

FIG. 6. Variation of B' with v' for ClO.

would be expected. Since the expression for the rotational energy levels with case (*c*) coupling is formally similar to the one for case (*a*) coupling, no change in the over-all structure of the bands is to be expected as the dissociation limit is approached although additional transitions permitted by the case (*c*) selection rules might begin to appear (Mulliken 1931). No such transitions have been identified although several weak lines remain unassigned.

It has been possible, however, to detect the variation of doublet splitting with vibrational quantum number in the following manner. From equation (4) it is seen that

$$(7)\quad P(J)_{^2\Pi_{1/2}} - P(J)_{^2\Pi_{3/2}} = (\nu_{0_{^2\Pi_{1/2}}} - \nu_{0_{^2\Pi_{3/2}}}) + (B'_{^2\Pi_{1/2}} - B'_{^2\Pi_{3/2}})J(J-1) - (B''_{^2\Pi_{1/2}} - B''_{^2\Pi_{3/2}})J(J+1)$$

neglecting terms involving D. A similar equation holds for the R lines. For case (*a*) coupling the effective B values for the two doublet components are given by

$$(8)\qquad B_{eff} = B(1 \pm B/A),$$

where the + and − signs refer to the $^2\Pi_{1/2}$ and $^2\Pi_{3/2}$ components respectively and A is the spin coupling constant. If the values of B^2/A for the upper and lower states are small quantities, the left-hand side of equation (7) will not vary appreciably with J. The rotational assignments for the $^2\Pi_{1/2}$—$^2\Pi_{1/2}$ subbands of the (5,0) and (10,0) bands given in Table IB are found to satisfy

this criterion. The value of $(\nu_{0_{^2\Pi_{1/2}}} - \nu_{0_{^2\Pi_{3/2}}})$ was found to be 197.2 cm^{-1} for the (5,0) band and 192.1 cm^{-1} for the (10,0) band. The doublet separation in the upper state therefore decreases slightly with increasing vibrational quantum number. A similar decrease was noted by Porter (1950) from band head measurements. Although it has not been possible to follow this decrease up to the dissociation limit it is interesting to note that it is varying in a manner consistent with the dissociation products given above.

The internuclear distances in the zero vibrational levels of the ground and excited states may be deduced from the B_0 values given above and are

$$r_0'' = 1.546 \text{ Å}, \qquad r_0' = 1.79 \text{ Å}.$$

These values apply to the $^2\Pi_{3/2}$ components of the two states. The ground state bond length is very similar to the Cl–O bond length found for ClO_2, viz. 1.53±0.02 Å (Pauling and Brockway 1935).

(*ii*) *BrO*

The only band of BrO for which a satisfactory rotational analysis could be carried out is the band at 3383 Å. In this band two heads are observed owing to the isotopic species $Br^{79}O$ and $Br^{81}O$ which occur in roughly equal natural abundances. Only approximate rotational constants could be obtained, since (*a*) the rotational lines are diffuse on account of predissociation, (*b*) the rotational lines of the $Br^{79}O$ species are not resolved from those of the $Br^{81}O$ species, and (*c*) the P lines overlap the R lines for both species. The constants were obtained in the following manner.

The condition for P lines to overlap R lines so that $R(J+n)$ coincides with $P(J)$ is

$$B' = [n/(n+2)]B''. \tag{9}$$

Under these circumstances it may be shown that equation (1) can be rewritten in the form

$$\nu_{R(J)} = \nu_{\text{head}} - \frac{2B''}{n+2}\left(J - \frac{n-1}{2}\right)^2, \tag{10}$$

neglecting terms due to centrifugal distortion. By plotting $\nu_{R(J)}$ against $[J-\frac{1}{2}(n-1)]^2$ a straight line is obtained with an intercept equal to ν_{head} and a slope equal to $2B''/(n+2)$. Since the wavenumbers of the band heads for the $Br^{79}O$ and $Br^{81}O$ species are known from direct measurement and the approximate B'' values can be estimated by comparison with other molecules, it is possible to show unambiguously that $n = 5$ and to determine the rotational assignments for the two species (see Table IV). The values of B'' determined by plotting $\nu_{R(J)}$ against $(J-2)^2$ are

$$B_0''(Br^{79}O) = 0.45_5 \text{ cm}^{-1}, \qquad B_0''(Br^{81}O) = 0.47_2 \text{ cm}^{-1}.$$

The values of the internuclear distances deduced from these constants are

$$r_0''(Br^{79}O) = 1.66_9 \text{ Å}, \qquad r_0''(Br^{81}O) = 1.63_5 \text{ Å}.$$

A mean value of $r_0'' = 1.65$ Å was therefore adopted and is probably accurate

to ±0.02 Å. A check on the validity of the analysis was obtained by a calculation of the spectrum with the value of r_0'' obtained here. Satisfactory agreement with observation was obtained within the line widths observed. In the region of maximum intensity the spacing between successive rotational lines is roughly equal to the vibrational isotope shift, so that the rotational lines of the two species coincide although the J numberings differ by 1. Further support for the value of r_0''(BrO) is obtained by comparison with the corresponding value for ClO. The value of $r_0(\mathrm{BrO})-r_0(\mathrm{ClO}) = 0.10$ Å is in satisfactory agreement with the values of $r_0(\mathrm{BrF})-r_0(\mathrm{ClF}) = 0.127$ Å, $r_0(\mathrm{HBr})-r_0(\mathrm{HCl}) = 0.139$ Å, and $\frac{1}{2}[r_0(\mathrm{Br_2})-r_0(\mathrm{Cl_2})] = 0.147$ Å (Herzberg 1950).

VIBRATIONAL ANALYSIS

(*i*) *ClO*

The vibrational numbering of the ClO bands has been determined by Porter by comparison of the absorption spectrum with the emission bands of Pannetier and Gaydon. It should be possible to obtain a check on the numbering by a study of the $Cl^{35}O$–$Cl^{37}O$ isotope effect but unfortunately the bands of the heavier isotope are obscured by the much stronger bands of the lighter isotope so that even with high resolution it has not been possible to identify with certainty the $Cl^{37}O$ bands. Further work is required with separated isotopes. Using the numbering given by Porter (see Table II) it was found that the origins of the absorption bands up to $v' = 20$ could be expressed by the equation

$$\nu_0 = 30869.7_1+554.0_8v'-9.25_8v'^2-0.070_2v'^3, \tag{11}$$

which was determined by the method of least squares. For higher values of v', however, a modified equation is required.

(*ii*) *BrO*

The absorption bands of BrO may be fitted into the vibrational scheme given by Coleman and Gaydon for the emission bands if it is assumed that the first band observed in the absorption spectrum is the (1,0) band, and the v'' numbering given by Coleman and Gaydon is raised by four units. The band heads of the absorption spectrum may then be represented by the equation

$$\nu_{\mathrm{head}} = 27{,}725+480.4v'-5.5_1v'^2-0.07_4v'^3 \tag{12}$$

and the band heads of the $v' = 0$ progression of the emission system by the equation

$$\nu_{\mathrm{head}} = 27{,}795-771.9v''+6.8_2v''^2, \tag{13}$$

both equations being determined by the method of least squares. The wavenumbers of the (0,0) band determined from the two systems may be considered to be in satisfactory agreement when it is remembered that the value deduced from the emission measurements involves an extrapolation of v'' by four units. The values of $\Delta G_{1/2}$ and $\Delta G_{3/2}$ deduced from the emission and the absorption measurements also agree within the accuracy of the measurements.

Further support for the vibrational numbering is obtained from the vibrational isotope shift of the 3383 Å band for which the calculated shift of 3.3 cm^{-1} is in satisfactory agreement with the observed shift of 3.8 cm^{-1} (± 1 cm^{-1}).

(iii) IO

The six bands observed in the absorption spectrum of IO fit satisfactorily into the vibrational scheme given by Coleman, Gaydon, and Vaidya without any change of vibrational numbering.

NATURE OF THE ELECTRONIC TRANSITION

The probable nature of the electronic transition responsible for the observed spectra of the halogen monoxides may be derived from a consideration of electron configurations. Using the nomenclature introduced by Mulliken (1932) the electron configuration and term type of the ground state is expected to be

$$(z\sigma)^2(y\sigma)^2(x\sigma)^2(w\pi)^4(v\pi)^3, \quad {}^2\Pi_i,$$

and of the first excited state

$$(z\sigma)^2(y\sigma)^2(x\sigma)^2(w\pi)^3(v\pi)^4, \quad {}^2\Pi_i.$$

The transition from the ground state to the first excited state should therefore be of the type ${}^2\Pi_i$—${}^2\Pi_i$ in agreement with the observed spectra. Furthermore the transition involves the transfer of an electron from a bonding $w\pi$ orbital to an antibonding $v\pi$ orbital and should be accompanied by an increase in the internuclear distance. This prediction is also in agreement with experiment, all three band systems being strongly degraded to the red.

The next excited state will probably have the configuration

$$(z\sigma)^2(y\sigma)^2(x\sigma)(w\pi)^4(v\pi)^4, \quad {}^2\Sigma^+,$$

while further excited states may be obtained by the promotion of electrons to $u\sigma$ or higher orbitals. Since the $u\sigma$ orbital is strongly antibonding it follows that these excited states will either be weakly bound states with internuclear distances considerably greater than in the ground state, or they will be repulsive states. Some of these repulsive states will be responsible for the extensive predissociation observed in the halogen monoxide spectra.

DISSOCIATION ENERGIES

The dissociation energies of the halogen monoxides can be obtained from the convergence limits of their absorption spectra provided that the states of the atoms into which the molecules dissociate are known. The electronic states of the halogen monoxides which can be formed from the low-lying electronic states of the halogen and oxygen atoms may be determined by the Wigner–Witmer correlation rules as follows:

$$\begin{aligned}
&X({}^2P_u)+O({}^3P_g) \rightarrow {}^2\Sigma^+, {}^2\Sigma^-(2), {}^2\Pi(2), {}^2\Delta, \\
&\qquad\qquad\qquad\quad {}^4\Sigma^+, {}^4\Sigma^-(2), {}^4\Pi(2), {}^4\Delta; \\
&X({}^2P_u)+O({}^1D_g) \rightarrow {}^2\Sigma^+(2), {}^2\Sigma^-, {}^2\Pi(3), {}^2\Delta(2), {}^2\Phi; \\
&X({}^2P_u)+O({}^1S_g) \rightarrow {}^2\Sigma^+, {}^2\Pi.
\end{aligned}$$

The $^2\Pi_i$ ground states of the halogen monoxides undoubtedly correspond to one of the two $^2\Pi$ states which may be formed from ground state atoms. The $^2\Pi_i$ excited states, however, cannot be correlated with the second $^2\Pi$ state which can be formed from ground state atoms since in all the observed spectra some diffuse bands are observed indicating predissociation in the excited state. The $^2\Pi_i$ excited states must therefore dissociate into $X(^2P_u) + O(^1D_g)$ or into $X(^2P_u) + O(^1S_g)$. The latter possibility may be ruled out in each case since it would lead to dissociation energies lower than some of the vibrational levels of the ground state observed in the emission spectra. The excited states therefore dissociate into $X(^2P_u) + O(^1D_g)$ (see Fig. 7). An ambiguity still remains, however, since it is not known whether the

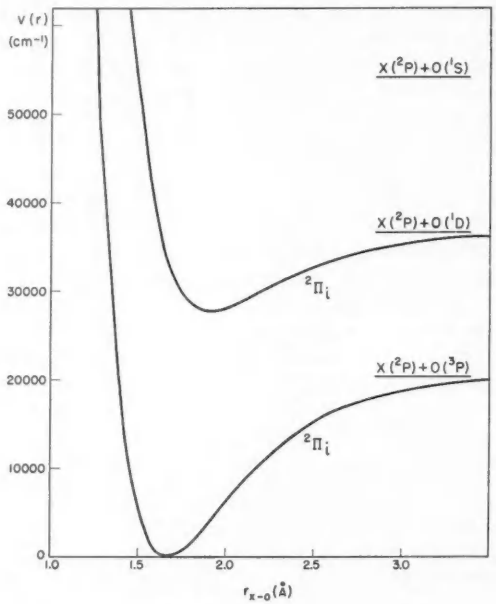

FIG. 7. Correlation diagram for the halogen monoxides and their dissociation products.

$X(^2P_u)$ atom is in the $^2P_{3/2}$ or $^2P_{1/2}$ state. Theoretical considerations given in the following section show that the halogen atom is very probably produced in the $^2P_{3/2}$ state. The individual dissociation energies will now be considered.

(*i*) *ClO*

The absorption spectrum of ClO has been observed to the dissociation limit. The rotational analysis shows that the origin of the last vibrational band analyzed ($v' = 25$) is at 37997.4 cm^{-1}. A short extrapolation of the vibrational intervals in the upper state gives a dissociation limit at ~38020 cm^{-1} and suggests that it should be possible to observe lines of the band with

$v' = 26$ and possibly a few lines of the band with $v' = 27$. A few absorption lines are observed in the region 37997 to 38026 cm^{-1} and may presumably be assigned to low J transitions involving these vibrational levels. The dissociation limit may therefore be taken as 38020 ± 10 cm^{-1}. Since the energy of excitation of an oxygen atom from a $^3P_2$ ground state to a ^1D state is 15868 cm^{-1} the ground state dissociation energy of ClO is

$$D_0(\text{ClO}) = 22152 \pm 10 \text{ cm}^{-1} = 63.31 \pm 0.03 \text{ kcal./mole} = 2.746 \pm 0.001 \text{ ev.}$$

(*ii*) *BrO*

The absorption spectrum of BrO was not observed to the dissociation limit, but values for the limit were determined from equation (12) by substituting the condition that $\Delta G = 0$, and from a graphical Birge–Sponer extrapolation. In both cases the limit was $\backsim 35{,}200$ cm^{-1}. The limit is thus $\backsim 700$ cm^{-1} beyond the last observed band and is probably accurate to about ± 200 cm^{-1}. Subtracting the ^1D—$^3P_2$ excitation energy of the oxygen atom, the dissociation energy of the ground state is found to be

$$D_0(\text{BrO}) = 19330 \pm 200 \text{ cm}^{-1} = 55.2 \pm 0.6 \text{ kcal./mole} = 2.40 \pm 0.02 \text{ ev.}$$

This value is considerably higher than the value of 40 kcal./mole estimated by Coleman and Gaydon from a long Birge–Sponer extrapolation of the ground state vibrational intervals.

(*iii*) *IO*

Since only six bands were observed in the absorption spectrum of IO, it is not possible to obtain an accurate value for the dissociation energy of the ground state. An upper limit may be determined, however, from the observed predissociation in the IO spectrum. Since the (1,0) band is diffuse, the dissociation energy of the ground state must be less than the energy of the $v' = 1$ level, i.e. $D_0(\text{IO}) < 21976$ cm^{-1} (= 62.8 kcal./mole = 2.72 ev.). Moreover, since Coleman, Gaydon, and Vaidya have observed vibrational levels up to $v'' = 12$ in the emission spectrum, the dissociation energy of IO must be higher than the energy of the $v'' = 12$ level, i.e. $D_0(\text{IO}) > 7477$ cm^{-1} (= 21.4 kcal./mole = 0.93 ev.).

Probably the best method for obtaining an estimate of the ground state dissociation energy is by means of a Birge–Sponer extrapolation of the observed vibrational levels in the upper state. Applying a linear extrapolation to the first four vibrational intervals we find $D_0' = 10200$ cm^{-1}. Now the accepted values of D' for ClO and BrO are $\backsim 10\%$ less than the values obtained by linear extrapolations of the first few vibrational intervals. Hence applying this correction to IO, we find $D'(\text{IO}) = 9200$ cm^{-1}. If now we add the wavenumber of the (0,0) band ($\nu_{00} = 21476$ cm^{-1}) and subtract the ^1D—$^3P_2$ excitation energy of the oxygen atom, we obtain $D_0''(\text{IO}) = 14800$ cm^{-1}. If we assume that the value of D' is accurate to 20%, then $D_0''(\text{IO}) = 14800 \pm 1800$ cm^{-1} $= 42 \pm 5$ kcal./mole $= 1.8 \pm 0.2$ ev. This value is in good agreement with the value of 44 ± 5 kcal./mole estimated by Coleman, Gaydon, and Vaidya from a Birge–Sponer extrapolation of the ground state vibrational intervals.

It is interesting to note that if the upper state is assumed to dissociate into $I(^2P_{1/2})+O(^1D)$ rather than into $I(^2P_{3/2})+O(^1D)$, then the value obtained for $D''(IO)$ is 7200 cm^{-1}, which is less than the vibrational energy of some of the observed vibrational levels of the ground state. The value is therefore unacceptable and we obtain a direct experimental proof that the upper state can only dissociate into $I(^2P_{3/2})+O(^1D)$ in agreement with the theoretical predictions in the next section. A similar distinction cannot be made in the case of the ClO and BrO since their dissociation energies are larger than for IO and the doublet separations for the chlorine and bromine atoms are much smaller than for the iodine atom.

NATURE OF THE DISSOCIATION PRODUCTS

In the previous section it was shown that the $^2\Pi_i$ excited state in the halogen monoxides dissociates into $X(^2P)+O(^1D)$ but it was not possible from the Wigner–Witmer correlation rules to determine if the halogen atom is produced in the $^2P_{3/2}$ or the $^2P_{1/2}$ state. In the case of iodine monoxide, however, it was possible to obtain strong experimental evidence that the iodine atom is produced in the ground $^2P_{3/2}$ state.

Theoretical evidence for the state of the halogen atom may be derived by the following method outlined in various papers by Mulliken (1928 *a*, *b*, 1930 *a*, *b*). This method involves a consideration of the Stark effect of atoms in very strong electric fields and of the electron configurations which may be assigned to molecules and atoms in strong electric fields.

Let us consider an atom with strong L^*, S^* coupling. In an electric field which is weak compared with the L^*, S^* coupling, the resultant angular momentum J^* is orientated so that its component parallel to the field is $M_J h/2\pi$, where $M_J = J, J-1, \ldots, -J$. In an electric field which is strong compared with the interaction of L^* and S^*, the orbital angular momentum L^* is orientated so that its component parallel to the field is $M_L h/2\pi$, where $M_L = L, L-1, \ldots, -L$. The spin angular momentum S^* is not influenced by the electric field but it is orientated by the average magnetic field associated with L^*. Since the latter is parallel to the electric field direction, the spin angular momentum S^* is orientated so that its component in the field direction is $M_S h/2\pi$, where $M_S = S, S-1, \ldots, -S$. The total angular momentum parallel to the field axis is $M_J h/2\pi$, where $M_J = M_L+M_S$.

Now the energy of an atom in an axially symmetric electric field depends on $|M_L|$ and $|M_J|$ rather than on M_L and M_J, i.e. $F(M_L) = F(-M_L)$ and $F(M_J) = F(-M_J)$. For this and other reasons Mulliken introduced the following symbols: $\Lambda = |M_L|$, $\Sigma = \pm M_S$, such that Σ is positive when M_S and M_L have the same sign and Σ is negative when they have opposite signs, $\Omega = |\Lambda+\Sigma| = |M_J|$.

A schematic diagram showing the energy levels of a ^2P chlorine atom in various electric fields is given in Fig. 8(*a*) together with the appropriate quantum numbers. The adiabatic correlations between the levels of the atom in various electric fields are also shown and are determined by means of the rules: (*a*) M_J remains constant as the field is varied, and (*b*) no two levels

with the same M_J can cross as the field is varied. The energy levels, quantum numbers, and adiabatic correlations for a ^1D oxygen atom in various electric fields are shown in Fig. 8(b).

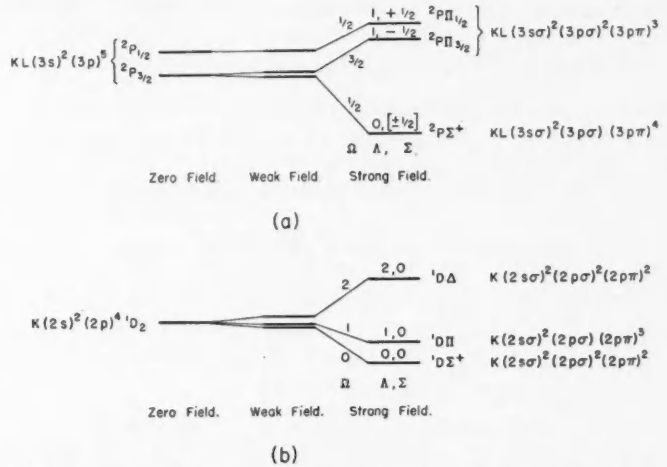

FIG. 8. Energy levels, quantum numbers, and electron configurations, (a) for a ^2P chlorine atom and (b) for a ^1D oxygen atom in various electric fields.

We shall now consider the electron configurations which may be assigned to the various levels of the atoms in a strong electric field. The electron configuration of a chlorine atom in its ^2P ground state is $KL(3s)^2(3p)^5$. In a strong axially symmetric electric field the p electrons become $p\sigma$ or $p\pi$ electrons. The two possible configurations and term types for the chlorine atom are

$$KL(3s\sigma)^2(3p\sigma)^2(3p\pi)^3, \qquad {}^2P\Pi_i,$$

$$KL(3s\sigma)^2(3p\sigma)(3p\pi)^4, \qquad {}^2P\Sigma^+.$$

In a similar manner the electron configurations and term types for a ^1D oxygen atom in a strong electric field are

$$K(2s\sigma)^2(2p\sigma)^2(2p\pi)^2, \qquad {}^1D\Sigma^+, {}^1D\Delta,$$

$$K(2s\sigma)^2(2p\sigma)(2p\pi)^3, \qquad {}^1D\Pi.$$

Now the electron configuration of the $^2\Pi_i$ excited state of ClO was shown in an earlier section to be

$$(z\sigma)^2(y\sigma)^2(x\sigma)^2(w\pi)^3(v\pi)^4.$$

If it is assumed that the internuclear distance is increased to infinity but the strong electric field is retained, then by Mulliken's "detailed $\sigma_{l\sigma}$ correlation rule", each σ electron in the molecule will become an $s\sigma$ or $p\sigma$ electron in one

of the atoms, and each π electron in the molecule will become a $p\pi$ atomic electron. Then the only possible dissociation products are

$$\mathrm{Cl}[KL(3s\sigma)^2(3p\sigma)(3p\pi)^4, {}^2P\Sigma^+] + \mathrm{O}[K(2s\sigma)^2(2p\sigma)(2p\pi)^3, {}^1D\Pi].$$

If the strong electric field is now removed, it is seen from Figs. 8(*a*) and 8(*b*) that

$$\mathrm{Cl}({}^2P\Sigma^+) \rightarrow \mathrm{Cl}({}^2P_{3/2}) \qquad \text{and } \mathrm{O}({}^1D\Pi) \rightarrow \mathrm{O}({}^1D_2).$$

Hence we have shown unambiguously that the ${}^2\Pi_i$ excited state of ClO dissociates to $\mathrm{Cl}({}^2P_{3/2})+\mathrm{O}({}^1D_2)$. It may be noted that these arguments apply equally to the ${}^2\Pi_{3/2}$ and ${}^2\Pi_{1/2}$ components of the excited state, i.e. both doublet components dissociate to the same multiplet components of the atoms.

REACTION MECHANISMS

(*i*) *ClO*

Porter and Wright (1953) have postulated that ClO is formed by the mechanism

$$\mathrm{Cl}+\mathrm{O}_2 = \mathrm{ClOO},$$
$$\mathrm{ClOO}+\mathrm{Cl} = 2\mathrm{ClO}.$$

Since the dissociation energy of oxygen is 117.96 ± 0.04 kcal./mole (Brix and Herzberg 1954) and the dissociation energy of ClO is 63.31 ± 0.03 kcal./mole, it is seen that the over-all reaction

$$2\mathrm{Cl}+\mathrm{O}_2 = 2\mathrm{ClO}$$

is exothermic by 8.66 ± 0.10 kcal./mole, if both chlorine atoms are in the ${}^2P_{3/2}$ ground state.

(*ii*) *BrO*

Since the dissociation energy of BrO is 55.2 ± 0.6 kcal./mole the reaction

$$2\mathrm{Br}({}^2P_{3/2})+\mathrm{O}_2 = 2\mathrm{BrO}$$

is endothermic by 7.6 ± 1.2 kcal./mole. The reaction is therefore unlikely to be sufficiently rapid to account for the formation of BrO in the present experiments. A more probable over-all reaction is

$$\mathrm{Br}({}^2P_{3/2})+\mathrm{Br}({}^2P_{1/2})+\mathrm{O}_2 = 2\mathrm{BrO},$$

which is exothermic by 2.9 ± 1.2 kcal./mole.

(*iii*) *IO*

Since the dissociation energy of IO is 42 ± 5 kcal./mole, it is clear that the IO observed in the present experiments could not be formed by the reaction

$$2\mathrm{I}({}^2P_{3/2})+\mathrm{O}_2 = 2\mathrm{IO}-34\pm10 \text{ kcal./mole}.$$

More probable courses for the over-all reaction are

$$\mathrm{I}({}^2P_{3/2})+\mathrm{I}({}^2P_{1/2})+\mathrm{O}_2 = 2\mathrm{IO}-12\pm10 \text{ kcal./mole}$$

and

$$2\mathrm{I}({}^2P_{1/2})+\mathrm{O}_2 = 2\mathrm{IO}+10\pm10 \text{ kcal./mole}.$$

The experiments with BrO and IO therefore furnish evidence for the participation of $^2P_{1/2}$ halogen atoms.

We are indebted to Dr. I. D. Liu for the spectrogram reproduced in Fig. 3 and to Miss L. L. Howe and Miss J. Ouimet for assistance with the computations. One of us (D.A.R.) wishes to acknowledge a stimulating discussion with Professor R. S. Mulliken concerning detailed correlation rules.

REFERENCES

BRIX, P. and HERZBERG, G. 1954. Can. J. Phys. **32**, 110.
CALLOMON, J. H. and RAMSAY, D. A. 1957. Can. J. Phys. **35**, 129.
COLEMAN, E. H. and GAYDON, A. G. 1947. Discussions Faraday Soc. **2**, 166.
COLEMAN, E. H., GAYDON, A. G., and VAIDYA, W. M. 1948. Nature, **162**, 108.
HERZBERG, G. 1950. Spectra of diatomic molecules (D. Van. Nostrand Co. Inc., Princeton, N.J.).
HERZBERG, G. and RAMSAY, D. A. 1950. Discussions Faraday Soc. **9**, 80.
MULLIKEN, R. S. 1928*a*. Phys. Rev. **32**, 186.
——— 1928*b*. Phys. Rev. **32**, 761.
——— 1930*a*. Phys. Rev. **36**, 1440.
——— 1930*b*. Revs. Modern Phys. **2**, 60.
——— 1931. Revs. Modern Phys. **3**, 89.
——— 1932. Revs. Modern Phys. **4**, 1.
PANNETIER, G. and GAYDON, A. G. 1948. Nature, **161**, 242.
PAULING, L. and BROCKWAY, L. O. 1935. J. Am. Chem. Soc. **57**, 2684.
PORTER, G. 1950. Discussions Faraday Soc. **9**, 60.
PORTER, G. and WRIGHT, F. J. 1953. Discussions Faraday Soc. **14**, 23.
VAIDYA, W. M. 1937. Proc. Indian Acad. Sci. A, **6**, 122.
——— 1938. Proc. Indian Acad. Sci. A, **7**, 321.

A LARGE-AREA LIQUID SCINTILLATION COUNTER AND SOME MEASUREMENTS ON HIGH-ENERGY COSMIC-RAY PARTICLES[1]

C. H. MILLAR, E. P. HINCKS, AND G. C. HANNA

ABSTRACT

A liquid scintillation counter is described which consists of a $29\frac{3}{4}$ in. by $29\frac{3}{4}$ in. by 2 in. Plexiglas tank of terphenyl plus α-naphthylphenyloxazole (αNPO) in triethylbenzene. The tank is surrounded by MgO powder and viewed by a total of eight RCA Type 5819 photomultiplier tubes along two opposite edges. For normally incident fast μ-mesons a peaked pulse height distribution is observed, 20.5% in width at half-maximum for the central area of the counter, broadening to 25–30% at the perimeter, and estimated to be 25% over-all. When the Landau distribution in energy loss (width 18% at half-maximum) and the geometric spread are taken into account, a counter resolution function 8% in width at half-maximum is obtained for the central area of the counter, or 18% for the counter as a whole.

The *most probable* pulse height for 0.30 Bev. μ-mesons is $1.6\pm0.5\%$ higher than for 2.2 Bev. μ-mesons, in close agreement with the Bethe–Bloch theory as extended by Symon and with a density correction calculated by the method of Sternheimer. Pulse heights from protons in the region 0.3 to 0.8 Bev. vary directly with the theoretically computed energy loss in the counter. Peak position and resolution are unchanged by a flux of 12 mr./hr. of thorium γ-rays.

1. INTRODUCTION

In the course of cosmic-ray experiments being carried out at Chalk River, a requirement developed for a large-area energy-sensitive counter capable of detecting fast cosmic-ray protons in the presence of a high flux of γ-rays from a naturally radioactive target.

The known properties of liquid scintillation solutions (e.g. Reynolds 1950) and the fact that large liquid scintillation counters had been used successfully by others (e.g. Baskin and Winckler 1953; Cowan *et al.* 1953) indicated that a liquid scintillation counter would fulfill our requirements.

Three intrinsic properties of this type of counter make it useful for our purpose. First, for the values of specific energy loss characteristic of fast protons, the pulse height from a liquid scintillation counter may be expected to vary directly as the energy deposited in it, and therefore the variation of pulse height with proton energy is given by the theoretical energy-loss formula (see Appendix). However this variation is rapid enough for pulse height to be a useful measure of proton energy only in the range below $\sim$600 Mev.

Secondly, the much greater stopping power of a liquid scintillation counter compared with that of gas-filled counters operating at reasonable pressures results in a narrower pulse-height distribution, that is in better energy resolution.

Thirdly, the fast response of liquid scintillators (a few millimicroseconds) aids in the suppression of background due to γ-rays from a radioactive target.

[1]Manuscript received October 2, 1957.
Contribution from the Physics Division, Atomic Energy of Canada Limited, Chalk River, Ontario.
Issued as A.E.C.L. No. 522.

By using a counter of sufficient thickness the proton pulses can be made considerably larger than those from single γ-rays, and, with the short pulse duration that is permitted by the fast scintillator response, a high γ-ray flux can be tolerated before the counting rate of "build-up" pulses becomes serious.

Plastic scintillation counters may also be constructed to meet these requirements but we chose to develop a liquid counter since at the time this work was started plastic scintillators were not available. A large-area counter made with the plastic scintillation material now produced commercially would be much simpler mechanically than the equivalent liquid scintillation counter; however this advantage would be to some degree offset by the higher cost of the plastic.

This paper describes the liquid scintillation counter which we developed and the various tests carried out on it. These include measurements of the counter's sensitivity and resolution over the active area, its discrimination against γ-ray background, and its response to fast protons. In addition an experiment is described in which the counter's response to μ-mesons near minimum ionization is shown to confirm with considerable precision the most recent theories of the energy loss by fast charged particles.

2. DESCRIPTION OF COUNTER

(*a*) *General*

The counter which was developed by one of us (C.H.M.) is shown in Fig. 1. It consists of a tank $29\frac{3}{4}$ in. by $29\frac{3}{4}$ in. by 2 in. (outside dimensions) built of $\frac{1}{4}$ in. Type II, ultraviolet-transmitting Plexiglas sheet. Eight RCA Type 5819

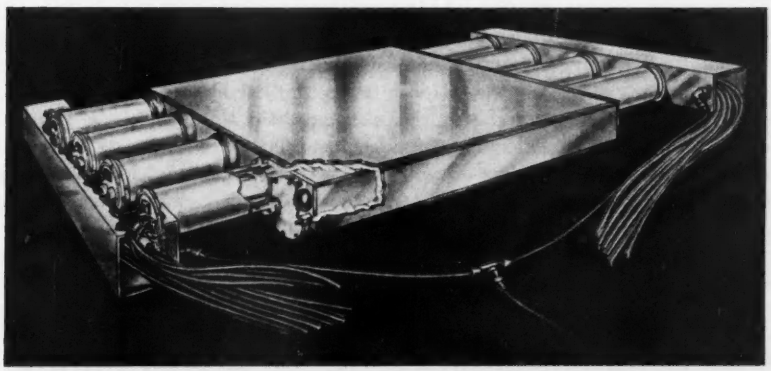

FIG. 1. General view of large-area liquid scintillation counter.

photomultiplier tubes view the interior of the tank along two opposite edges through short Plexiglas light pipes which are cemented to the tank. The outer faces of these light pipes are machined to match the curvature of the faces of the photomultiplier tubes and optical coupling is effected by a thin layer of mineral oil.[2] Surrounding the Plexiglas tank is a $\frac{1}{4}$ in. layer of MgO powder

[2]In later experiments the non-hardening optical cement described by Shipp (1952) has proved to be easier to retain than mineral oil.

contained in a thin aluminum box which also serves as a light shield and as a base for mounting the photomultiplier assemblies. The tank is filled with a scintillation solution of 2.7 g./l. *p*-terphenyl in *x*-triethylbenzene[3] to which has been added 50 mg./l. α-naphthylphenyloxazole (αNPO).

(*b*) *Mechanical Details*

The Plexiglas tank is supported and held centered in the aluminum container by the tapered steel collars pressed against the Plexiglas light pipes, one of which is shown in Fig. 2. These tapered joints also separate the MgO powder from the mineral oil used for optical coupling, the seal being made with

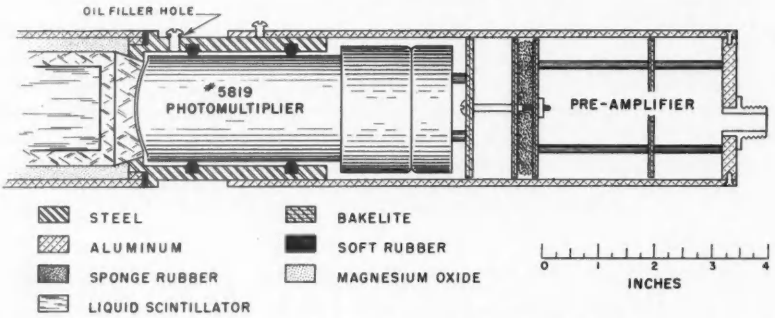

FIG. 2. Section view showing method of attachment of photomultiplier to scintillator tank.

Glyptal cement. The collars themselves provide a mechanical support for the photomultiplier tubes and preamplifiers as well as providing magnetic shielding for the portions of the photomultiplier tubes that are most sensitive to stray magnetic fields. The photomultiplier tubes are held aligned by two O-rings fitted into grooves in the collars, the foremost of these also serving as a seal for the mineral oil. A compressive force to hold the photomultipliers against the light pipes is applied through the sponge rubber tube base mountings in the preamplifier assemblies. These mountings also act as flexible couplings between preamplifiers and tubes which provide shock insulation and make allowance for tube base misalignments. Live rubber gaskets are included between the steel collars and the aluminum box to allow for cumulative assembly errors and to ensure tight fits of the tapered joints on opposite sides of the counter. In addition, a pattern of $\frac{1}{4}$ in. Plexiglas spacers in the top and bottom MgO space prevents sagging of the Plexiglas tank with respect to the aluminum shield.

The tank is filled through a threaded hole in the edge and an O-ring seal is incorporated which prevents spilled liquid from penetrating to the MgO powder. The filling hole is sealed by a Teflon plug and a gasket cut from Tygon tubing.

[3]*x*-Triethylbenzene is available from Dow Chemical Company as "Alkazene-3". For the suggestion to use this chemical, which dissolves *p*-terphenyl but not Plexiglas, we are indebted to Dr. F. N. Hayes of the Los Alamos Laboratory.

No particular provision for expansion of the scintillation liquid is made since a calculation showed that the differential expansion of the Plexiglas and scintillator over the normal range of operating temperature would be easily taken up by minute bulging of the two broad faces of the tank without building up appreciable internal pressure or seriously altering the uniformity of scintillator thickness. However, it is necessary to provide a strong steel clamp which can be placed around the counter to prevent bulging of the large faces due to hydrostatic pressure when the tank has to be placed on edge either for handling or filling.

In assembling the Plexiglas tank the most satisfactory joining technique proved to be a simple solvent welding process. One of the parts to be joined was soaked for 4 minutes in chloroform and then held firmly but lightly in position against the dry half of the joint for about half a day. It was found necessary to anneal Plexiglas which was to be welded in order to avoid surface crazing caused by the action of the solvent on the surface layers of material which had been strained in machining or polishing. This annealing was carried out by raising the temperature of the finished pieces to about 82° C. in a laboratory oven for several hours. The oven was then turned off and allowed to cool to room temperature over a period of a few hours.

(*c*) *Optical Details*

For best results with a scintillation counter it is desirable that as large a fraction as possible of the light produced in the scintillator should reach the photomultiplier tubes, and also that this fraction should be the same for light generated anywhere within the active volume.

Preliminary experiments were carried out with a small volume liquid scintillation counter made of a 250 cc. Pyrex beaker to determine what type of surface reflector produced the largest pulse height for a given γ-ray source. Polished aluminum foil placed either inside or outside the beaker, high-reflectivity white paint, on either inside or outside surface, and MgO powder placed outside the beaker are typical of the combinations tested, and of these the last proved to be by far the best. Accordingly, the counter tank was constructed of Type II ultraviolet-transmitting Plexiglas (which is more transparent to ultraviolet light than Pyrex) surrounded by MgO powder.

Since the indices of refraction of Plexiglas and the liquid scintillator are nearly equal (n = 1.49 to 1.50) optical effects at the Plexiglas–scintillator interface are negligible. The large relative index of refraction at the Plexiglas–air interface causes 75% of the light reaching the top and bottom surfaces of the tank from a scintillation within to proceed by a series of total internal reflections to the edges of the tank. Of the remaining 25% of the light, which is diffusely reflected by the MgO, more than half is converted to critically reflectable light at each such diffuse reflection.

(*d*) *Electronic Circuits*

The choice of electronic circuits used to amplify and measure the pulses from the counter was governed by the degree to which we wished to exploit its fast response. The main amplifier system that has been used for the measure-

ments described in this paper is of only moderate speed, having a resolving time of the order of 10^{-7} sec., and is fairly conventional so it will not be described in any detail.

The photomultiplier connections and the method of combining the eight photomultiplier signals that was used are shown in Fig. 3. The photomultiplier anode pulse, whose width is determined by the discharge of the total stray

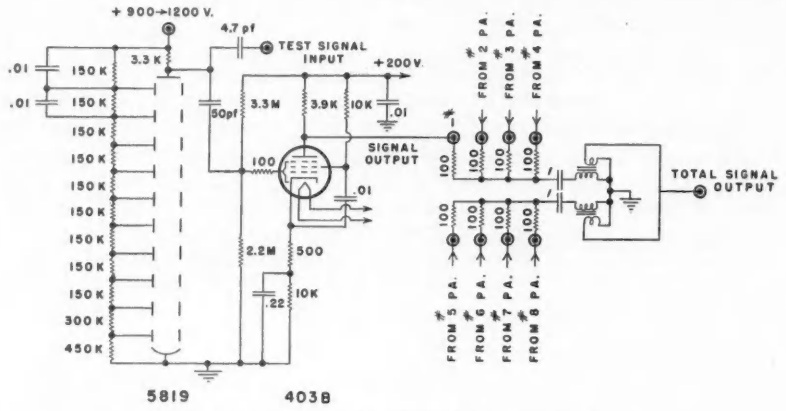

FIG. 3. Circuit diagram of photomultiplier preamplifiers.

capacity through the 3300 ohm load resistor, is fed through a single-stage preamplifier. The outputs from the four preamplifiers along one side of the counter are connected in parallel and this combined output is added to that from the opposite four preamplifiers and matched to the main output cable by means of pulse transformers.

The bleeder chain from which the dynode potentials are obtained has a total resistance of only 2.1 megohms and carries a current of about 0.5 ma. Even at γ-ray background counting rates of the order of 10^7 counts per second the mean current flowing out of the last dynode with normal photomultiplier gain is much less than this, so that the dynode potentials are not significantly altered.

3. COUNTER CHARACTERISTICS FROM MEASUREMENTS OF FAST μ-MESONS

(*a*) *Variation of Response over Counter Area and Estimate of Over-all Response*

Though the counter was designed for use with fast protons, cosmic-ray μ-mesons were used for testing its characteristics. To select collimated μ-mesons for this work the scintillation counter was operated in triple coincidence with two large-area counters placed one above and one below it. (Geiger, Čerenkov, and liquid scintillation counters were used at various times for this purpose.) Enough lead was interposed in this telescope to eliminate the soft component of cosmic rays so that the test beam consisted mainly of high-energy μ-mesons directed within a few degrees of the vertical.

Sufficiently large collimating counters were not readily available to test the whole counter area at one time but an arrangement that selected particles within a 15 in. square area was used to test the response of various typical regions of the counter and these results were combined to give an estimate of the response of the whole counter to vertically directed particles.

Fig. 4 is a diagram of the various areas studied in this manner and Table I gives the positions and widths of the peaks in the pulse-height distributions observed for μ-mesons passing through these areas.

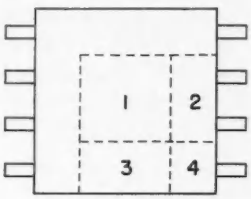

FIG. 4. Diagram showing the regions of the large-area liquid scintillation counter that were studied separately.

TABLE I

COUNTER RESPONSE TO FAST μ-MESONS

Counter area	Position of counter area	Most probable pulse height (normalized)	Width of peak at half-maximum (per cent)	Calculated width at half-maximum of counter resolution function (per cent)
1	Center	0.96	20.5	9
2	P.M. edge	1.08	25.5	18
3	Blank edge	0.96	30.5	24
4	Corner	1.02	27.0	20
1–4	Weighted estimate for whole counter	1.00	25	18

The theoretical energy loss by fast μ-mesons passing normally through the counter has a most probable value of 5.8 Mev., and a Landau distribution whose width at half-maximum is 17.8%. The geometric width under the conditions of the above tests was approximately 4% so that it is possible to obtain an indication of the counter resolution function for the various areas studied by assuming that the observed width at half-maximum of the distribution function is the r.m.s. value of the Landau spread, the geometric spread, and the counter resolution function. This calculation is not entirely valid since neither the Landau distribution nor the geometric spread function is Gaussian in shape; however, a more exact calculation which will be described later indicates that this is a good approximation. The widths thus calculated for the counter resolution function for the various areas studied are shown in the last column of Table I together with an estimate for the whole counter.

(*b*) *Effect of γ-Ray Background*

The effect of a high flux of γ-rays on the performance of the counter was studied by measuring the pulse-height distribution for a wide-angle beam of cosmic rays when the counter was placed on both a $\frac{3}{4}$ in. slab of lead and a $\frac{3}{4}$ in. slab of thorium. Cosmic-ray particles were selected by coincidences with a Plexiglas Čerenkov counter, 13 in. square, placed centrally on top of the liquid scintillation counter. The thorium produced a γ-ray field of 12 milliroentgens per hour at the scintillation counter which was mainly due to the 2.6 Mev. γ-rays from ThC″. The test was carried out using circuits whose time constants resulted in a pulse with a width (at half-maximum height) of about 0.2 μsec. The results are shown in Fig. 5, where it will be seen that while there is a low-level background of γ-ray build-up pulses, the main part of the peak is unaffected. For particles of greater than minimum ionization there would be even less distortion and with faster circuits even greater background intensity would be tolerable.

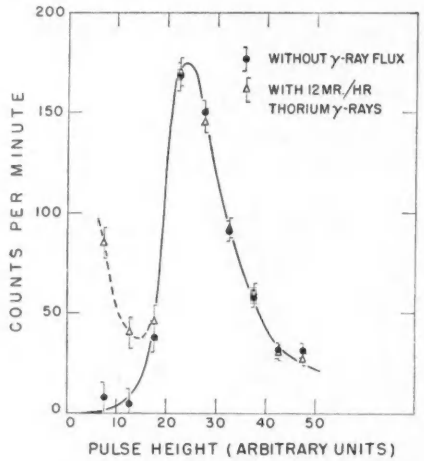

FIG. 5. Observed pulse-height distribution for fast μ-mesons with and without 12 mr./hr. γ-rays.

(*c*) *Relative Energy Losses of μ-Mesons above 0.3 Bev.*

As it was desired to obtain operational experience with the counter before incorporating it in the proton experiment for which it was designed, an experiment was set up to measure the most probable energy deposited in the counter by fast μ-mesons of selected energies. The disposition of counters and absorbers used in this experiment is shown in Fig. 6 and a block diagram of the electronic circuitry is shown in Fig. 7. Penetrating charged cosmic-ray particles which passed through the central area of the counter under test (SC1) within 13.5° of the vertical were selected by a prompt triple-coincidence either of the two Geiger counter trays (GC1, GC2) and SC1, or of SC1, GC2, and SC3.

From the collimated beam μ-mesons of two specific ranges were selected by observing their decay electrons in one of the lower scintillation counters, SC2, SC3, or SC4. Thus a meson which came to rest in the vicinity of SC2 and produced a decay electron pulse in SC2 with a delay between 0.5 and 3 μsec. gave rise to an "SC2 delayed coincidence"; from the amount of material in the telescope it is estimated that such a meson passed through SC1 with an energy of 0.30 Bev. Similarly a meson whose decay electron was detected in SC3 or SC4 ("SC3 or SC4 delayed coincidence") traversed SC1 with an energy of 2.2 Bev.

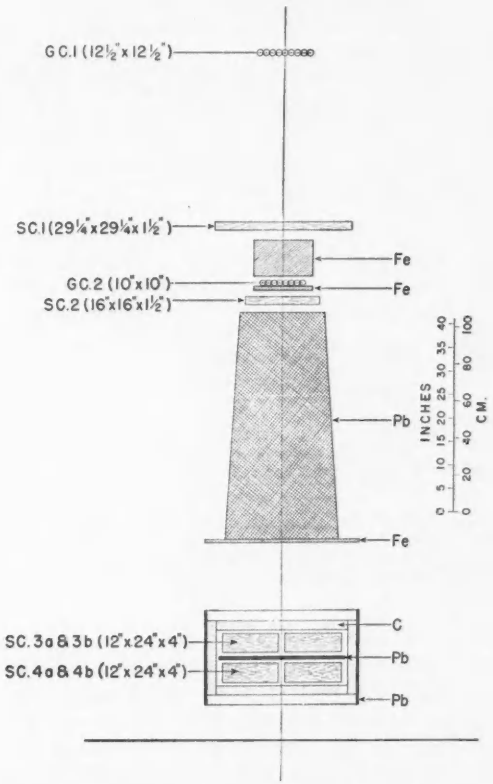

FIG. 6. Disposition of counters and absorbers for measuring response of large-area liquid scintillation counter to μ-mesons of specific energies.

The four counters comprising SC3 and SC4 contained a total of 20 gallons of scintillator and these together with the surrounding graphite provided an absorber of considerable mass from which decay electrons could be detected with high efficiency. The surrounding lead shielding helped to ensure that decay

electrons originating in the laboratory floor and walls were not detected by the counters. Since SC3 and SC4 were separately observed and sufficient absorber was placed between them to prevent decay electrons originating in one counter from reaching the other, a coincidence between these two counters indicated that a penetrating particle had arrived by chance during the open period of the delayed gate and such an event was discarded.

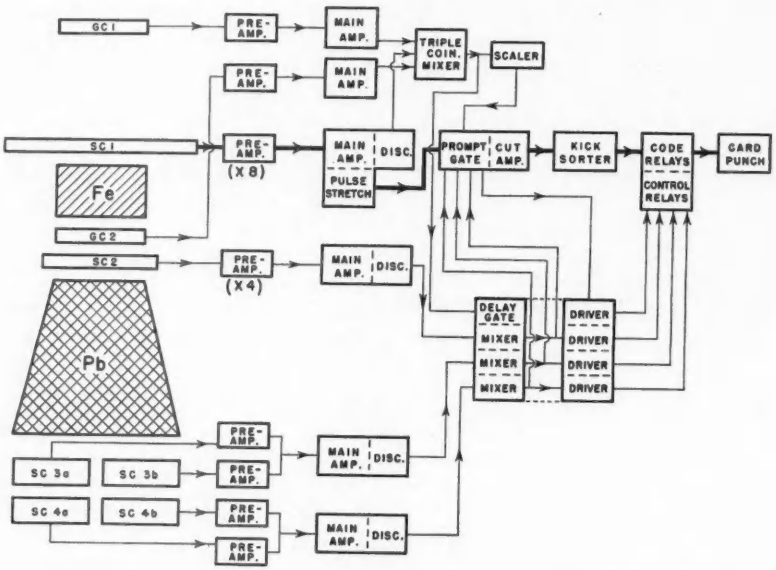

FIG. 7. Block diagram of electronic apparatus used with the disposition shown in Fig. 6 for measuring response of large-area liquid scintillation counter to μ-mesons of specific energies. Not shown on the diagram is the arrangement for adding the output of SC3 discriminator to that of GC1 main amplifier before it enters the triple coincidence mixer.

Pulse heights from SC1 were analyzed by a 30-channel kicksorter which was gated by any delayed coincidence. The kicksorter information was recorded on an I.B.M. punched card together with information as to which prompt triple coincidence and which of the SC2, SC3, SC4 delayed coincidences were involved in the event. In addition, cards were punched for a 3% sample (selected by a scale-of-32) of all particles selected by a three-fold prompt coincidence without the requirement of a delayed coincidence. Pulse-height distributions were thus obtained simultaneously for μ-mesons of two well-defined energies traversing SC1, and in addition for a representative sample of the cosmic-ray μ-meson spectrum above 0.27 Bev. It was also possible to select on the basis of the coincidence information a group containing mesons of all energies above 2.2 Bev. The energies of the various groups and the coincidences by which they were selected are summarized in Table II.

TABLE II

ENERGIES OF SELECTED μ-MESON GROUPS

Group	Energy (Bev.)	Prompt coincidence	Delayed pulse
1	0.30	GC1, SC1, GC2	SC2 only
2	2.2	SC1, GC2, SC3	SC3 only or SC4 only
3	>0.27	GC1, SC1, GC2	—
4	>2.2	SC1, GC2, SC3	—

The sample distribution served to provide for each day's run a peak whose statistical accuracy made it suitable for monitoring the over-all gain of the system. This was desirable since the counting rate for the mesons of selected energies (Groups 1 and 2) was of the order of one per hour and a month's running time was required to provide reasonable statistics.

Fig. 8 shows the distributions observed for 0.30 and 2.2 Bev. μ-mesons after subtracting a small chance distribution computed from an auxiliary experiment. The solid curves show the statistically more accurate 'sample' distribu-

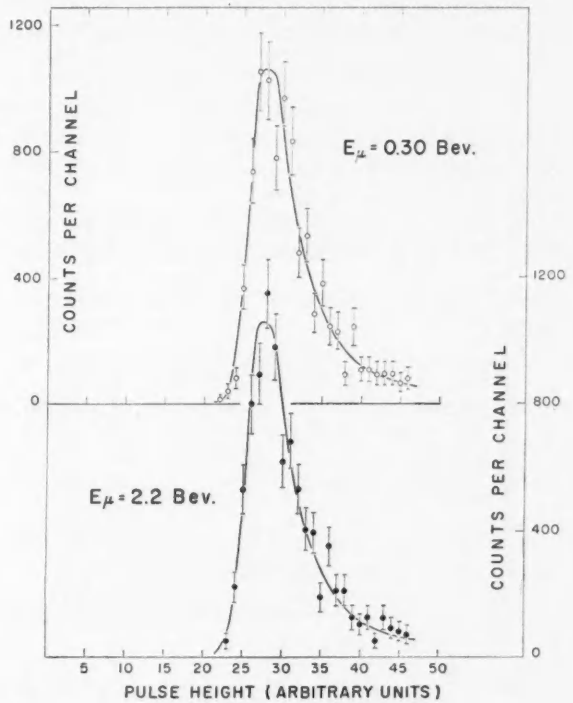

FIG. 8. Observed pulse-height distributions for 0.30 and 2.2 Bev. μ-mesons passing through central area of the counter.

tion function adjusted along the abscissa to give the best fit to the observed points, and it will be seen that to within the statistics of the experiment the two curves have the same shape as the 'sample'.

The relative position of the peaks in the two cases has been obtained by plotting the logarithm of the cumulative intensity versus the logarithm of the pulse height and visually adjusting the two curves to match. This method places the emphasis on a good fit in the region of the peak and the sharply-rising lower edge, and minimizes the effect of the upper side of the peak where the poor statistics could possibly conceal a real change in curve shape. The ratio of the *most probable* pulse heights obtained by averaging the results of three different observers is

$$V_p(0.30 \text{ Bev.})/V_p(2.2 \text{ Bev.}) = 1.016 \pm 0.005.$$

The theoretical value (see Appendix) of the ratio of the most probable energy losses for μ-mesons of these energies traversing the counter normally is 1.022, which is in good agreement with the observed pulse height ratio.

A second comparison with theory was made by separating the 'sample' events into those of energies >0.27 Bev. and those of energies >2.2 Bev. by means of the coincidence information. The observed most probable pulse heights were compared as previously and these were found to have a ratio

$$V_p(>0.27 \text{ Bev.})/V_p(>2.2 \text{ Bev.}) = 1.000 \pm 0.005.$$

The theoretical variation of most probable energy loss with μ-meson energy was combined with the sea-level μ-meson spectrum (Puppi 1956) cut off at the two appropriate energies to obtain a calculated ratio of 0.997 which compares well with the experimental value.

These two results are shown graphically in Fig. 9. Here the curve shows the theoretical energy dependence of the most probable energy loss for μ-mesons

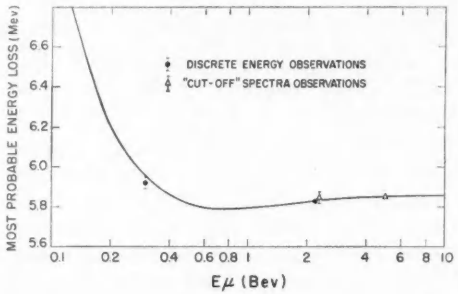

FIG. 9. Observed variation with μ-meson energy of the most probable pulse height compared with theory (solid curve).

in triethylbenzene, and the points are the observed values for both the specific μ-meson energies and the cutoff cosmic-ray spectra. Differences in the characteristics of the electronics for the two types of observations require that each

be separately normalized, and in each case the higher energy value has been adjusted to fit the curve. In the case of the cutoff spectra a computed effective μ-meson energy has been used for purposes of comparing the experimental data with the differential curve.

Our results confirm with somewhat greater precision the earlier conclusions of Baskin and Winckler (1953), who used xylene, and Bowen and Roser (1952), who used an anthracene crystal. Both these groups found agreement with theory including a correction for the density of the material, and concluded that the density effect must indeed be invoked to explain the observed energy independence of the *most probable* pulse height for μ-mesons at high energies.

(d) Detailed Consideration of Response Curve Shape and Counter Resolution

The sample pulse-height distribution (Fig. 10) may also be used for more detailed study of the counter characteristics, since its shape in the region of the most probable pulse height does not sensibly change over the energy range of the μ-mesons selected for the sample. The observed points show the sharp rise and slow fall-off characteristic of a Landau distribution but the width at half-maximum is somewhat greater than the theoretical value of 17.8%.

It was assumed that the resolution function of the counter was Gaussian in form with a width proportional to the signal amplitude. By combining such a function with the theoretical Landau–Symon distribution for the energy lost in the counter, it was possible, by trial, to fit the observed points and thus obtain a measure of the counter resolution. The solid line in Fig. 10 is such a calculated curve drawn on the assumption that the total instrumental and geometric resolution function is 11% in width. Since the geometric spread was 2% in this experiment, the instrumental resolution was only slightly less than 11%. However, it should be noted that the width of the observed curve (23%) is somewhat greater than the measured value of 20.5% for the central area of

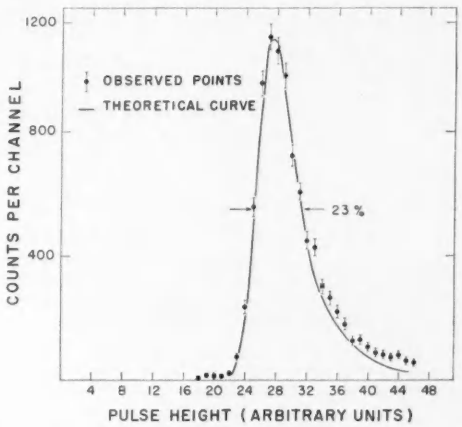

FIG. 10. "Sample" pulse-height distribution for cosmic-ray μ-mesons >0.27 Bev. passing normally through the central area of the counter.

the counter as recorded in Table I, and this broadening is attributed to gain changes of the system over the 1 month period during which the sample distribution was observed. On the basis of the 20.5% width observed in a short-term measurement (Table I), the same method of curve fitting as used in Fig. 10 gives a width of the counter resolution function of 8%. This may be compared with the cruder estimate of 9% given in Table I.

It will be noted that in the high-energy tail there is a definite departure of the observed from the theoretical curve which amounts to a few per cent of the total area. Some extra intensity in this region of the curve is to be expected with a counter of finite thickness from the high-energy knock-on electrons which lose only a portion of their energy before escaping from the counter volume. It may be shown by means of the appropriate integral Landau–Symon curve (Rossi 1952, p. 34) that the amount of extra intensity appearing on the high-energy side of the peak due to this effect should be of the order of 1%. This is less than the observed value of ~5% but in view of the assumptions made in the choice of parameters for the calculation of the "predicted" curve, and the arbitrary procedure of fitting the curve to the observed points by means of the width at half-maximum, it is not considered that this discrepancy indicates any inadequacy of the theory.

The presence of high-energy knock-on electrons is demonstrated experimentally in Fig. 11, which shows the sample distribution observed under conditions of low amplifier gain so that larger pulses come within the range of the kicksorter. It will be seen that a second small peak occurs at twice the most probable pulse height and this is presumed to arise from high-energy electrons knocked on by μ-mesons in the atmosphere or in other material above the scintillation counter and which traverse the counter together with the μ-meson.

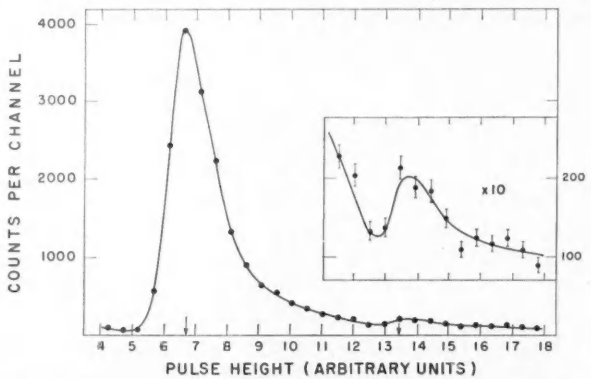

FIG. 11. Pulse-height distribution for cosmic-ray μ-mesons >0.27 Bev. observed at low amplifier gain. The geometry was the same as for Fig. 8. Arrows indicate *most probable* and 2×*most probable* pulse height.

4. COUNTER RESPONSE TO PROTONS

In the course of carrying out the cosmic-ray experiment for which this scin-

tillation counter was designed, data were obtained on its response to fast protons. The observed variation of most probable pulse height with proton energy over the range 300–800 Mev. is shown in Fig. 12. The cosmic-ray protons were selected and their energies determined by a telescope containing three Čerenkov counters using, from top to bottom, the following media: liquid nitrogen, water, Plexiglas. By correlating the pulse heights from these three counters with their Čerenkov intensity vs. energy curves and over-all resolution functions it was possible to separate the protons[4] into groups corresponding to different energy bands, and to estimate very roughly for each group an energy sensitivity curve giving as a function of its energy the probability that a proton be counted in that group. The solid circles in Fig. 12 are plotted at those energies, referred to the center of the scintillation counter, for which these probabilities are estimated to be maxima. The energy limits shown are the upper and lower deciles of the sensitivity curve and give a rough idea of the spread of energies involved in each point.

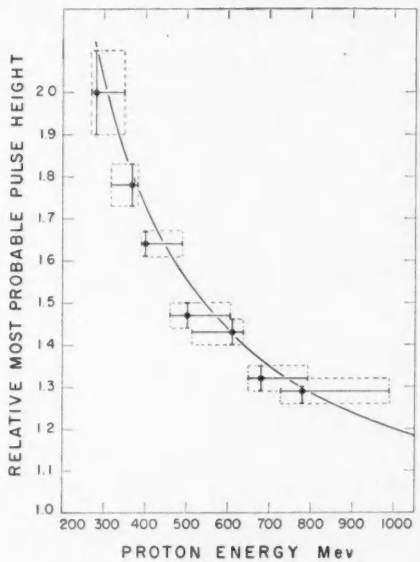

FIG. 12. Observed variation with proton energy of the *most probable* pulse height. The significance of the energy value at which each experimental point is plotted and of the energy limits attached to it is given in the text. Most probable pulse heights are measured relative to that observed for fast μ-mesons. The solid curve shows the theoretical most probable energy loss.

The experimental pulse heights are expressed in units of the observed most probable pulse height for fast μ-mesons. The μ-meson pulses were obtained by

[4]Mu-mesons were eliminated by having an appropriate amount of absorber in the telescope. In addition, precautions were taken to ensure, as far as possible, that single charged particles only were counted.

using the same telescope without the Čerenkov proton criteria, and were used to calibrate the scintillator.

In Fig. 12 is shown also the theoretical variation (see Appendix) of most probable energy loss with proton energy. In this case the normalization is to the theoretical most probable energy loss of μ-mesons of 2 Bev., roughly the effective energy of the μ-meson spectrum accepted by the telescope in the sense used in Section 3. It may be seen that the scintillation counter output gives a good measure of the theoretically predicted energy loss for protons of energies down to 300 Mev.; in particular, there is no evidence for saturation in the light output occurring for values of specific ionization less than twice minimum as has been suggested by some authors (e.g. Baskin and Winckler 1953; Bowen and Roser 1952). In view of the method of proton selection it would, however, not be wise to draw quantitative conclusions about the linearity between light output and energy loss from these data. Indeed, we have preferred in other work to regard the Čerenkov information and the scintillation counter response as mutually supporting data for the identification and energy measurement of protons selected from the cosmic-ray beam.

5. CONCLUSIONS

A large-area liquid scintillation counter has been described which is particularly suitable for use in a cosmic-ray telescope, and which has proved to be a valuable aid in the selection and identification of cosmic-ray protons.

Tests with fast μ-mesons normal to the plane of the counter show a peaked pulse-height distribution whose width at half-maximum is 20.5% for the central area of the counter deteriorating to 25–30% at the edges to give an over-all (calculated) value of 25%. Since the Landau–Symon theory of energy loss fluctuations predicts a theoretical spread of 17.8%, it is deduced that the actual counter resolution function has a width of 8% for the central area, or 18% over-all.

The counter has been operated, with moderately fast electronics, in a field of 12 mr./hr. of 2.6 Mev. γ-rays without distortion of the fast μ-meson peak.

An experiment in which μ-mesons of 0.30 and 2.2 Bev. were selected by delayed coincidence detection of their decay electrons indicates that the relative most probable energy losses in the counter for mesons of these two energies are in excellent agreement with theory including a correction for the density effect. This confirms the earlier conclusions of Baskin and Winckler (1953) and Bowen and Roser (1952).

Tests with cosmic-ray protons show that over the proton energy range 0.3 to 0.8 Bev. the counter's response is proportional to the theoretical energy loss.

ACKNOWLEDGMENTS

The authors wish to thank M. Bercovitch for taking the cosmic-ray proton data at Echo Lake, Colorado, J. F. Steljes for his assistance in the installation and operation of the I.B.M. equipment, F. S. Goulding for some electronic design work, and A. S. C. Hyde, Mrs. P. I. K. Lennox, and J. M. Kennedy for technical and computing assistance during the course of the experiments.

APPENDIX. THE THEORETICAL ENERGY LOSS IN TRIETHYLBENZENE

The theoretical estimate of the energy loss by a charged particle traversing the scintillation counter is based ultimately on the mean energy loss given by the Bethe–Bloch formula, but two important extensions must be taken into account for the interpretation of the measurements described in this paper. The first of these is concerned with the fluctuations in energy loss, the theory for which was first developed rigorously by Landau (1944) and later given in a more general form by Symon (1948). The fluctuation theory enables one to calculate the spectrum of energy losses for a particle of given incident energy, and, in particular, to relate the *most probable* to the *mean* energy loss.

The second extension to the theory is the correction for the "density effect", first formulated by Fermi (1940) and later refined by Wick (1943), Halpern and Hall (1948), and Sternheimer (1952, 1953, 1956). The effect of the density correction is to limit the increases in both mean and most probable energy losses at energies above those corresponding to "minimum ionization", so that both approach constant values at very high particle velocities.

For μ-mesons and protons we have used the basic energy loss formula in the form quoted by Sternheimer in his later papers (1953, 1956). This gives the mean energy loss (Mev.) by a particle of kinetic energy E (Mev.) in an absorber of thickness t (g. cm.$^{-2}$) and density ρ,

$$(1) \qquad \overline{\Delta E} = -\frac{t}{\rho}\frac{dE}{dx} = \frac{At}{\beta^2}\left[B+0.693+2\ln\frac{p}{\mu c}+\ln T-2\beta^2\right],$$

where $v = \beta c$, p, μ are the velocity, momentum, and mass respectively of the particle, T (Mev.) is the maximum energy transferable in a single collision, and A, B are constants describing the medium. Note that $p/\mu c = \beta\gamma$, where $\gamma = 1/(1-\beta^2)^{\frac{1}{2}}$. T, A, and B are given by

$$T = \frac{U^2-\mu^2c^4}{\mu c^2(\mu/2m+m/2\mu+U/\mu c^2)} = \frac{1.022(\beta\gamma)^2}{1+2\gamma m/\mu+(m/\mu)^2},$$

$$A = 2\pi n r_0^2 mc^2/\rho = 0.1536\,\Sigma Z/\Sigma A \text{ Mev. g.}^{-1}\text{ cm.}^2,$$

$$B = \ln(mc^2/I^2),$$

where U is the total energy of the incident particle in Mev.,
m, r_0 are the mass and classical radius of the electron,
n is the number of electrons per cm.^{3} of the medium,
I is the effective ionization potential of the medium in Mev.,
and mc^2 is in Mev.

The most probable energy loss is given by Symon (1948) as

$$(2) \qquad (\Delta E)_p = \frac{At}{\beta^2}\left[B+0.693+2\ln\frac{p}{\mu c}+\ln\frac{At}{\beta^2}-\beta^2+j\right]$$

so that

$$(3) \qquad \overline{\Delta E}-(\Delta E)_p = \frac{At}{\beta^2}\left[\ln\frac{1}{G}-\beta^2-j\right],$$

where $G = At/T\beta^2$ and j is a function of G and β^2. The value of j may be

obtained from curves given by Symon, which are reproduced by Rossi (1952). (The symbol G is used by Rossi; Symon uses $1/C$.) In the "Landau limit" when $G \to 0$, $j = 0.37$. For rather small values of G near the Landau limit, where Symon's asymptotic formulae converge poorly, we may either read j off his adjusted curves, or we may use the approximate expression

$$j = 0.37 - 2.58\beta^2 G. \tag{4}$$

Equation (4) is obtained directly from equation (16.10) of Symon's thesis by adjusting it to fit the Landau limit when $G \to 0$, and dropping terms that are negligible ($<0.01j$) when $G < 0.1$. While there is a slight discrepancy between the values obtained by these two methods, in the application of interest here it may be ignored. Thus for a 0.3 Bev. μ-meson traversing the scintillator ($G = 0.022$ and $j = 0.32$) the discrepancy is ~ 0.014 in j, or less than 0.1% in $(\Delta E)_p$. At 2.2 Bev. the Landau term (0.37) only is significant.

Finally, the values of $\overline{\Delta E}$ and $(\Delta E)_p$ given by (1) and (2) respectively must be corrected for the density effect. This is done, following Sternheimer (1952, 1956), by subtracting in both cases the term $At\delta/\beta^2$. Thus the *corrected* energy losses are

$$\begin{aligned} \overline{\boldsymbol{\Delta E}} &= \overline{\Delta E} - At\delta/\beta^2, \\ (\boldsymbol{\Delta E})_{\boldsymbol{p}} &= (\Delta E)_p - At\delta/\beta^2. \end{aligned} \tag{5}$$

The quantity δ is calculated from

$$\delta = \sum_i f_i \ln \frac{l_i^2 + l^2}{l_i^2} - l^2(1-\beta^2), \tag{6}$$

where, for a non-conductor, $l_i = \rho_i \nu_i / \nu_p$, ρ_i are adjustment factors determined by measurements of effective ionization potentials, and l is the solution of

$$\frac{1}{\beta^2} - 1 = \sum_i \frac{f_i}{l_i^2 + l^2}. \tag{7}$$

The constants for triethylbenzene $[(C_2H_5)_3C_6H_3]$ are given in Table AI, which lists the ionization potentials ($h\nu_i$) and oscillator strengths (f_i) that were used (cf. Sternheimer 1952), together with the calculated values of plasma

TABLE AI

IONIZATION POTENTIALS, OSCILLATOR STRENGTHS, AND ENERGY LOSS CONSTANTS FOR TRIETHYLBENZENE

$h\nu_1$	23.0	Rydbergs
$h\nu_2$	4.1	"
$h\nu_3$	1.3	"
$h\nu_4$	1.0	"
$h\nu_p$	1.472	"
f_1	24/90	
f_2	24/90	
f_3	24/90	
f_4	18/90	
I	4.33	Rydbergs
A	0.0852	Mev. g.$^{-1}$ cm.^{2}
B	18.81	

energy ($h\nu_p$), effective ionization potential I (Sternheimer 1956), and the constants A and B. The ionization potential adjusting factors ρ_i used were: for carbon $\rho_1 = \rho_2 = \rho_3 = 1.155$,[5] and for hydrogen $\rho_4 = 1.40$. With these constants values of l were computed from (7) for chosen values of β with the Chalk River Datatron; from these, exact values of δ were calculated.

Sternheimer has also given a simple analytical expression for δ as a function of β, the constants in which may be chosen to give a good fit to the exact formula (6), (7). This expression is

$$\begin{aligned} \delta &= 4.606X+C+a(X_1-X)^m \qquad (X_0 < X < X_1), \\ \delta &= 4.606X+C \qquad\qquad\qquad\quad (X > X_1), \end{aligned} \tag{8}$$

where $X = \log_{10}(\beta\gamma)$, X_0 is the value of X below which δ vanishes,

$$C = -2\ln(I/h\nu_p)-1,$$

and a, X_1, and m are adjustable constants which are chosen to give a good fit. Since Sternheimer does not include triethylbenzene in his comprehensive table of constants, we have determined their values for this substance and present them in Table AII. With these constants equation (8) gives values of δ that lie within about ± 0.02 of the exact values, that is the errors in $(\Delta E)_p$ do not exceed $\pm 0.1\%$.

TABLE AII

VALUES OF THE "STERNHEIMER CONSTANTS" FOR TRIETHYLBENZENE

C	−3.16
a	0.44
m	2.80
X_1	2
X_0	0.15

The theoretical relations summarized above have been used for all energy loss calculations in this paper. Thus the $(\Delta E)_p$ curve for μ-mesons (Fig. 9) and the ratios of most probable energy losses given in the text (Section 3 (*c*)) were calculated using formulae (2), (4), (5), (6), and (7). For protons (Fig. 12) of energies up to 680 Mev. equation (2) was used (in this region $\delta = 0$) and the Symon "thin absorber" curves for j; above 680 Mev. the small density correction was subtracted. That the "thin absorber" curves are sufficiently accurate in this range was demonstrated by comparing with the "thick absorber" calculations at the lowest proton energy. Symon's curves were also used to obtain the theoretical distribution of energy losses (Sections 3 (*a*), (*d*)).

We have used mass values for the μ-meson, $\mu c^2 = 105.7$ Mev., and for the proton, $\mu c^2 = 938.2$ Mev., which, with $mc^2 = 0.511$ Mev., are consistent with $\mu/m = 206.9$ (μ-meson) and $\mu/m = 1836$ (proton). The thickness of the counter ($t = 3.31$ g. cm.$^{-2}$) was calculated assuming triethylbenzene (Alkazene-3) to have a density of 0.870 g. cm.$^{-3}$.

[5]There appears to be an error in Table I of Sternheimer's (1956) paper.

REFERENCES

BASKIN, R. and WINCKLER, J. R. 1953. Phys. Rev. **92**, 464.
BOWEN, T. and ROSER, F. X. 1952. Phys. Rev. **85**, 992.
COWAN, C. L., Jr., REINES, F., HARRISON, F. B., ANDERSON, E. C., and HAYES, F. N. 1953. Phys. Rev. **90**, 493.
FERMI, E. 1940. Phys. Rev. **57**, 485.
HALPERN, O. and HALL, H. 1948. Phys. Rev. **73**, 477.
LANDAU, L. 1944. J. Phys. U.S.S.R. **8**, 201.
PUPPI, G. 1956. *In* Progress in cosmic ray physics, Vol. 3, *edited by* J. G. Wilson (North-Holland Publishing Co., Amsterdam).
REYNOLDS, G. T. 1950. Nucleonics, **6**, 68 (May).
ROSSI, B. 1952. High energy particles (Prentice-Hall Inc., New York, N.Y.).
SHIPP, R. L. 1952. Revs. Sci. Instruments, **23**, 773.
STERNHEIMER, R. M. 1952. Phys. Rev. **88**, 851.
——— 1953. Phys. Rev. **91**, 256.
——— 1956. Phys. Rev. **103**, 511.
SYMON, K. R. 1948. Harvard University Thesis.
WICK, G. C. 1943. Nuovo cimento, **1**, 302.

MASS ASSIGNMENT OF THE 1.8 HOUR YTTERBIUM ACTIVITY[1]

R. H. Betts, Olive F. Dahlinger, and Donna M. Munro

ABSTRACT

The rate of growth of Lu^{177} into neutron-irradiated ytterbium has been measured by radioassay of lutetium fractions separated by ion-exchange techniques. Such measurements show the parent of Lu^{177} to be the 1.8 hour Yb; this latter nuclide is therefore Yb^{177}. Confirmatory values of 3.71 ± 0.04 hours and 6.75 ± 0.05 days have been obtained for the half-lives of Lu^{176m} and Lu^{177}.

INTRODUCTION

Several studies have been reported on the nuclear properties of the radionuclides produced by neutron capture in natural ytterbium (Mihelich, Ward, and Jacob 1956; Mize, Bunker, and Starner 1956; Cork *et al.* 1950; Sunyar and Mihelich 1951; Martin *et al.* 1951). Some of the properties of these nuclides are listed in Table I. A standard compilation (Hollander *et al.* 1953) identifies the 1.85 hour Yb activity as probably Yb^{177}, i.e., a class B nuclide in the terminology of these authors. However, a recent study (Cork *et al.* 1956) questions this particular mass assignment, in that none of the characteristic radiations of the 6.8 day Lu^{177} could be observed growing into a freshly irradiated sample of Yb. Furthermore, no 6.8 day component could be observed in the radioactive decay of such a sample. This latter criterion is not, however, a sensitive indicator of the presence or absence of Lu^{177}; calculations using currently accepted cross sections (Hughes and Harvey 1955) indicate that even for short irradiations, where interference from Yb^{175} and Yb^{169} is minimized, the β-activity of Lu^{177} would be only about 3% of that arising from Yb^{175}.

TABLE I

Some properties of the Yb nuclides

Mass No.	Half-life	Daughter	σ_c (barns)
168	Stable	—	$11{,}000\pm3000$
169	30.4 d.	Tm^{169} stable	—
170	Stable	—	—
171	"	—	—
172	"	—	—
173	"	—	—
174	"	—	60 ± 4.0
175	4.2 d.	Lu^{175} stable	—
176	Stable	—	5.5 ± 1.0
177?	1.85 hr.	Lu^{177} 6.8 d.	—

In work to be described elsewhere (Betts, Dahlinger, and Munro 1957) we have used neutron-activated ytterbium as a radio-tracer for this element,

[1]Manuscript received September 11, 1957.
Contribution from Chemistry and Metallurgy Division, Atomic Energy of Canada Limited, Chalk River, Ontario.
Issued as A.E.C.L. No. 526.

and we were particularly interested, therefore, in the rate and extent of growth of radioactive lutetium into the sample. This paper describes investigations to establish the genetic relationship of Lu^{177} to the ytterbium nuclides. The procedure used has been to separate lutetium from neutron-activated ytterbium at suitable time intervals after the end of the irradiation. The change in the radioactivity of the Lu fraction, relative to that of the Yb fraction (both corrected to some common time to allow for decay), has been used as a measure of the rate of growth of Lu. A second criterion used to establish the parent–daughter relationship depends on the fortuitous presence of about 0.2% impurity of Lu in the Yb target. Neutron activation of Lu leads to:

$$Lu^{175}(97.4\%)n, \gamma \longrightarrow Lu^{176m} \xrightarrow[3.7\text{ hr.}]{\beta^-} Hf^{176} \text{ stable},$$

$$Lu^{176}(2.6\%)n, \gamma \longrightarrow Lu^{177} \xrightarrow[6.8\text{ d.}]{\beta^-} Hf^{177} \text{ stable}.$$

The ratio of Lu^{177} to Lu^{176m} was measured by counting techniques for Lu fractions extracted from irradiated Yb. The growth of Lu^{177} relative to Lu^{176m} could then be used as a second indicator of the half-life of the parent of Lu^{177}. This method has the advantage that it is independent of the chemical yield of lutetium associated with a given amount of ytterbium.

EXPERIMENTAL

Samples of ytterbium were irradiated in the pneumatic carrier facility of the NRX reactor at a flux of $\sim 7 \times 10^{13}$ neutrons $cm.^{-2}$ $sec.^{-1}$. In some cases, Yb_2O_3 was irradiated, and was afterwards dissolved in dilute hydrochloric acid. In other experiments, an aqueous solution of $Yb(NO_3)_3$ was irradiated in a sealed silica tube. In either case, aliquots of the solution were taken at suitable intervals of time for separation of Lu from Yb by ion-exchange techniques.

The resin used for the separation was Dowex 50w, 12% cross linked; it was graded to a fine particle size by elutriation with water. The eluting agent employed was 0.13 *M* α-hydroxyisobutyric acid, adjusted to pH 4.2–4.3 with ammonia (Choppin and Silva 1956). The preparation of the resin and the loading and operation of the 5 cm. by 1.5 mm. I.D. column were carried out essentially as described by Thompson *et al.* (1954). About 0.01 mg. of ytterbium was used for each separation.

Fig. 1 is an illustration of the separation obtained of Lu from Yb. The separation factors for these two elements, given by the ratio:

$$\frac{\text{volume to peak (Yb)} - 1 \text{ free column volume}}{\text{volume to peak (Lu)} - 1 \text{ free column volume}},$$

was 1.35 ± 0.05, as measured in nine separate experiments. The value quoted by Choppin and Silva (1956) for this system is 1.36.

Consecutive samples of one drop each (0.02 ml. per drop) were collected on Al counting trays across both peaks. The samples were dried, and the rate

of decay of β^--activity was measured on samples selected from near the two peaks of the elution. After the short-lived components had decayed to a negligible level (Lu^{176m} in the first peak, and 1.85 hour Yb in the second) the counting rates of all samples in each fraction were determined. These

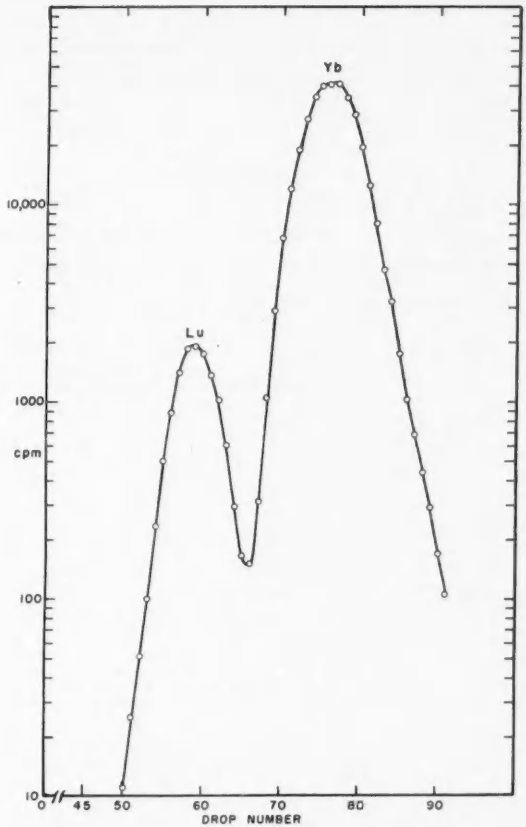

FIG. 1. Separation of Lu from Yb by ion exchange.

activities (Lu^{177} in the first peak and $Yb^{175+169}$ in the second) were then corrected to the end of the irradiation using decay curves which had been established experimentally. The area under each peak illustrated in Fig. 1 was then calculated in terms of total counts per minute. Allowance was made for the relative contributions of Lu and Yb to the valley between the peaks. Even gross errors in this latter rather subjective operation do not appreciably affect the precision of the results, since 90% of the activity in each fraction is accounted for in a few drops across the peak. It is felt that the ratios of the activity of Lu to Yb obtained in this way are precise to at least $\pm 5\%$.

The β-activity in the samples was measured with a methane-flow proportional β-counter. The counter was equipped with a 0.9 mg./cm.^{2} aluminum-coated Mylar window. The usual corrections for dead-time losses, background counts, etc., were made. A sufficient number of counts was recorded to reduce the probable statistical error in the cumulative counting rates for each peak to less than 0.5%.

Measurements of γ-rays referred to below were made with a 1.5×1.0 inch NaI Tl-activated crystal optically coupled to an RCA 5819 photomultiplier in conjunction with a 24 channel pulse-height analyzer (Moody *et al.* 1951).

RESULTS AND DISCUSSION

1. Identification of Radionuclides Formed

Fig. 2 gives a typical decay curve of a sample from the major (second) peak in the elution. Resolution of three components is also shown, indicating

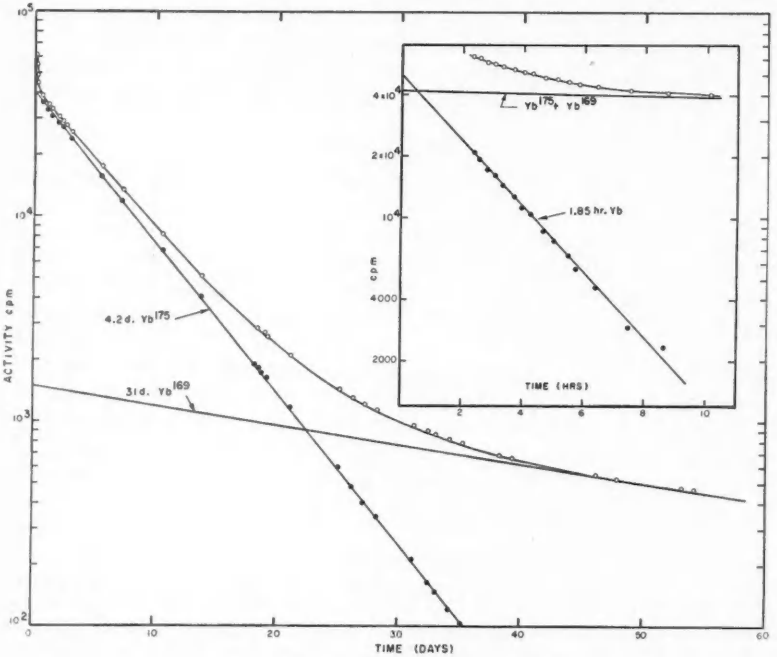

FIG. 2. Decay of ytterbium fraction.

a 1.85 hour activity, a 4.2 day activity, and a longer-lived component, presumably 30 day Yb^{169}. At the end of a 1 hour irradiation their relative activities were (in order of increasing half-life): 1.2:1.00:0.04. Measurements of the γ-ray spectra made after the 1.85 hour and 4.2 day activities had decayed

out showed peaks at 64, 110, 190, 260, and 310 kev., in agreement with a recent report for γ-rays of Yb^{169} (Hatch *et al.* 1956). Other measurements made when the 4.2 day activity was predominant gave γ-rays at 115, 280, and 400 kev., which correspond to those reported for Yb^{175} (Hatch *et al.* 1956). There is no doubt therefore, on the basis of the half-lives and γ-ray measurements, that this fraction is correctly identified as Yb.

Fig 3 shows the radioactive decay of a typical sample from the first peak of the elution. A 3.71 ± 0.04 hour activity (average of results on measurements

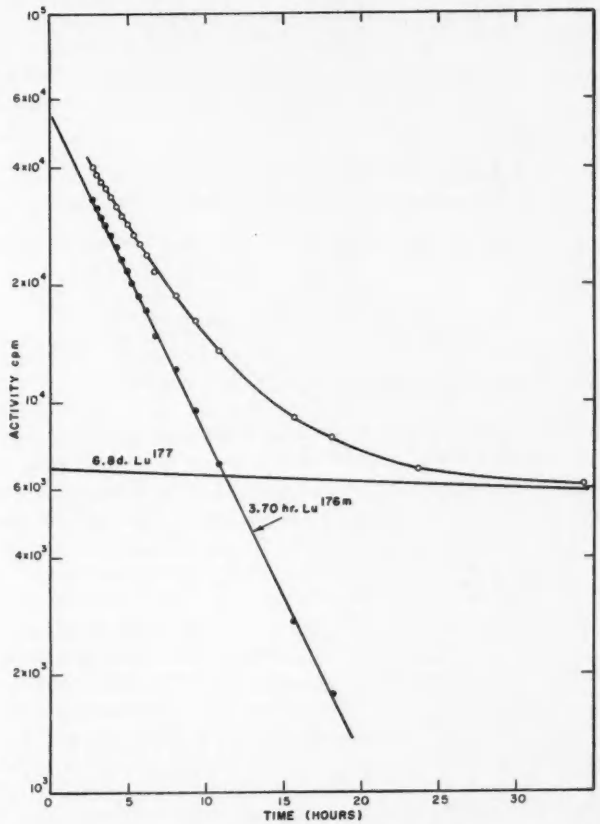

FIG. 3. Decay of lutetium fraction.

of 20 separate samples) is present, and is predominant for about 12 hours after the end of the irradiation. The longer-lived component decays with a half-life of 6.75 ± 0.05 days. This latter result is the average for two samples, each followed for 20 days (not shown in Fig. 3). Gamma rays of 72, 110, 210, 250, and 320 kev. were observed for the 6.75 day component, in agree-

ment with those reported for Lu^{177} (Marmier and Boehm 1955). These results, together with the relative positions of the two peaks in the elution curve, confirm that this fraction is composed of Lu^{177} and Lu^{176m}.

2. Derivation of Growth Equation

Consider the sequence:

$$\begin{array}{ccccc} A^1(n,\gamma) & \longrightarrow & A & & \\ & & \downarrow{\scriptstyle \lambda_A} & & \\ B^1(n,\gamma) & \longrightarrow & B & \xrightarrow[\lambda_B]{} & C \text{ stable} \end{array}$$

where λ_A and λ_B are the disintegration constants for species A and species B, respectively, and where A^1 and B^1 represent stable target nuclides. At the end of the irradiation ($t = 0$), let

A_0 = number of atoms of species A,

B_0 = number of atoms of species B.

Then at time t after the end of the irradiation, the number of atoms of B will be given by:

$$B_t = A_0 \frac{\lambda_A}{\lambda_B - \lambda_A}(e^{-\lambda_A t} - e^{-\lambda_B t}) + B_0 e^{-\lambda_B t}. \tag{1}$$

If equation (1) is multiplied through by $e^{\lambda_B t}$, it takes the form

$$B_t e^{\lambda_B t} = A_0 \frac{\lambda_A}{\lambda_B - \lambda_A}[e^{(\lambda_B - \lambda_A)t} - 1] + B_0. \tag{2}$$

Equation (2) may be used to test the genetic relation between the 1.85 hour Yb and 6.8 day Lu^{177}. Substitution of the values $\lambda_A = 0.3746$ hr.$^{-1}$ (1.85 hour Yb) and $\lambda_B = 0.004246$ hr.$^{-1}$ (Lu^{177}) into equation (2) leads to

$$B_t e^{\lambda_B t} = 1.011\ A_0(1 - e^{-0.3703t}) + B_0. \tag{3}$$

Two independently determined quantities have been used as a *relative* measure of $B_t e^{\lambda_B t}$ as a function of time. These are: (1) the observed activity of Lu^{177} relative to that of Yb^{175} as determined from the various elution curves (cf. Fig. 1), and (2) the activity of Lu^{177} relative to that of Lu^{176m}, both at $T = 0$, as determined by extrapolation of the radioactive decay curves of selected samples of the Lu fraction.

3. Growth of Lu^{177} Relative to Yb^{175}

The results obtained from the irradiation of two samples are given in Table II. Sample A was irradiated for 62.7 hours, and then Yb–Lu separations made at the times indicated. For this sample, the Lu^{177}/Yb^{175} activity ratio is essentially constant at 0.0239 ± 0.0003. Now if the 1.85 hour Yb is indeed the parent of Lu^{177}, then for this sample, 99.5% of the parent nuclide will have decayed to daughter nuclide (Lu^{177}) by the time of the first separation. The constant value of the activity ratio is thus not in disagreement with this

parent–daughter relation, and moreover provides positive evidence that 6.8 day Lu does not grow in from a long-lived precursor, e.g., 4.2 day Yb.

TABLE II

GROWTH OF Lu^{177} IN IRRADIATED Yb

Time of separation (hours)*	Lu^{177}/Yb^{175} activity ratio	Lu^{177}/Lu^{176m} activity ratio
Sample A. Irradiation time = 62.7 hours		
7.0	0.0243	—
26.0	0.0238	—
55.0	0.0241	—
79.0	0.0240	—
84.0	0.0231	—
Av. = $\overline{0.0239}\pm0.0003$		
Sample B. Irradiation time = 60.0 minutes		
0.93	0.0151	0.104
2.17	0.0181	0.124
2.97	0.0197	0.136
4.72	0.0211	0.149
6.15	0.0224	0.156
77.6	0.0231	—
124.9	0.0238	—
168.0	0.0236	—
290.0	0.0230	—
Av. (last four) = $\overline{0.0234}\pm0.0003$		

*Measured from end of the irradiation.

Sample B in Table II was irradiated for 60.0 minutes, and separations made at the times indicated. Here a significant growth of Lu^{177} is observed in the period 0.9 to 6 hours, and no further growth in the period 77 to 290 hours. These results may be used to test the proposed growth relation (equation (3)) by plotting for each sample the Lu^{177}/Yb^{175} activity ratio (which is proportional to $B_t e^{\lambda_B t}$) vs. $(1-e^{-0.3703t})$; this plot is shown in the upper line of Fig. 4. A good straight line is obtained, providing a clear indication that equation (3) describes the growth rate of Lu^{177} in the sample after irradiation, and thereby confirming that the 1.85 hour Yb is the parent of Lu^{177}.

The average final value of Lu^{177}/Yb^{175} for sample B may be related to that for sample A by correcting for the difference in the irradiation time, i.e. for differences in the extent of saturation of Yb^{175} and Lu^{177}. The result for sample A, adjusted to a 60.0 minute irradiation, gives 0.0226, which agrees within experimental error with the value of 0.0234 for sample B.

The consistency of the experimental data may be checked in another way. The growth of Lu^{177} from zero time, as shown in Fig. 4, is 0.0119 ± 0.0004 referred to Yb^{175} activity. The associated Yb^{177} *activity* at zero time relative to Yb^{175} should therefore be

$$0.0119\,\lambda_{Yb^{177}}/\lambda_{Lu^{177}} = 0.0119(6.8\times24)/1.85 = 1.05\pm0.04.$$

The observed value for this ratio obtained from analysis of the decay of Yb fractions is 1.2 ± 0.06, in reasonably good agreement. This latter comparison,

to be strictly valid, requires that the counter detect the β-particles of Lu^{177} (E_{max} = 0.50 Mev.) and Yb^{177} (E_{max} = 1.40 Mev.) with equal efficiency. In fact the counter probably detects Yb^{177} with a slightly higher efficiency, relative to Lu^{177}; this discrepancy between 1.05 (calc.) and 1.2 (obs.) is in the direction expected for this effect. In any event, this comparison shows that the *initial* activity of Yb^{177} is compatible with the total growth of Lu^{177} activity.

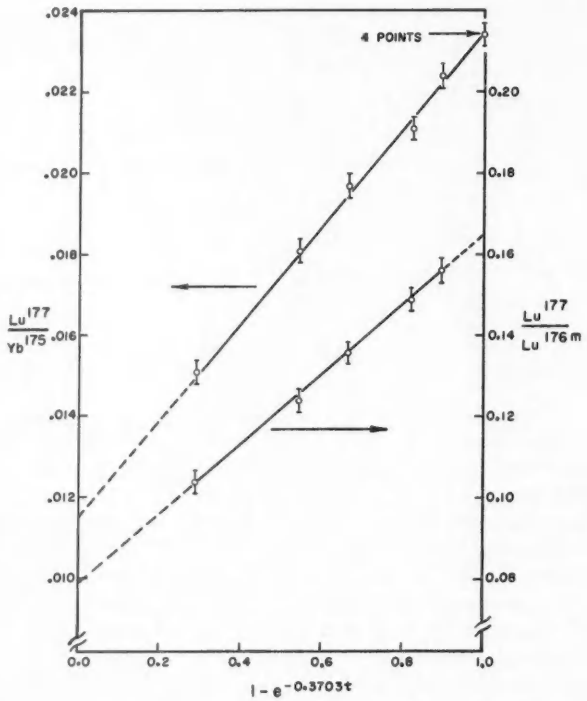

FIG. 4. Tests of equation for growth of Lu^{177}.

4. Growth of Lu^{177} Relative to Lu^{176m}

The decay of samples from the first five lutetium fractions of irradiation B was followed to measure the Lu^{177}/Lu^{176m} activity ratio. The results are given in the last column of Table II. A plot of this ratio vs. $(1-e^{-0.3703t})$ is shown in the lower line in Fig. 4. A good straight line is obtained as before, providing additional verification that Lu^{177} grows in from a parent with a 1.85 hour half-life. The total increase in Lu^{177}, obtained by extrapolation of the lower line in Fig. 4, is 107±4%; the corresponding value obtained from the Lu^{177}/Yb^{175} measurements is 103±5%, in good agreement with this result.

A useful check may be made on the reliability of the analyses of the Lu

decay curves. Calculations based on the upper line in Fig. 4 indicate that $20\pm5\%$ of the Lu^{177} present at $T = 0$ comes from decay of Yb^{177} during the irradiation in the reactor; the rest is therefore produced by neutron capture in Lu^{176}. The initial Lu^{177}/Lu^{176m} ratio in the Lu fraction extracted from irradiated Yb should therefore be $25\pm7\%$ higher than that obtained by irradiating pure Lu. As a check on this point several 1 hour irradiations of pure Lu were made; the average Lu^{177}/Lu^{176m} activity ratio, extrapolated to the end of the irradiation, was 0.059 ± 0.001 (average of four results). The corresponding value from Fig. 4 is 0.079 ± 0.002, which is higher by the ratio 1.34 ± 0.04, in satisfactory agreement with the value of 1.25 ± 0.07 predicted.

CONCLUSION

Both methods of comparison lead to the same result. i.e. Lu^{177} grows in to irradiated ytterbium at a rate consistent with the assumption that its parent is the 1.85 hour Yb. Moreover, the total growth of Lu^{177} activity is equivalent to the initial activity of 1.85 hour Yb. If the mass number of 6.8 day Lu is taken as established (and there appears no reason to doubt this), it is concluded that the 1.85 hour Yb nuclide is Yb^{177}.

REFERENCES

BETTS, R. H., DAHLINGER, O. F., and MUNRO, D. M. 1957. UNESCO Conference on Radioisotopes, Paris, Paper 212.

CHOPPIN, G. R. and SILVA, R. J. 1956. J. Inorg. and Nuclear Chem. **3**, 153.

CORK, J. M., BRICE, M. K., MARTIN, D. W., SCHMID, L. C., and HELMER, R. G. 1956. Phys. Rev. **101**, 1042.

CORK, J. M., KELLER, H. B., RUTLEDGE, W. C., and STODDARD, A. E. 1950. Phys. Rev. **78**, 95.

HATCH, E. N., BOEHM, F., MARMIER, P., and DUMOND, J. W. M. 1956. Phys. Rev. **104**, 745.

HOLLANDER, J. M., PERLMAN, I., and SEABORG, G. T. 1953. Revs. Modern Phys. **25**, 469.

HUGHES, D. J. and HARVEY, J. A. 1955. Report BNL-325, Brookhaven National Laboratory.

MARMIER, P. and BOEHM, F. 1955. Phys. Rev. **97**, 103.

MARTIN, D. S. Jr., JENSEN, E. N., HUGHES, F. J., and NICHOLS, R. T. 1951. Phys. Rev. **82**, 579.

MIHELICH, J. W., WARD, T. J., and JACOB, K. P. 1956. Phys. Rev. **103**, 1285.

MIZE, J.-P., BUNKER, M. E., and STARNER, J. W. 1956. Phys. Rev. **103**, 182.

MOODY, N. F., HOWELL, W. D., BATTELL, W. J., and TAPLIN, R. H. 1951. Rev. Sci. Instr. **22**, 551.

SUNYAR, A. W. and MIHELICH, J. W. 1951. Phys. Rev. **81**, 300.

THOMPSON, S. G., HARVEY, B. G., CHOPPIN, G. R., and SEABORG, G. T. 1954. J. Am. Chem. Soc. **76**, 6229.

THE EFFECT OF HEAT TREATMENT ON LOW TEMPERATURE INTERNAL FRICTION MAXIMA[1]

T. S. Hutchison and G. J. Hutton

ABSTRACT

Measurements of the attenuation of sound at a frequency of 5 megacycles have been made over the temperature range 100° to 200° K. on polycrystalline high purity aluminum subjected to various thermal and mechanical treatments. With samples annealed at 520° C. a maximum in the attenuation versus temperature relation had been observed at 155° K. This maximum was greatly increased by small amounts of plastic deformation of the order of 1.0 to 1.5%.

Aluminum initially annealed for extended periods at temperatures much closer to the melting point shows, however, either no increase in the attenuation maximum at 155° K. or, in extreme cases, no maximum in this region at all, after plastic deformation of the same order as before. It is believed that this indicates a dependence of the deformation-induced maximum on the distribution and possibly on the number of dislocations in the metal prior to deformation and on the arrangement of the dislocations after deformation.

INTRODUCTION

Hutchison and Filmer (1956) describe low temperature internal friction peaks found at 155° K. with 5 Mc. sound waves on 99.99$_4$% pure aluminum of grain size 3–4 mm. The height of these peaks was markedly increased by small amounts of plastic deformation of the order of 1.0–1.5%, and decreased by subsequent low temperature annealing. The activation energy for the peak was similar to that calculated for the low temperature internal friction peak in aluminum by Mason (1955), using the experimental results of Bömmel (1954) and Bordoni (1954). Mason's dislocation relaxation mechanism proposed locking of the dislocations at irregular intervals with a maximum in the distribution at loop lengths of the order of 10^{-4} cm. It was assumed that the locking was by Cottrell impurity atmospheres.

Later experiments (Niblett and Wilks 1956; Hutchison and Hutton 1956) indicate that, regardless of the relaxation mechanism involved, the process is not related to pinning of dislocations by impurities. This has been discussed by Seeger (1956). Since the temperature at which the peaks occur was not affected by the amount of prestrain, Seeger concluded that the density of the dislocation "forest" and distance between dislocation nodes was not of importance. The present investigation indicates that this conclusion is not completely justified.

EXPERIMENTAL METHOD AND RESULTS

The material used for these experiments was 99.99$_4$% aluminum, supplied by Aluminium Laboratories Ltd., containing 0.004% Fe, 0.002% Cu, <0.001% Mg, <0.001% Si, <0.001% Zn. The internal friction was measured using 5 Mc. sound waves over the range 200° to 100° K., with an average rate of

[1]Manuscript received October 4, 1957.
Contribution from the Department of Physics, Royal Military College of Canada, Kingston, Ont. This work was performed under Defence Research Board Grant No. 7510-14, Project D44-75-10-14.

cooling of about 3° K. per minute. The nature of the dependence of acoustic losses on temperature using this method of measurement is discussed in the previous paper by Hutchison and Filmer (1956).

The preparation of each specimen will be reported in detail since the value of the internal friction has been found to be very sensitive to mechanical and heat treatment. Indeed it is felt that the usefulness of some of the earlier work has been reduced by the omission of the detail of specimen preparation.

The first specimen was prepared as follows.

Specimen I

(1) Annealed at 625° C. for 9 hours.
(2) Cold worked 0.53%.
(3) Annealed 105 hours at 625° C. Cooled in furnace at 1° C. per minute to 240° C. and then at 3° C. per minute to room temperature.
Final grain size 1.5–2.0 cm.

Experiment I

A series of internal friction measurements over the temperature range 250° to 100° K. was then taken as follows.

A. Specimen as annealed.
B. Specimen cold worked 0.63%, cooled from 295° K. to 250° K. during the next minute, and measurements of internal friction vs. temperature then started.
C. Specimen allowed to warm to room temperature, held at room temperature for 16 hours, and internal friction vs. temperature measured as before.

The reason for this sequence of operations is discussed in a previous paper by the authors (Hutchison and Hutton 1956). The results of this series of measurements are shown in Fig. 1.

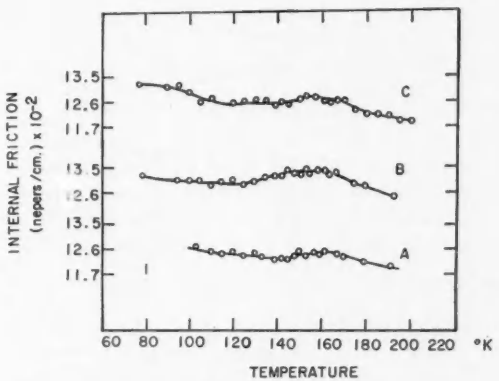

FIG. 1. Aluminum annealed 105 hours at 625° C.
A. As annealed.
B. Cold worked 0.63%.
C. After 16 hours at room temperature.

It is apparent that the increase in size of the internal friction peak on cold working is very small (Table I) and indeed in case C where the specimen was allowed to stand at room temperature for several hours after deformation the height of the internal friction peak found in the specimen after cold work is exactly the same as in the original "as annealed" specimen. It is noted that the background internal friction increased on cold working and decreased slightly on room temperature annealing. This will be discussed later with reference to Table I. The next series of experiments was designed to investigate the ultimate effect of such heat treatment.

Specimen II

(1) Annealed 20 hours at 656–659° C.

(2) Annealed 150 hours at 625–630° C. Furnace cooled to room temperature at an average rate of about 1° C./minute.
Final grain size ~2.5 cm.

Experiment II

A series of internal friction measurements was taken as in Experiment I.

A. Specimen as annealed.

B. Specimen cold worked 1.1%; cooling commenced after one minute; temperature reduced from 300° K. to 235° K. in 4 minutes and measurements of internal friction commenced immediately.

C. Specimen allowed to warm to room temperature, held at room temperature for 40 hours, and internal friction measured as before.

The results of this series of measurements are shown in Fig. 2.

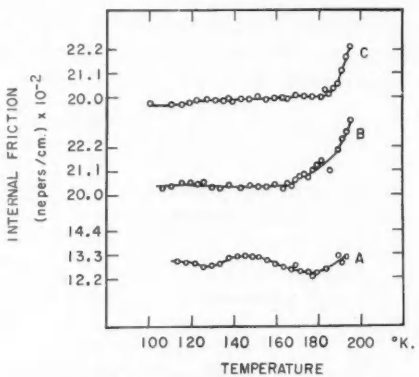

FIG. 2. Aluminum annealed 20 hours at 656–659° C. and 150 hours at 625–630° C.
A. As annealed.
B. Cold worked 1.08%.
C. After 40 hours at room temperature.

In the temperature range under investigation no internal friction peak is apparent in the case of the slightly cold worked specimen.

In order to demonstrate that small differences in specimen purity or homogeneity were not the cause of the difference between the observed phenomena

and the results of previous authors, a similar series of measurements was carried out on a specimen cut from the same block of aluminum as I and II, but with heat treatment similar to that used by Hutchison and Filmer (1956).

Specimen III

(1) Original ingot annealed 2 hours at 500° C., compressed 30%, annealed 12.5 hours at 500° C. The two successive recrystallizations removed most, if not all, of the original rolling texture and gave a fairly uniform grain size.

(2) Specimen removed from furnace and cooled in air to room temperature. Final grain size 0.5–2.0 mm.

Experiment III

A series of internal friction measurements was taken as before.

A. Specimen as annealed.

B. Specimen cold worked 1.4% (0.4%, 0.6%, and 0.4% at 30 second intervals). Cooling and measurement of internal friction commenced after 3 minutes.

C. Specimen allowed to warm to room temperature, held at room temperature for 45 hours, and internal friction measured as before.

The results of this series of measurements are shown in Fig. 3.

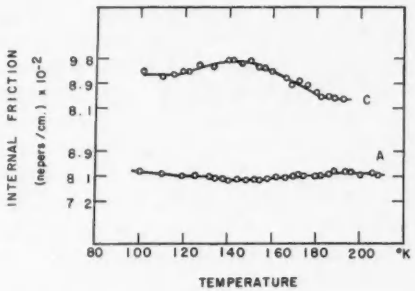

FIG. 3. Aluminum annealed 12.5 hours at 500° C.
A. As annealed.
C. Cold worked 1.4%, then held 45 hours at room temperature.

In case B the coupling fluid between the quartz crystal and the specimen lost cohesion with the face of the specimen at around 160° K. The results of runs A and C are clearly similar to the previous results found by Hutchison and Filmer (1956) using a specimen of similar thermal and mechanical history.

DISCUSSION

Changes in the background value of internal friction seem to depend on the dislocation density changes produced by cold working and annealing. Specimen II should initially contain the fewest dislocations. The proportional change of dislocation density on cold working should therefore be greatest in this case and give rise to a large increase in background internal friction. Also, Table I indicates that the type of low temperature internal friction

peak investigated here is quite reproducible, in that in all three cases of small grained specimens where the peak increased on cold working, similar amounts of cold work (1.4%, 1.4%, and 1.16% respectively) produced the same order of increase in the height of the peak above background (9.4, 9.0, and 11.2×10^{-3} nepers/cm.). It might also be noted that the smaller the grain size of the specimen the smaller the amount of cold work that would appear to be necessary to produce a certain increase in peak height.

TABLE I

Specimen	Treatment	Background (nepers/cm.)	Background change (%)	Peak height above background (nepers/cm.)
I (Grain size 15–20 mm.)	105 hr. at 625° C.			
	A. As annealed	0.123	—	4.6×10^{-3}
	B. Cold worked 0.63%	0.129	4.9	6.5×10^{-3}
	C. 16 hr. at room temperature	0.125	3.1	4.6×10^{-3}
II (Grain size ≃25 mm.)	20 hr. at 656–659° C. 150 hr. at 625–630° C.			
	A. As annealed	0.128	—	7.2×10^{-3}
	B. Cold worked 1.08%	0.205	61	No peak
	C. 40 hr. at room temperature	0.199	3.0	No peak
III (Grain size 0.5–2.0 mm.)	12.5 hr. at 500° C.			
	A. As annealed	0.081	—	No peak
	B. Cold worked 1.4%	0.097	20	—
	C. 45 hr. at room temperature	0.092	5.1	9.4×10^{-3}
IV (Grain size ≃4 mm.) (Ref. 1)*	10 hr. at 520° C.			
	A. As annealed	0.109	—	6.5×10^{-3}
	B. Cold worked 1.4%	0.115	5.1	15.5×10^{-3}
	C. 6 hr. at 180° C.	0.114	0.5	9.2×10^{-3}
V (Grain size ≃0.25 mm.) (Ref. 2)	1 hr. at 400° C.			
	A. As annealed	0.094	—	11.5×10^{-3}
	B. Cold worked 1.16%	0.113	21	22.7×10^{-3}
	C. 30 hr. at room temperature	0.113	0	22.7×10^{-3}

*Ref. 1, Hutchison and Filmer (1956). Ref. 2, Hutchison and Hutton (1956).

Since the individual grains are large in the case of specimen II, orientation effects might be responsible for some of the larger background increase. It was however ascertained that the quartz crystal covered portions of at least four grains of markedly different orientations (revealed by etching), and orientation is therefore not the complete explanation.

Several investigators have proposed that the internal friction maximum found using high frequency sound in the temperature range investigated is due to a relaxation process involving dislocation loops. The results of this series of experiments tend to confirm that if this is so then the loop lengths involved are produced by locking of dislocations by other dislocations or arrays. If the dislocations produced by cold work are on intersecting slip planes, the locking may well be predominantly by the network so formed. In the case of recrystallized specimens, annealed for extended periods at temperatures near their melting points, so that the grain size is very large

and the dislocation density relatively low, a small amount of cold work would be expected to produce little (or effectively no) cross slip and therefore little network pinning. We would then expect little, if any, increase in the internal friction maximum with small amounts of cold work.

The experimental results confirm this. Specimen I had received a small amount of cold work prior to the final high temperature anneal and therefore probably contained some residual dislocation arrays arising from polygonization. It had a slightly smaller grain size than specimen II and thus a slightly greater probability of cross slip. Specimen I showed a very slight increase in the internal friction peak on cold working while specimen II showed none at all.

Sack (1957) and Caswell (1957) have observed in single crystals of copper that small amounts of cold working produced no increase in the peak in crystals rolled in one direction only, while in crystals deformed along two perpendicular axes, slightly greater amounts of cold work did produce an increase in the internal friction peak.

These observations confirm our conclusion that no peak increases result from single slip and suggest that cross slip is necessary.

Although these results do not entirely contradict the alternative theory proposed by Seeger to explain this internal friction maximum, they do indicate that the mechanism is not solely related to intrinsic properties of dislocations as he suggests. The only difference between specimens I and II on the one hand, and specimen III and those investigated by Hutchison and Filmer (1956) on the other, is the density and arrangement of dislocations.

Seeger further suggested that kinks on these dislocations lying only in close packed directions contribute to the internal friction peaks. Slight cold working of specimen II would increase in the greatest proportion just those dislocations. However, in this specimen cold work produces no observed peak. This is a further difficulty in reconciling the observed results with the mechanism proposed by Seeger.

CONCLUSIONS

These experiments suggest that cross slip is necessary to produce an increase in the height of the low temperature internal friction peak in aluminum on cold working, and indeed that some sort of dislocation network is necessary to produce such a peak at all. The results also definitely confirm the previous conclusion of the authors (Hutchison and Hutton 1956) that locking of dislocations by impurity atmospheres plays no part in this particular attenuation mechanism.

REFERENCES

BÖMMEL, H. E. 1954. Phys. Rev. **96**, 220.
BORDONI, P. G. 1954. J. Acoust. Soc. Am. **26**, 495.
CASWELL, H. L. 1957. O. S. R. Report and Ph.D. Thesis, Cornell University, Ithaca, N.Y.
HUTCHISON, T. S. and FILMER, A. J. 1956. Can. J. Phys. **34**, 159.
HUTCHISON, T. S. and HUTTON, G. J. 1956. Can. J. Phys. **34**, 1498.
MASON, W. P. 1955. J. Acoust. Soc. Am. **27**, 643.
NIBLETT, D. H. and WILKS, J. 1956. Phil. Mag. **1**, 415.
SACK, H. S. 1957. Canadian Metal Physics Conference, Kingston, Ont.
SEEGER, A. 1956. Phil. Mag. **7**, 651.

PRESSURE-INDUCED INFRARED ABSORPTION OF HYDROGEN AND HYDROGEN – FOREIGN GAS MIXTURES IN THE RANGE 1500–5000 ATMOSPHERES[1]

W. F. J. HARE[2] AND H. L. WELSH

ABSTRACT

The pressure-induced infrared absorption of hydrogen was studied in pure hydrogen and in hydrogen–helium, hydrogen–argon, and hydrogen–nitrogen mixtures at pressures up to 5000 atm. at room temperature. The integrated absorption coefficient can be expressed in the form $\alpha_1\rho_a\rho_p+\alpha_2\rho_a\rho_p^2$ over the whole range of densities (ρ_a = density of H_2, ρ_p = density of the perturbing gas, $\rho_a \ll \rho_p$ in the mixture experiments). The coefficient α_2 is much smaller than predicted from the effect of finite molecular volumes; this is interpreted as a partial cancellation of the induced moments in ternary collisions. The splitting of the Q branch of the fundamental, which is due to the participation of the relative kinetic energies of the colliding molecules in the absorption process, increases linearly with the density because of ternary collisions; a more rapid increase observed at very high densities is not yet explained. The components of the overtone and double vibrational transition, like the Q_Q and S components of the fundamental, show no splitting or broadening with increasing density; these absorptions are believed to be due to quadrupole interactions while the Q_P and Q_R components of the fundamental are due to overlap interactions.

INTRODUCTION

The fundamental infrared absorption band of hydrogen, induced by intermolecular forces, has been studied in the pure gas and in hydrogen–helium, hydrogen–argon, and hydrogen–nitrogen mixtures for gas pressures up to 1500 atm. and temperatures in the range 80° to 376° K. (Chisholm, MacDonald, Crawford, and Welsh 1952; Chisholm and Welsh 1954). If the absorption coefficient, $\alpha(\nu)$, is defined by the equation $I = I_0\epsilon^{-\alpha l}$, where l is the path length, the integrated absorption coefficient obeys a relationship of the form

$$\int \alpha d\nu = \alpha_1\rho_a\rho_p+\alpha_2\rho_a\rho_p^2,$$

in which ρ_a and ρ_p are the densities of the absorbing and perturbing molecules, respectively, and $\rho_a \ll \rho_p$ under the conditions of the gas mixture experiments. Since α_1 is much greater than α_2, only the term $\alpha_1\rho_a\rho_p$ is important at lower densities, where for pure hydrogen ($\rho_a \equiv \rho_p$) the intensity varies as the square of the density and the enhancement of the absorption by foreign gases varies linearly with ρ_p; the intensity of the absorption is thus proportional to the number of binary collisions of a given type. At higher densities the term $\alpha_2\rho_a\rho_p^2$ causes a more rapid increase in the absorption; this effect was interpreted in terms of the finite volume of the molecules, which becomes at high densities an appreciable fraction of the space which they occupy, so that the number of collisions (and the pressure) increases rapidly. However, when the coefficient α_2 is used to calculate molecular diameters, the results are consistently less than kinetic theory values. It therefore appears that the finite

[1]Manuscript received August 21, 1957.
Contribution from the McLennan Laboratory, University of Toronto, Toronto, Ontario.
[2]Holder of a Scholarship from the National Research Council of Canada, 1953–1955. Present address: Bell Telephone Laboratories, Inc., Murray Hill, New Jersey, U.S.A.

volume effect does not give a complete explanation of the second order term $\alpha_2\rho_a\rho_p^2$.

The fundamental absorption band consists essentially of the Q component, corresponding to a purely vibrational transition of the absorbing molecule, and the $S(0)$ and $S(1)$ components, for which the vibrational transition is accompanied by the rotational transitions $J = 0 \rightarrow J = 2$ and $J = 1 \rightarrow J = 3$, respectively. An interesting feature of the absorption at higher densities is the splitting of the Q branch. The separation of the maxima of the lower and higher frequency components, Q_P and Q_R, was found to increase linearly with the density of the perturbing gas from a finite value at zero density, obtained by extrapolation. From the intensity distribution in the components and its temperature variation, it was concluded that the relative kinetic energies of the colliding pair and of the surrounding molecules take part in the absorption process.

As the separation of the Q_P and Q_R maxima increases with increasing pressure, it was observed that in some cases a third maximum, designated Q_Q, was uncovered at the band origin. This component and the rotation-vibrational lines, $S(0)$ and $S(1)$, have frequencies nearly the same as those calculated for the free molecule, and show no splitting with increasing densities. Their behavior is thus very different from the Q_P and Q_R components. The theoretical calculations of van Kranendonk and Bird (1951) show that the intensity of the Q branch arises mainly from interactions in the region of overlap forces, whereas the S lines arise mainly from quadrupole interactions; the experimental evidence appears to confirm this view.

Since the experiments at pressures up to 1500 atm. revealed properties of induced absorption not apparent in the lower pressure work, an extension of the study to still higher pressures was undertaken. The trend of the integrated absorption coefficient and the splitting of the Q branch at high densities were of especial interest. In addition, it was hoped to establish the existence of the Q_Q component unequivocally. With the equipment at hand it was possible to work up to nearly 5000 atm.; for convenience, the observations were confined to room temperature.

EXPERIMENTAL

For the production of high pressures a 1500 atm. gas compressor and a 5000 atm. oil press were available. The absorption cell was designed so that the gas, compressed initially in the cell to 1500 atm., could be further compressed in stages to 5000 atm. by the oil press connected to the cell by a mercury link. The small change in the volume of the gas in the pressure range 1500–5000 atm. simplified the execution of this arrangement.

The absorption cell (Fig. 1) was of the reflection type in which light entered through a fused quartz window, 18 mm. thick, and, after reflection from a mirror, left by the same window. The window seat and pressure seal have been previously described (Welsh, Pashler, and Dunn 1951). The absorption chamber at the center of a block of annealed alloy steel, $6\frac{1}{2}$ in. by $8\frac{1}{2}$ in. by $10\frac{3}{4}$ in., was connected directly to the gas compressor and through a mercury reservoir

to the oil press. A catchpot was provided to prevent mercury from flowing into the oil press in case of a sudden release of pressure. The stainless steel mirror was designed to float on the surface of the mercury column, thus furnishing a means of monitoring the position of the mercury level during the initial compression. A small screw projecting from the bottom of the mirror float

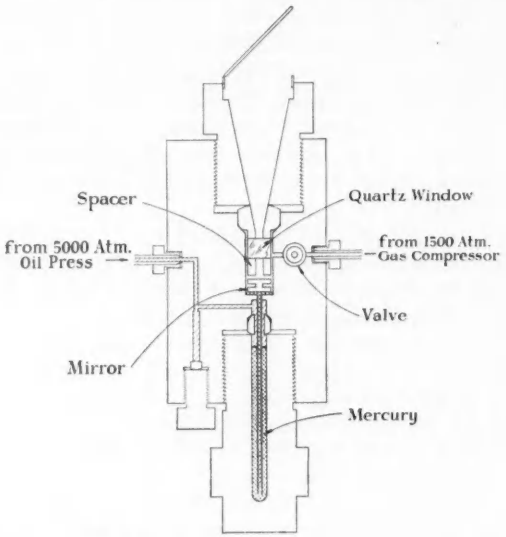

FIG. 1. Infrared absorption cell for gases at pressures up to 5000 atm.

caused the mirror to tilt when the mercury level was lowered below the bottom of the chamber. The length of the absorbing path, twice the distance between the window and the mirror, could be varied up to 4 cm. by suitable spacers cemented to the bottom of the window. Since the mirror had to be in contact with the spacer at the lowest pressure (~1500 atm.) at which measurements were to be made, and since the mercury could not rise above the mirror at the highest pressure, the design of the mirror and its float was rather critical.

The introduction of the gas into the compression chamber required considerable care since the position of the mercury column was extremely unstable at low pressures. Oil was pumped in until the mirror was horizontal, i.e., floating on the mercury; the gas pressure was then increased until the mercury was driven from the cell, as indicated by the tilting of the mirror. This process was repeated until the gas pressure in the cell was 1000–1500 atm. The position of the floating mirror was determined by means of a telescope placed at a safe distance from the absorption cell, the parallax between a copper cross-hair cemented across the lower end of the spacer and its image in the mirror being used as an indicator. After the initial compression the needle valve at the gas inlet was closed and the oil pressure raised by stages.

In experiments in which the enhancement of the hydrogen absorption by a foreign gas was investigated, a hydrogen – foreign gas mixture with partial densities in the ratio of $\backsim 1:20$ in Amagat units was prepared. To ensure homogeneity the mixing was carried out at a lower pressure with an auxiliary 600 atm. compressor connected to the 1500 atm. compressor. The volume of the auxiliary compressor could be maintained precisely at a fixed, though unknown, value of the order of 1 liter by adjusting the level of the mercury which made electrical contact with a vertical steel rod extending into the compression chamber. The pressure of the foreign gas in this compressor was determined with an accuracy of ± 0.03 atm. by means of a dead-weight tester. A small amount of hydrogen was then added from the 1500 atm. compressor and the pressure of the mixture measured. Adequate mixing of the gases was obtained by flushing the mixture back and forth between the two compressors and allowing it to stand for at least 12 hours.

To determine the mixture ratio, ρ_a/ρ_p, where ρ_a and ρ_p are the partial densities in Amagat units of the hydrogen and the foreign gas respectively, the following method was used. The volume was held constant in the preparation of the mixture, so that $\rho_a+\rho_p = \rho_m$, where ρ_m is the density of the mixture in Amagat units, and the pressures, P_p and P_m, were accurately measured. The equation

$$\rho_p/\rho_m = (P_p/P_m)(P_m V_m/P_p V_p)$$

is then valid provided that the volumes V_p and V_m are expressed in Amagat units. The value of $P_p V_p$ is known from isothermal data, and the value of $P_m V_m/P_p V_p$ is close to unity, its value for ideal gases. Assuming the density ratio given by the ideal gas approximation, a value of $P_m V_m$ was obtained from available mixture isothermals and used to calculate a new density ratio, and so on. Two or three repetitions of this procedure were sufficient to obtain a consistent result. The isothermals of Gibby, Tanner, and Masson (1929), Tanner and Masson (1930), and Wiebe and Gaddy (1938) were used for mixtures of hydrogen with helium, argon, and nitrogen, respectively.

A Perkin-Elmer spectrometer, model 12B, with a LiF prism and a PbS detector was used to record the spectra. A 750 watt projection bulb with a planar filament, operated somewhat below its rating to ensure stability, was used as the source. Radiation from the lamp, focused by a spherical mirror, entered and left the cell in $f/8$ cones by way of a plane mirror mounted on the top of the cell (Fig. 1). The wavelength drive of the spectrometer was geared to the slit-width adjusting screws to give nearly constant intensity, and also a constant spectral resolution of 9 cm.$^{-1}$, across the band.

In the reduction of the data the average of three consistent traces taken at each pressure was transferred onto paper ruled with a logarithmic intensity scale, the line for infinite density being shifted slightly to correct for light scattered in the spectrometer. A frequency calibration was carried out using the bands in 1,2,4-trichlorobenzene, carbon disulphide, and water, as well as emission lines from a quartz mercury arc, as recommended by Plyler and Acquista (1952). The water band at 3700 cm.$^{-1}$ which appeared on each trace

was used as a frequency correlation point. The frequency scale was superimposed on the paper and the absorption coefficient, $\alpha = (2.303/l)\log_{10}(I_0/I)$, determined at intervals of 10 cm.$^{-1}$ across the band. The pressure in the absorption cell, measured with a calibrated manganin resistance gauge, was maintained constant within 0.1% during each trace. Using the calculated density ratio and the isothermals for the pure gases at high pressures measured by Hare (1955) and Michels and Goudeket (1941), the mixture densities were calculated by interpolation at the experimental pressures; since the mixture ratio was small a linear interpolation was sufficiently accurate.

RESULTS AND DISCUSSION

In Figs. 2, 3, 4, and 5 representative sets of absorption profiles of the fundamental absorption of hydrogen are reproduced for the pure gas and for hydro-

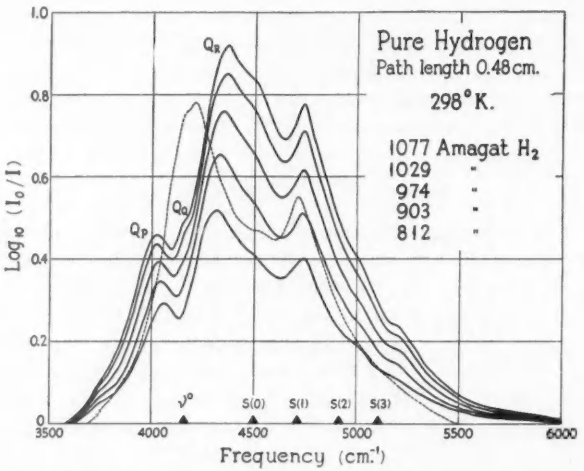

FIG. 2. The fundamental absorption of hydrogen at various pressures in the range 2006–4003 atm. The dotted line is the lower pressure contour extrapolated by the square law to a density of 1077 Amagat units.

gen–helium, hydrogen–argon, and hydrogen–nitrogen mixtures. In each case the constant mixture ratio and the partial densities of the perturbing gas for the various curves are given. The highest densities reached were considerably greater than the densities of the corresponding liquids at their normal boiling points; for example, in the hydrogen–helium mixture, the highest density was 2.2 times the density of liquid helium.

A pronounced feature of the absorption profiles is the wide separation of the Q_P and Q_R maxima, which is of the order of 400 cm.$^{-1}$ at the highest densities. To emphasize this point the low density contour for pure hydrogen (Welsh, Crawford, MacDonald, and Chisholm 1951), extrapolated by the square law to a density of 1077 Amagat units, is shown by the dotted curve in Fig. 2; in

this curve the Q_P and Q_R components are scarcely resolved. In all cases except the hydrogen–helium mixture the wide splitting of the Q branch uncovers the Q_Q component near the band origin, ν_0. As was conjectured previously (Chisholm and Welsh 1954), the Q_Q component appears to be intimately connected with the S lines; however, the comparison can be made only with the $S(1)$ line since the $S(0)$ line is obscured by the broad Q_R component. It can be seen that the $S(1)$ and Q_Q lines are strong and comparatively sharp in the hydrogen–argon mixture, and weaker and broader in the hydrogen–nitrogen mixture; both are absent in the hydrogen–helium mixture.

In Figs. 2 to 5 the frequencies of ν_0 and the S lines of the free molecule, as

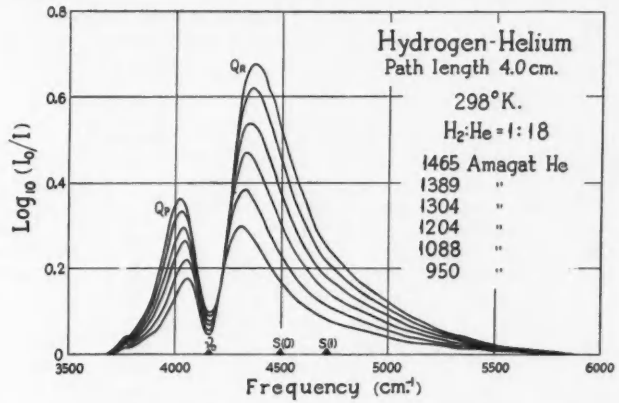

FIG. 3. The fundamental absorption of hydrogen in a hydrogen–helium mixture at various total pressures in the range 1995–4540 atm.

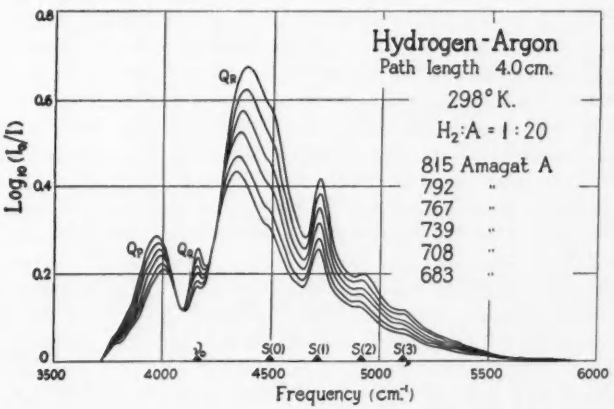

FIG. 4. The fundamental absorption of hydrogen in a hydrogen–argon mixture at various total pressures in the range 2289–4528 atm.

determined from the Raman effect in gaseous hydrogen (Cumming 1952), have been plotted on the frequency axis. The correspondence of these frequencies with the more or less broad maxima in the induced absorption contours is, on the whole, very close. However, it is apparent in Fig. 2 that the maximum of the $S(1)$ line for pure hydrogen at high densities occurs at a higher frequency ($\sim$4745 cm.$^{-1}$) than in the low density gas for which the frequency coincides with the Raman frequency (4713 cm.$^{-1}$). The explanation may be that in the high density gas the $S(1)$ line is produced in a double transition, in which the vibrational transition takes place in one molecule and the rotational transition

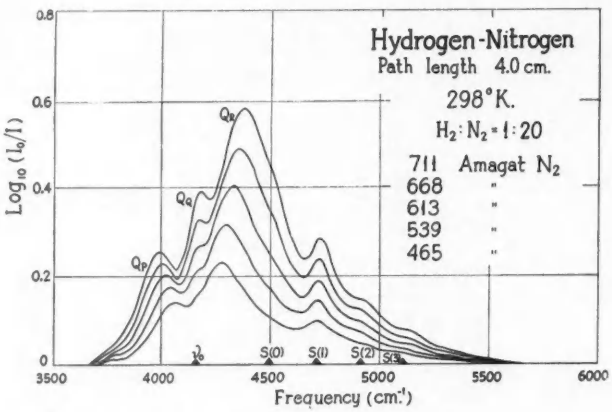

FIG. 5. The fundamental absorption of hydrogen in a hydrogen–nitrogen mixture at various total pressures in the range 1137–4665 atm.

in the ground vibrational state of a second molecule. The frequency of the double transition is greater than that of the single transition because of the rotation–vibration interaction. The high probability of such double transitions as compared with single transitions at high densities has been shown recently in the infrared spectrum of liquid and solid hydrogen (Allin, Gush, Hare, and Welsh 1957). For the gas mixtures a small but systematic trend of the $S(1)$ maximum towards higher frequencies with increasing density could be established on the original recorder traces, especially in the case of hydrogen–nitrogen mixtures; this is probably evidence of a slight perturbation of the rotational frequency of the hydrogen molecule. The broadness of the Q_0 and $S(1)$ lines in hydrogen–nitrogen mixtures as compared with hydrogen–argon mixtures can perhaps be ascribed to accompanying rotational transitions in the nitrogen molecule; double rotational transitions of this type have been observed in the infrared absorption of liquid and solid hydrogen (Allin, Hare, and MacDonald 1955).

In the following paragraphs the variation of the integrated absorption coefficient and the splitting of the Q branch as a function of the gas density will be discussed. In some cases the data obtained with the 5000 atm. cell are

supplemented with measurements made with a 30 cm. transmission cell and a 3000 atm. gas compressor. These later experiments have been useful in confirming some of the results obtained with the 5000 atm. cell and in establishing the correct trend of the absorption at pressures lower than 1500 atm. The long absorbing path, 30 cm., had the advantage that lower mixture ratios could be used; the interpretation of the results was thereby facilitated.

The Integrated Absorption Coefficient

The variation of the integrated absorption coefficient, $\int \alpha d\nu$, is shown by the graphs in Fig. 6, in which $(1/\rho_a)\int \alpha d\nu$, in cm.$^{-1}$ per cm. per Amagat unit of density, is plotted as a function of the density, ρ_p, of the perturbing gas. The

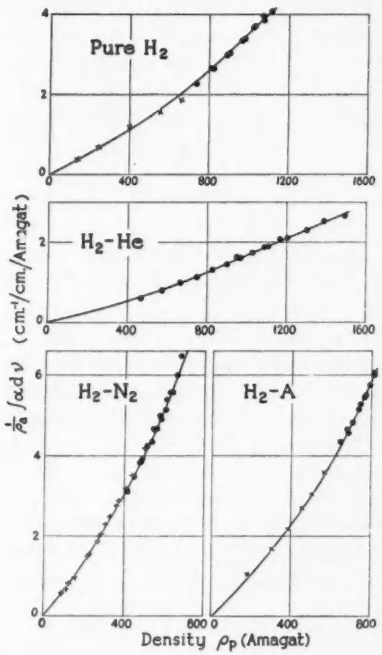

FIG. 6. The relation between the integrated absorption coefficient and the density of the perturbing gas: ●—this investigation, ×—Chisholm and Welsh (1954).

values of $(1/\rho_a)\int \alpha d\nu$ for the gas mixtures were corrected by subtracting the small contribution due to H_2–H_2 collisions using the absorption coefficient measured for the pure gas; data for the mixtures thus refer to the *enhancement* of the absorption by the foreign gas. For pure hydrogen, as well as hydrogen–nitrogen and hydrogen–argon mixtures, the lower density data of Chisholm and Welsh (1954) have been added to the graphs. The earlier lower pressure results for hydrogen–helium mixtures appeared unsatisfactory and have been replaced with measurements obtained with the 30 cm. transmission cell.

In Fig. 7 the data are replotted with $(1/\rho_a\rho_p)\int\alpha d\nu$ as ordinate and ρ_p as abscissa. The points on each graph appear to fall on a straight line over the whole range of densities confirming the relation

$$\int\alpha d\nu = \alpha_1\rho_a\rho_p + \alpha_2\rho_a\rho_p^2.$$

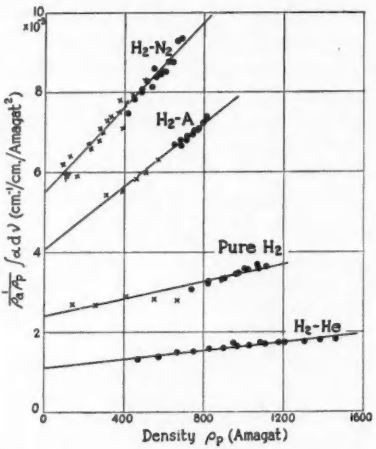

FIG. 7. The variation of $(1/\rho_a\rho_p)\int\alpha d\nu$ with ρ_p.

The values of α_1 and α_2, as determined from intercepts and slopes of the straight lines in Fig. 7, are given in Table I. These values, especially those of α_2, must be considered to be more accurate than those obtained in the lower pressure range (Chisholm and Welsh 1954).

TABLE I

ABSORPTION COEFFICIENTS FOR THE H_2 FUNDAMENTAL AT 298° K.

	Absorption coefficients		Molecular diameters	
Perturbing gas	α_1 (cm.$^{-1}$/cm./Amgt.^{2})	α_2 (cm.$^{-1}$/cm./Amgt.^{3})	D^* (Å)	$\sigma\dagger$ (Å)
Hydrogen	2.4×10^{-3}	1.1×10^{-6}	1.8	2.87
Helium	1.1×10^{-3}	0.55×10^{-6}	1.6	2.63
Argon	4.1×10^{-3}	3.9×10^{-6}	2.0	3.40
Nitrogen	5.4×10^{-3}	5.5×10^{-6}	2.1	3.70

*From α_2/α_1 in induced absorption.
†The constant σ from the Lennard-Jones formula, determined from the second virial coefficient.

The term $\alpha_2\rho_a\rho_p^2$ in the expression for the absorption coefficient can conceivably have its origin in the superposition of three effects: (*a*) the finite volume effect, (*b*) ternary collisions, and (*c*) the change of molecular polarizability with pressure. The effect of finite molecular volumes was discussed by

Chisholm and Welsh (1954), and expressions for α_2/α_1 in terms of the diameter, D, of the perturbing molecule were derived from a simple theory. These formulae, applied to the present data, lead to the molecular diameters given in column 4 of Table I. Values of σ, the distance of closest approach of two molecules which collide with zero initial relative kinetic energy, are given for comparison in column 5; these values, taken from the summary by Hirschfelder, Curtiss, and Bird (1954), are derived from the second virial coefficients of the gases. In all cases the molecular diameters calculated from the finite volume effect in induced absorption are markedly smaller than σ. If the calculation is reversed and the values of σ are used to calculate the absorption coefficient α_2, the calculated values of α_2 are four to five times greater than the experimental values. Although the method used here for the calculation of the finite volume effect is greatly oversimplified, it is practically certain that some mechanism must be present which tends to reduce the magnitude of the induced absorption at high pressures.

Qualitative considerations show that ternary and higher order collisions would annul to some extent the action of binary collisions; thus, in the limit when a particular molecule is surrounded by a symmetrical configuration of perturbing molecules the induced transition moment of the molecule is zero. This "cancellation" effect is intimately bound up with the finite volume effect, and an accurate assessment of both effects can be made only by an extended calculation based on a suitable molecular distribution function for the high pressure gas.

A decrease in atomic and molecular polarizabilities at high densities is predicted by quantum mechanical considerations (Michels, de Boer, and Bijl 1937; de Groot and ten Seldam 1947), and may be responsible in part for the decrease observed in the Lorentz–Lorenz function in highly compressed gas (cf., for example, Michels and Hamers 1937). In pressure-induced absorption a decrease in polarizability would lower the absorption coefficient, but the magnitude of the effect, which is difficult to estimate, is probably very small for hydrogen. It is therefore concluded that the coefficient α_2 consists essentially of two terms, a positive term due to the finite volume effect and a smaller, but by no means negligible, negative term due to the cancellation effect. It thus appears that even at lower pressures some effect of triple and higher order collisions is present.

The Splitting of the Q Branch

The frequency separation of the Q_P and Q_R maxima, $\Delta\nu_{PR}^{\max}$, is plotted in Fig. 8 as a function of the density, ρ_p, of the perturbing gas. The curves show the following characteristics: (*a*) a non-zero value of the separation when the curve is extrapolated to $\rho_p = 0$, (*b*) an approximately linear increase of the separation with increasing ρ_p over a large range of low and intermediate densities, and (*c*) a considerably more rapid increase in the region of high densities. The departure from the linear law, which was not apparent in the earlier experiments at lower densities, is most pronounced for the heavier perturbing molecules.

Before proceeding with the discussion it is necessary to point out a complication in the interpretation of the experimental data for gas mixtures. The absorption profile for a given mixture is a superposition of two profiles, one

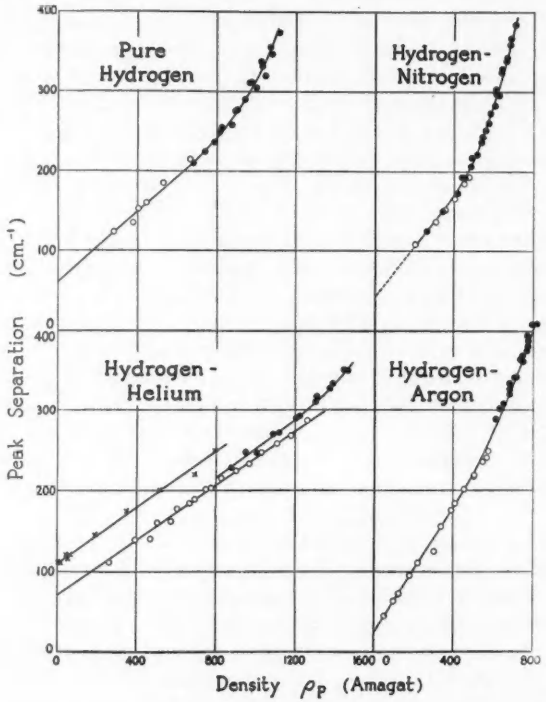

FIG. 8. The separation of the Q_P and Q_R maxima as a function of the density of the perturbing gas. The points ○ and ● refer to mixtures containing 5.0% and 1.2% hydrogen respectively; the points ×, from Chisholm and Welsh (1954), refer to mixtures with a constant base density of hydrogen of 168 Amagat units.

produced by H_2 – foreign gas collisions and a *different* one produced by H_2–H_2 collisions; these component profiles cannot be separated by any simple method. The peak separation, $\Delta\nu_{PR}^{\max}$, is therefore some mean of the separations for the two types of collisions. If the mixture ratio, ρ_a/ρ_p, is small the effect of H_2–H_2 collisions on the separation can obviously be neglected; this is especially true if the absorption coefficient is greater for H_2 – foreign gas collisions than for H_2–H_2 collisions, as is the case for argon and nitrogen as perturbing gases. For H_2–He collisions, on the other hand, the absorption coefficient is smaller than for H_2–H_2 collisions; the graph of $\Delta\nu_{PR}^{\max}$ vs. ρ_p thus shows a dependence on the mixture ratio, as is evident in Fig. 8. However, the variation of $\Delta\nu_{PR}^{\max}$ with ρ_p is quite similar for hydrogen–helium mixtures and for pure hydrogen; one would therefore expect that, if $\Delta\nu_{PR}^{\max}$ is plotted against the *total density*,

$\rho_p+\rho_a$, as in Fig. 9, all mixture ratios would give more or less the same curve. For small mixture ratios the experimental points do in fact fall on one curve. There is some discrepancy, as might be expected, when a constant base density of hydrogen is used; for this latter case the ratio, ρ_a/ρ_p, does not remain small over the whole range of densities.

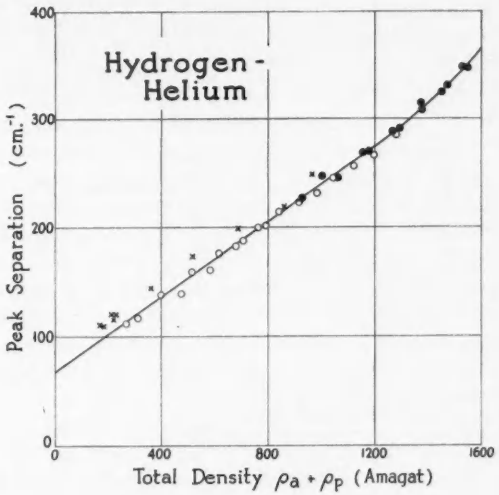

FIG. 9. The separation of the Q_P and Q_R maxima in hydrogen–helium mixtures as a function of the total density, $\rho_a+\rho_p$. The points ○ and ● refer to mixtures containing 5.0% and 1.2% hydrogen respectively; the points ×, from Chisholm and Welsh (1954), refer to mixtures with a constant base density of hydrogen of 168 Amagat units.

In Table II characteristic data from the $\Delta\nu_{PR}{}^{\max}$ vs. ρ_p curves are summarized; these are the limiting values at $\rho_p = 0$ of $\Delta\nu_{PR}{}^{\max}$ and $d(\Delta\nu_{PR}{}^{\max})/d\rho_p$. As pointed out by Chisholm and Welsh (1954) the splitting of the Q branch can be understood as arising from the participation of the relative kinetic energies of the absorbing molecule and the neighboring molecules in the absorption process. The limiting value of $\Delta\nu_{PR}{}^{\max}$ at $\rho_p = 0$ is characteristic of the collision pair producing the induced absorption. Since the Q branch is produced predominantly by collisions in the region of overlap forces (van Kranendonk and Bird 1951), the relative kinetic energy which has not been transformed into potential energy in these close collisions is mainly in the form of rotational energy. At the moment of closest approach when the probability of absorption is greatest, the collision pair might be considered to form a diatomic molecule with a rotational angular momentum, j, which depends on the impact parameter. The split Q branch thus resembles a Bjerrum double band in the infrared spectrum of a diatomic molecule, and the value of $\Delta\nu_{PR}{}^{\max}$ at $\rho_p = 0$ can be used to estimate an average distance of closest approach, r_0, from the formula

$$\Delta\nu_{PR}{}^{\max} = \sqrt{(8BkT/hc)} = 2.4\sqrt{BT},$$

where $B = h/8\pi c\mu r_0^2$, μ is the reduced mass of the collision pair, and T the absolute temperature. This elementary method used for calculating r_0 has several obvious defects; for example, the distribution of the rotational angular momenta, j, of the collision pairs is assumed to be the same as for a diatomic gas in temperature equilibrium. The values of r_0 calculated in this way for the various perturbing gases are given in Table II. For comparison the values of the Lennard-Jones potential constant, σ, are given; these have been estimated for the various collision pairs from the relation $\sigma_{\alpha\beta} = \frac{1}{2}(\sigma_\alpha + \sigma_\beta)$, using force constants for the pure gases from the summary of Hirschfelder, Curtiss, and Bird (1954).

TABLE II

THE SPLITTING OF THE Q BRANCH OF THE H_2 FUNDAMENTAL AT 298° K.

Perturbing gas	$\Delta\nu_{PR}^{\max}$ at $\rho_p = 0$ (cm.$^{-1}$)	$\frac{d(\Delta\nu_{PR}^{\max})}{d\rho_p}$ (cm.$^{-1}$/Amgt.)	Collision diameters	
			r_0* (Å)	$\sigma_{\alpha\beta}$† (Å)
Hydrogen	62	0.22	4.8	2.9
Helium	71	0.17	3.6	2.8
Argon	26	0.39	8.3	3.2
Nitrogen	43	0.32	5.0	3.3

*From $\Delta\nu_{PR}^{\max}$ at $\rho_p = 0$ in induced absorption.
†From $\sigma_{\alpha\beta} = \frac{1}{2}(\sigma_\alpha + \sigma_\beta)$; σ_α and σ_β determined from the second virial coefficients of the pure gases.

For helium as the perturbing gas the agreement between r_0 and $\sigma_{\alpha\beta}$ is satisfactory and can be considered as an experimental proof that the Q_P and Q_R components are produced by induction in the region of overlap forces. For the other gases the values of r_0 are considerably greater than $\sigma_{\alpha\beta}$, but this discrepancy is probably caused by the presence of the relatively strong Q_Q component in these cases (Figs. 2, 4, and 5). On the whole the agreement is such that the simple physical model proposed for the Q branch splitting at zero density must be essentially correct.

The increase in the Q branch splitting with increasing density of the perturbing gas must be interpreted in terms of ternary collisions for which the amount of kinetic energy available for participation in the absorption process is greater than for binary collisions. Thus, $\Delta\nu_{PR}^{\max}$ increases linearly with the density, as does, in the first approximation, the ratio of ternary to binary collisions. In an earlier explanation along similar lines (Chisholm and Welsh 1954) it was assumed that the third molecule in the collision need be only in the region of van der Waals attractive forces; however, the effect of ternary collisions on the absorption coefficient, which was discussed above, shows that the third molecule is in fact in the region of the overlap forces which produce the Q branch absorption.

The process involved in the splitting of the Q branch can now be given in more detail. To produce absorption at the Q_R maximum the absorbed photon contributes to the molecules involved in the collision a "most probable"

amount of kinetic energy which depends on the type of perturbing molecule and on the ratio of ternary to binary collisions; the separation of the Q_R maximum from the band origin thus increases linearly with the density. In absorption at the Q_P maximum the molecules in the collision contribute a most probable amount of energy to the excitation of the first vibrational state of the hydrogen molecule, and the Q_R maximum recedes from the band origin linearly with the density. The rate of increase of $\Delta\nu_{PR}{}^{\max}$ depends of course on the type of perturbing molecule; as might be expected, it is much greater for argon and nitrogen than for hydrogen and helium (Table II, column 3).

The Q_P and Q_R components can thus be considered to be the spectrum of difference and summation tones, $\nu_0 \mp \nu_k$, where ν_0 is the vibrational frequency of the hydrogen molecule and ν_k is the kinetic energy (in cm.$^{-1}$) which is taken from or given up to the surrounding molecules. As shown by Chisholm, MacDonald, Crawford, and Welsh (1952), the ratio of the relative intensities, $I_P(\nu_k)/I_R(\nu_k)$, depends on ν_k/T in the way which would be expected for difference and summation tones. For a given perturbing molecule, a given pressure, and a given temperature, ν_k has a characteristic spectrum which extends over perhaps 2000 cm.$^{-1}$ (Figs. 2–5). In the transition to the ordered arrangement of the crystalline state, the kinetic energy spectrum goes over into a vibrational spectrum of the crystal lattice; this has been shown in the investigations of the infrared spectrum of solid hydrogen by Allin, Hare, and MacDonald (1955) and Hare, Allin, and Welsh (1955).

The graphs of Fig. 8 show that, while $\Delta\nu_{PR}{}^{\max}$ increases linearly with ρ_p at low and intermediate densities, the increase is more rapid at the highest densities. This trend resembles somewhat the effect of finite molecular volumes on the variation of $(1/\rho_a)\int\alpha d\nu$, but there are some outstanding differences. For example, the departure from the linear variation is rather abrupt so that a relation of the form $\Delta\nu_{PR}{}^{\max} = a+b\rho_p+c\rho_p{}^2$ does not adequately represent the data. The anomalous rate of increase of $\Delta\nu_{PR}{}^{\max}$ appears to begin when the density of the perturbing gas reaches a more or less critical value of $\sim$500 Amagat units for argon and nitrogen, $\sim$800 for hydrogen, and $\sim$1300 for helium. The reason for this behavior of $\Delta\nu_{PR}{}^{\max}$ is not clear.

The present experiments showed no splitting or broadening of the Q_Q and $S(1)$ components with increasing density. It must therefore be concluded that the participation of the kinetic energy is slight when the absorption is induced by the longer range quadrupole forces. At lower pressures and somewhat higher spectral resolution Coulon, Galatry, Robin, and Vodar (1955) detected two absorption maxima in the $S(1)$ and Q_P components. These splittings are however relatively minor as compared with the main splitting of the Q branch; their origins have been discussed recently by Gush, Nanassy, and Welsh (1957).

The Absorption in the Overtone Region

With a path length of 4 cm. the absorption of pure hydrogen in the first overtone region could be recorded with fair intensity at pressures above 2000 atm.; the profiles of the absorptions for different densities are given in Fig. 10. As has been shown by Welsh, Crawford, MacDonald, and Chisholm (1951) the

absorption consists of the superposition of two bands, the overtone with components Q, $S(0)$, and $S(1)$, and a double vibrational transition with components Q', $S'(0)$, and $S'(1)$. In the double transition two interacting hydrogen molecules perform the fundamental transition simultaneously, producing an absorption which is shifted from the overtone band towards higher frequencies.

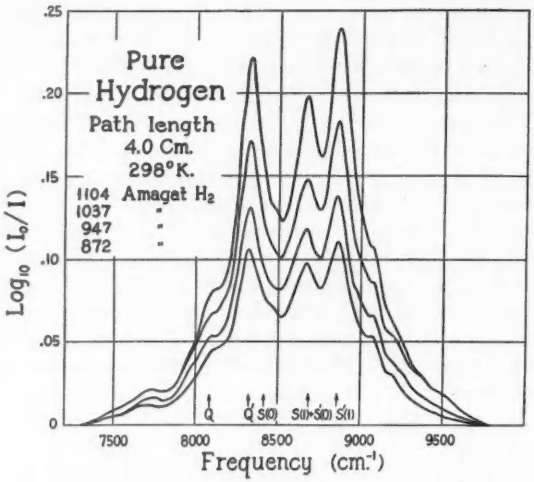

FIG. 10. The absorption of pure hydrogen in the overtone region at various pressures in the range 2327–4364 atm. Q, $S(0)$, and $S(1)$ are the components of the overtone, and Q', $S'(0)$, and $S'(1)$ the components of the double vibrational transition.

Both overtone and double transition absorptions have very nearly the same shape at very high densities as at low densities; the components show no splitting and remain relatively sharp. The Q and Q' branches are very weak and therefore seem to correspond to the Q_Q component of the fundamental. From these characteristics it appears that the interaction producing the overtone and the double transition must be the same as that giving rise to the Q_Q and S lines in the fundamental, namely, quadrupole interaction. The overtone and the double transition arise of course from mechanical and electrical anharmonicities. For the overlap interaction the two anharmonicities appear to cancel one another; a similar cancellation of the anharmonic effects has been shown to be present in the Raman spectrum of carbon tetrachloride (Welsh, Crawford, and Scott 1948).

ACKNOWLEDGMENTS

The authors are greatly indebted to Dr. D. A. Chisholm for his assistance in the design of the high pressure absorption tube, and to the National Research Council of Canada for their continued support of research in high pressures at the University of Toronto.

REFERENCES

ALLIN, E. J., GUSH, H. P., HARE, W. F. J., and WELSH, H. L. 1957. Phys. Rev. **106**, 1101.
ALLIN, E. J., HARE, W. F. J., and MACDONALD, R. E. 1955. Phys. Rev. **98**, 554.
CHISHOLM, D. A., MACDONALD, J. C. F., CRAWFORD, M. F., and WELSH, H. L. 1952. Phys. Rev. **88**, 957.
CHISHOLM, D. A. and WELSH, H. L. 1954. Can. J. Phys. **32**, 291.
COULON, R., GALATRY, L., ROBIN, J., and VODAR, B. 1955. J. phys. radium, **16**, 728.
CUMMING, C. 1952. Ph.D. Thesis, University of Toronto, Toronto, Ont.
GIBBY, C. W., TANNER, C. C., and MASSON, I. 1929. Proc. Roy. Soc. A, **122**, 283.
DE GROOT, S. R. and TEN SELDAM, C. A. 1947. Physica, **13**, 47.
GUSH, H. P., NANASSY, A., and WELSH, H. L. 1957. Can. J. Phys. **35**, 712.
HARE, W. F. J. 1955. Ph.D. Thesis, University of Toronto, Toronto, Ont.
HARE, W. F. J., ALLIN, E. J., and WELSH, H. L. 1955. Phys. Rev. **99**, 1887.
HIRSCHFELDER, J. O., CURTISS, C. F., and BIRD, R. B. 1954. Molecular theory of gases and liquids (John Wiley and Sons, Inc., New York; Chapman and Hall, Ltd., London).
VAN KRANENDONK, J. and BIRD, R. B. 1951. Physica, **17**, 953, 968.
MICHELS, A., DE BOER, J., and BIJL, A. 1937. Physica, **4**, 981.
MICHELS, A. and GOUDEKET, M. 1941. Physica, **8**, 347.
MICHELS, A. and HAMERS, J. 1937. Physica, **4**, 995.
PLYLER, E. K. and ACQUISTA, N. 1952. J. Research Natl. Bur. Standards, **49**, 13.
TANNER, C. C. and MASSON, I. 1930. Proc. Roy. Soc. A, **126**, 268.
WELSH, H. L., CRAWFORD, M. F., MACDONALD, J. C. F., and CHISHOLM, D. A. 1951. Phys. Rev. **83**, 1264.
WELSH, H. L., CRAWFORD, M. F., and SCOTT, G. D. 1948. J. Chem. Phys. **16**, 97.
WELSH, H. L., PASHLER, P. E., and DUNN, A. F. 1951. J. Chem. Phys. **19**, 340.
WIEBE, R. and GADDY, V. L. 1938. J. Am. Chem. Soc. **60**, 2300.

THE LUMINESCENCE RESPONSE OF PHOSPHORS TO LOW ENERGY ION BOMBARDMENT[1]

C. F. EVE[2] AND H. E. DUCKWORTH

ABSTRACT

The luminescence response of samples of ZnS:Ag and Zn_2SiO_4:Mn to bombardment with various ions was determined as a function of the ion energy. For ZnS:Ag, within the range of ion energies studied ($E < 25$ kev.), the luminescence response, L, is related to the ion energy, E, according to $L \propto (E-E_0)^n$. E_0 is a threshold energy which is not a very sensitive function of ion mass. For Zn_2SiO_4:Mn no threshold energy was observed except in the case of Li^{7+} ions, the lightest ions used with this phosphor. The experimental results for ZnS:Ag appear to be consistent with a theory in which it is assumed that the bombarding particles penetrate the phosphor as neutral atoms and produce luminescence by electronic excitation of the lattice atoms due to small impact parameter collisions.

INTRODUCTION

When a low energy ion penetrates a solid, most of its energy is expended by elastic collisions with the atoms of the solid and only a small proportion in electronic excitation (see, for example, Seitz 1949). If the production of luminescence in a phosphor is the result of electronic excitation in the host lattice, one would therefore expect the bombardment of the phosphor with low energy ions to produce only a small amount of luminescence but possibly a considerable degree of deterioration due to the formation of lattice defects in the crystal. For this reason, most of the previous work concerning the bombardment of phosphors with low energy ions has been devoted to a study of the modifications of the luminescence properties of the phosphor produced by the bombardment rather than of the luminescence response itself. Smith and Turkevich (1954) give a comprehensive list of references to work concerning the effect of α-particle bombardment on the luminescence properties of ZnS phosphors. Smith and Turkevich themselves investigated the modifications produced in ZnS:Cu by neutron bombardment. In addition to this work the deterioration of the luminescence efficiency of phosphors under low-energy ion bombardment has been studied by Hanle and Rau (1952), Berthold (1955), and Young (1955). Martin (1957) has made a detailed study of the effect of prolonged H_2^+ ion bombardment on many of the properties of phosphors.

The only previous work known to the authors in which the luminescence response of phosphors to low energy ion bombardment has been studied as

[1]Manuscript received October 30, 1957.

Contribution from the Department of Physics, Hamilton College, McMaster University, Hamilton, Ontario, Canada.

This work was supported by the Ontario Research Foundation, the U.S. Air Force through the Air Force Office of Scientific Research and Development Command, and the National Research Council of Canada.

[2]Holder of postgraduate scholarships awarded by: The Research Council of Ontario, 1954–1955; The Shell Oil Company of Canada, 1955–1956; The Ontario Research Foundation, 1956–1957.

This work forms part of a thesis submitted in partial fulfillment of the requirements for the Ph.D. degree, McMaster University.

a function of the ion energy is that of Hanle and Rau (1952). These authors found that under H_2^+ ion bombardment the luminescence response of ZnS:Ag was approximately proportional to the ion energy for energies between 15 and 35 kev. Richards and Hays (1950) introduced a scintillation detector in their time-of-flight mass spectrometer, and some general observations were made concerning the light output as a function of ion energy for K^+ and Rb^+ ions with energies up to 30 kev. However, in subsequent work with this instrument the scintillation detector was replaced by an electron multiplier.

The work described in this paper was also initiated with a view to the possible development of a scintillation detector of positive ions in a mass spectrometer. As the work proceeded, however, the authors became more interested in the fundamental aspects of the problem, so that the project has been continued more in the nature of a fundamental study of the luminescence response of phosphors to low energy ion bombardment.

APPARATUS

The general principle of operation of the apparatus is illustrated diagrammatically in Fig. 1. The ion source, shown at A, was built into the inner member of a ground-glass joint and could be inserted at the lower end of the

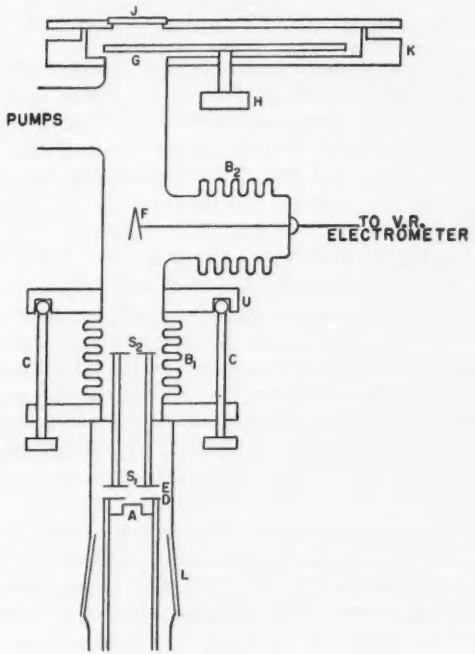

FIG. 1. Apparatus.

apparatus. For the production of ions of the alkali metals a thermal ion source was used. To obtain H_2^+ and A^+ ions an electron bombardment source was employed. The ions emerging from the source were accelerated upwards by an electrostatic field applied between the electrodes D and E and were collimated into a narrow beam by the slits S_1 and S_2. The direction of the beam could be controlled by adjusting the screw rods C which controlled the curvature of the bellows B_1. The ion beam could be collected in a small Faraday cup F and the ion current measured by means of a vibrating reed electrometer. By extending the bellows B_2 the Faraday cup could be retracted from the beam to permit the ions to pass on to the phosphor samples. These consisted of thin layers of powdered phosphor deposited onto 18 mm. diameter microscope cover glasses. The glasses had previously been coated with a transparent electrically-conducting layer of cadmium oxide. The phosphors used were ZnS:Ag (Sylvania Phosphor No. CR-20) and Zn_2SiO_4:Mn (Sylvania Phosphor No. 161). The samples were mounted, phosphor side down, in holes in the horizontal brass disk G. The holes were arranged around the disk close to its periphery. By rotation of the calibrated dial H the sample disk could be rotated so as to bring any desired sample into the path of the ion beam. Light emitted by the phosphor, after transmission through the phosphor layer and the glass backing, passed through the lucite window J and was detected by a 1P21 photomultiplier.

ANALYSIS OF THE ION BEAM

Magnetic analysis was used to separate and identify the various types of ion present in the beam. This analysis was accomplished by applying a magnetic field in the region between the slit S_2 and the Faraday cup F (Fig. 1). The mass spectrum could be scanned by adjusting the deflection of the bellows B_1. In the early stages of this work the homogeneity of the ion beam was checked by magnetic analysis and then the experiments on the phosphor samples performed with the magnetic field removed. This practice unfortunately led to an incorrect identification of the ions used in the experiments reported by Eve and Duckworth (1956). The error arose owing to the inadvertent substitution of a tungsten filament in the ion source for one of tantalum without subsequent rechecking of the composition of the ion beam. It was later discovered that the commercial grade of tungsten used contained potassium as an impurity, and that with such a filament the ion current from the source consisted predominantly of K^+ ions, regardless of the material coating the surface of the filament. It was then established that the results quoted in the above paper in fact corresponded to K^+ ions and not to Li^+ ions as stated there.

In order to avoid further errors concerning the identification of the ions used, the magnetic analyzer was retained during all the experiments described in this paper. To obtain ions of the alkali metals other than potassium a platinum filament coated with an appropriate salt was used.

DETECTION OF THE LUMINESCENCE

The light emitted from the bombarded phosphor sample, after transmission

through the lucite window J (Fig. 1), was detected by a 1P21 photomultiplier. The d-c. output of the photomultiplier was displayed on the chart of a Brown Electronik Recorder.

In order to minimize the deterioration of the phosphor samples by the ion bombardment during the course of the experiments, the samples were kept in motion throughout the period of bombardment. The sample disk was first adjusted so that no sample was in the path of the ion beam. After the ion current was determined, the Faraday cup was retracted and a phosphor sample then passed across the path of the ion beam by manual rotation of the sample disk. The Faraday cup was then reinserted into the beam and a second determination of the ion current made. As the phosphor sample passed across the path of the ion beam, the photomultiplier produced a peak on the recorder chart, the peak height being proportional to the light output from the sample. The mean time taken to pass a sample across the path of the ion beam was about 5 seconds. The direction of the motion of the sample was perpendicular to the lengths of the collimating slits, so that the irradiation was effectively distributed over a large area of the sample. Evidence is presented below to show that this technique of continuous scanning of the samples did indeed restrict the deterioration of the phosphor to negligible proportions.

VARIATION WITH ION CURRENT

The luminescence was first studied as a function of the ion current at constant ion energy. In all cases it was found that the light output was directly proportional to the ion current. In these experiments the ion current was varied between 10^{-13} and 10^{-12} amp. and the cross-sectional area of the beam was 0.40 mm.^{2} In Fig. 2 results are shown for ZnS:Ag under bombardment with Na^+ ions. The gradient, L, of each line is proportional to the light output per ion.

FORM OF THE ENERGY DEPENDENCE

In order to determine how the luminescence response varies with ion energy, values of L, determined in the manner explained above, were plotted as a function of the ion energy E. The results obtained for ZnS:Ag under bombardment with Li^{7+} ions are shown in Fig. 3. On a logarithmic scale the curve of L versus E is concave towards the energy axis. It was found that a straight line was obtained if L was plotted against $E-4$ kev. The variation of light output with ion energy is therefore of the form

$$L \propto (E-E_0)^n,$$

where the constant E_0 is the quantity that must be subtracted from E to obtain a straight line plot, and n is the gradient of the line so obtained.

The points represented by triangles in Fig. 3 were obtained with an optical interference filter interposed between the phosphor sample and the photomultiplier. The transmission spectrum of the filter was approximately matched to the emission spectrum of the phosphor (as given in the Sylvania Phosphor catalogue). It was found that the form of the L versus E curve

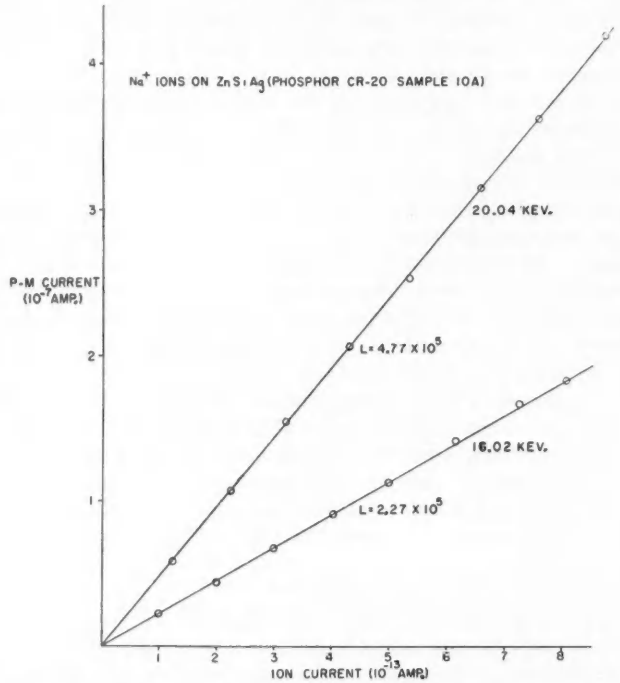

FIG. 2. The variation of light output with ion current for ZnS:Ag under bombardment with Na^+ ions at two different energies. The L-values shown are the gradients of the two lines.

was not affected by the presence of the filter. This was taken to indicate the absence of any shift in the emission spectrum of the phosphor with increasing ion energy. The sensitivity of the photomultiplier was therefore independent of the ion energy.

Although desirable, a full spectral analysis of the light emitted by the phosphor was not feasible because of its low intensity. This intensity could only be sufficiently increased at the expense of a serious deterioration of the phosphor sample.

EFFECT OF THE NATURE OF THE BOMBARDING IONS

The values of E_0 and n for various ions impinging on ZnS:Ag and Zn_2SiO_4:Mn are given in Table I. All these values were obtained using a single sample of ZnS:Ag and a single sample of Zn_2SiO_4:Mn. The results of each experiment were plotted for several different values of the constant E_0. The limiting lines in which curvature was just detectable were taken to indicate the experimental limits between which the value of E_0 lay. These are the limits assigned to E_0 in Table I. The limits assigned to n are the gradients of the limiting lines.

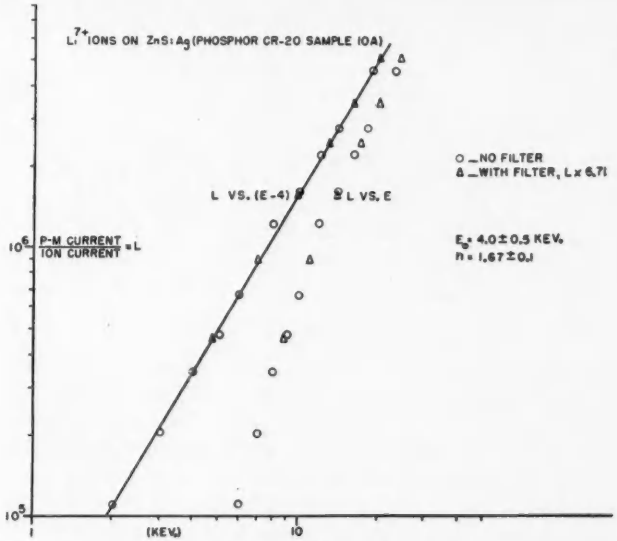

FIG. 3. L versus E and L versus $E-4$ kev. for Li^{7+} ions impinging on ZnS:Ag. The experimental points represented by triangles were obtained with an optical interference filter interposed between the phosphor sample and the photomultiplier.

TABLE I

VALUES OF E_0 AND n FOR DIFFERENT IONS AND PHOSPHORS

	ZnS:Ag		Zn_2SiO_4:Mn	
Ion	E_0 (kev.)	n	E_0 (kev.)	n
H_2^+	3.5±0.5	1.11±0.06		
Li^{7+}	4.0±0.5	1.67±0.10	2.5±0.5	1.29±0.07
Na^+	3.5±0.5	3.26±0.20	<1.0	1.72±0.08
K^+	4.0±0.5	2.35±0.13	<1.0	1.72±0.07
A^+	2.0±1.0	3.11±0.27	<2.0	1.64±0.17
Rb^+	1.8±1.8	3.89±0.60	<1.0	1.85±0.07

In the case of ZnS:Ag, E_0 does not appear to vary significantly with ion mass. The value of n shows a general tendency to increase with increasing ion mass. For H_2^+ ions, n is very close to unity. This result is in agreement with that found by Hanle and Rau (1952). In the case of Zn_2SiO_4:Mn, the only bombarding ions used for which E_0 was distinguishable from zero were Li^{7+} ions. The experiment with these ions was repeated, and again values of E_0 and n within the limits given in Table I were obtained.

The results for ZnS:Ag under bombardment with Na^+, K^+, A^+, and Rb^+ ions are shown in Fig. 4, where L is plotted against $(E-E_0)$, with E_0 given in each case by Table I. Curves of L versus E are shown for Li^{7+}, Na^+, K^+, and Rb^+ ions impinging on Zn_2SiO_4:Mn in Fig. 5. The anomalous nature of the Li^{7+} results in comparison with those for the other ions is clearly illustrated

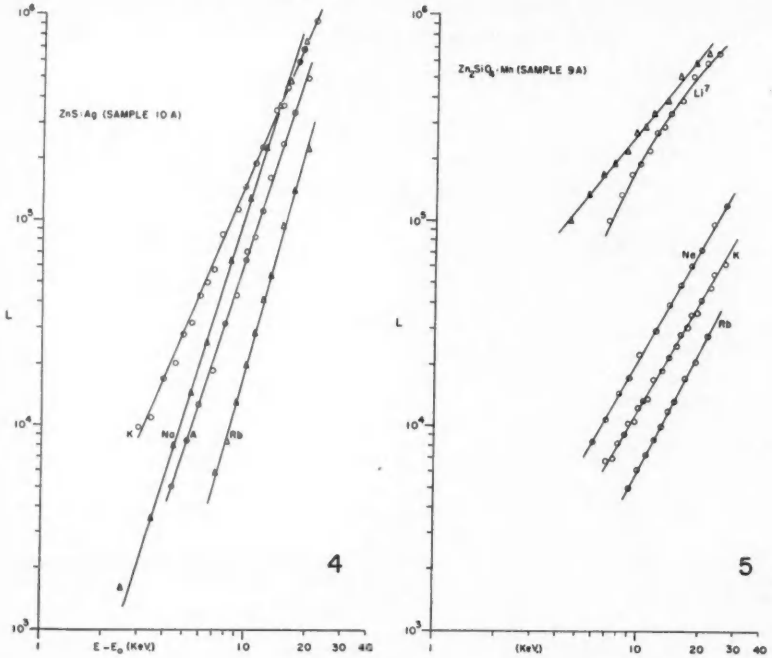

FIG. 4. L versus $(E-E_0)$ for Na^+, K^+, A^+, and Rb^+ ions impinging on a sample of ZnS:Ag. E_0 is given in each case in Table I.

FIG. 5. The experimental points shown as circles represent L versus E for Li^{7+}, Na^+, K^+, and Rb^+ ions impinging on Zn_2SiO_4:Mn. The points shown as triangles for Li^{7+} ions represent L versus $E-2.5$ kev. The solid curve through the points of L versus E for Li^{7+} ions represents relation (4) with $C = 11.6$ kev.

in this figure. In comparing the results shown in Figs. 4 and 5, it should be noted that no correction has been made for the difference in sensitivity of the photomultiplier to the light from the two different phosphors.

ABSOLUTE EFFICIENCIES

Hanle and Rau (1952) made absolute determinations of the luminescence efficiency of ZnS:Ag and Zn_2SiO_4:Mn under bombardment with various ions. Each of these determinations was made at an ion energy between 20 and 30 kev. The present results show, however, that, except in the case of H_2^+ ion bombardment of ZnS:Ag, the luminescence efficiency is a sensitive function of the ion energy. The energy dependence of the efficiency was not taken into account by Hanle and Rau. However, if it is assumed that their values for ZnS:Ag and Zn_2SiO_4:Mn under bombardment with H_2^+ and A^+ ions, respectively, are correct at 25 kev., then these values can be used to normalize the present results to an absolute scale. This assumption leads to the values given in Table II.

TABLE II

EFFICIENCIES OF PHOSPHORS FOR VARIOUS IONS

Ion	Efficiency at 25 kev. (%)	
	ZnS:Ag	Zn_2SiO_4:Mn
H_2^+	25	
Li^{7+}	15	9.2
Na^+	3.3	1.3
K^+	2.3	0.8
A^+	2.2	0.8
Rb^+	1.0	0.4

THE EFFECT OF DETERIORATION

In the Introduction reference was made to work demonstrating the deterioration of the luminescence efficiency of phosphors under prolonged ion bombardment. This deterioration effect is especially important in the case of ZnS:Ag. Martin (1957) found that under H_2^+ ion bombardment this phosphor deteriorated more rapidly than any of the other phosphors that he studied (including Zn_2SiO_4:Mn). It is therefore very important to show that, during the course of the experiments on ZnS:Ag, no appreciable deterioration of the phosphor sample occurred. This was shown by the experiments described below.

(i) The experiment with Li^{7+} ions, which was the first of the series, was repeated at the conclusion of the series, and the same L versus E curve was obtained.

(ii) After the conclusion of the series, the light output of the ZnS:Ag sample used was compared with that of a fresh sample of the same phosphor under bombardment with A^+ ions at three different energies, viz. 10, 15, and 20 kev. The ratio of the light outputs of the two samples was independent of the ion energy. It was therefore concluded that the form of the L versus E curve was not affected by the ion bombardment to which the used sample had previously been subjected. The light output from the used sample was in fact slightly greater at each energy than that from the fresh sample. This was attributed to a difference in sample thickness.

(iii) The rate of deterioration of ZnS:Ag under prolonged bombardment with 15 kev. A^+ ions was measured. The deterioration was found to follow the law given by Hanle and Rau (1952) and confirmed by Martin (1957). The value found for the deterioration constant was approximately that given by Hanle and Rau for A^+ ions on ZnS:Ag. Assuming this constant to be independent of the type of ion used, the maximum deterioration of the L versus E curves was estimated at 6.5%, by summing the ion flux to which this sample had been subjected, account being taken of the fact that the sample had been kept in motion during the bombardment. This maximum deterioration is that produced near the surface of the sample in a region penetrated by all the ions. In deeper lying regions, penetrated only by ions of higher energy or lower mass, the deterioration will be less than this value.

Hence, in order to correct the L versus E curves for the effect of deterioration, the value of L corresponding to each point of a given curve must be increased by an amount between zero and 6.5%, the percentage correction being greater for the lower energy points. The maximum possible change in the form of the L versus E curve is obtained by applying the maximum correction of 6.5% to the lowest energy point, zero correction to the highest energy point, and intermediate corrections to the other points according to their energies. When this was done it was found that the mean values obtained for E_0 and n in no case lay outside the experimental limits stated in Table I.

INTERPRETATION OF E_0

If the empirical relationship

$$L \propto (E-E_0)^n$$

can be extrapolated down to zero light output, then E_0 is to be interpreted as a threshold energy. A similar relationship is found to govern the variation of cathodoluminescence with electron energy (see, for example, the review article by Garlick (1950)). In this case the threshold energy has been ascribed to surface contamination of the phosphor. In the present case of ionoluminescence a similar interpretation of E_0 seems unlikely in view of the observed nature of the dependence of E_0 on ion mass. In order to throw further light on this question, the following experiment was performed.

A sample of ZnS:Ag was subjected to prolonged bombardment with an intense beam of 6 kev. K^+ ions. In this experiment the sample was held stationary in the beam so that the irradiation was confined to a small area of the sample. The energy of the ions was only 2 kev. above the threshold energy so that only a small intensity of light was observed. When the light output had fallen by 85%—owing to deterioration—the phosphor sample was removed from the ion beam. The response of all regions of the phosphor sample to a beam of 12 kev. K^+ ions was then examined by passing the sample across such a beam. It was found that in the region subjected to 6 kev. bombardment the response to 12 kev. ions was reduced by about 83%. If it is assumed that the 85% deterioration observed under the 6 kev. bombardment is uniformly distributed throughout the depth of penetration of the 6 kev. ions, as the results of Young (1955) suggest, then it follows that practically all the light normally due to a 12 kev. ion originates within this depth, while the latter portion of the range of a 12 kev. ion gives rise to practically no luminescence. This suggests that the constant E_0 is not associated with any surface layer, but is a true threshold energy in the sense that an ion having energy less than E_0 cannot excite luminescence in any part of the phosphor.

THEORY

An attempt will now be made to account theoretically for the observed dependence of the luminescence on the energy of the bombarding ions. Consideration will be confined to the case of ZnS:Ag, in which it is fairly certain that the luminescence is the result of electronic excitation in the host lattice.

It will be assumed that the luminescence intensity is always proportional to the amount of such excitation.[3] An expression must then be found for the rate of electronic excitation due to the passage of a heavy particle through a solid. The usual formulas for $-dE_x/dx$ are inapplicable here because they do not take into account the phenomenon of charge exchange which causes the average charge on the incoming particles to approach zero for small velocities (see, for example, Allison and Warshaw (1953) and Bethe and Ashkin (1953)). According to Nielsen (1956), when the velocity of the incident particles is less than $e^2/2\hbar$, the cross section for electron capture is so large that the incoming particles can be regarded as uncharged throughout the penetration of the solid. This condition is well satisfied in the present experiments except in the case of H_2^+ ions at the upper end of the energy range.

In most of the published theoretical work dealing with the slowing down of low velocity atomic particles in solids, the energy loss due to electronic excitation has been considered only to the extent necessary to show that it is small compared with the energy loss by elastic scattering at sufficiently low velocities. The subject has therefore received only rather qualitative treatment. To the best of the authors' knowledge, the work in which this aspect has been considered in most detail is that of Seitz and Koehler (1956). In this work an expression is derived for the probability, P, that an electronic transition will be induced in a stationary atom by the close passage of a slow atomic particle. The expression is of the form

$$P = (P_0/E_x)\exp(-C/E_x), \tag{1}$$

where

$$C = (W^2R^2/8R_h a_0^2)(M/m), \tag{2}$$

E_x is the energy of the moving particle, W is the energy of the electronic transition considered, R_h is the Rydberg energy, a_0 is the radius of the first Bohr orbit in hydrogen, m is the electronic mass, and M the mass of the moving particle. In the derivation of equation (1) it is assumed that P is constant if the impact parameter p is less than some constant R, and zero if p is greater than R. R may therefore be defined as the range of the interaction. The assumption of a sharply defined interaction range is most nearly justified if the moving particle is uncharged so that there is no long-range Coulomb interaction. As was pointed out above, this is just the case we are concerned with here.

The total number of excitations per incident particle is proportional to

$$\int_0^X P\,dx, \tag{3}$$

where X is the range of the incident particle. Nielsen (1956) shows that the total rate of energy loss, $-dE_x/dx$, is a constant independent of energy. He gives references to experimental work confirming this result. Additional

[3]This assumption ignores the possibility that the probability of non-radiative recombination of electrons and holes may be an explicit function of depth beneath the crystal surface.

confirmation is given by Young (1955). The integral (3) is therefore proportional to

$$\int_0^E P\, dE_x,$$

where E is the incident energy. By substitution for P from equation (1), it can be shown that

$$\int_0^E P\, dE_x \propto -\mathrm{Ei}(-C/E), \tag{4}$$

i.e.

$$L \propto -\mathrm{Ei}(-C/E).$$

The right-hand side of this relationship is the well-known exponential integral for which tabulated values are available.

By suitable choice of the constant C, expression (4) can be fitted to the experimental L versus E curves for ZnS:Ag. Two examples are shown in Figs. 6 and 7 for Li^{7+} and H_2^+ ions, respectively.

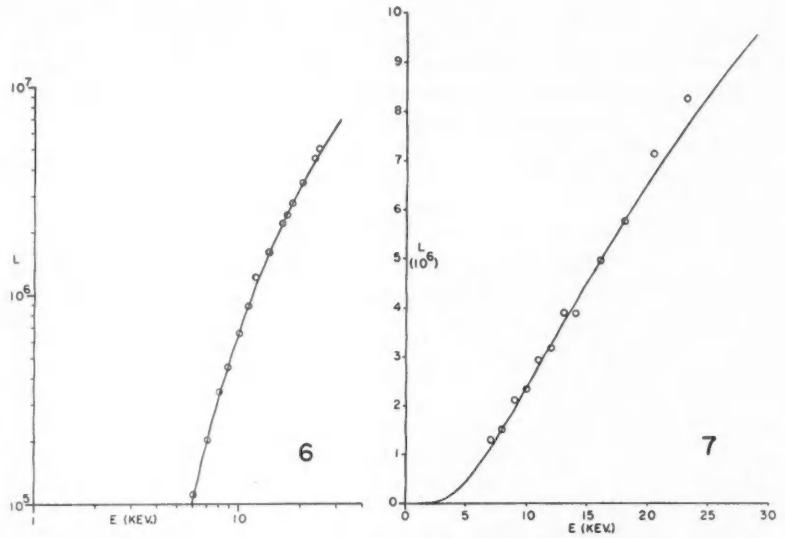

FIG. 6. Comparison of theory with experiment. The experimental points represent L versus E for Li^{7+} ions impinging on ZnS:Ag. The solid curve represents relation (4) with $C = 22.2$ kev.

FIG. 7. Comparison of theory with experiment. The experimental points are for H_2^+ ions impinging on ZnS:Ag. The solid curve represents relation (4) with $C = 11.2$ kev.

The form of the function $-\mathrm{Ei}(-C/E)$ is such that the value of L increases more rapidly with E for larger values of C. From equation (2) it can be seen that if R is an insensitive function of M, then C is roughly proportional to M. One would, therefore, expect the exponent n in the empirical relationship

between L and E to increase with increasing ion mass. This tendency was indeed observed. However, in order to obtain the best possible fit with the experimental curves, C had to be chosen in such a way as to imply a small variation of R with ion mass. In each case the value of R was calculated from equation (2) using $W = 3$ ev. for the energy of the band-to-band transition in ZnS:Ag. The values of R so obtained are given in Table III.

TABLE III

VALUES OF R FOR VARIOUS IONS

Incident particle	Mass (a.m.u.)	R (Å)
H_2	2	3.23
Li^7	7	2.43
Na	23	1.95
K	39	1.25
A	40	1.20
Rb	85.5	1.02

It is conceivable that the gradual decrease in the value of R with increasing particle mass might be due to decreasing average charge of the particle. The effective interaction range will increase with increasing average charge because of the long-range nature of the Coulomb interaction.

Because of the good fit of the theoretical curves to the experimental points, the theory indicates the existence of the energy thresholds to the same extent that they are implied by the experimental results. In Fig. 7, for H_2^+ ions, the theoretical curve is plotted on a linear scale down to zero energy. The prediction of an effective threshold energy is clearly illustrated here, for the curve remains very close to the axis for small values of E and then turns up sharply, after which it remains approximately linear over a large range of E.

In the case of Zn_2SiO_4:Mn, relationship (4) cannot be fitted to any of the experimental curves except that for Li^{7+} ions. These were the lightest ions used with this phosphor. Because of the general nature of expression (1) for the probability of electronic excitation, it seems likely that in the case of Zn_2SiO_4:Mn under bombardment with the heavier ions the luminescence is not connected with the electronic excitation of the lattice. Whether or not such excitation still occurs, it apparently no longer constitutes the dominant mechanism for the production of luminescence. It is hoped that further experiments will elucidate this question.

ACKNOWLEDGMENTS

Valuable assistance was given by Arie van Wijngaarden in the preparation of the phosphor samples and also during some of the experiments. The authors are also indebted to Dr. H. E. Petch, Dr. R. H. Tomlinson, and Dr. P. R. Zilsel for helpful discussions during the course of this work.

REFERENCES

ALLISON, S. K. and WARSHAW, S. D. 1953. Revs. Modern Phys. **25**, 779.
BERTHOLD, W. 1955. Naturwissenschaften, **42**, 436.

BETHE, H. A. and ASHKIN, J. 1953. Experimental nuclear physics, *edited by* E. Segre (John Wiley and Sons, Inc., New York), Chap. **2**.
EVE, C. F. and DUCKWORTH, H. E. 1956. Can. J. Phys. **34**, 896.
GARLICK, G. F. J. 1950. Advances in electronics, Vol. II (Academic Press Inc., New York).
HANLE, W. and RAU, K. H. 1952. Z. Physik, **133**, 297.
MARTIN, W. 1957. Z. Physik, **147**, 582.
NIELSEN, K. O. 1956. Electromagnetically enriched isotopes and mass spectrometry, *edited by* M. L. Smith (Butterworth's Scientific Publications, London).
RICHARDS, P. I. and HAYS, E. E. 1950. Rev. Sci. Instr. **21**, 99.
SEITZ, F. 1949. Discussions Faraday Soc. **5**, 271.
SEITZ, F. and KOEHLER, J. S. 1956. Solid state physics, Vol 2, *edited by* F. Seitz and D. Turnbull (Academic Press Inc., New York).
SMITH, A. W. and TURKEVICH, J. 1954. Phys. Rev. **94**, 857.
YOUNG, J. R. 1955. J. Appl. Phys. **26**, 1302.

DIURNAL VARIATIONS IN THE NUMBER OF SHOWER METEORS DETECTED BY THE FORWARD-SCATTERING OF RADIO WAVES

PART III. ELLIPSOIDAL THEORY[1]

C. O. HINES

ABSTRACT

A theory of meteor 'observability' relating to forward-scatter radio experiments was developed in Part I of this series, with the use of a simplifying 'cylindrical approximation'. The application of the theory to data obtained during meteor showers provides a promising new method for studying the intrinsic strengths of the showers. The principal limitation of the method is due to the inaccuracies of the cylindrical approximation. In the present paper, these inaccuracies are removed by a full development of the ellipsoidal geometry inherent in the forward-scatter process. The more rigorous results are compared with the approximate results at various stages throughout the analysis.

INTRODUCTION

Radio techniques have increased greatly the scope of meteor studies in recent years, by utilizing signals scattered from the ionized meteor trails. The scattering process is strongly specular, at frequencies low in the V.H.F. range, so the incident and scattered rays make supplementary angles with the axis of the meteor trail (see Fig. 1). When this condition is applied to a specific transmission path with transmitter at T and receiver at R, it implies that

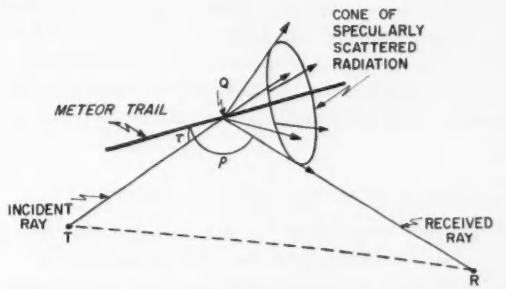

FIG. 1. Three-dimensional view of meteoric forward-scatter geometry. Radiation incident from T to Q is specularly scattered into a cone about the axis of the meteor trail, such that $\tau+\rho = 180^{\circ}$.

scattered signals will be received only from those trails which lie tangent to one member or another of the family of ellipsoids of revolution which can be drawn about T and R as common foci. In backscatter (radar) work, the ellipsoids reduce to spheres and the analysis of the scattered signals becomes relatively straightforward. The ellipsoidal geometry of the general forward-scatter system is naturally more involved, but it has been incorporated in at

[1]Manuscript received August 19, 1957.
Contribution from the Radio Physics Laboratory of the Defence Research Board, Ottawa. The work was performed under project PCC No. D48-95-11-01.

least one field of theoretical analysis, that concerning the spatial distribution of the effective scattering trails (Eshleman and Manning 1954; Pugh 1956).

A complementary field, concerning the orientational distribution of effective trails, has been developed with the aid of a 'cylindrical approximation' (Hines 1955). With it, when the tangency condition for specularity is being applied, the ellipsoids of revolution are replaced by circular cylinders drawn about the *T–R* line as common axis. The approximation is useful when the transmitter and receiver are widely separated (by several hundred kilometers, say) and it has been applied with profit to the analysis of data obtained during times of meteor shower activity (Forsyth, Hines, and Vogan 1955; Hines and Vogan 1957). This type of analysis has, in fact, demonstrated the value of forward-scatter observations when variations in the intrinsic strength of a shower are sought.

The approximation fails, however, even with long transmission paths, for meteor trails which are nearly parallel to the *T–R* axis. In some cases, all the trails associated with a given shower will fulfill this unfavorable condition during certain periods, and the approximate analysis must then be abandoned.

If the possibilities of the forward-scatter technique are to be realized in full, it will be necessary to apply a more accurate theory which incorporates the inherent ellipsoidal geometry. Such a theory is outlined in the present paper, and its consequences are compared with those of the cylindrical approximation at various stages.

The development will follow a now-familiar form. The 'potentially observable' trails—those that provide a specularly-scattered signal at the receiver—will be located first, and their distribution determined. The fraction of these that are in fact observable—that provide a signal exceeding some counting level—will then be found. Finally, the total number of observable trails will be determined as a function of trail orientation, by integrating over the spatial distribution.

CONDITIONS FOR SPECULAR SCATTERING

A cartesian coordinate system will be employed, with origin at the mid-point of the *T–R* axis. The x axis will lie along *T–R*, the z axis will be directed vertically upwards, and the y coordinate will measure horizontal distance to either side of the *T–R* axis.

Attention is to be confined to trails having some particular orientation, specified by the direction cosines λ, μ, ν. For the moment, it may be confined further to such a trail passing through a particular point, Q, specified by the coordinates x_0, y_0, z_0. The height z_0 will be taken as a standard height, typical of meteor trails, which may be independent of x_0 and y_0 (plane earth) or may vary with them in a prescribed way (spherical earth). A general point P on the trail will have coordinates $x_0+\lambda s$, $y_0+\mu s$, $z_0+\nu s$, where s is the distance from Q to P. If the coordinates of the transmitter are $-D$, 0, 0, then those of the receiver are D, 0, 0, and the total distance $TP+PR$ is given by

$$(1) \qquad p = [(x_0+\lambda s+D)^2+(y_0+\mu s)^2+(z_0+\nu s)^2]^{\frac{1}{2}} + [(x_0+\lambda s-D)^2+(y_0+\mu s)^2+(z_0+\nu s)^2]^{\frac{1}{2}}.$$

This may be expanded as a power series in s, to yield

$$(2) \qquad p = r_T[1+(s/r_T)\cos\tau+(s^2/2r_T^2)\sin^2\tau+\ldots] \\ +r_R[1+(s/r_R)\cos\rho+(s^2/2r_R^2)\sin^2\rho+\ldots]$$

where

$$r_T = [(x_0+D)^2+y_0^2+z_0^2]^{\frac{1}{2}},$$
$$r_R = [(x_0-D)^2+y_0^2+z_0^2]^{\frac{1}{2}},$$
$$\cos\tau = [\lambda(x_0+D)+\mu y_0+\nu z_0]/r_T,$$
$$\cos\rho = [\lambda(x_0-D)+\mu y_0+\nu z_0]/r_R;$$

τ and ρ are the angles formed by the axis of the trail with the directions TQ and RQ respectively, while r_T and r_R are the distances TQ and RQ.

The specular point on the axis of the trail is the point whose total distance from T and R is a minimum, and it may therefore be located by setting $\partial p/\partial s$ equal to zero. If $s \ll r_T, r_R$, it is sufficient to retain in p only those terms which are shown explicitly in (2), when differentiating, and the condition

$$(3) \qquad -s = [\cos\tau+\cos\rho][\sin^2\tau/r_T+\sin^2\rho/r_R]^{-1}$$

is thereby obtained. The condition that the specular point should lie at the z_0 level is obtained by setting $s = 0$ in (3):

$$(4) \qquad \cos\tau+\cos\rho = 0,$$

which implies that τ and ρ are supplementary angles in such circumstances.

Equation (4) defines a relation between x_0 and y_0 which must be satisfied if specular scattering is to occur at the z_0 level. The corresponding curve, drawn in projection on the x, y plane, serves to indicate the regions from which specularly scattered signals may be expected. Different curves will be obtained for different trail orientations. A number of these curves are displayed in Fig. 2,

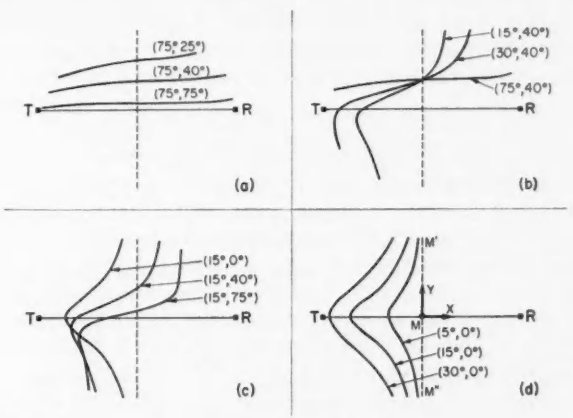

FIG. 2. Plan views of the lines which locate potentially observable trails having various orientations (θ, ψ).

which was drawn for a path length TR of 1000 km. (D = 500 km.), and a meteor height of 100 km. above a spherical earth. The various curves are distinguished by a pair of angular coordinates (θ, ψ) which specify the radiant position corresponding to the orientation λ, μ, ν:

$$\lambda = \cos\theta,$$
$$\mu = -\sin\theta\sin\psi,$$
$$\nu = \sin\theta\cos\psi.$$

Thus, θ measures the angle between the radiant and the T–R axis direction, while ψ measures the angle between the vertical plane through T–R and the inclined plane in which θ is measured. (The angle θ corresponds to the radiant angle β previously employed in the cylindrical development; the change has been made here to avoid an ambiguity that would otherwise arise, involving another angle β which is defined differently.)

The curves displayed in Fig. 2 may be contrasted with those derived from the cylindrical approximation (Part I of this series; Hines 1955). The latter are essentially straight lines, lying parallel to the T–R axis and separated from it by distances depending on ψ alone. The curves in (*a*) are most closely comparable to these straight lines, and it will be noted that they pertain to a relatively large value of θ. The effect of decreasing θ while keeping ψ constant is illustrated in (*b*). The successive distortion of the curve is clearly seen, as is the fact that all curves cross the mid-plane $M'M''$ at a single point. ($M'M''$ is indicated in Fig. 2 (*d*).) The coincidence is not accidental: the ellipsoids and cylinders are tangent at the mid-plane, so the cylindrical approximation is accurate there, and, with that approximation, the location of the curves is independent of θ as already noted. All of the curves obtained in the ellipsoidal development cross the mid-plane at the same points as do the corresponding curves in the cylindrical development.

The further distortion of the curves is illustrated in (*c*) and (*d*), where relatively low values of θ and ψ are considered. The extreme cases displayed in (*d*) illustrate well the need for the present development, since the corresponding curves in the cylindrical theory would lie outside of the antenna coverage possible from T and R.

POTENTIALLY OBSERVABLE TRAILS

Equation (4) provides the condition for specular scattering at the z_0 level only, whereas the trails themselves extend over a finite range of heights. Accordingly, (4) may be violated to some extent without loss of the specular process. The extent to which this is possible varies along the curve defined by (4), and from one curve to another, and it provides a weighting function which gives the distribution of potentially observable trails. In determining the function, it will be assumed that the length of a trail is proportional to ν^{-1}, that is, to the secant of the zenith angle of the radiant (neglecting earth curvature). This implies that all trails extend over the same range of height, and it corresponds to the theoretical conclusion (Herlofson 1947) that the variation of ionization with height is independent of the orientation of the trail. The

height variation could itself be taken into account by an appropriate integration, but its effect on the present problem is not sufficient to warrant such a detailed treatment.

The fact that (4) may be violated implies that the curves in Fig. 2 may be broadened into ribbons, while still representing the regions of the z_0 level through which the trails must pass if they are to provide specularly-scattered signals at R. Such ribbons have already been depicted, in another context, by Villard *et al.* (1956). Elementary considerations show that the width of the ribbon, w, will equal the length of the trails divided by the horizontal gradient of s, the latter being determined from (3) at the $s = 0$ curve. (This assumes that the trails are short compared with other relevant distances, and it neglects earth curvature.) The occurrence rate of potentially observable meteors which may be associated with an element of length $d\sigma$ along the $s = 0$ curve is proportional to $\nu w d\sigma$, with the factor of proportionality being dependent only on the incidence rate of meteors from the radiant direction concerned. The factor ν is a projection factor required because the ribbon does not lie perpendicular to the line of flight of the meteors, and it cancels the factor ν^{-1} implicit in w. Accordingly, the occurrence rate of potentially observable trails is proportional to

$$W_\sigma\, d\sigma = d\sigma / |\text{horiz. grad. } s|_{s=0}$$

$$= \frac{r_T^{-1} r_R^{-1} (r_T + r_R) \sin^2\tau \, d\sigma}{[(\partial\chi/\partial x_0)^2 + (\partial\chi/\partial y_0)^2]^{\frac{1}{2}}_{s=0}}, \tag{5}$$

where $\chi = \cos\tau + \cos\rho$. Although the derivatives appearing in (5) may be determined explicitly, it has been found more convenient in practice to employ a graphical method. By computing $\cos\tau$ and $\cos\rho$ as functions of x_0 for various y_0's, and as functions of y_0 for various x_0's, the curve $s = 0$ is readily defined and the derivatives of χ are readily evaluated. With this technique, it is also convenient to replace the differential (5) by

$$W_x\, dx = r_T^{-1} r_R^{-1} (r_T + r_R) \sin^2\tau |\partial\chi/\partial y_0|^{-1} dx \tag{6}$$

or

$$W_y\, dy = r_T^{-1} r_R^{-1} (r_T + r_R) \sin^2\tau |\partial\chi/\partial x_0|^{-1} dy, \tag{7}$$

and to compute the subsequent integrations as summations which involve equal increments in x or y, rather than equal intervals along the $s = 0$ curve.

OBSERVABLE TRAILS

The amplitude of the signal received from a meteor trail, after specular scattering, has the functional form

$$A \propto q G_1^{\frac{1}{2}} G_2^{\frac{1}{2}} |\sin\alpha| [r_1 r_2 (r_1 + r_2)(1 - \cos^2\beta \sin^2\phi)]^{-\frac{1}{2}} \tag{8}$$

(Eshleman and Manning 1954), where q is the line density of ionization in the trail, G_1 and G_2 are the antenna gains in the directions TP and RP respectively, r_1 and r_2 are the corresponding distances, α is the angle between the (linearly polarized) electric vector in the incident wave and the direction PR, β is the

angle between the axis of the trail and the plane TPR, and 2ϕ is the angle TPR. Although (8) applies only to the so-called 'underdense' trails, its use in the present work can be justified for any circuit whose sensitivity is sufficiently great.

Meteor trails which provide received signals exceeding some counting level, specified by an amplitude A_c, will be termed 'observable'. It is assumed that a trail must be potentially observable—in the sense already described—if it is to be observable, and even then it must have an ionization density which exceeds

$$q_c \propto A_c G_T^{-\frac{1}{2}} G_R^{-\frac{1}{2}} |\operatorname{cosec} \alpha| [r_T r_R (r_T + r_R)(1 - \cos^2\beta \sin^2\phi)]^{\frac{1}{2}} \tag{9}$$

as implied by (8). Here, the subscripts 1 and 2 have been replaced by T and R, to indicate that (9) may be evaluated along the $s = 0$ curve without appreciable loss of accuracy.

Following Herlofson (1947), it will be assumed that q is proportional to the mass, m, of the parent meteoric particle, and to the cosine of the zenith angle of the radiant point: $q \propto mv$. Following Watson (1956), it will be assumed that the number of meteors, N, which have masses greater than a given mass, m, is inversely proportional to that mass: $N \propto m^{-1}$. These assumptions combine with (9) to imply that the fraction of potentially observable trails which are in fact observable is proportional to

$$N_c \propto m_c^{-1} \propto v q_c^{-1} \propto v A_c^{-1} G_T^{\frac{1}{2}} G_R^{\frac{1}{2}} |\sin \alpha| [r_T r_R (r_T + r_R)(1 - \cos^2\beta \sin^2\phi)]^{-\frac{1}{2}}. \tag{10}$$

The distribution of observable trails along the $s = 0$ curve is then proportional to $W_\sigma N_c$, and the total number of observable trails is proportional to $\int W_\sigma N_c \, d\sigma$. The factor of proportionality depends on the incidence rate of meteors from the radiant concerned in the integral. The integral itself, after normalization if desired, is termed the 'observability function' for the radiant direction θ, ψ.

The $|\sin \alpha|$ factor in (8) applies only if the receiving antenna is capable of accepting all polarizations equally well. If, instead, the receiving antenna accepts only a particular linearly polarized component, then the $|\sin \alpha|$ factor should be replaced by $|\cos \gamma|$, where γ is the angle between the polarization vector of the wave incident on the trail and the polarization vector accepted by the receiving antenna. In particular, if the transmitting antenna radiates, and the receiving antenna accepts, only a horizontally polarized component, then

$$|\cos \gamma| = \frac{|y_0^2(1 - \tan^2 A) + x_0^2 - (D + z_0 \tan A)^2|}{(y_0^2 \sec^2 A + [D + x_0 + z_0 \tan A]^2)^{\frac{1}{2}} (y_0^2 \sec^2 A + [D - x_0 + z_0 \tan A]^2)^{\frac{1}{2}}} \tag{11}$$

as given by Pugh (1956); A is half of the angle subtended by the T–R axis at the earth's center, and $A = 0$ in the plane-earth approximation. Equations (9) and (10) must be modified in similar fashion, with (11) replacing the $|\sin \alpha|$ factor in (10) and hence in the observability function. The other relations required for the evaluation of (10) are

$$\sin^2\beta = \sin^2\theta (y_0 \cos \psi + z_0 \sin \psi)^2 (y_0^2 + z_0^2)^{-1}$$

and

$$\sin 2\phi = 2D(y_0^2 + z_0^2)^{\frac{1}{2}} r_T^{-1} r_R^{-1},$$

both of which may be established by simple operations involving the vectors TQ, RQ, and QP. (It may be noted that $\beta = \theta$ when $x_0 = 0 = s$, for the cylindrical approximation leads directly to the relation $z_0 = y_0 \tan \psi$.) Finally, the antenna gains G_T and G_R must be calculated as functions of x_0 and y_0 at the z_0 level, for the particular antenna systems employed.

THE OBSERVABILITY FUNCTION

The observability function has been computed, in the manner described, for a 1000 km. path using broad-beamed antennas. The formula employed for antenna gain was

$$(12) \qquad G^{\frac{1}{2}} \propto \sin[(2\pi h/\lambda)\sin e] \frac{\sin[(\pi a/\lambda)\sin e]}{\sin e} \frac{\sin[(\pi b/\lambda)\cos e \sin d]}{\cos e \sin d},$$

where e measures elevation above the local horizontal plane and d measures azimuth from the great-circle path joining T and R. This is the Fraunhofer form appropriate to an effective aperture of vertical dimension a and horizontal dimension b, radiating at wavelength λ, and situated at a height h above a perfectly conducting ground. The antennas contemplated were five-element horizontal Yagis, with vertical beam width (between half-power points) of 64° and horizontal beam width of 50°, corresponding to $a = 0.84\lambda$ and $b = 1.05\lambda$. An antenna height $h = 1.6\lambda$ was adopted, to provide maximum illumination at the 100 km. level (above a spherical earth) over the mid-point of the T–R axis. The resultant amplitude gain pattern of one antenna is indicated on the left-hand side of Fig. 3 (after normalization), and the total gain function

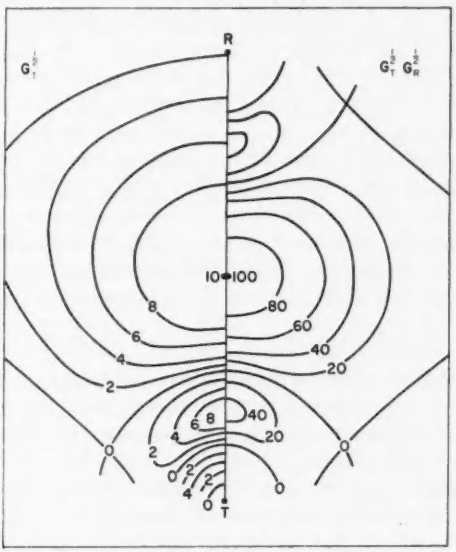

FIG. 3. Contour charts of the transmitting antenna amplitude gain, $G_T^{\frac{1}{2}}$, and of the combined gain factor, $G_T^{\frac{1}{2}} G_R^{\frac{1}{2}}$, in plan at the 100 km. level.

$G_T^{\frac{1}{2}} G_R^{\frac{1}{2}}$ required for the observability function is indicated on the right-hand side; the contours refer to the 100 km. level, but they are shown in projection on the x, y plane.

The observability function derived in this way is displayed by means of a contour chart on the right-hand side of Fig. 4. It is treated as a function of θ and ψ, the former being measured radially outwards from the point O, and the latter being measured as an angle from the vertical line OZ. The chart may be

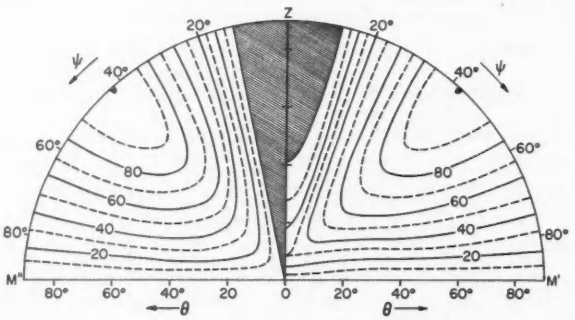

FIG. 4. Observability contours deduced from the cylindrical approximation (left-hand side) and from the present ellipsoidal theory (right-hand side). The observability is shown as a function of trail orientation (θ, ψ), and it is normalized to a maximum value of 100 in each case.

interpreted readily as a map on the celestial hemisphere, seen from the mid-point of the T–R axis: the point O is the point where this axis intersects the horizon, OM' is one quarter of the horizon, and Z is the zenith point. Other quadrants of the celestial hemisphere can be obtained by symmetry, and the observability function at any point on the chart applies to meteors which have the corresponding radiant point on the celestial hemisphere.

The contours displayed on the left-hand side of Fig. 4 are those derived by means of the cylindrical approximation. (They differ from a set given in Part I of this series because of the difference in the antenna patterns employed; the earlier analysis ignored secondary lobes.) It will be seen that the cylindrical approximation leads to valid results when θ is large, but it fails seriously when θ decreases to 40° or less, particularly if ψ also is small.

OBSERVABILITY OF METEOR SHOWERS

The observability function is most readily interpreted in connection with meteor showers. The meteors of a given shower tend to come from a well-defined region—approximating to a point radiant—on the celestial sphere. The radiant circles the celestial pole in the course of a day, and so sweeps periodically through a succession of observability values. The particular path traced on the observability contour chart depends not only on the celestial coordinates of the radiant, but also on the geographic location and orientation of the forward-scatter circuit (as discussed in Part I of this series). The variation in the observability factor throughout the day provides the expected diur-

nal variation in the rate of detection of meteors belonging to the shower, provided that the intrinsic incidence rate of the shower meteors remains constant. Deviations from the expected rate, other than those due to statistical fluctuations, would then be attributed to changes in the intrinsic strength of the shower. It is the application of this type of analysis which has led to the advance in shower studies mentioned previously (Hines and Vogan 1957), and which may be expected to provide even further advantage with the use of the more accurate observability contours.

The variations expected in the detection rate of shower meteors are illustrated in Fig. 5, for an east–west path and a north–south path, each having its mid-point at 45° north latitude. Curves derived from the ellipsoidal theory are

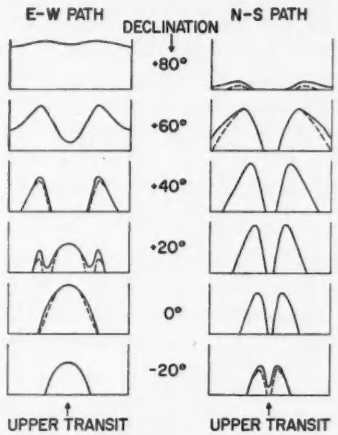

FIG. 5. Diurnal variations in observability (plotted vertically) for meteor showers having various declinations, as determined for an East–West path and for a North–South path, each with mid-point at 45° north latitude. The abscissa measures time over a 24 hour period, centered at the time of upper transit of the shower.

drawn in full, while those derived from the cylindrical theory are dotted in when they differ appreciably from the others. The dotted curves are analogous to a set of curves presented elsewhere (Hines 1956) for a particular pair of paths, except that the geographic location and orientation are somewhat different, and the more refined antenna pattern (12) is now employed.

The theory can be applied to the sporadic meteors which arrive from all directions, if their incidence pattern is assumed. The calculation involves a weighted integration of the observability function over the whole of the celestial hemisphere, and a diurnal variation in the weighting factor. Variations in the detection rate of sporadic meteors have been predicted (Hines 1956), on the basis of a specific assumed incidence pattern, and these require some modification in view of the revision in the observability function. No major change in their general form is expected, however. Qualitative arguments suggest that the ratio of maximum rate to minimum rate will decrease, and that, on a north–

south path, a shallow depression (secondary minimum) might develop in the center of the maximum. In view of the uncertainties in the incidence pattern, it is doubtful whether a quantitative re-evaluation of the diurnal variation would serve any useful purpose at this time, and none will be undertaken here.

REFERENCES

ESHLEMAN, V. R. and MANNING, L. A. 1954. Proc. Inst. Radio Engrs. **42**, 530.
FORSYTH, P. A., HINES, C. O., and VOGAN, E. L. 1955. Can. J. Phys. **33**, 600.
HERLOFSON, N. 1947. Repts. Progr. in Phys. **11**, 444.
HINES, C. O. 1955. Can. J. Phys. **33**, 493.
——— 1956. J. Atmospheric and Terrest. Phys. **9**, 229.
HINES, C. O. and VOGAN, E. L. 1957. Can. J. Phys. **35**, 703.
PUGH, R. E. 1956. Can. J. Phys. **34**, 997.
VILLARD, O. G., PETERSON, A. M., MANNING, L. A., AND ESHLEMAN, V. R. 1956. J. Geophys. Research, **61**, 233.
WATSON, F. G. 1956. Between the planets (Harvard Univ. Press, Cambridge, Mass.).

AN EXPERIMENTAL STUDY OF THE BAND INTENSITIES IN THE CN RED SYSTEM[1]

R. N. DIXON[2] AND R. W. NICHOLLS

ABSTRACT

Experimental band intensities in the CN red system, $A(^2\Pi_i) \rightarrow X(^2\Sigma^+)$, have been measured using an active nitrogen – carbon tetrachloride source. Using calculated Franck–Condon factors $q_{v'v''}$ the electronic transition moment $R_e(r)$ is found to vary little over the range $1.04 < r < 1.27$ Å.

INTRODUCTION

The red system, $A(^2\Pi_i) \rightarrow X(^2\Sigma^+)$, of the CN radical is excited in a variety of laboratory sources and is also present in the spectra of comets and carbon stars. Consequently it would be useful to have available an array of vibrational transition probabilities for this system in order that the excitation conditions in these sources may be inferred. Experimentally determined intensities and calculated Franck-Condon factors have been used to derive such an array.

The integrated intensity in emission of the vibration bands in an electronic transition can be expressed by the well-known equation:

$$I_{v'v''} = kN_{v'}\nu^4_{v'v''}p_{v'v''}, \tag{1}$$

where k is a constant depending on the geometry and the units employed, $N_{v'}$ is the population of the upper vibrational level of the transition, $\nu_{v'v''}$ is the transition frequency, and $p_{v'v''}$ is the relative vibrational transition probability of the band. $p_{v'v''}$ can be expressed as

$$p_{v'v''} = |\int \psi_{v'} R_e(r) \psi_{v''} dr|^2 \tag{2}$$

(Herzberg 1950, p. 200), where $R_e(r)$ is the electronic transition moment. Fraser (1954) has shown the conditions under which it is possible to write

$$p_{v'v''} = R_e^2(\bar{r}_{v'v''})q_{v'v''}. \tag{3}$$

$q_{v'v''}$ is the square of the overlap integral of the two vibrational wave functions, $|\int \psi_{v'}\psi_{v''}dr|^2$, (Franck–Condon factor); $R_e(\bar{r}_{v'v''})$ is the electronic transition moment for the transition, and is a function of internuclear distance; $\bar{r}_{v'v''}$ is the r-centroid of the transition, which takes a unique value of internuclear separation for each band of the system. Both $q_{v'v''}$ and $\bar{r}_{v'v''}$ can be calculated if the forms of the potential curves of the upper and lower electronic states are assumed.

From a study of the band intensities in the CN red system it has been possible to determine the variation of $R_e(r)$ with r.

EXPERIMENTAL

A Perkin Elmer Model 12-C spectrometer equipped with glass optics and a

[1]Manuscript received September 26, 1957.
Contribution from the Department of Physics, University of Western Ontario, London, Ontario.

[2]Now National Research Laboratories Postdoctorate Fellow, Ottawa, Ontario.

lead sulphide cell was available for measurements in the region of the CN red system, 0.5–2.0 μ. With this instrument accurate intensity measurements require a source of high intensity in order that the relatively low sensitivity of the spectrometer does not put great limitations on the accuracy of the results. This condition is satisfied for the CN red system both by the carbon arc in air, and also by a discharge through nitrogen containing an organic vapor, but in both of these cases the rotational temperatures are so high that the closely spaced vibrational bands overlap badly. However, the system is also emitted, with lower intensity, when an organic vapor, and especially carbon tetrachloride, is introduced into a stream of active nitrogen (Jenkins, Roots, and Mulliken 1932). This source has a low rotational temperature and thus the rotational structures of adjacent bands do not overlap. It was found that by suitable design of such a source the CN red system was radiated sufficiently strongly for the measurement of the integrated band intensities with the Perkin Elmer spectrometer.

The active nitrogen was excited by three 15 kv. 450 va. condensed sparks in an apparatus based on that described by Benson (1951) using prepurified nitrogen supplied by the Mattheson Co., New Jersey. With normal commercial nitrogen the presence of impurities made the excitation very weak. The stream of active nitrogen flowed through a side-arm into a reaction tube 1.2 cm. in internal diameter and 70 cm. long, in which a 50 liter/minute rotary vacuum pump maintained the pressure at about 8 mm. Hg. Carbon tetrachloride vapor was introduced into this stream at the point where it entered the reaction tube. An orange "flame", extending about 30 cm. down the reaction tube, was viewed through a quartz window sealed on one end, the flame being focused on the spectrometer slit by a glass lens. Apiezon W wax sealed all joints in the glassware, which became too hot for greases, even with fan cooling. A 4 liter ballast tank inserted between the reaction tube and the pump served to stabilize the pressure, and the source intensity remained constant during the experiment. Unfortunately electrical noise from the excitation sparks interfered with the spectrometer amplifier, despite screening. This reduced the accuracy of the measurements below that hoped for, as estimated from a comparison of two sets of recordings.

A Phillips standard tungsten lamp was used for the intensity calibration of the spectrometer, in conjunction with the tungsten emissivity curves of De Vos (1954) and the black body emission tables of Lowan and Blanch (1940), care being taken to use the spectrometer within the range of linear response. A photographic survey to 0.95 μ with a Hilger constant deviation spectrograph determined which bands were clear from overlapping and thus suitable for intensity measurements.

RESULTS

A rapid scan of the spectrum with the Perkin Elmer spectrometer is given in Fig. 1. Table I gives the values of $I_{v'v''}/\nu^4_{v'v''}$ obtained for 28 bands in the sequences $\Delta v = 6, 5, 4, 3, 2, 1, 0, -1$, from the mean integrated band areas measured with a planimeter from two sets of recordings. The published table

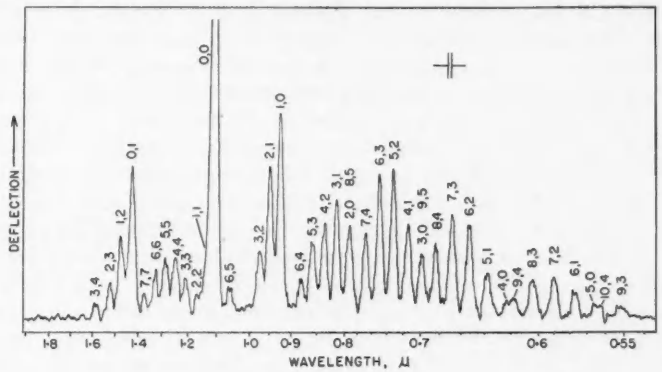

FIG. 1. The CN red system.

TABLE I

THE EXPERIMENTAL VALUES OF $I_{v'v''}/\nu^4_{v'v''}$ COMPARED WITH THE CALCULATED VALUES OF $q_{v'v''}$ FOR THE CN RED SYSTEM*

v' \ v''	0	1	2	3	4	5	6	7	8	9
	—	1.72	—	—	—	—				
0	1.000	0.742	0.223	0.035	0.0032	0.0002				
	1.204	1.254	1.310	1.374	1.449	1.540				
	0.798	—	0.936	—	—	—	—			
1	0.643	0.092	0.698	0.446	0.110	0.014	0.0010			
	1.166	1.210	1.260	1.317	1.380	1.455	1.546			
	—	0.535	—	0.512	—	—	—	—	—	
2	0.252	0.484	0.024	0.418	0.574	0.213	0.035	0.0030	0.0002	
	1.130	1.171	1.216	1.266	1.322	1.386	1.461	1.553	1.669	
	—	0.395	0.265	0.286	—	—	—	—	—	—
3	0.079	0.391	0.200	0.181	0.165	0.589	0.323	0.069	0.0072	0.0004
	1.098	1.136	1.177	1.222	1.272	1.328	1.392	1.468	1.560	1.677
	—	0.249	0.425	—	0.397	—	—	—	—	—
4	0.022	0.189	0.368	0.031	0.301	0.025	0.514	0.422	0.116	0.014
	1.068	1.104	1.142	1.183	1.228	1.278	1.335	1.399	1.475	1.566
	—	0.115	0.403	0.365	—	0.572	—	—	—	—
5	0.0058	0.072	0.269	0.249	0.0042	0.317	0.0036	0.387	0.494	0.174
	1.041	1.074	1.110	1.148	1.189	1.235	1.285	1.341	1.405	1.481
	—	0.049	0.242	0.497	0.256	0.154	0.484	—	—	—
6	0.0014	0.024	0.135	0.287	0.118	0.064	0.251	0.058	0.248	0.531
	1.016	1.046	1.081	1.116	1.154	1.195	1.241	1.291	1.347	1.411
	—	—	0.086	0.299	0.366	—	—	0.243	—	—
7	0.0004	0.0072	0.055	0.191	0.247	0.029	0.145	0.152	0.141	0.127
	0.992	1.022	1.052	1.087	1.122	1.161	1.201	1.247	1.298	1.354
	—	—	—	0.102	0.225	—	—	—	—	—
8	0.0001	0.0021	0.020	0.097	0.221	0.171	0.0000	0.201	0.063	0.214
	0.970	0.998	1.028	1.058	1.093	1.128	1.167	1.208	1.254	1.304
		—	—	0.018	—	—	—	—	—	—
9		0.0006	0.0068	0.042	0.138	0.218	0.091	0.021	0.212	0.010
		0.976	1.005	1.033	1.065	1.099	1.135	1.173	1.214	1.260

*The three entries for each value of v' and v'' are $I_{v'v''}/\nu^4_{v'v''}$ (in arbitrary units), $q_{v'v''}$ (calculated), and $\bar{r}_{v'v''}$ (calculated).

of Franck–Condon factors for the CN red system (Fraser, Jarmain, and Nicholls 1954) has been extended by Fraser (1957) to a 9×9 array, using the FERUT computer of the University of Toronto, assuming Morse potential functions and the constants quoted by Herzberg (1950, p. 520). The values agree substantially with those calculated by Wyller (1957) using the WKB method, and are included in Table I together with r-centroids calculated by a method given by Nicholls and Jarmain (1956). From these data experimental values of $[I_{v'v''}/\nu^4_{v'v''}.q_{v'v''}]$, which is proportional to $[N_{v'}^{\frac{1}{2}}.R_e(\bar{r}_{v'v''})]$, were derived in arbitrary units. The arrays for each v' progression were scaled to allow for the differing vibrational population factors (plotted in Fig. 4 normalized to $N_{0'} = 1.00$) by the method of Turner and Nicholls (1954). The values of $R_e(r)$ thus obtained are plotted as a function of internuclear distance in Fig. 2. The scatter of the points is such that it was thought best to represent the "smoothed" variation of $R_e(r)$ with r by the least squares straight line through them. Weighting the points according to their accuracy this line is:

$$R_e(r) = 1.044+0.174\,r, \qquad 1.04<r<1.27\text{ Å}, \tag{4}$$

in arbitrary units. Thus the electronic transition moment for this system is essentially constant over the important range of r, which implies that in this case $q_{v'v''}$ is a good measure of $p_{v'v''}$.

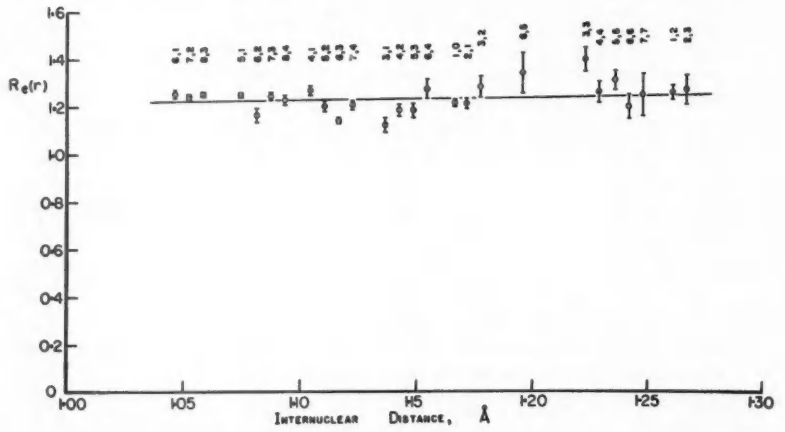

FIG. 2. The variation of the electronic transition moment (in arbitrary units) for the CN red system.

Using equations (3) and (4) an array of "smoothed" relative vibrational transitional probabilities $p_{v'v''}$ was calculated for those bands for which the r-centroid lay between 1.01 and 1.30 Å. For the bands with $r < 1.04$ or >1.27 Å these values are only indications of the trend, and are bracketed in Table II, which gives the array normalized to $p_{0,0} = 1.000$.

TABLE II

"SMOOTHED" RELATIVE VIBRATIONAL TRANSITION PROBABILITIES

$p_{v'v''} = q_{v'v''}.R_e^2(\bar{r}_{v'v''})$ FOR THE CN RED SYSTEM*

v' \ v''	0	1	2	3	4	5	6	7	8	9
0	1.000	0.752								
1	0.636	0.092	0.710							
2	0.247	0.480	0.024	0.425						
3	0.770	0.384	0.199	0.182	(0.167)					
4	0.021	0.184	0.361	0.031	0.303	(0.026)				
5	0.0055	0.069	0.262	0.246	0.0042	0.320	(0.0037)			
6	(0.0013)	0.023	0.130	0.280	0.117	0.064	0.254	(0.059)		
7		(0.0068)	0.053	0.185	0.241	0.029	0.145	0.153	(0.144)	
8			(0.019)	0.094	0.215	0.168	0.0000	0.201	0.064	(0.220)
9				(0.040)	0.133	0.211	0.089	0.021	0.212	0.011

*A value in parentheses indicates a trend.

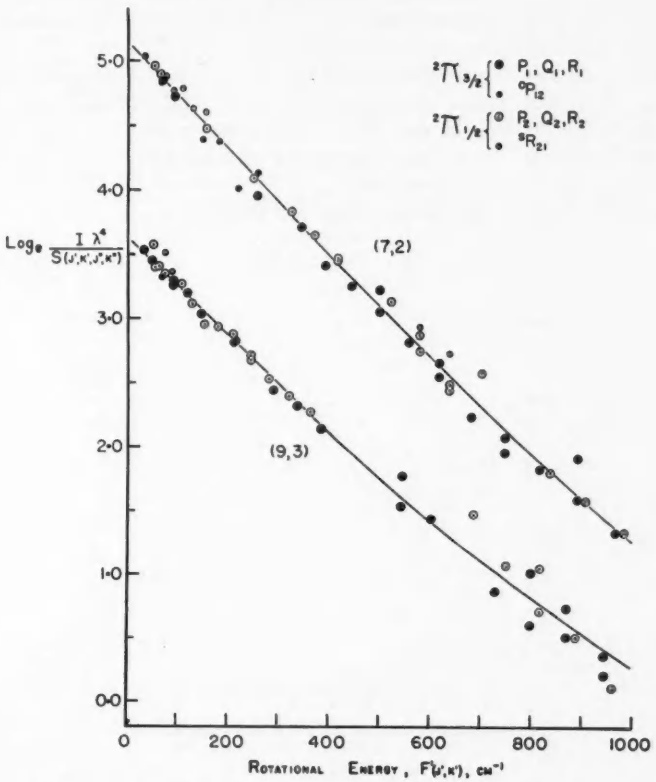

FIG. 3. Rotational distribution plot for the (7, 2) and (9, 3) CN red bands.

THE ROTATIONAL AND VIBRATIONAL DISTRIBUTIONS

When there is thermal equilibrium in the upper vibration levels of a band system a suitable plot of the line intensities in each band against the rotational energy of the upper levels for that band gives a straight line; these lines have the same slope, which is inversely proportional to the rotational temperature (Herzberg 1950, p. 205). The fine structure of the (7, 2) and (9, 3) CN red bands was recorded with a Leeds and Northrup photoelectric grating spectrometer, together with intensity calibrations. Fig. 3 gives this plot for the (7, 2) and (9, 3) bands, using the line frequencies measured by Jenkins, Roots, and Mulliken (1932) and strength factors $S(J', K', J'', K'')$ calculated according to the equations of Earls (1935). Self-absorption is not important with this source, as it has a low rotational temperature, and the flame extends right up to the quartz window of the reaction tube. Although the points lie close to straight lines for low rotational energy there is a significantly greater intensity of the lines with high rotational quantum number than would be consistent with the "effective temperatures" of 345° K. for $v' = 7$ and 375° K. for $v' = 9$ obtained from the straight line portions of the plots.

Fig. 4 shows the vibrational distribution in the CN ($A^2\Pi_i$) state deduced from the scaling factors (which are proportional to $N_{v'}{}^{\frac{1}{4}}$) discussed above. It will be observed that the separation between the two maxima of Fig. 4 is 1.282 ev., which is very close to the energy separation between the ^2P and ^2D levels of atomic nitrogen (1.192 ev.).

It is therefore tempting to speculate that the reaction

$$CCl_4 + N^* \rightarrow CN^* + 2Cl_2, \tag{5}$$

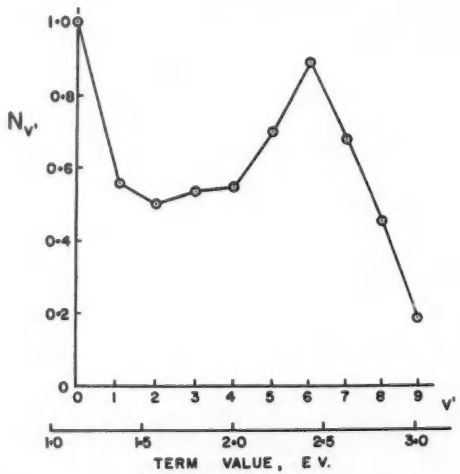

FIG. 4. The relative populations of the vibration levels in the CN $A(^2\Pi_i)$ state.

which is energetically consistent with our observations, may play some part in producing the luminosity. However, in view of the known complexity of reactions involving active nitrogen, a complete discussion of possible and probable luminosity producing reactions must await more experimental work, which is in progress.

ACKNOWLEDGMENTS

The authors wish to express their sincere thanks to Dr. P. A. Fraser for many helpful discussions on this work, and to Mr. R. P. McEachran for calculating the r-centroids. The research reported in this paper was sponsored by the Defence Research Board of Canada through Grant DRBC 5001-15, the Air Force Cambridge Research Centre through Contract AF:19(604)-1718, and a research grant from the Imperial Oil Co. of Canada Ltd.

REFERENCES

BENSON, J. M. 1951. Natl. Advisory Comm. for Aeronautics, Washington, Tech. Note 2293.
DE VOS, J. C. 1954. Physica, **20**, 690.
EARLS, L. T. 1935. Phys. Rev. **48**, 423.
FRASER, P. A. 1954. Can. J. Phys. **32**, 515.
——— 1957. Private communication.
FRASER, P. A., JARMAIN, W. R., and NICHOLLS, R. W. 1954. Astrophys. J. **119**, 286.
HERZBERG, G. 1950. Spectra of diatomic molecules, 2nd ed. (D. Van Nostrand Co., Inc., New York).
JENKINS, F. A., ROOTS, Y. K., and MULLIKEN, R. S. 1932. Phys. Rev. **39**, 16.
LOWAN, A. N. and BLANCH, G. 1940. J. Opt. Soc. Am. **30**, 70.
NICHOLLS, R. W. and JARMAIN, W. R. 1956. Proc. Phys. Soc. A, **69**, 253.
TURNER, R. G. and NICHOLLS, R. W. 1954. Can. J. Phys. **32**, 475.
WYLLER, A. 1957. Private communication.

NOTES

RESONANCE EFFECTS IN THE THEORY OF METEOR OBSERVABILITY*

D. R. Moorcroft and C. O. Hines

The theory of forward-scattering of radio waves from meteor trails, initiated by Eshleman and Manning (1954), has been applied to determine the "observability" of meteor showers as a function of radiant position (Hines 1955). This theory showed qualitative agreement with preliminary data obtained for four showers (Forsyth, Hines, and Vogan 1955), and more recently has led to a quantitative analysis of the 1956 Quadrantid shower (Hines and Vogan 1957). The latter comparison revealed the forward-scattering technique as a valuable tool for the study of meteor showers. The further development of this technique will require some improvement on the approximations implicit in the original observability theory. Resonance effects in the scattering process, which were ignored in the original developments, provide one possible source of error, and they are considered briefly here.

The resonance in question occurs only when there is a component of the incident electric vector transverse to the axis of the meteor trail, and it results in an enhancement of the corresponding component of the scattered field (Herlofson 1951; Feinstein 1951). The degree of enhancement varies with the electron density in the trail: an increase by a factor of two has been predicted, in the case of backscatter, when the density is 10^{10} electrons/cm. or less, but the factor diminishes as the density increases, and eventually reaches unity for densities of 10^{12} electrons/cm. and more (Kaiser and Closs 1952). Experimental results (Billam and Browne 1956) confirm this tendency, though they suggest that somewhat greater enhancements may arise in practice.

No similar investigations are available for the general case of forward-scattering, but there appears to be no reason to expect any marked change in the behavior. A reformulation of the observability theory, which included the dependence of the resonance effect on electron density, would yield theoretical predictions dependent in a very complicated way on the sensitivity of the observing system. This was avoided in the preliminary analysis by considering the limiting case of an extremely sensitive system. For this case, an enhancement factor of two will be applicable to the vast majority (in effect, to all) of the detected meteor trails. The phase of the resonant scattered component, relative to that of the non-resonant component, varies through 180° in the course of resonance (Kaiser 1955), which makes possible an effective reduction in the resonant signal due to interference between the two components. This complication was ignored, and only the maximum possible increase (phase shift = 0° between the two components) was considered.

*The work was performed under project PCC No. D48–95–11–01.

The analysis followed exactly as in the earlier work, except that the incident electric vector was separated into longitudinal and transverse components relative to the axis of the trail; the transverse component was doubled and recombined with the longitudinal component to produce an effective incident electric vector. A polarization factor, $\cos \gamma'$, appropriate to this vector, was then inserted in the theory to replace the $\cos \gamma$ factor which originally appeared. All other aspects of the theoretical development remained unchanged.

The observability contours which result from the revised theory are displayed by solid lines in Fig. 1; superimposed are contours drawn in broken lines to represent the original theory. In each case, normalization to a maximum value of 100 has been introduced. The contours provide estimates of the

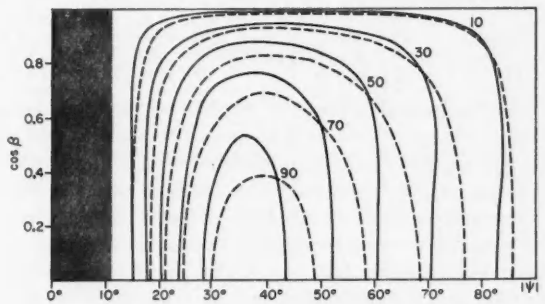

FIG. 1. Normalized contours of meteor observability as a function of trail orientation. The present investigation (solid lines) is compared with the original theory (broken curves).

relative number of forward-scattered meteor signals expected to exceed some arbitrary counting level in unit time interval, as a function of the position of the shower radiant. The radiant position is defined by the angle β between the radiant direction and the direction of the transmitter–receiver axis, and by the angle ψ between the vertical plane through this axis and the inclined plane in which β is measured. The effect of resonance on signal strength is greatest at small β's and small ψ's, and decreases to zero at $\beta = \psi = 90°$. This effect is, of course, modified by renormalization in the contour chart.

The new set of contours and the old have been applied separately to data which were obtained during the 1957 Quadrantids, and which will be discussed in detail separately. Neither set showed any marked superiority in the interpretation of these data, but there was some indication that better empirical observability contours might be constructed by averaging the new and the old. Some justification of this procedure can be advanced on the grounds that the observing equipment is not sufficiently sensitive to validate the full factor of two in the resonance. Further comparisons with experimental data will be required, however, before any certain conclusion can be drawn.

BILLAM, E. R. and BROWNE, I. C. 1956. Proc. Phys. Soc. B, **69**, 98.
ESHLEMAN, V. R. and MANNING, L. A. 1954. Proc. Inst. Radio Engrs. **42**, 530.
FEINSTEIN, J. 1951. J. Geophys. Research, **56**, 37.

FORSYTH, P. A., HINES, C. O., and VOGAN, E. L. 1955. Can. J. Phys. **33**, 600.
HERLOFSON, N. 1951. Arkiv Fysik, **3**, 247.
HINES, C. O. 1955. Can. J. Phys. **33**, 493.
HINES, C. O. and VOGAN, E. L. 1957. Can. J. Phys. **35**, 703.
KAISER, T. R. 1955. Meteors, Spec. Suppl. J. Atmospheric and Terrest. Phys. (Pergamon Press, Ltd., London).
KAISER, T. R. and CLOSS, R. L. 1952. Phil. Mag. **43**, 1.

RECEIVED AUGUST 19, 1957.
RADIO PHYSICS LABORATORY,
DEFENCE RESEARCH BOARD,
OTTAWA, CANADA.

MEASUREMENT OF ARTIFICIAL RADIOACTIVITY IN THE ATMOSPHERE AT OTTAWA, CANADA*

F. TERENTIUK

Investigation of the natural radioactivity in the atmosphere has been carried on for many years, and in the last decade there has been considerable interest in the artificial radioactivity in the atmosphere originating from atomic and thermonuclear explosions. A bibliography on both natural and artificial radioactivity in the atmosphere has recently been prepared by Thuronyi (1956).

For the past year daily measurements of the artificial radioactivity in the atmosphere have been carried out at Ottawa. Samples of air were drawn through a dust filter and the gross beta activity from the filter measured with an end-window Geiger counter. A high-volume air sampler was used to draw air through type B.M. 2133 filter paper 4 inches in diameter. The sampler was located in such a way as to prevent snow or rain from reaching the filter. Sampling was initially carried out for a 5-hour period daily, but for the past 3 months it has been extended to a 23-hour period. The sampling times correspond to air volumes of 425 cubic meters and 2000 cubic meters respectively. The flow rate was checked at the beginning and end of each sampling period and an average taken. The flow rate was generally constant to $\pm 10\%$.

The filters were kept for a period of 3 days before measurements were made in order to permit the natural activity resulting from daughter products of radon and thoron to decay to a negligible value. Measurements of the gross beta activity from the filter were made directly with an end-window Geiger tube having a mica window thickness of 2.0 mg./cm.^{2} Active filters gave counting rates several times the background. The daily counting rates above background obtained from the filters, on the basis of a 5-hour collection period, are plotted in Fig. 1 for the period 21 May, 1956, to 21 May, 1957. In addition, the times at which nuclear explosions were reported to have occurred are indicated along the top of Fig. 1. Table I gives the reported dates of nuclear explosions, the country responsible for the explosion, and the country reporting the explosion. These announcements were obtained from local newspapers and

*Issued as N.R.C. No. 4549.

publications such as Atomic Energy Newsletter and have no official confirmation. They are indicated in Fig. 1 only to give an idea of the relation between the nuclear explosions and observed atmospheric activity.

TABLE I

REPORTED NUCLEAR EXPLOSIONS

Number	Date	Exploded by	Reported by
1	24 August, 1956	U.S.S.R.	U.S.A.
2	30 August, 1956	U.S.S.R.	U.S.A.
3	3 September, 1956	U.S.S.R.	U.S.S.R.
4	9 September, 1956	U.S.S.R.	U.S.S.R.
5	October	U.S.A.	U.S.A.
6	17 November, 1956	U.S.S.R.	U.S.A.
7	19 January, 1957	U.S.S.R.	U.S.A.
8	8 March, 1957	U.S.S.R.	Japan
9	3 April, 1957	U.S.S.R.	U.K.
10	6 April, 1957	U.S.S.R.	U.S.S.R.
11	10 April, 1957	U.S.S.R.	U.S.S.R.
12	23 April, 1957	U.S.S.R.	U.S.A.

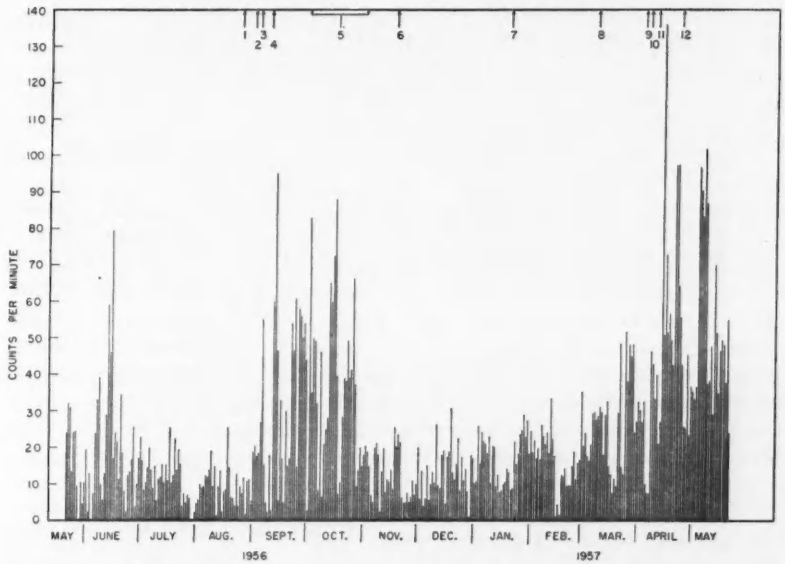

FIG. 1. Daily variation of the gross beta activity from dust filters for the period 21 May, 1956, to 21 May, 1957. The numbers at the top of the figure refer to the reported nuclear explosions described in Table I.

Filters showing considerable initial radioactivity were remeasured at intervals of a few days in order to obtain the rate of decay of the activity. It has been found (Hunter and Ballou 1951) that the intensity of the radioactivity resulting from nuclear fission decreases in accordance with the equation

$$I = At^{-k},$$

where I is the intensity of the gross activity, A is a constant which depends on the initial number of fissions, t is the time elapsed since the nuclear fission took place, and k is a constant which depends on the elapsed time t. Observed values for k which have been published range from 1.2 to 1.4. If the date of the nuclear explosion is known, then a log–log plot of I vs. t should yield a straight line with a slope of -1.2 to -1.4. It should also be possible to choose an explosion time which will give such a slope to the log–log plot of the decay curve for a filter, and in this way to arrive at the date of the explosion responsible for the filter activity. However, in the event that several nuclear fissions originate in a short time this method becomes unreliable. The material collected will consist of radioactive material decaying at several different rates and the dating of any particular explosion becomes very uncertain. This was the case with most of the active filters collected here. In all cases, if the initial points of the decay curve were fitted to a particular explosion date, the later points departed from the straight line slope, and this is probably due to a mixture of radioactive material having different times of origin. Similar results have been observed by Tajima and Doke (1956).

Aluminum absorption measurements were made for some of the more active filters and a semilog plot indicates that the beta activity is usually made up of several component energies. The half-thicknesses obtained ranged from 4 mg./cm.^{2} to 200 mg./cm.^{2} and are in agreement with published values (Heininger and Turkevich 1955, and Tajima and Doke 1956).

An approximate estimate of the radioactivity in the atmosphere at times of maximum activity can be made. The efficiency of the counting system was determined by making use of the 1.5 Mev. beta emission from the naturally occurring radioactive isotope K^{40} in a sample of potassium chloride. A thick sample of potassium chloride having the same area as a filter gave a counting rate comparable to that from a moderately active filter and the efficiency of the counting system was found to be approximately 2.0%. Calibration in this way assumes a uniform distribution of the radioactivity over the filter area and autoradiographs of the filters showed this to be the case in general. A typical autoradiograph is shown in Fig. 2. It can be seen that the activity of some particles is considerably higher than most and this condition makes the observed filter activity somewhat dependent on geometry and decreases the accuracy of any quantitative estimate of the atmospheric radioactivity. A comparison of the B.M. 2133 filter paper with a high collection efficiency glass fiber filter indicates that the collection efficiency of the B.M. 2133 filter for radioactive material is about 70%. Combining the collection and detection efficiencies with the observed counting rates an estimate of the radioactivity in the atmosphere can be made. Following a series of explosions activities up to approximately 10^{-14} curies/liter were observed. As can be seen from Fig. 1, this activity persists for some time after the tests are carried out. Some measurements on the natural radioactivity in the atmosphere have been made and activities ranging from 10^{-13} curies/liter to 10^{-15} curies/liter have been observed.

No detailed attempt has been made to correlate the observed radioactivity

with meteorological phenomena; however, some evidence of scavenging action of rain is indicated.

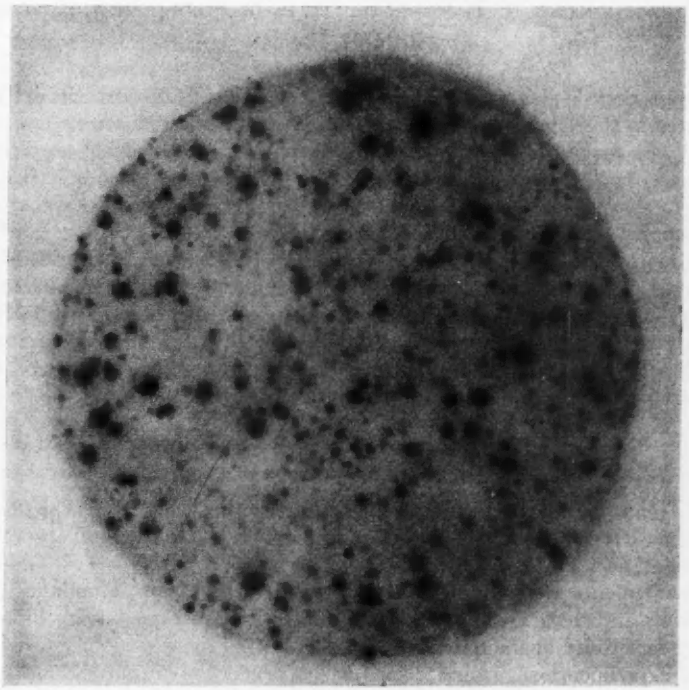

FIG. 2. Autoradiograph of a typical active dust filter.

The author would like to thank Dr. G. N. Whyte for his assistance in recording some of the data, and Dr. F. D. Sowby of the Radiation Services Section of the Department of National Health and Welfare for making available some of the filters.

HEININGER, C. and TURKEVICH, J. 1955. Progress Report Princeton University, Report NYO-3434.
HUNTER, H. F. and BALLOU, N. E. 1951. Nucleonics, **9**, No. 5, C-2.
TAJIMA, E. and DOKE, T. 1956. Science, **123**, 211.
THURONYI, G. 1956. Meteorol. Abstr. and Bibl. **7**, 616.

RECEIVED SEPTEMBER 23, 1957.
DIVISION OF APPLIED PHYSICS,
NATIONAL RESEARCH COUNCIL,
OTTAWA, CANADA.

A NOTE ON THE ELECTRONIC ATTENUATION COEFFICIENTS FOR SOME LOW Z ABSORBERS

J. L. BERGSTEINSSON, L. B. ROBINSON,[1] A. K. M. SIDDIQ,[2] R. J. HORSLEY,[3] AND R. N. H. HASLAM

Over a period of years total X-ray attenuation coefficients have been measured in this laboratory for several low Z absorbers, with a view to ascertaining the magnitude of the nuclear contribution to the total absorption coefficient in the energy range 10–25 Mev. The measurements have also yielded values of electronic X-ray absorption coefficients which may usefully be compared with theoretically predicted values.

The method of "nuclear detectors" as outlined by Haslam *et al.* (1953) was employed. This method involves the measurement of X-ray induced residual activity in various samples, with and without an absorber shielding them from the betatron beam. The ratio of the two activities thus obtained was measured as a function of the peak energy, E_0. These experimental ratios were then compared to the theoretical total attenuation ratio R,

$$R = \int_{E_t}^{E_0} \sigma(E)P(E, E_0)dE \Big/ \int_{E_t}^{E_0} \sigma(E)P(E, E_0)e^{-\mu_T(E)X}dE,$$

where $\sigma(E)$ is the cross section of the detecting reaction, $P(E, E_0)$ is the photon spectrum, E_t the threshold of the detecting reaction, $\mu_T(E)$ the total absorption coefficient, and X the absorber thickness.

Measurements were carried out using water, beryllium, aluminum, and carbon as absorbing media, and various detecting reactions having different energy sensitivity characteristics.

The experiments were carried out in "good geometry" and the measured ratios were corrected for secondary scattered radiation, this correction in all cases being less than 1.0% of the total absorption ratio. Also, precautions were taken to eliminate spurious activities in the detectors.

It should be noted that the method of "nuclear detectors" gives good counting statistics, allowing a fairly precise determination of a weighted average attenuation coefficient over an energy range of several Mev., but not giving a measurement of the coefficient at a particular energy. This situation is just the reverse of that for the case of "threshold detectors", as outlined by Adams (1948).

For details concerning the contributions of nuclear processes to the total absorption coefficient in the various absorbing media the reader is referred to Haslam *et al.* (1953) for the carbon absorber, Robinson (1954) for the beryllium and aluminum absorber, and Siddiq (1956) for the oxygen absorber.

[1]Now with Atomic Energy of Canada, Limited, Chalk River, Ontario.
[2]Now with the Department of Physics, University of Dacca, Dacca, East Pakistan.
[3]Now with the Ontario Cancer Commission, Hamilton, Ontario.

The theoretical total absorption ratio R was computed using nuclear absorption cross sections measured in this laboratory and elsewhere; the electronic absorption coefficients used were those due to White (1952). The cross sections $\sigma(E)$ of the detecting reactions were measured in this laboratory, and the spectral distribution $P(E, E_0)$ of the bremsstrahlung beam given by Katz and Cameron (1951) was used.

In the four absorbers used it was observed that the measured values of R were considerably smaller than the calculated ones. This was true even in the energy range where nuclear absorption was negligible so that practically the whole contribution to the calculated total absorption was due to electronic effects. It was thus concluded that the electronic absorption coefficients which had been used to calculate R were too high.

An arbitrary lowering of electronic coefficients by a constant percentage, which differed slightly for different absorbers, was carried out in order to secure agreement with experiment in energy regions where the nuclear effect was negligible, and the same percentage correction was extended to energy regions in which nuclear absorption played an appreciable part.

TABLE I

ELECTRONIC ABSORPTION COEFFICIENTS FOR CARBON

E, Mev.	White NBS 1003, barns/atom	White's values revised to fit experiment, barns/atom	Grodstein NBS 583, barns/atom
15.0	0.338	0.334	0.331
20.0	0.312	0.308	0.307

For example, Table I shows values of the electronic absorption coefficients for carbon. Column two contains the values as given by White (1952), column three the values of White lowered to give the best fit between experimental and calculated R values, and column four the values given by the same author in a more recent publication (Grodstein 1957). It is observed that the latter values are in better agreement with our values, adjusted on the basis of experiment, though somewhat lower.

Similar conclusions may be drawn for beryllium and for water absorbers from an examination of Fig. 1, which shows the results obtained with a zinc detector for these two absorbers. For data on the detecting reaction cross section, $Zn^{64}(\gamma, n)Zn^{63}$, the reader is referred to Katz *et al.* (1951).

Although experiments were carried out using an aluminum absorber these results are not discussed here since at the time of publication the cross section for the reaction $Al^{27}(\gamma, n)Al^{26}$ is in some doubt (Katz 1957).

Our conclusions are thus that in the energy range 15–20 Mev. the electronic absorption coefficients presented by Grodstein (1957) yield better agreement with experiment for water, beryllium, and carbon than those in the earlier tables, but appear rather too low.

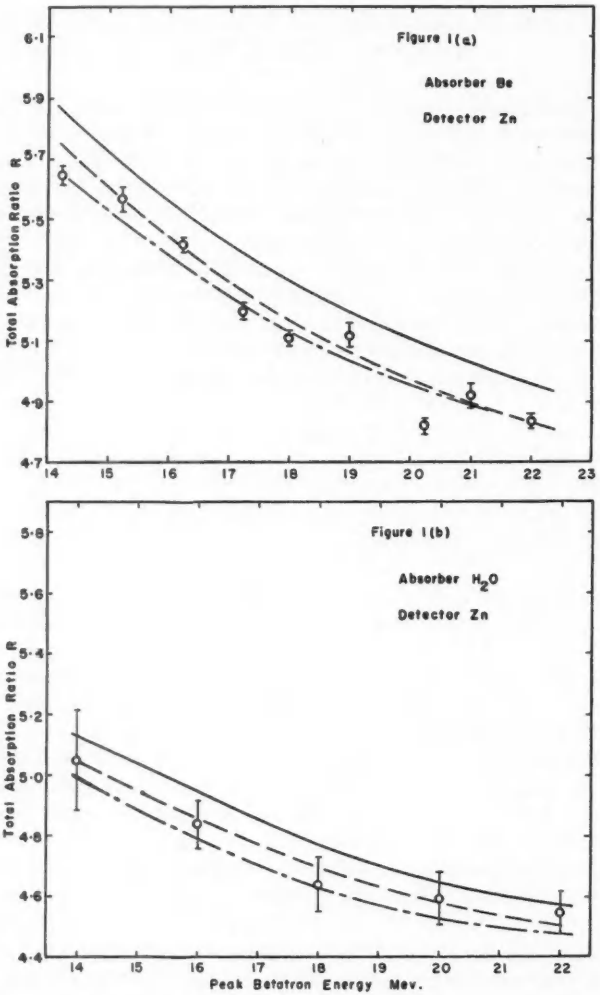

FIG. 1 Total absorption ratio vs. betatron operating energy for beryllium (*a*) and water (*b*). In each case the detecting reaction is $Zn^{64}(\gamma, n)Zn^{63}$. The solid curve represents R values obtained by use of electronic absorption coefficients from White; the dashed curve uses these coefficients lowered by 1.0%, while the "center-line" curve shows the result of using the new attenuation values (Grodstein).

ADAMS, G. D. 1948. Phys. Rev. **74**, 1707.
GRODSTEIN, G. R. W. 1957. National Bureau of Standards Circular No. 583.
HASLAM, R. N. H., HORSLEY, R. J., JOHNS, H. E., and ROBINSON, L B. 1953. Can. J. Phys. **31**, 636.
KATZ, L. 1957. Private communication.
KATZ, L. and CAMERON, A. G. W. 1951. Can. J. Phys. **29**, 518.
KATZ, L., JOHNS, H. E., BAKER, R. G., HASLAM, R. N. H., and DOUGLAS, R. A. 1951. Phys. Rev. **82**, 271.
ROBINSON, L. B. 1954. M.A. Thesis, University of Saskatchewan, Saskatoon, Sask.
SIDDIQ, A. K. M. 1956. Ph.D. Thesis, University of Saskatchewan, Saskatoon, Sask.
WHITE, G. R. 1952. National Bureau of Standards Report No. 1003.

RECEIVED OCTOBER 15, 1957.
PHYSICS DEPARTMENT,
UNIVERSITY OF SASKATCHEWAN,
SASKATOON, SASKATCHEWAN.

Under this heading brief reports of important discoveries in physics may be published. These reports should not exceed 600 words and, for any issue, should be submitted not later than six weeks previous to the first day of the month of issue. No proof will be sent to the authors.

Paramagnetic Resonance of Chromium in Guanidine Aluminum Sulphate

We have investigated the paramagnetic resonance spectrum of Cr^{+++} replacing Al^{+++} in guanidine aluminum sulphate hexahydrate, $C(NH_2)_3Al(SO_4)_2.6H_2O$. The measurements were made on a crystal in which about 2 atom per cent of the Al^{+++} was replaced by Cr^{+++}, at 3 cm. wavelength at the following temperatures: room temperature, 195° K., 77° K., and about 35° K., this last temperature being produced by desorbing helium from charcoal. Guanidine aluminum sulphate grows in hexagonal plates with trigonal ($C_{3v}^2 - P31m$) symmetry. Spectra were observed with the external magnetic field in the plane perpendicular to the trigonal axis, and in a plane containing the trigonal axis.

Two sets of spectra, a total of six lines, were observed, set 1 being about twice as intense as set 2. The lines were 40 gauss wide and signal-to-noise ratios of about 50:1 were observed on an oscilloscope display at room temperature. The line shape was approximately gaussian. No variation of the position of the lines was observed as the external magnetic field was rotated in the plane perpendicular to the trigonal axis. Measurements of the spectra with the field rotated in the plane containing the trigonal axis show that both sets of spectra can be fitted to the spin Hamiltonian

$$H = g\beta \mathbf{H}.\mathbf{S} + D\{S_z^2 - \tfrac{1}{3}S(S+1)\},$$

where $S = 3/2$. The z axis is the trigonal axis of the crystal. The symbols have their usual meanings (Bowers and Owen 1955). The values of the constants g and D for both spectra at different temperatures are given in Table I. The variation of the D's with temperature is shown in Fig. 1.

Interest in this salt is due to the fact that it is ferroelectric (Holden *et al.* 1955), and the

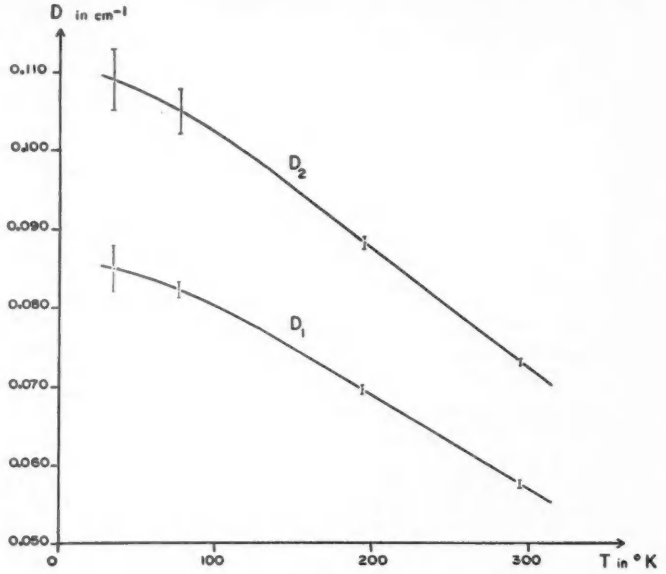

FIG. 1.

lattice distortions caused by ferroelectricity should change the crystalline field and hence show up in the paramagnetic resonance spectrum. Unfortunately, this salt starts to lose water of

TABLE I

D_1 AND D_2 AS FUNCTIONS OF T

	295° K.	195° K.	77° K.	35° K.
D_1 (in cm.$^{-1}$)	0.0576±0.0005	0.0696±0.0006	0.0822±0.0010	0.085±0.003
D_2 (in cm.$^{-1}$)	0.0730±0.0005	0.0882±0.0010	0.105±0.003	0.109±0.005

Extrapolated point of intersection at about $D = 0$ cm.$^{-1}$ and $T = 775°$ K.
$g = 1.975 \pm 0.005$ for all four temperatures.

crystallization above 100° C., a much lower temperature than the ferroelectric Curie temperature. The Curie temperature is not known, and has been estimated to be above 200° C. Guanidine aluminum sulphate hexahydrate has three aluminum ions in the unit cell, two of which are equivalent from symmetry considerations. This is sufficient to explain the relative intensities of the two sets of spectra. Holden *et al.* (1956) observed that different parts of a guanidine aluminum sulphate crystal have different electrical properties. We have examined the spectrum of crystal fragments cleaved from different parts of a large crystal and observed no difference in the paramagnetic resonance spectrum.

The crystals were also polarized in a strong electric field in the direction of the trigonal axis and depolarized in a weakening alternating electric field, with no effect on the paramagnetic resonance spectrum.

The paramagnetic properties of the Cr^{+++} ion are not very sensitive to changes in crystalline field. We have tried to grow crystals with Ti^{+++} as impurities, as these ions should show much more clearly the effect of lattice distortions, but we have so far had no success in these efforts.

Grateful acknowledgment is made to the National Research Council of Canada and to the President's Research Fund, U.B.C., for support of this work.

BOWERS, K. D. and OWEN, J. 1955. Repts. Progr. in Phys. **18**, 304.
HOLDEN, A. N., MATTHIAS, B. T., MERZ, W. J., and REMEIKA, J. P. 1955. Phys. Rev. **98**, 546.
——— 1956. Phys. Rev. **101**, 962.

RECEIVED AUGUST 23, 1957.
DEPARTMENT OF PHYSICS,
UNIVERSITY OF BRITISH COLUMBIA,
VANCOUVER, B.C.

J. M. DANIELS
H. WESEMEYER

A Study of the Boron Sites in Colemanite, $CaB_3O_4(OH)_3.H_2O$

A centrosymmetrical structure (Christ, Clark, and Evans 1954) was proposed for colemanite, $CaB_3O_4(OH)_3.H_2O$, at room temperature. However, it has been found (Davisson 1956) that this material is weakly piezoelectric and pyroelectric at room temperature and therefore apparently lacks a center of symmetry. At −2.5° C. colemanite undergoes a change of phase and is ferroelectric below this temperature (Goldsmith 1956). Nevertheless, the dielectric breakdown patterns are centrosymmetrical above and below the transition temperature of −2.5° C. and X-ray and optical techniques have failed to reveal any evidence of the transition. We have used nuclear magnetic resonance methods to obtain information about the boron sites and to observe some effects of the phase change.

The splitting of the B^{11} nuclear magnetic resonance signal in colemanite, caused by the perturbation of the nuclear Zeeman levels by the interactions between the nuclear electric quadrupole moments and the inhomogeneous electric fields existing at the boron sites, has been studied. The crystal, with its **b**×**c**, **b**, and **c** directions in turn held parallel to the rotation axis (i.e., perpendicular to the magnetic field), was rotated and the B^{11} spectrum was recorded at 15° intervals with a spectrometer employing an oscillating detector. At room temperature 14 resolved absorption lines, whose frequencies depend on the orientation of the crystal with respect to the magnetic field (H_0 = 8.75 kilogauss), were observed centered about a much stronger line which remained fixed at about 11.98 Mc./sec. When the crystal was oriented with the *b* axis either perpendicular or parallel to the magnetic field, the lines of related pairs coincided so that the spectrum consisted of only seven lines in addition to the strong central line.

The room-temperature spectra can be explained in complete detail if one assumes that the 12 boron sites in the unit cell are derived by the operation of the point group $2/m$ on the asymmetric unit (a single formula unit) and that the electrostatic interactions at two of the

three sites in the asymmetric unit are weak whereas the interaction at the third is strong. A quantitative analysis of the spectra gives values for the quadrupole coupling constants $(eQ/h)\partial E_z/\partial z$, the asymmetry parameters $\eta \equiv (\partial E_x/\partial x - \partial E_y/\partial y)/(\partial E_z/\partial z)$, and the direction cosines of the principal axes of the electric field gradient tensors. The values for the quadrupole coupling constants and asymmetry parameters are listed in Table I. Sites represented by different letters, K, L, and M, are unrelated so that the electric field gradient tensors at these sites differ in magnitude and orientation. Sites represented by the same letter but with different subscripts can be related by symmetry. For example, at room temperature the sites K_1, K_2, K_3, and K_4 are related by the point group $2/m$ so that the $\nabla\mathbf{E}$ tensors, at these sites, are identical in magnitude and differ only in orientation.

TABLE I

QUADRUPOLE COUPLING CONSTANTS AND ASYMMETRY PARAMETERS AT THE BORON SITES IN COLEMANITE

Boron sites	Quadrupole coupling constant $\frac{eQ}{h}\frac{\partial E_z}{\partial z}$ (Mc./sec.)	Asymmetry parameter $\eta = \left(\frac{\partial E_x}{\partial x} - \frac{\partial E_y}{\partial y}\right) \Big/ \frac{\partial E_z}{\partial z}$
K_1, K_2, K_3, K_4	0.436±0.002	0.48 ±0.01
L_1, L_2, L_3, L_4	0.309±0.002	0.83 ±0.01
M_1, M_2, M_3, M_4	2.540±0.003	0.058±0.001

It is interesting to speculate on a possible correlation between the electric field gradient tensors found in this work and the boron positions proposed by Christ, Clark, and Evans (1954). They propose that the three boron atoms in the asymmetric unit are located near the centers of two slightly distorted O_4 tetrahedra and a slightly distorted O_3 equilateral triangle. In the discussion to follow it will be assumed that only the oxygen nearest-neighbors make significant contributions to $\nabla\mathbf{E}$ at each of the boron sites. At the center of a perfect tetrahedron the symmetry is cubic so that $\nabla\mathbf{E}$ must be zero. In a slightly distorted tetrahedron, one would expect $\nabla\mathbf{E}$ to be small at the center although it need no longer be zero, but there seems to be no reason to expect the asymmetry parameter to take any specific value within its range (by definition $0 \leq \eta \leq 1$). One might reasonably expect $\nabla\mathbf{E}$ to be larger at the boron site near the center of the slightly distorted equilateral triangle than at the boron sites at the centers of the slightly distorted tetrahedra because in the triangle the average B—O distance is shorter than in the tetrahedra (Christ, Clark, and Evans 1954) and the symmetry is not as close to being cubic. Unless the triangle is greatly distorted, η should be small because the symmetry at the center of a perfect equilateral triangle requires that η be zero. There is little one can say regarding the orientations of the electric field gradient tensors except that the z principal axis of the tensor at the boron site near the center of the O_3 triangle should be approximately perpendicular to the plane of the triangle. As shown in Table I we have indeed found that the quadrupole coupling constants are small and the values of η are not unusual at two of the boron sites (K and L) in the asymmetric unit, whereas the quadrupole coupling constant is considerably larger and η is very small at the third site (M). Also, it follows from the atomic coordinates (Christ, Clark, and Evans 1957) that the z principal axis of the tensor at M is nearly normal to the plane of the O_3 triangle. This is shown by the direction cosines with respect to the **b**×**c**, **b**, and **c** directions, respectively, listed below:

Direction cosines of z principal axis	+0.123±0.005	−0.826±0.005	−0.549±0.005
Direction cosines of normal to plane	+0.094	−0.848	−0.521

These arguments strongly suggest that the boron sites which we have labelled K and L are in the O_4 tetrahedra and the M site is in the O_3 triangle.

Preliminary examinations of the B^{11} spectrum have been made at 15° C., which is still above the transition temperature of −2.5° C., and at −12° C. and −40° C. At 15° C. the point group, at least as far as the boron sites are concerned, is still $2/m$. However, at the temperatures −12° C. and −40° C. each absorption line, which at room temperature was due to resonances at two sites related by the center of symmetry, is split into two components indicating that the center of symmetry has disappeared. The members of related pairs of lines still coincide whenever the crystal is oriented with the b axis either parallel or perpendicular to the magnetic field, indicating that the twofold axis still exists. Thus colemanite in its ferroelectric phase appears to have the symmetry of point group 2. The phase transition is completely reversible, as the temperature of the crystal has been cycled many times between room temperature and −40° C. with no apparent effect on the room-temperature spectrum.

Further work is in progress.

We wish to thank Dr. C. L. Christ and Mrs. Joan R. Clark for making available, in advance of publication, the colemanite atomic coordinates. F. Holuj is grateful for financial support in the form of a Cominco Fellowship awarded by The Consolidated Mining and Smelting Company of Canada Limited. H. E. Petch gratefully acknowledges the award of a Summer Research Associateship by the National Research Council of Canada. We are happy to have this opportunity to acknowledge the generous contribution made by the Ontario Research Foundation for the purchase of the large electromagnet.

The research for this paper was supported by the Defence Research Board of Canada, under Grant number 9510–08.

CHRIST, C. L., CLARK, J. R., and EVANS, H. T. 1954. Acta Cryst. 7, 453.
——— 1957. Private communication.
DAVISSON, J. W. 1956. Acta Cryst. 9, 9.
GOLDSMITH, G. J. 1956. Bull. Am. Phys. Soc., Ser. II, 1, 322.

RECEIVED OCTOBER 28, 1957.
F. HOLUJ
H. E. PETCH
DEPARTMENT OF PHYSICS AND DEPARTMENT OF METALLURGY AND METALLURGICAL ENGINEERING,
HAMILTON COLLEGE, MCMASTER UNIVERSITY,
HAMILTON, ONTARIO.

The Zeeman Effect in the Spectra of Polyatomic Molecules[1]

Though the Zeeman effect in the spectra of atoms and diatomic molecules has been investigated in considerable detail in the optical region, no similar investigation of the Zeeman effect in polyatomic molecules has been carried out. Recently I have undertaken a study of the Zeeman effect of the absorption spectra of some relatively simple polyatomic molecules in the hope that it would provide some information regarding the nature of the excited electronic states of these molecules.

The study of the Zeeman effect always requires a strong magnetic field. Since many of the most interesting absorption spectra are weak, a magnetic field of large dimensions is required. In the present work, such a field has been obtained by discharging a 1200 μf. condenser at potentials up to 3000 volts through a single layer solenoid which surrounds the absorption tube. Solenoids from 40 to 100 cm. long have been used with the magnetic field varying between 40,000 and 15,000 oersteds. The magnetic field decayed as a highly damped oscillation with a frequency of about 1000 cycles. The continuous background for the absorption spectra was obtained from a Lyman-type discharge which was "fired" when the magnetic field reached its maximum. The duration of the Lyman flash is about 50 μsec. and therefore the magnetic field is essentially constant during the exposure. The spectra were photographed with a 10-meter grating spectrograph.

The band systems which have been examined and the results obtained are shown in Table I. Here it can be seen that only two of the band systems which have been examined are sensitive

TABLE I

Molecule	Band system, Å	Is a Zeeman effect observed?
Benzene	2600	No
Pyridine	3000	No
Pyrazene	3200	No
Acetylene[a]	2200	No
Diacetylene	2800	No
Sulphur dioxide	3000	No
Sulphur dioxide	3800	Yes
Carbon disulphide	3600	Yes

[a]This band system was photographed with a Hilger Littrow spectrograph.

to the magnetic field. A section of each of these is shown in Fig. 1. In this figure it can be seen that the magnetic field alters the general appearance of the SO_2 band but it is not possible to determine anything further in this complex band. The other bands of this system of SO_2

[1]Issued as N.R.C. No. 4577.

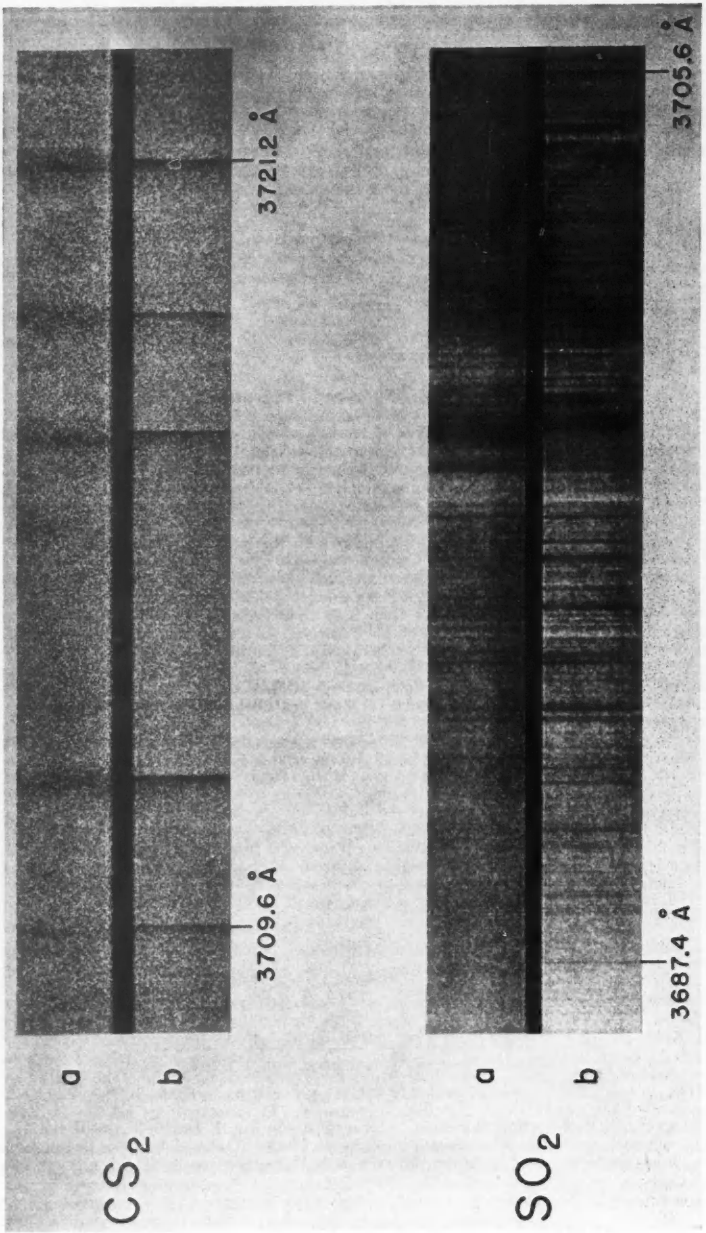

FIG. 1.

behave in a similar way. In CS_2, the fact that the field has broadened the sharp band heads is readily seen in the figure. In the absence of a magnetic field, other stronger bands of CS_2 show a rather simple rotational structure but, with the magnetic field present, no structure can be seen. All the CS_2 bands near the long wavelength limit of the spectrum behave similarly but towards shorter wavelengths there are a number of bands which are much less affected by the field.

The theory of the Zeeman splitting of the energy levels of a polyatomic molecule has not been worked out but any Zeeman splitting of an energy state implies that the molecule in that state possesses a magnetic moment. The large observed effects of the magnetic field on the CS_2 and SO_2 spectra show that the magnetic moment of the molecule in the upper state must be of the order of one Bohr magneton. By an extension of the theory of the Zeeman effect of diatomic molecules (Crawford 1939) it appears that a magnetic moment due to orbital angular momentum of the electrons could not give the observed effect. Also since both molecules are non-linear in the upper states investigated here, no orbital angular momentum is to be expected. Thus it appears that the magnetic moment must be due to electron spin and the observed Zeeman effect can be interpreted only if, contrary to what has usually been assumed, the upper states of the 3600 Å bands of CS_2 and the 3800 Å bands of SO_2 are triplet rather than singlet states.

The SO_2 bands appear to be too complex to yield much further information. The CS_2 bands, on the other hand, are relatively simple and have been analyzed in considerable detail by Lieberman (1940) and by Kleman (1957), and it appears that a detailed investigation of the Zeeman splitting of the rotational levels of this state is possible. This work will be carried on in the near future.

Crawford, F. H. 1939. Repts. Progr. in Phys. **6**, 155.
Kleman, B. 1957. Private communication; to be published.
Lieberman, L. N. 1940. Phys. Rev. **58**, 183.

Received November 14, 1957.
A. E. Douglas
Division of Pure Physics,
National Research Council,
Ottawa, Ontario.

Modification of the Basis for Roentgen Calibrations Between 0.5 and 3 Mev.*

As a result of recently accumulated information the National Bureau of Standards (U.S.) and the National Research Council (Canada) have decided to change the base for instrument calibrations in roentgens in the energy region from 0.5 to 3 Mev. This note announces the date the change will become effective and the reasons for it.

Only a few measurements with free-air chambers have been attempted in the megavolt region, and there seems to be some doubt as to the adequacy of all of these measurements. Most roentgen measurements in this region are actually made with cavity ionization chambers. Their sensitivity is determined either from the Bragg–Gray relation with a stopping-power correction, or from the calibration of a chamber with radium together with a value for the number of roentgens per hour at 1 cm. from 1 mg. of radium encapsulated in 0.5 mm. of platinum. Because the value of this constant (k) is determined from cavity-chamber measurements, it is evident that all measurements in roentgens in the megavolt region depend upon a stopping-power correction at the present time.

Until now the stopping-power corrections used by the National Bureau of Standards and the National Research Council have depended on the analysis of Laurence (1937), which was based on a theoretical assumption about the dependence of stopping power on atomic number. When this analysis was applied to the experimental determinations of k, the mean value obtained was close to 8.4 r./hour at 1 cm. from 1 mg. of radium encapsulated in 0.5 mm. of platinum. This value has been widely used. However, subsequent measurements of stopping powers by Bakker and Segre (1951) give a somewhat different dependence on atomic number. Furthermore, independent measurements recently made at the National Research Council (Whyte 1957*a*) and the National Bureau of Standards (Attix and Ritz 1957) of the ionization produced within cavity chambers having different wall materials are more nearly consistent with the values of Bakker and Segre than with those used by Laurence. Attix and Ritz (1957) have made a careful redetermination of k, using stopping-power corrections based on the values of Bakker and Segre and a stopping power for air based on a mean excitation potential of 80.5 ev., and including a correction for the difference in the "density effect" between the cavity wall and the gas based on the calculations of Sternheimer (1952); their value is

*Issued as N.R.C. No. 4578.

$k = 8.26 \pm 0.05$. Henry (1957) has recently obtained the value 8.24 ± 0.08. Finally, a re-evaluation by Whyte (1957*b*) of a number of measurements appearing in the literature gives a mean value of 8.22.

The evidence indicates the desirability of modifying the calibration basis for megavolt radiation. Therefore, after January 1, 1958, calibrations in the energy region from 0.5 to 3 Mev. at the National Bureau of Standards and the National Research Council will be based on the Bakker and Segre stopping-power values, an average excitation potential of 80.5 ev. for air, and the Sternheimer density correction. The value $k = 8.25$ r./hour at 1 cm. from 1 mg. of radium encapsulated in 0.5 mm. of platinum will be used instead of 8.4. For all instruments that were calibrated in roentgens with cobalt-60 gamma-rays prior to this date, the calibration factor should be reduced by 1.8% in order to agree with the new value (i.e., the calibration factor should be multiplied by 0.982).

ATTIX, F. H. and RITZ, V. H. 1957. J. Research N.B.S. (In press).
BAKKER, C. J. and SEGRE, E. 1951. Phys. Rev. **81**, 489.
HENRY, W. H. 1957. Private communication.
LAURENCE, G. C. 1937. Can. J. Research, A, **15**, 67.
STERNHEIMER, R. M. 1952. Phys. Rev. **88**, 851.
WHYTE, G. N. 1957*a*. Radiation Research, **6**, 371.
——— 1957*b*. Private communication.

RECEIVED OCTOBER 30, 1957.

C. GARRETT
X-RAYS AND NUCLEAR RADIATIONS,
DIVISION OF APPLIED PHYSICS,
NATIONAL RESEARCH COUNCIL,
OTTAWA, CANADA.

THE PHYSICAL SOCIETY

MEMBERSHIP of the Society is open to all who are interested in Physics.

FELLOWS pay an Entrance fee of £1 1*s*. ($3.00) and an Annual Subscription of £2 2*s*. ($6.00).

STUDENTS: A candidate for Studentship must be between the ages of 18 and 26, and pays an Annual Subscription of 5*s*. ($0.75).

MEETINGS: Fellows and Students may attend all Meetings of the Society including the annual Exhibition of Scientific Instruments and Apparatus.

PUBLICATIONS include the *Proceedings of the Physical Society*, published monthly, and *Reports on Progress in Physics*, published annually. Volume XX, 1957, is now available (price £3 3*s*. ($9.00)). Members are entitled to receive any of the Publications at a reduced rate.

Further information can be obtained from:

THE PHYSICAL SOCIETY
1, LOWTHER GARDENS, PRINCE CONSORT ROAD
LONDON, S.W.7, ENGLAND

CANADIAN JOURNAL OF PHYSICS

Notes to Contributors

Manuscripts

(i) General. Manuscripts, in English or French, should be typewritten, double spaced, on paper 8½×11 in. **The original and one copy are to be submitted.** Tables and captions for the figures should be placed at the end of the manuscript. Every sheet of the manuscript should be numbered.

Style, arrangement, spelling, and abbreviations should conform to the usage of recent numbers of this journal. Names of all simple compounds, rather than their formulas, should be used in the text. Greek letters or unusual signs should be written plainly or explained by marginal notes. Superscripts and subscripts must be legible and carefully placed.

Manuscripts and illustrations should be carefully checked before they are submitted. Authors will be charged for unnecessary deviations from the usual format and for changes made in the proof that are considered excessive or unnecessary.

(ii) Abstract. An abstract of not more than about 200 words, indicating the scope of the work and the principal findings, is required, except in Notes.

(iii) References. References should be listed **alphabetically by authors' names,** unnumbered, and typed after the text. The form of the citations should be that used in current issues of this journal; in references to papers in periodicals, titles should not be given and only initial page numbers are required. The names of periodicals should be abbreviated in the form given in the most recent *List of Periodicals Abstracted by Chemical Abstracts.* All citations should be checked with the original articles and each one referred to in the text by the authors' names and the year.

(iv) Tables. Tables should be numbered in roman numerals and each table referred to in the text. Titles should always be given but should be brief; column headings should be brief and descriptive matter in the tables confined to a minimum. Vertical rules should not be used. Numerous small tables should be avoided.

Illustrations

(i) General. All figures (including each figure of the plates) should be numbered consecutively from 1 up, in arabic numerals, and each figure referred to in the text. The author's name, title of the paper, and figure number should be written in the lower left corner of the sheets on which the illustrations appear. Captions should not be written on the illustrations (see Manuscripts (i)).

(ii) Line Drawings. Drawings should be carefully made with India ink on white drawing paper, blue tracing linen, or co-ordinate paper ruled in blue only; any co-ordinate lines that are to appear in the reproduction should be ruled in black ink. Paper ruled in green, yellow, or red should not be used. All lines should be of sufficient thickness to reproduce well. Decimal points, periods, and stippled dots should be solid black circles large enough to be reduced if necessary. Letters and numerals should be neatly made, preferably with a stencil (**do NOT use typewriting**) and be of such size that the smallest lettering will be not less than 1 mm. high when reproduced in a cut 3 in. wide.

Many drawings are made too large; originals should not be more than 2 or 3 times the size of the desired reproduction. Whenever possible two or more drawings should be grouped to reduce the number of cuts required. In such groups of drawings, or in large drawings, full use of the space available should be made; the ratio of height to width should conform to that of a journal page (4¾×7½ in.), but allowance must be made for the captions.

The original drawings and one set of clear copies (e.g. small photographs) are to be submitted.

(iii) Photographs. Prints should be made on glossy paper, with strong contrasts. They should be trimmed so that essential features only are shown and mounted carefully, with rubber cement, on white cardboard, with no space between them. In mounting, full use of the space available should be made to reduce the number of cuts required (see Illustrations (ii)). Photographs or groups of photographs should not be more than 2 or 3 times the size of the desired reproduction.

Photographs are to be submitted in duplicate; if they are to be reproduced in groups one set should be mounted, the duplicate set unmounted.

Reprints

A total of 50 reprints of each paper, without covers, are supplied free. Additional reprints, with or without covers, may be purchased at the time of publication.

Charges for reprints are based on the number of printed pages, which may be calculated approximately by multiplying by 0.6 the number of manuscript pages (double-spaced typewritten sheets, 8½×11 in.) and including the space occupied by illustrations. An additional charge is made for illustrations that appear as coated inserts. Prices and instructions for ordinary reprints are sent out with the galley proof.

Any reprints required in addition to those requested on the author's reprint requisition form must be ordered officially as soon as the paper has been accepted for publication.

Contents

Page

A continuously recording automatic auroral radar—*A. G. McNamara* - 1

On the theory of propagation of electromagnetic waves along a curved surface—*James R. Wait* - - - - - - - - - - - - 9

Evidence for the formation of long-lived Bi^{208} by the (*n*, 2*n*) reaction on bismuth—*J. C. Roy, T. A. Eastwood, and R. C. Hawkings* - - 18

The viscosity of liquid helium at frequencies of 11.8 and 35.5 kc./sec. —*K. M. Eisele and A. C. Hollis Hallett* - - - - - - - - - - 25

Absorption spectra of the halogen monoxides—*R. A. Durie and D. A. Ramsay* - - - - - - - - - - - - - - - - - - - 35

A large-area liquid scintillation counter and some measurements on high-energy cosmic-ray particles—*C. H. Millar, E. P. Hincks, and G. C. Hanna* - - - - - - - - - - - - - - - - - - - 54

Mass assignment of the 1.8 hour ytterbium activity—*R. H. Betts, Olive F. Dahlinger, and Donna M. Munro* - - - - - - - - - 73

The effect of heat treatment on low temperature internal friction maxima—*T. S. Hutchison and G. J. Hutton* - - - - - - - - 82

Pressure-induced infrared absorption of hydrogen and hydrogen–foreign gas mixtures in the range 1500–5000 atmospheres—*W. F. J. Hare and H. L. Welsh* - - - - - - - - - - - - - - - - - - 88

The luminescence response of phosphors to low energy ion bombardment—*C. F. Eve and H. E. Duckworth* - - - - - - - - - - 104

Diurnal variations in the number of shower meteors detected by the forward-scattering of radio waves. Part III. Elipsoidal theory—*C. O. Hines* - - - - - - - - - - - - - - - - - 117

An experimental study of the band intensities in the CN red system—*R. N. Dixon and R. W. Nicholls* - - - - - - - - - 127

Notes:

Resonance effects in the theory of meteor observability—*D. R. Moorcroft and C. O. Hines* - - - - - - - - - - - - - - 134

Measurement of artificial radioactivity in the atmosphere at Ottawa, Canada—*F. Terentiuk* - - - - - - - - - - - - 136

A note on the electronic attenuation coefficients for some low *Z* absorbers—*J. L. Bergsteinsson, L. B. Robinson, A. K. M. Siddiq, R. J. Horsley, and R. N. H. Haslam* - - - - - - - - 140

Letters to the Editor:

Paramagnetic resonance of chromium in guanidine aluminum sulphate—*J. M. Daniels and H. Wesemeyer* - - - - - - - - 144

A study of the boron sites in colemanite, $CaB_3O_4(OH)_3.H_2O$—*F. Holuj and H. E. Petch* - - - - - - - - - - - - - - - 145

The Zeeman effect in the spectra of polyatomic molecules—*A. E. Douglas* - 147

Modification of the basis for Roentgen calibrations between 0.5 and 3 Mev.—*C. Garrett* - - - - - - - - - - - - - - - 149

Printed in Canada *by* University of Toronto Press